UNIVERSITAT POLITÈCNICA DE VALÈNCIA

DEPARTAMENT DE COMUNICACIONS

Integrated Optical Filters for Microwave Photonic Applications

Javier Sánchez Fandiño

Supervisors:
Dr. Pascual Muñoz Muñoz
Prof. Dr. José Capmany Francoy

Valencia, May 2016

UNIVERSITAT POLITÈCNICA DE VALÈNCIA

DEPARTAMENT DE COMUNICACIONS

Integrated Optical Filters for Microwave Photonic Applications

Ph.D. Thesis by

Javier Sánchez Fandiño

Supervisors:
Dr. Pascual Muñoz Muñoz
Prof. Dr. José Capmany Francoy

Valencia, May 2016

A mis padres

I can live with doubt, and uncertainty, and not knowing.
I think it is much more interesting to live not knowing,
than to have answers which might be wrong.

Richard P. Feynman

Agradecimientos

Con estas breves líneas de texto se culminan más de cuatro largos años de trabajo y esfuerzo. Y, con ellas, se cierra también una etapa de mi vida.

Esta tesis y lo que para mí representa son fruto y consecuencia del trabajo directo e indirecto de muchas personas. Gracias en primer lugar a mis supervisores, Pascual Muñoz y José Capmany, por haberme dado la oportunidad de descubrir este mundo que es la ciencia y de guiarme a lo largo del camino. Gracias también a mis compañeros del Grupo de Comunicaciones Ópticas y Cuánticas (GCOC), por los momentos que hemos compartido. Un saludo especial para Christian, por nuestras estimulantes conversaciones a la hora del almuerzo; a Manuel, por su paciencia en el laboratorio; y cómo no a Iñigo, mi proselitista compañero de escalada, por su sabiduría de sobremesa y su apoyo en los momentos difíciles.

No puedo ni quiero olvidarme de agradecer a Francisco Soares y a Moritz Baier, y a toda la gente del grupo de diseño de láseres en el Fraunhofer Heinrich Hertz Institute, por su hospitalidad y amabilidad, y por haberme brindado la oportunidad de disfrutar de unos meses únicos en una ciudad tan especial como Berlín. Gracias también a Marcin y a Stephanos, mis compañeros de laboratorio, por regalarme su amistad y sentido del humor.

Por último, quiero dar las gracias a todas aquellas personas que han estado siempre cerca y que forman una parte fundamental de mi vida. A Sonia, porque somos un equipo. Y mis padres, porque si algo soy, a ellos se lo debo. Mamá, espero poder volar cada día más alto, más lejos, mejor.

Abstract

Microwave photonics (MWP) is a well-established research field that investigates the use of photonic technologies to generate, distribute, process and analyze RF waveforms in the optical domain. Despite its great potential to solve long-standing problems faced by both the microwave and electronics industries, MWP systems are bulky, expensive and consume a lot of power. Integrated microwave photonics (IMWP) is an emerging area of research that promises to alleviate most of these drawbacks through the use of photonic integrated circuits (PIC).

In this work, we have aimed at further closing the gap between the worlds of MWP and integrated optics. In particular, we have focused on the design and experimental characterization of PICs with reconfigurable, ring-assisted Mach-Zehnder interferometer filters (RAMZI), and demonstrated its potential use in different IMWP applications. These filters consist of a symmetric MZI loaded with ring resonators, which are coupled to the MZI branches by different optical couplers.

The contributions of this thesis can be split into two sections. In the first one, we demonstrate integrated optical couplers and reflectors with variable power splitting and reflections ratios. These exploit the well-known properties of tapered multimode interference couplers (MMI), and their inherent robustness makes them highly suitable for the implementation of both RAMZI and reflective filters. Besides, we study in detail the impact of manufacturing deviations in the performance of a 4x4 MMI-based 90° hybrid, which is a fundamental building block in coherent optical communication systems.

In the second section, we demonstrate the use of integrated RAMZI filters for three different IMWP applications, including instantaneous frequency measurement (IFM), direct detection of frequency-modulated signals in a MWP link, as well as in tunable, coherent MWP filters. A theoretical analysis of the limits and trade-offs that exist in photonics-based IFM systems is also provided. Even though these are early proof-of-concept experiments, we hope that further technological developments in the field will finally turn MWP into a commercial reality.

Resumen

La fotónica de microondas (MWP) es un campo de investigación que estudia el uso de tecnologías ópticas para generar, distribuir, procesar y analizar señales de RF. A pesar de su gran potencial para resolver algunos de los problemas a los que se enfrentan las industrias electrónica y de microondas, estos sistemas son voluminosos, caros y consumen mucha potencia. La fotónica de microondas integrada (IMWP) es un área emergente que promete solucionar todos estos inconvenientes a través de la utilización de circuitos ópticos integrados (PIC).

En esta tesis, hemos pretendido avanzar un poco más en el acercamiento entre estas dos disciplinas. En concreto, nos hemos centrado en el diseño y caracterización experimental de PICs con filtros reconfigurables basados en interferómetros Mach-Zehnder cargados con anillos (RAMZI), y demostrado su potencial uso en diferentes aplicaciones de IMWP. Los filtros RAMZI están hecho básicamente de un MZI simétrico cargado con anillos, los cuales a su vez se acoplan a las ramas del interferómetro a través de distintos acopladores ópticos.

Las contribuciones de este trabajo se pueden dividir en dos partes. En la primera, hemos demostrado acopladores y reflectores ópticos integrados con coeficientes de acoplo y reflexión variables. Éstos explotan las propiedades de los acopladores por interferencia multimodal (MMI), y su robustez les hace muy atractivos para la implementación de filtros RAMZI y de tipo reflectivo. Además, hemos analizado el impacto que las tolerancias de fabricación tienen en el rendimiento de un híbrido óptico de 90° basado en un MMI 4x4, el cual es un elemento fundamental en los sistemas de comunicaciones ópticas coherentes.

En la segunda parte, hemos demostrado el uso de filtros RAMZI en tres aplicaciones distintas de IMWP. En concreto, hemos utilizado dichos filtros para implementar sistemas de medida de frecuencia instantánea (IFM), detección directa de señales moduladas en frecuencia para enlaces fotónicos, así como en filtros coherentes y sintonizables de MWP. También hemos desarrollado un análisis teórico de las limitaciones y problemas que existen en los sistemas IFM. A pesar de que todos los experimentos realizados han consistido en prototipos para una prueba de concepto, esperamos que futuros avances tecnológicos permitan que la fotónica de microondas se convierta algún día en una realidad comercial.

Resum

La fotònica de microones (MWP) és un camp d'investigació que estudia l'ús de tecnologies òptiques per a generar, distribuir, processar y analitzar senyals de radiofreqüència. A pesar del seu gran potencial per a resoldre alguns dels problemes als que s'enfronten les indústries electrònica i de microones, estos sistemes son voluminosos, cars i consumixen molta potència. La fotònica de microones integrada (IMWP) és un àrea emergent que promet solucionar tots estos inconvenients a través de la utilització de circuits òptics integrats (PIC).

En esta tesi, hem pretés avançar un poc més en l'acostament entre estes dos disciplines. En concret, ens hem centrat en el disseny i caracterització experimental de PICs amb filtres reconfigurables basats en interferòmetres Mach-Zehnder carregats amb anells (RAMZI), i demostrat el seu potencial en diferents aplicacions de IMWP. Els filtres RAMZI estan fets bàsicament d'un MZI simètric carregat amb anells, els quals, al seu torn, s'acoblen a les branques del interferòmetre a través de distints acobladors òptics.

Les contribucions d'este treball es poden dividir en dos parts. En la primera, hem demostrat acobladors i reflectors òptics integrats amb coeficients de transmissió i reflexió variables. Estos exploten les propietats dels acobladors per interferència multimodal (MMI), i la seua robustesa els fa molt atractius per a la implementació de filtres RAMZI i de tipo reflectiu. A més a més, hem analitzat l'impacte que les toleràncies de fabricació tenen en el rendiment d'un híbrid òptic de 90 graus basat en un MMI 4x4, el qual és un element fonamental en els sistemes de comunicacions òptiques coherents.

En la segona part, hem demostrat l'ús de filtres RAMZI en tres aplicacions diferents de IMWP. En concret, hem utilitzat estos filtres per a implementar sistemes de mesura de freqüència instantània (IFM), detecció directa de senyals modulades en freqüència per a enllaços fotònics, així com en filtres coherents i sintonitzables de MWP. També hem desenvolupat una anàlisi teòrica de les limitacions i problemes que existixen en els sistemes IFM. A pesar de que tots els experiments realitzats han consistit en prototips per a una prova de concepte, esperem que futurs avanços tecnològics permeten que la fotònica de microones es convertisca algun dia en una realitat comercial.

Contents

Agradecimientos **viii**

Abstract **x**

Resumen **xii**

Resum **xiv**

Table of contents **xv**

List of figures **xix**

List of tables **xxvii**

I Introduction and basic concepts **1**

1 Introduction **3**
- 1.1 Objectives 6
- 1.2 Thesis outline 7

2 Design and synthesis of optical lattice filters **9**
- 2.1 Introduction 9
- 2.2 Optical lattice filters and the Z-transform 10
- 2.3 Optical lattice architectures 13
- 2.4 Ring-assisted Mach-Zehnder interferometer filters 15
  - 2.4.1 Description and basic properties 15
  - 2.4.2 Synthesis algorithm 16
  - 2.4.3 Practical considerations 19
- 2.5 Conclusions 22

II Optical couplers and reflectors based on multimode interference mechanisms 23

3 2x2 Multimode interference couplers with variable power splitting ratios 25
- 3.1 Introduction 25
- 3.2 Basic MMI theory 26
- 3.3 Tapered 2x2 MMIs 30
- 3.4 Design procedure 32
- 3.5 Tapered 2x2 MMIs in SOI 34
  - 3.5.1 Design 34
  - 3.5.2 Experimental results 35
- 3.6 Tolerance analysis case study: A 4x4 MMI-based 90° optical hybrid in InP 40
  - 3.6.1 Introduction 40
  - 3.6.2 Simulation procedure 41
  - 3.6.3 Results 44
- 3.7 Conclusions 46

4 Multimode interference reflectors based on aluminium mirrors in thick SOI 49
- 4.1 Introduction 49
- 4.2 Operation principle 50
- 4.3 2-port MIRs with arbitrary reflectivity 52
- 4.4 Aluminium mirror modelling 54
- 4.5 Device design 57
- 4.6 Measurement procedure and experimental results 59
- 4.7 Conclusions 64

III Microwave photonic applications of integrated optical filters 67

5 Instantaneous frequency measurement 69
- 5.1 Introduction 69
- 5.2 A photonic-based IFM receiver integrated in InP 71
  - 5.2.1 Operation principle 71
  - 5.2.2 Fabrication 74
  - 5.2.3 Experimental procedure 74
  - 5.2.4 Results and discussion 75
- 5.3 Exploring the practical limits of photonic IFM receivers 78
  - 5.3.1 Introduction 78
  - 5.3.2 IFM Theory 79
  - 5.3.3 Simulation results and discussion 88
- 5.4 Conclusions 94

6 Frequency discrimination for microwave photonic links 97
- 6.1 Introduction . . . 97
- 6.2 Theoretical background . . . 98
- 6.3 Design and layout . . . 103
- 6.4 Experimental characterization and discussion . . . 105
  - 6.4.1 Optical filters . . . 105
  - 6.4.2 Linearity and dynamic range . . . 107
- 6.5 Conclusions . . . 111

7 Coherent microwave photonic filters 115
- 7.1 Introduction . . . 115
- 7.2 Theoretical background . . . 117
- 7.3 Design and layout . . . 119
  - 7.3.1 Tunable lasers . . . 120
  - 7.3.2 RAMZI filter . . . 121
  - 7.3.3 Dual-drive MZM . . . 122
- 7.4 Experimental results . . . 122
  - 7.4.1 Fabrication and packaging . . . 122
  - 7.4.2 Experimental setup . . . 124
  - 7.4.3 Tunable lasers . . . 125
  - 7.4.4 Photodiodes . . . 127
  - 7.4.5 Thermo-optic heaters . . . 128
  - 7.4.6 RAMZI filter and polarization rotation issues . . . 129
  - 7.4.7 Dual-drive MZM . . . 134
  - 7.4.8 Coherent MWP filtering . . . 136
- 7.5 Conclusions and future work . . . 141

8 Conclusions and future work 143
- 8.1 Future work . . . 145

Appendix A 2D simulation of 3D devices: the effective index method 147

Appendix B List of publications 151
- B.1 Journal papers . . . 151
- B.2 Conference papers . . . 152
- B.3 Others . . . 153

Bibliography 154

List of Figures

1.1 Reconfigurable microwave photonics processor. 6

2.1 (a) Unbalanced Mach-Zehnder interferometer. (b) Equivalent digital filter representation. (c) Magnitude response (in dB) in the frequency domain. (d) Idem in the equivalent Z-transform domain. 11
2.2 (a) Modification of the magnitude response of an MZI (in dB) and the position of its zero as a consequence of a change in the lower-arm phase shift. (b) Idem when the amplitude of the zero ($\rho = |z_0|$) is changed due to a modification of the coupling constants. 12
2.3 Schematic diagram of an N-th order filter based on (a) cascaded MZIs, (b) cascaded ring-loaded MZIs, and (c) cascaded ring resonators. 13
2.4 (a) Schematic diagram of an N-th order ring-assisted MZI filter. (b) Equivalent digital filter representation. 15
2.5 (a) Magnitude response (in dB) of a 4-th order Chebyshev type II filter designed using Matlab$^{\mathrm{TM}}$ (black solid line). The response of the synthesized filter is also shown as a dotted grey line. (b) Idem for the phase transfer function (in rad.). The phase of the synthesized filter is shown here as a solid grey line. It differs only by a constant phase, which has no physical meaning. 18
2.6 (a) Magnitude response (in dB) of the ideal Chebyshev type II filter of Table 2.2 (black solid line). Ten simulations considering phase and amplitude errors with independent, uniform random distributions are plotted superimposed as solid grey lines. (b) Idem for the phase response. (c) Magnitude response (in dB) of the same filter when losses are taken into account. (d) Idem for the phase response. 20

3.1 (a) General diagram of an NxM MMI. (b) 3D diagram of a 2x2 MMI. (c) SEM picture of a 2x2 MMI fabricated in thick SOI. . . . 27
3.2 (a) Field profiles of the lowest order propagation modes. (b) Quadratic dependence of β_n with mode number n. 28

3.3 (a) Field propagation within an MMI. (b) Simulation of a real device, where the self-imaging effect becomes evident. 29

3.4 (a) Schematic diagram of types “A”, “C” and “D” with no crosscoupler. (b) Idem for type “B”. Note that this is a symmetrized version of the original device proposed in [56]. (c) Schematic diagram of types “A”, “C” and “D” when a crosscoupler is employed. (d) Idem for type “B”. 31

3.5 (a) Cross-section of the SOI waveguide. (b) Microscope picture of the fabricated devices. 35

3.6 (a) Measured transmission spectrum of a test straight waveguide. FP peaks due to spurious reflections are clearly observed. (b) Same spectra, but smoothed with a 0.71 nm window. 36

3.7 (a) and (b) Measured coupling ratios for MMIs#2 and #3 on die A1, respectively. Measured data is shown as solid red and black lines, while second-order polynomial fittings are also shown as dashed lines with the same colours. 37

3.8 (a) to (d) Measured spectral averages and standard deviations of the coupling ratios for MMIs#1 to #4, over the 1525-1575 nm wavelength range, for all dies. 38

3.9 (a) to (d) Measured spectral averages and standard deviations of the coupling ratios for MMIs#5 to #8, over the 1525-1575 nm wavelength range, for all dies. 39

3.10 Impact of coupling losses variability ($\Delta/2$) on the calculation of measured cross coupling ratios ($K_{1,1}$), as predicted by equation 3.21. 40

3.11 (a) Schematic diagram of a 90° hybrid. (b) Location of it within a coherent optical communication system. 41

3.12 (a) Cross-section of the simulated InP waveguide. (b) 3D diagram of the 4x4 MMI under consideration. Fabrication tolerances are shown along with the nominal design values. 42

3.13 (a) Conceptual representation of the dimensional stacking visualization technique. (b) Representation of the simulated figures of merit as compared against OIF specifications. Bandwidths over which these specifications are met for all possible manufacturing deviations are enclosed by solid red lines. 43

3.14 (a) Simulated CMRRs for the I and Q channels when the hybrid is accessed through either the local oscillator or signal ports (In-2 and In-4, respectively). Onlly nominal design values are considered. (b) Simulated CMRRs in the worst case tolerance scenario. (c) Simulated phase errors for the nominal design. (d) Simulated phase errors for the worst case tolerance scenario. 45

4.1 (a) 2x2 MMI. (b) Equivalent 2-port MIR with an aluminium mirror. 51

4.2 (a) Geometry of tapered 2x2 MMIs for types “A”, “C” and “D”. (b) Idem for type “B”. (c) and (d) Equivalent 2-port MIRs. 52

4.3 (a) Cross-section of the aluminium mirror layer stack. (b) 3D Model of a 2-port MIR with an aluminium mirror. (c) SEM picture of a fabricated device. 54
4.4 (a) Equivalent slab waveguide after applying the EIM. Each mode (n = 0, 1...) is represented here as a plane wave bouncing back and forth at the waveguide interfaces with a certain angle (θ_i^n). (b) Schematic representation of the resonant reflection of a plane wave (mode) upon incidence on the multilayer structure that forms the aluminium mirror. 55
4.5 (a) Simulated reflectivities for the type "B" device of Table 4.2 ($\rho/\tau = 0/100$), both using FDTD (grey solid line) and the quasi-analytical theory (black dashed line). (b) Idem for the type "A" device of Table 4.2 ($\rho/\tau = 50/50$). 57
4.6 (a) Schematic diagram of the structures employed to measure the effective reflectivities of the devices under test. (b) SEM picture of a test structure. 59
4.7 (a) Measured spectrum of the type "A" device of Table 2 ($\rho/\tau = 50/50$), after normalization with a test straight waveguide. (b) Simulated spectrum of the same structure using the theoretical model. (c) Measured transmission spectrum of a reference straight waveguide. (d) Relative contributions of the different resonant cavities present in the structure. 60
4.8 (a) Measured spectrum of the type "A" device of Table 4.2 ($\rho/\tau = 50/50$), after normalization with a test straight waveguide and smoothed with a 30 point moving average ($\simeq$120 pm). Maxima and minima are also shown as black triangles. (b) Extracted extinction ratios for different wavelengths. (c) Measured reflectivity and third-order polynomial fit (solid black line). (d) Reduction in reflectivity for each device in Table 4.2, as the smoothing window goes from zero to a size equal to the FSR of the FP. 61
4.9 (a) to (e) Average reflectivities (solid black lines) and standard deviations (grey dashed lines) for the 5 MIRs shown in Table 4.2, computed after measuring 9 different dies. (f) Black diamonds: Measured average and standard deviations of the reflectivities versus the simulated values at 1550 nm. Grey dashed line: Slope fitted to the data that provides an estimate of the average intrinsic losses both in the mirror and in the access waveguides. 63

5.1 Schematic diagram of the photonics-based IFM system. TL: Tunable laser. MZM: Mach-Zehnder Modulator. RAMZI: Ring-assisted Mach-Zehnder Interferometer filter. BC: Bias Controller. PD: Photodetector. ACF: Amplitude Comparison Function. 71
5.2 (a) Schematic diagram of a 2nd-order RAMZI filter (b) Picture of the fabricated filter. 72

5.3 (a) Complementary transfer functions of the elliptic filter under consideration (see Table 5.1). The optical sidebands of a DSB-SC are shown as they move away in frequency from the carrier, serving to illustrate the operation mechanism. (b) Idem for a single MZI filter, shown for comparison. (c) Simulated ACF of the ideal elliptic filter. (d) Simulated ACF of the MZI. 73

5.4 (a) Measured transmission spectra (solid red and blue lines) of the RAMZI filter. Ideal responses are shown as dashed black and grey lines, for comparsion. (b) Measured Sideband-to-Carrier (SCR) ratio versus modulation frequency. The inset shows a measured modulation spectra as a solid grey line, where the SCR is defined. . . . 75

5.5 a) Measured mean ACF (solid black line) and simulated ACF for the same power (dashed grey line). The simulation includes the data of Figs. 5.4(a) and 5.4(b), as explained in the text. (b) Simulated ACFs for different RF powers, showing how the ACF changes with input power. 76

5.6 (a) Measured RMS value of the frequency error as a function of modulation frequency (solid black line). The simulated value for the same RF power is also shown as a dashed grey line, for comparison. (b) Simulated RMS values of the frequency error for different RF powers. 77

5.7 Schematic diagram of the photonic IFM system under analysis. TL: Tunable laser. MZM: Mach-Zehnder Modulator. MZI: Mach-Zehnder Interferometer. BC: Bias Controller. PD: Photodetector. ACF: Amplitude Comparison Function. 80

5.8 (a) Difference between single-drive and series push-pull operation in a MZM. Note that in the former case the carrier amplitude in each arm is different, while in the latter it remains balanced since the modulation process affects both arms equally. (b) MZI and MZM parameters considered in the theoretical analysis. 81

5.9 Temporal evolution of signals inside the IFM system. (a) Input RF pulse. (b) Delayed RF pulse after propagation through the long MZI arm. (c) Resulting low-speed photocurrent term containing the information of the instantaneous frequency. 85

5.10 Simulated ACFs for different system imperfections. (a) Bias phase error in the MZI (ϕ_I^e). (b) Bias phase error in the MZM (ϕ_M^e). (c) Finite extinction ratio in the MZI (ER$_I$). (d) Finite extinction ratio in the MZM (ER$_M$). Simulation values for all four figures are: Z$_{in}$ = 50 Ω, P$_{RF}$ = 0 dBm, V_π^{AC} = 3 V, P$_o$ = 20 mW and $\mathcal{R}$ = 0.9 A/W. All other parameters, except that under analysis, are assumed ideal. 89

5.11 Effect of (a) high powers and (b) low powers in the ACF. Simulation values are: Z$_{in}$ = 50 Ω, V_π^{AC} = 3 V, P$_o$ = 20 mW, $\mathcal{R}$ = 0.9 A/W and I_{Dark} = 1 nA. All other parameters are ideal. 90

5.12 Contribution of different order harmonic terms ($n = 1, 3, 5$) to the upper photocurrent (i^{up}). Simulation values are the same of those of Fig. 5.11, with $\mathrm{P}_{RF} = +25$ dBm. 91
5.13 (a) Evolution of ACF with different RF powers. (b) Normalized frequency bias error versus input RF power, assuming different values of both ER_M and ER_I. All other simulation parameters are listed in Table 5.2. 93

6.1 Architecture of a FM-DD MWPL link. 99
6.2 (a) V-shaped filter with linear ramps in *optical intensity*. (b) X-shaped filters with linear ramps in *electric field* (quadratic in intensity). 100
6.3 Diagram of the designed FM-DD PIC. Transfer functions are schematically shown at the different output ports of each filter for illustration purposes. 102
6.4 (a) Simulated transfer functions of the two complementary outputs (*Bar* and *Cross*) of the *Input filter*. (b)-(c) Simulated transfer functions of *Filter 1* and *Filter 2*, respectively, designed to provide a linear ramp in optical intensity. (d) Total response at the input of each branch of the photodetector. 104
6.5 Pictures of the manufactured chips. 105
6.6 Experimental setup employed for the characterization and adjustment of the RAMZI filters. 106
6.7 (a) Measured transfer functions of the two complementary outputs (*Bar* and *Cross*) of the *Input filter*. (b) Measured transfer function for the *Bar* output of *Filter 1*. (c) Idem for the *Cross* output of *Filter 2*. (d) Cascaded responses at both inputs of the photodetector. Three wavelength points were the system linearity was measured are marked for clarity: Left = 1549.022 nm, Null = 1549.109 nm and Right = 1549.184 nm. 107
6.8 (a) Experimental setup employed for the two-tones test. (b) Close up picture of the chip mount during measurement. 108
6.9 (a) Schematic diagram of the most important frequency components that appear in a two-tones test. (b) Typical SFDR measurement. . 109
6.10 (a) Fitted slopes for the fundamental component. (b) Fitted slopes for the IMD3 products. Those points close to the ideal value (3) are enclosed with a dashed grey line. 110
6.11 (a) and (b) SFDR measurements for the best and worst cases, respectively. 111

7.1 Schematic diagram of a coherent MWP filtering system. TL: Tunable laser. SSB Mod.: Single-sideband modulator. PD: Photodetector. 117
7.2 (a) Block diagram of the designed InP PIC. (b) Mask layout. . . . 119

7.3 (a) Block diagram of the designed DBR laser. (b) Simulated reflection spectra for both the rear and front DBR sections. Cavity modes are also shown. 120
7.4 (a) Magnitude response (in dB) of the ideal (solid black line) and lossy (solid grey line) RAMZI filter. (b) Idem for the phase response. 122
7.5 Mask layout of the designed dual-drive MZM modulator. 123
7.6 (a) Picture of a fabricated die. (b) Packaged chip. 123
7.7 (a) Diagram of the experimental setup employed for BB characterization. TL: Tunable laser. PC: Polarization controller. OPA: Optical polarization analyzer. Pol: In-line fiber polarizer. PM: Power meter. OC: Optical coupler. OSA: Optical spectrum analyzer. (b) Picture of the package during characterization. 124
7.8 (a) and (b) CW spectra of both TL 1 and TL 2. (c) Cavity formed by the output of TL 2 and a termination photodiode, which creates spurious side modes. (d) PI curve of TL 1. 126
7.9 (a) Wavelength shift versus current when pumping the rear DBR section of TL 1. (b) Idem when pumping the intra-cavity phase shifter (PS). 127
7.10 (a) to (c) Dark currents of PD 1 to PD 3, respectively, for different reverse voltages and operation temperatures. 127
7.11 (a) Measured currents at the output of the three DC PDs when the current injected into the heater of the 2x3 MZI was varied between 0 and 85 mA. (b) Calculated phase shift versus electrical power. P_π is also shown. 128
7.12 Polarization alignment procedure employed to characterize the RAMZI filter. 129
7.13 (a) and (b) Filter transmission spectra for two random input polarizations. (c) Measured state of polarization at the *Output* fiber for different currents pumped into the rear DBR section of TL 1. (d) Idem for one of the thermo-optic heaters of the RAMZI filter, with TL 1 kept at a fixed wavelength. 130
7.14 (a) and (b) Schematic diagram and picture, respectively, of the free-space setup used to measure polarization rotation inside the 2x3 MZI. (c) Transmission spectra for both output polarizations (TE and TM) when only TE is excited at the input. (d) Idem for TM excitation. 132
7.15 (a) Cross-section of the deeply etched waveguides in the Oclaro platform. (b) and (c) Polarization rotation in a 90° bend, which can be modelled as a symmetric MZI. 133
7.16 (a) to (c) Evolution of the TE and TM powers at the output of a bend with R =150 μm, as a function of the arc length (L), for different values of θ. (d) Polarization crosstalk (TE/TM, in dB) for a 90° bend with R =150 μm. 134

7.17 (a) Experimental setup employed for characterizing the dual-drive MZM. VNA: Vector network analyzer. H90°: 90° RF hybrid. OSA: Optical spectrum analyzer. (b) Median SSB extinction as a function of the bias voltage. (c) Overlapped spectra for a bias voltage of -8 V (optimum). (d) Dependence of the SSB extinction with modulation frequency for the same bias point. 135

7.18 (a) Experimental setup of the electrical to optical (E/O) measurement. VNA: Vector network analyzer. LCA: Lightwave component analyzer. H90°: 90° RF hybrid. EDFA: Erbium-doped fiber amplifier. OC: Optical coupler. OSA: Optical spectrum analyzer. OPA: Optical polarization analyzer. (b) Idem for the electrical to electrical (E/E) measurement. 137

7.19 (a) to (c) Measured emission spectra of TL 1 vs current injected into the PS section, for three different sets of currents in the thermo-optic phase shifters of the RAMZI filter (#1, #2 and #3). (d) to (f) Shift in the central frequency of TL 1 for the same conditions. 138

7.20 (a) to (c) Measured RF responses (E/O) of the coherent MWP filter as the central wavelength of TL 1 is shifted (see Fig. 7.19), for three different sets of currents in the thermo-optic heaters of the RAMZI filter (#1, #2 and #3). The solid black line corresponds to the initial response, while the dashed red line is the measured response for the maximum pumping current. All the measurements in between are shown as light grey lines. (d) to (f) Evolution of the -3 dB bandwidth as a function of the PS current. (g) to (i) Polarization rotation observed at the output. 139

7.21 (a) Measured E/E response when TL 1 is switched on. (b) Idem when TL 1 is switched off. 140

A.1 (a) Waveguide cross-section. (b) Sectioning of the original problem with the EIM. (c) Step I. (d) Step II. 148

A.2 (a) 3D 1x2 MMI under analysis. (b) Equivalent 2D structure after the reduction procedure. 149

A.3 (a) and (b) Fundamental and first order modes (n^0_{eff} and n^1_{eff}, respectively) of the 1x2 MMI. (c) and (d) Fundamental and first order modes (n^0_{Slab} and n^1_{Slab}, respectively) of the equivalent slab waveguide. 150

List of Tables

1.1 Typical values and capabilities for some photonic integration platforms. 5

2.1 Main optical lattice filter architectures. The number of required couplers and phase shifters is shown as a function of the filter order (N). 14
2.2 Coefficients of both the numerator (p_n) and denominator (q_n) of the target filter. The synthesized values of the coupling constants (κ_n) and phase shifts (ϕ_n, β_u and β_d, in radians) are also shown. . 19

3.1 Types and properties of MMIs with restricted interference mechanisms [80]. 30
3.2 Geometrical parameters of the MMIs with non-uniform power splitting ratios proposed by Bachmann et al. [77]. The minimum width ($W_{\min}$) is also shown as a function of both the access taper width (W_t) and the minimum waveguide spacing (g). 32
3.3 MMI design parameters. All dimensions are given in μm. A common width for the access and multimode waveguides of 0.45 μm and 10 μm were employed, respectively. The length of the taper is also equal for all designs ($l_t = 50\ \mu m$). 34

4.1 Geometrical parameters of 2-port MIRs. Those in italics are obtained after introduction of a crosscoupler. N/A = Not applicable. 53
4.2 Physical dimensions and BPM simulation results of the 5 different fabricated devices. The width is common for all designs (11.7 μm), and no crosscouplers are employed ($\mathrm{L_c}/2$=0). 58
4.3 Estimated reduction in measured reflectivity due to smoothing. . . 62

5.1 Coefficients of both the numerator (p_n) and denominator (q_n) of the target filter. The synthesized values of the coupling constants (κ_n) and phase shifts (ϕ_n, β_u and β_d, in radians) are also shown. . 72

5.2 Simulation parameters. 92

6.1 Coupling constants (in lin. units) and optical phase shifts (in *rad*) for the three filters. 103
6.2 Physical dimensions and BPM simulation results of the 4 MMI couplers. A common width of 12 μm was used for all designs. 105
6.3 Measured slopes of the fundamental (b) and IMD3 products (d), IIP3s, OIP3s, Gains and SFDRs for the selected points of Fig. 6.10(b). 110

7.1 DBR design parameters. 121
7.2 Dimensions (in μm) and BPM simulation results of the RAMZI filter couplers. 122
7.3 Measured resistance of all the on-chip thermo-optic heaters. 128

Part I

Introduction and basic concepts

Chapter 1

Introduction

Ever since the demonstration of the first laser sources in the 1960s by Maiman and Javan [1, 2], and the following predictions by Kao that led to the realization of the first low loss silica fibers in the 1970s [3], optical fiber communication has evolved to become one of the key enabling technologies of modern information society. The Internet as we know it today, for example, would have not been possible without the existence of optical transmission systems with ever increasing complexity, which have been able to deliver increases of orders of magnitude in transmission capacities [4]. In turn, this has created a new range of industries that have had a profound socio-economic impact at a global scale. As a proof of its great importance, Kao himself was awarded the 2009 Nobel prize in Physics for his *groundbreaking achievements concerning the transmission of light in fibers for optical communication* [5].

The explosive growth of optical networks and communication systems has been fuelled by the rapid progress in the performance of its fundamental components. These include for example the development of efficient directly-modulated semiconductor lasers, external electro-optic modulators and photodetectors [6, 7]; as well as high gain and broad bandwidth optical amplifiers [8]. The availability of these basic elements and their significant cost reduction brought about by mass manufacturing not only has spurred optical communications, but it has also given birth to an interdisciplinary research field that is widely known today as microwave photonics (MWP). Generally speaking, MWP is *the study of photonic devices operating at microwave frequencies, and their application to microwave and optical systems* [9]. As a research area at the interface between the worlds of RF and optics, it draws techniques, concepts and ideas from both of them, either seeking to improve upon already existing solutions or by providing new capabilities that would otherwise prove impossible with previous approaches. Applications include radio-over-fiber for antenna remoting and CATV systems [10, 11]; optical beamforming networks [12]; photonics-based tunable RF filters, phase shifters and true time-delay lines [13]; ultra-wideband signal generation [14]; instantaneous microwave frequency measurement [15, 16]; photonic analog-to-digital conversion [17, 18]; as well as interrogation of fiber Bragg grating sensors [19].

Despite the numerous results and experimental demonstrations that have been published in the scientific literature so far, most of these applications have not yet become a widespread commercial reality. The reason behind this lack of success can be attributed to several factors, including lack of substantial investment and/or key figures of merit falling behind those of their electronic counterparts. In particular, MWP systems are typically bulky, consume a lot of power and are significantly expensive, as they have been mostly implemented by interconnecting discrete optical components [20, 21]. This has relegated the deployment of MWP systems to a few niche markets, like in distributed antenna systems [9, 10, 22], military [23–25] and radio astronomy applications [26].

Cost, size and power consumption are drawbacks that are not unique to MWP, but also apply to all other existing optical communication systems. It is for that reason that, similarly to what had happened before in the semiconductor industry, significant efforts have been made over the past few decades to develop photonic integration processes that could be capable of embedding a whole optical system into a single monolithic chip [27]. Starting from the early proposals by Shubert and Harris [28], as well as Miller at Bell Labs [29], integrated optics has slowly but steadily evolved over time, opening the door to the creation of photonic integrated circuits (PICs) with unprecedented levels of complexity. Arguably, the most notable and commercially successful example of the revolutionary potential of this approach is the 100 Gb/s and 500 Gb/s superchannel transceivers developed by the US company Infinera [30, 31], featuring more than 600 functions in an area of a few squared millimetres.

Despite its attractiveness, complex PIC manufacturing is very expensive, as it requires not only building and/or maintaining a clean room, but also improving the fabrication process itself. As a consequence, PIC research and development has usually stayed out of reach, financially speaking, for most small research groups as well as small to medium-sized companies [32]. In early 2007, and by mimicking the concept of fabless manufacturing in electronics, several european players joined forces to provide a solution to this problem. The purpose of the ePIXnet initiative was to strengthen the european position in photonic integration research by organising a *shared access to unique and expensive technological infrastructures* [33]. In essence, big research institutes and foundries would offer other external players (users) the possibility to manufacture PICs at their facilities with a reduced price, sharing the costs of fabrication via the organization of multi-project wafer runs (MPW). In a MPW run, the area of a single wafer is distributed among several users, so the fabrication costs can also be shared at the expense of receiving a fewer number of dies. Besides, complex devices that require a great deal of expertise in semiconductor materials and fabrication, such as lasers and modulators, are offered as building blocks (BB) by the foundry so the users can directly place them in their designs. The concept of *generic photonic integration* was born [34, 35].

As of 2016, several broker organizations are currently offering MPW run services in different integration technologies, each one with their own advantages

Technology	InGaAsP/InP			SOI	Si_3N_4/SiO_2	
Foundry	Oclaro	HHI	Smart	IMEC	TriPleX	
Wav. type	Deep	E1700	Deep	Strip	Double strip	Strip
Width [μm]	1.5	2.0	1.5	0.45	1.2	2.8
Height [μm]	3.6	1.7	2.15	0.2	0.5	0.08
Loss [dB/cm]	[5.5-6]	[0.75-0.85]	[3-5]	[1.68-1.76]	[0.1-0.5]	0.03
Radius	150	250	100	5	125	2000
Optical amplifier	√	√	√	×	×	×
Photodetector	√	√	√	√	×	×
Thermo-optic	√	√	√	√	√	√
Electro-optic	√	×	√	√	×	×
Current-injection	√	√	×	√	×	×

Table 1.1: Typical values and capabilities for some photonic integration platforms.

and disadvantages. For example, ePIXfab offers access to state-of-the-art Silicon on Insulator (SOI) european foundries such as IMEC, CEA-Leti and VTT, while the now extinct OpSIS initiative did the same in the USA in collaboration with the Institute for Microelectronics (IME) in Singapore. Silicon photonics is indeed an exciting research field, which has gained significant momentum since the early 2000s as it is a potential candidate for seamless photonic-electronic integration [36]. However, the creation of highly efficient, electrically-pumped silicon lasers has so far proved elusive, as it is not a direct bandgap semiconductor material [37]. In this regard, quaternary materials such as InGaAsP/InP are very promising candidates, capable of integrating both active and passive BBs in the same substrate, though at the expense of a lower integration density. Europe is still leading the way in generic InP photonic manufacturing, with JePPIX organizing MPW runs for the HHI, Oclaro and Smart Photonics platforms [35]. Last but not least, LioniX in the Netherlands has recently developed a passive technology based on a combination of silicon nitride (Si_3N_4) and silicon oxide (SiO_2), called TriPleX, which has achieved record low propagation losses with optimized waveguide cross-sections [38]. Some key metrics for these platforms, like propagation losses and bending radius, are shown for illustration purposes in Table 1.1, along with some of the offered BBs.

From all the above, it is clear that integrated optics has the potential to solve some of the practical challenges that have plagued the commercial development of MWP, in particular cost and size. This has lead to the emergence of yet another exciting research area, which is known as integrated microwave photonics (IMWP) [20]. Even though it is still in its infancy, multiple applications have been demonstrated so far employing different integration technologies. These include, for example, programmable optical beamformers [39]; coherent reconfigurable MWP filters [40, 41]; tunable true time-delay lines [42]; as well as optical phase-locked loops and integrated frequency discriminators for detection of phase and frequency modulated signals [43, 44], to name just a few. Up to now, each reported chip has implemented a single functionality. However, more recent studies already foresee that, with the further development of photonic integration,

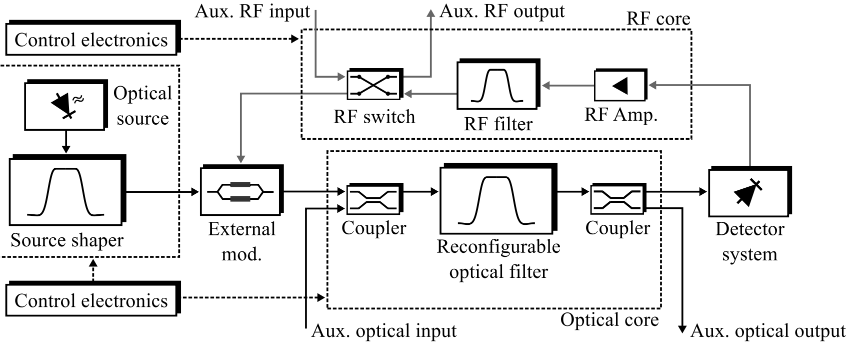
Aux. RF input
Aux. RF output
RF core
Control electronics
Optical source
RF switch
RF filter
RF Amp.
Source shaper
External mod.
Coupler
Reconfigurable optical filter
Coupler
Detector system
Control electronics
Aux. optical input
Optical core
Aux. optical output

Figure 1.1: Reconfigurable microwave photonics processor.

multi-purpose and fully reconfigurable MWP processors might become viable in the near future [21, 45, 46]. The idea of implementing multiple applications in the same monolithic substrate is similar to that of electronic Field Programmable Gate Arrays (FPGAs) and Programmable Systems on a Chip (PSOC), where the physical interconnections among a set of hardware elements are defined via software.

A block diagram of the MWP processor concept is shown in Fig. 1.1, after [45]. As it can be seen, there exists an optical core that is made of a reconfigurable, integrated optical filter. Filters in planar lightwave technology are typically made of a periodic concatenation of simpler unit cells, such as Mach-Zehnder interferometers (MZIs) and ring resonators. They are of special interest because they offer the possibility to use on-chip actuators, such as thermo-optic and current-injection phase shifters, to synthesize virtually any transfer function in real time. This has been exploited for example in dispersion compensation and gain equalization systems for wavelength divison multiplexed (WDM) transmission networks [47, 48]. However, it definitely constitutes an advantage in the case of MWP, where multitude of the aforementioned functionalities either rely on or will significantly benefit from the existence of such a tunable optical core. Tunable optical lattice filters have been demonstrated already in a variety of technology platforms, including InGaAsP/InP [40, 49], SOI [50–52], thick SOI [53] and TriPleX [46, 54].

1.1 Objectives

In this thesis, we aim to further bridge the gap between the worlds of MWP and integrated optical filters. In particular, we will focus on the design, synthesis and experimental characterization of reconfigurable, ring-assisted Mach-Zehnder interferometer filters (RAMZI) in different photonic integration platforms. RAMZIs are a specific lattice filter architecture that consists of a symmetric MZI loaded with a series of equal length ring resonators [55]. The rings are coupled to the MZI arms by a set of optical couplers, each one with a different power coupling constant.

Different transfer functions can be obtained by tuning the coupling constants and optical phases of the rings.

On one hand, couplers with arbitrary power splitting ratios will be investigated in detail, as they are a essential for the implementation of such filters. To be more precise, we will demonstrate how these couplers, as well as their reflective counterparts, can be implemented by means of tapered 2x2 multimode interference couplers (MMIs) [56]. Detailed simulation and experimental results of both type of devices will also be provided, together with an overall theoretical description of their operation principle.

On the other hand, we will explore the applicability of integrated optical filters in different MWP systems. By combining them with other BBs in a single chip, applications such as instantaneous frequency measurement receivers, frequency discriminators for frequency-modulated links and reconfigurable MWP filters will be demonstrated.

1.2 Thesis outline

This thesis is organized in 3 well-defined sections.

- Section I, to which this introductory chapter belongs, motivates the work and introduces the reader to the world of optical lattice filters. Chapter 2 first starts exploring the connection between optical lattice and digital filters, providing the basic mathematical tools and notions required to understand the following sections. It then compares the advantages and disadvantages of different lattice architectures, and focuses on RAMZI filters because of their greater flexibility and simplicity. The chapter concludes with an in-depth discussion of the steps and algorithms that need to be followed to design and synthesize RAMZI filters, as well as some general comments on more practical aspects.

- In section II we tackle a frequent problem that PIC designers face when implementing RAMZI filters. That is, how to design compact and robust optical couplers with an arbitrary power splitting ratio. This difficulty is solved with the use of tapered 2x2 MMIs. Chapter 3 first provides a comprehensive description of the theoretical principles behind MMIs, which is later followed by the design and experimental characterization of several of these devices in a SOI platform. Even though they are in general resilient against fabrication errors, the suitability of MMIs for some specific applications can be impacted by the tolerances of the manufacturing process. As an example, chapter 3 ends with an exhaustive simulation analysis of the impact that manufacturing errors have on the performance of 4x4 MMI working as a 90° in a coherent receiver system.

  Chapter 4 continues by expanding the ideas exposed in chapter 3, and shows how tapered 2x2 MMIs might be adapted to create broadband mirrors with arbitrary reflection/transmission ratios, also known as multimode interference reflectors (MIRs). After a theoretical description, experimental results of multiple devices fabricated in a thick SOI technology are provided, demonstrating the feasibility of this approach. MIRs might be interesting for the future implementation of on-chip mode-locked and CW lasers, as well as reflective filters.

- Section III explores different MWP applications in which RAMZI filters can be employed. We first start in chapter 5 experimentally demonstrating an instantaneous frequency measurement (IFM) receiver implemented with a second-order RAMZI filter in InP. Afterwards, we proceed to theoretically explore what are the fundamental limitations of this kind of systems, trying to both raise and answer questions that had not been previously addressed in the literature. As we will see, the precision of photonics-based IFM receivers critically depends on the RF power of the signal under test, as well on the non-ideal behaviour of some of their basic elements, such as the Mach-Zehnder modulator that generates the double sideband suppressed-carrier modulation.

  In chapter 6 the use of frequency discriminators for detecting frequency-modulated optical signals is introduced. This is motivated by its potential to increase the linearity of MWP links. The chapter starts with a short theoretical discussion, where the subtleties that arise when considering different types of discriminator slopes and shapes are examined. Next, we provide details about the design, synthesis and fabrication of a reconfigurable frequency discriminator in a generic InP platform, which includes a high-speed balanced photodetector. The chapter ends with experimental results at both device and system levels. In particular, the measured transfer functions of the discriminator and a standard two-tones test for quantifying its linearity.

  Chapter 7 reports the last of the MWP applications explored in section III: a fully integrated coherent MWP filter. First, a brief theoretical introduction is given. Afterwards, the chapter moves on to describe the design, fabrication and characterization of an InP PIC that works as a coherent MWP filter, among other functionalities. Experimental results include both individual characterization of the basic BBs, such as lasers, modulators and photodetectors, as well as system level experiments. The issue of polarization rotation in the performance of optical filters, which was found to be a highly detrimental effect for this particular PIC, is also examined by means of simulations.

  Finally, chapter 8 summarizes all the previous work by compiling a set of conclusions and highlighting the main contributions of this thesis. Future lines of work are also discussed.

Chapter 2

Design and synthesis of optical lattice filters

2.1 Introduction

Optical filters are extensively used in photonic integrated circuits (PICs), as they are passive components that provide the capability to linearly process optical signals. Multitude of PICs incorporating integrated optical filters have been demonstrated so far in a broad range of applications, including: multiplexers and demultiplexers for coherent and intensity modulated transceivers [34]; tunable gain and dispersion compensation modules for WDM optical networks [47,48]; interrogation of fiber Bragg gratings [57]; gain flattening of on-chip mode-locked lasers [58]; integrated receivers for optical orthogonal frequency division multiplexing (O-OFDM) modulated signals [59]; as well as generation of ultra-wideband RF waveforms [60].

Because of their great practical importance, integrated optical filters have been the subject of a considerable research effort over the past few decades, including the recent generic integration platforms in InP, Silicon-On-Insulator (SOI) and Triplex [35, 38, 61]. Approaches for the design and implementation of optical integrated filters have exploited different well-known optical phenomena, such as resonance, coherent interference, multimodal dispersion and spatial diffraction effects. This has led to the demonstration of integrated arrayed waveguide and Echelle gratings [62, 63], ultra-high-Q microcravities [64], multimodal interference-based devices [65] and optical lattice filters [55, 66].

In this chapter, we will deal with the design and synthesis of this last family of devices. Compared to the other mentioned approaches, optical lattice filters can be easily reconfigurable, which is a highly desirable feature for many applications, and in particular for microwave photonics (MWP). As we will see, optical lattice filters can be beautifully described using the same mathematical formalism that digital filters. Thus, similar techniques can be employed for their design provided that a suitable synthesis algorithm exists. We will start exploring this connection with a simple example based on a Mach-Zehnder interferometer (MZI), which will help us to understand some basic concepts. Next, a brief review of the most common optical lattice architectures will be given, while discussing their main advantages and disadvantages. Finally, a more in-depth analysis of the ring-assisted Mach-Zehnder interferometer (RAMZI) architecture will be presented, which has been in fact the main focus of this work. In particular, we will briefly summarize the design and synthesis procedure of such kind of filters, as well as discussing some practical aspects such as the implications of manufacturing deviations during device fabrication.

2.2 Optical lattice filters and the Z-transform

Optical lattice filters are, to put it simply, photonic structures made of a repetitive concatenation of more simple basic units. In general, those basic unit cells are made of combinations of interconnected integrated waveguides and optical power couplers. Additionally, extra elements such as current-injection phase shifters or thermo-optic heaters can be included for post-fabrication tuning. Optical filters based on serial and parallel coupled ring resonators are a well-known example of such kind of structures [67].

In order to understand the previously mentioned link between optical lattice and digital filters, lets consider now the simplest of these unit cells: an unbalanced Mach-Zehnder interferometer (MZI). An schematic diagram of such structure is shown for clarity in Fig. 2.1(a). If we assume that the waveguides are lossless and that the optical couplers have an operation bandwidth much larger than the wavelength range of interest, then the optical transfer function of this structure (except for a common phase factor) can be expressed in the wavelength domain as

$$H(\lambda) = \sqrt{1-\kappa_1}\sqrt{1-\kappa_2}e^{-j2\pi n_e(\lambda)\Delta L/\lambda} - \sqrt{\kappa_1}\sqrt{\kappa_2}e^{j\phi} \tag{2.1}$$

where λ is the vacuum wavelength, $n_e(\lambda)$ is the wavelength-dependent effective index of the propagating mode, ΔL is the differential length between arms, ϕ accounts for a wavelength-indepenent tunable phase shift and κ_1/κ_2 are the power coupling constants of the input/output optical couplers, respectively. Please note that here we have assumed a nominal 90° phase shift between the two output ports of an optical coupler, so its 2x2 transfer matrix is simply given by

$$\begin{bmatrix} E_1^o \\ E_2^o \end{bmatrix} = \begin{bmatrix} \sqrt{1-\kappa} & -j\sqrt{\kappa} \\ -j\sqrt{\kappa} & \sqrt{1-\kappa} \end{bmatrix} \begin{bmatrix} E_1^i \\ E_2^i \end{bmatrix} \tag{2.2}$$

where E_1^o/E_1^i and E_2^o/E_2^i are the upper and lower output/input ports of the coupler, respectively.

From equation 2.1, it is easy to see that there exists a rapidly varying wavelength-dependent phase contribution arising from the differential propagation delay of the optical signal through the MZI arms. Assuming that the group index of the waveguides is constant over the bandwidth of interest, it is easy to prove that the transfer

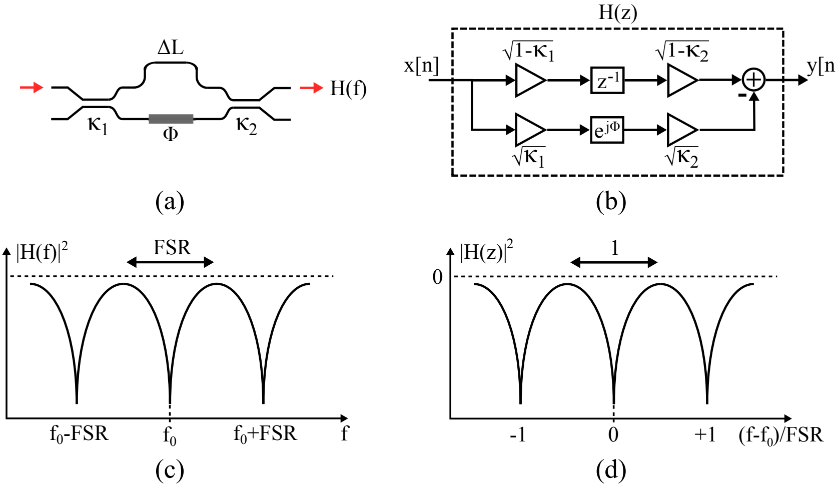

Figure 2.1: (a) Unbalanced Mach-Zehnder interferometer. (b) Equivalent digital filter representation. (c) Magnitude response (in dB) in the frequency domain. (d) Idem in the equivalent Z-transform domain.

function of the MZI can be rewritten in the frequency domain as

$$H(f) = \sqrt{1-\kappa_1}\sqrt{1-\kappa_2}e^{-j2\pi(f-f_0)/\mathrm{FSR}} - \sqrt{\kappa_1}\sqrt{\kappa_2}e^{j\phi} \tag{2.3}$$

where $f_0 = c_0/\lambda_0$ is an arbitrarily chosen reference frequency at which the transmission function has a minimum, provided that $\phi = 0$. FSR stands for Free Spectral Range. It is the fundamental period of the frequency response, and it is given by

$$\mathrm{FSR} = \frac{c_0}{n_g \Delta L} \tag{2.4}$$

with c_0 being the speed of light in vacuum. The group index (n_g), on the other hand, can be calculated with the following formula

$$n_g = n_e(\lambda_0) - \lambda_0 \left.\frac{dn_e(\lambda)}{d\lambda}\right|_{\lambda=\lambda_0} \tag{2.5}$$

Note that, under the previous assumptions, the transfer function of the MZI is infinitely periodic in the frequency domain, just like the response of digital filters. In fact, the differential delay between the MZI arms might be though of as the basic unit delay in digital filters, or z^{-1}, as is commonly written using Z-transform notation. As a consequence, a simple MZI might be understood and mathematically modelled as a digital Finite Impulse Response (FIR) filter with a double tap complex response

$$H(z) = \sqrt{1-\kappa_1}\sqrt{1-\kappa_2}z^{-1} - \sqrt{\kappa_1}\sqrt{\kappa_2}e^{j\phi} \tag{2.6}$$

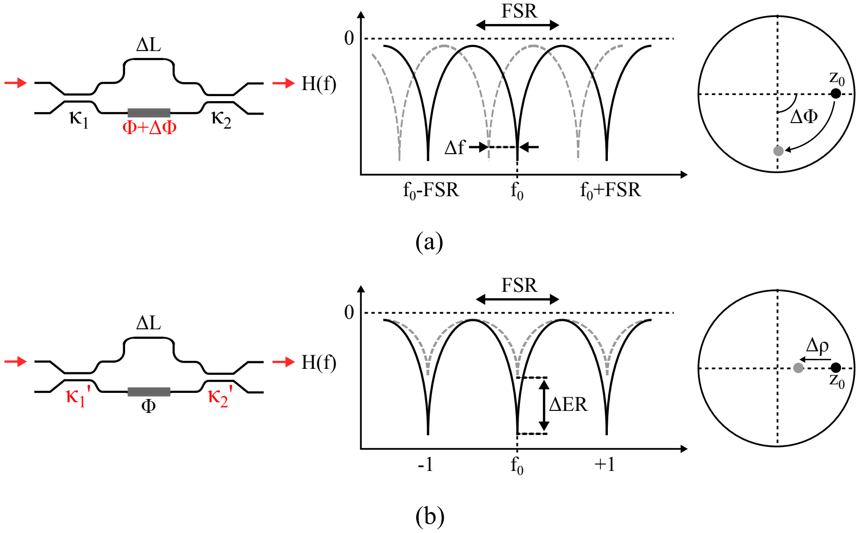

Figure 2.2: (a) Modification of the magnitude response of an MZI (in dB) and the position of its zero as a consequence of a change in the lower-arm phase shift. (b) Idem when the amplitude of the zero ($\rho = |z_0|$) is changed due to a modification of the coupling constants.

where z^{-1} needs to be evaluated in the unit circle ($z^{-1} = e^{-j2\pi(f-f_0)/\mathrm{FSR}}$). Figure 2.1(b) shows the equivalent digital filter representation of an unbalanced MZI, while Figs. 2.1(c) and 2.1(d) show the magnitude response (in dB) of the original frequency response and its equivalent in the Z-transform domain, respectively.

This apparently irrelevant fact is indeed of extreme importance, as it provides a fundamental connection between the optical domain and the rich field of digital filter synthesis and design. While in the latter the coefficients are stored in internal registers inside a digital signal processing unit (DSP), the coefficients of integrated optical filters depend on the exact phase and amplitude differences between optical paths. For example, a cascade of unbalanced MZIs might be regarded as a multiple tap FIR filter, where only delayed copies of the input signal are employed, whereas a cascade of ring resonators can be though of as an Infinite Impulse Response (IIR) filter, where each resonator acts as a feedback element. Also note that by changing both the coupling constants of the couplers and the phase differences in the delay lines, the taps of the integrated filter can be modified. This modification leads to a change in the position of the filter poles and zeros on the complex plane. As a result, the optical filter response can be electrically tuned on demand by using, for example, thermo-optic heaters.

In our simple example, changing the phase (ϕ) of the lower arm moves the position of the single zero (z_0) on the complex plane, which is expressed as

$$z_0 = \frac{\sqrt{1-\kappa_1}\sqrt{1-\kappa_2}}{\sqrt{\kappa_1}\sqrt{\kappa_2}} e^{-j\phi} = \rho e^{-j\phi} \tag{2.7}$$

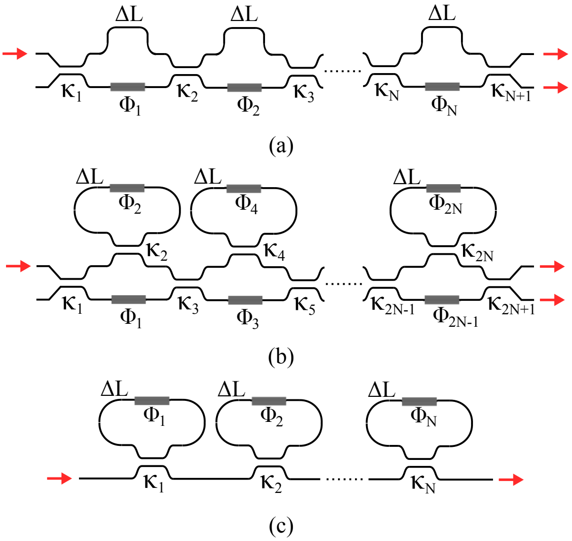

Figure 2.3: Schematic diagram of an N-th order filter based on (a) cascaded MZIs, (b) cascaded ring-loaded MZIs, and (c) cascaded ring resonators.

As it can be seen in Fig. 2.2(a), increasing the original phase by an increment ($\Delta\phi$) leads to a shift of the whole frequency response of the MZI. In particular, the frequency at which the MZI has a minimum (f_0) is reduced according to $f_0' = f_0 - \mathrm{FSR}\Delta\phi/2\pi$. Besides, note that changing the amplitude of the zero, which is equivalent to modifying the relative amplitudes of the interfering fields (κ_1 and κ_2), leads to a modification of the MZI extinction ratio, as is depicted in Fig. 2.2(b).

2.3 Optical lattice architectures

Generally speaking, the simplicity in the mathematical modelling of optical lattice filters is good for a fast and precise characterization of their spectral response. In fact, commercial software packages exist that incorporate advanced modelling techniques to analyze this particular family of devices. They can account for losses due to propagation in straight waveguides and bends, or more sophisticated phenomena like imbalance and phase errors in the optical couplers.

In practice, one is not so much interested in inferring the optical response from an already known set of phase shifts and coupling constants (analysis), but just the opposite (synthesis). Given certain filter specifications, the designer needs to find the structure that best suits the application constraints, and then compute the phase shifts and coupling constants that yield the desired response. In the previous example, we saw that an MZI can be regarded as a single pole filter. Furthermore, it was rather simple to infer and predict the behaviour of its single

Name	Diagram	Filter type	#Couplers	#Shifters
Cascaded MZIs	Fig. 2.3(a)	FIR	N+1	N
Cascaded ring-loaded MZIs	Fig. 2.3(b)	IIR	2N+1	2N
Cascaded rings	Fig. 2.3(c)	IIR	N	N
Ring-assisted MZIs	Fig. 2.4	IIR	N+2	N+2

Table 2.1: Main optical lattice filter architectures. The number of required couplers and phase shifters is shown as a function of the filter order (N).

zero. Unfortunately, the complexity of this dependence scales rapidly for bigger and more complicated structures. It is at this point that synthesis algorithms play a crucial role. In brief, synthesis algorithms are provided with a set of filter coefficients that implement the desired frequency response, and then provide the values of the coupling constants and optical phase shifts that are required in order to achieve that transfer function. Thus, the designer only needs to design its filter using well-known DSP techniques, and later translate the resulting coefficients into a set of physically meaningful constants (i.e. coupling constants and phase shifts).

Luckily, several optical lattice filter architectures have been proposed over the course of the years for which well-defined and robust synthesis algorithms have been derived [55, 66]. The most important ones are shown in Figs. 2.3(a) to (c) and Fig. 2.4(a), whereas Table 2.1 summarizes their main features. Each structure has its own advantages and limitations. Cascaded MZI architectures (Fig. 2.3(a)), for example, can only implement FIR filters, which leads to a higher order for the same specifications as compared to IIR architectures. However, FIR filters can be designed with a perfectly linear phase. This might be interesting for certain applications, such as tunable optical delay lines. Cascaded ring-loaded MZIs (Fig. 2.3(b)), on the other hand, can implement IIR filters with no restrictions whatsoever on the position of the poles and zeros. This leads to the maximum design flexibility, while also offering the maximum performance for a given filter order. Chains of uncoupled ring resonators (Fig. 2.3(c)) behave as all-pass filters. The poles and zeros are related in such a way that a flat magnitude response is obtained provided that there are no losses, but an arbitrary phase response can still be synthesized. They are typically employed as tunable optical delay lines or integrated dispersion compensation modules. Finally, ring-assisted MZIs (Fig. 2.4(a)) are a simplified version of the cascaded ring-loaded MZIs structure. They can also implement IIR filters but without offering complete control over the position of the poles and zeros. By contrast, the number of required couplers and phase shifters is reduced by approximately half, which significantly reduces the device footprint. They are, in fact, the main focus of this work, and they will be explained in detail in the next subsection. The interested reader is nevertheless referred to [66] and [55] for a more detailed discussion about the different structures.

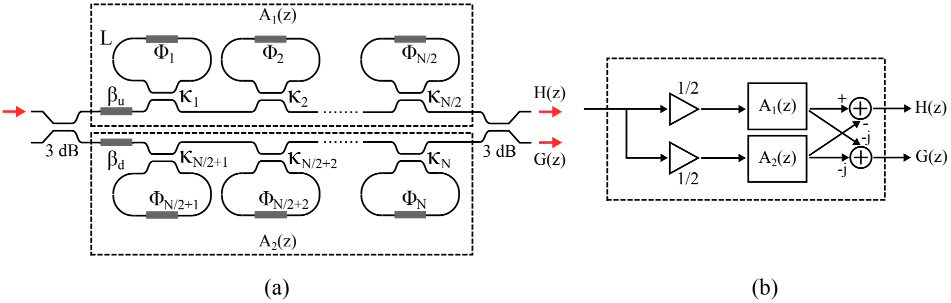

Figure 2.4: (a) Schematic diagram of an N-th order ring-assisted MZI filter. (b) Equivalent digital filter representation.

2.4 Ring-assisted Mach-Zehnder interferometer filters

2.4.1 Description and basic properties

An schematic diagram of a ring-assisted Mach-Zehnder interferometer (RAMZI) filter is shown in Fig. 2.4(a), where the relevant tunable power couplers and optical phase shifters have been highlighted for clarity. Figure 2.4(b) shows its equivalent digital filter representation. As it can be seen, a RAMZI filter is made of an MZI whose arms have been loaded with ring resonators of the same perimeter (same Free Spectral Range, or FSR). This loading is determined by optical couplers with different coupling constants that, together with the relative optical phase shifts, completely define the transfer function of the structure. Note that the input and output couplers are standard 3 dB couplers with $\kappa = 0.5$.

Another way of looking at the structure is by realizing that each arm of the interferometer might be regarded as an individual all-pass filter, made of a concatenation of isolated ring resonators. The purpose of the ring resonator chains ($A_1(z)$ and $A_2(z)$) is to imprint a certain relative phase shift between the two arms, that leads to a certain magnitude and phase response when the signals are coherently combined at the output 3 dB coupler. In that case, the generic response of the filter using Z-transform notation can be expressed as

$$H(z) = \frac{1}{2}\left[A_1(z) - A_2(z)\right] \tag{2.8}$$

$$G(z) = \frac{-j}{2}\left[A_1(z) + A_2(z)\right] \tag{2.9}$$

where $H(z)$ and $G(z)$ are the bar and cross output responses, respectively (see Fig. 2.4(a)). Note that, due to power conservation, the magnitude response of the filter is intrinsically complementary. That is

$$|H(e^{j\omega})|^2 + |G(e^{j\omega})|^2 = 1 \tag{2.10}$$

The transfer functions of both $A_1(z)$ and $A_2(z)$ are in turn given by the product of N/2 individual ring resonators

$$A_1(z) = e^{j\beta_u} \prod_{i=1}^{(N/2)} \frac{e^{j\phi_i}[\sqrt{1-\kappa_i}e^{-j\phi_i} - z^{-1}]}{1-\sqrt{1-\kappa_i}e^{j\phi_i}z^{-1}} \tag{2.11}$$

$$A_2(z) = e^{j\beta_d} \prod_{i=(N/2)+1}^{N} \frac{e^{j\phi_i}[\sqrt{1-\kappa_i}e^{-j\phi_i} - z^{-1}]}{1-\sqrt{1-\kappa_i}e^{j\phi_i}z^{-1}} \tag{2.12}$$

where β_u and β_d are extra phase shifts in the upper and lower arms, respectively.

This results in an all-pass filter, whose zeros (z) and poles (p) are related by $z = 1/p^*$. Here, N is the order of the RAMZI filter, which is equal to the total number of rings. The most important properties of these structures are succinctly enumerated below.

1. Thanks to the existence of both direct paths and feedback loops, IIR filters can be implemented. This leads to a more compact layout, as a smaller order is required in order to achieve the same filter specifications.

2. A direct synthesis algorithms exists, so that the phase shifts and coupling constants can be directly extracted from the target filter coefficients.

3. Two optical inputs and outputs are available. This is especially interesting from a practical point of view, since the unused input/output ports can be employed for testing purposes. Furthermore, the optical outputs are complementary in power, a peculiar characteristic that will be actually exploited in chapter 5.

4. Poles and zeros can not be arbitrarily located on the complex plane, as opposed to the more general IIR architecture based on cascaded ring-loaded MZIs (Fig. 2.3(b)). However, optimum passband IIR filters (such as Butterworth, Chebyshev type I/II and Elliptic designs) can still be implemented. This is very handy, as well-known software packages such as Matlab$^{\text{TM}}$ offer direct synthesis algorithms for these canonical filters, allowing the designer to obtain the numerator and denominator coefficients by just specifying the filter spectral characteristics.

2.4.2 Synthesis algorithm

In this section, we will review the different steps that need to be taken during the synthesis of a RAMZI filter. That is, the computations required to obtain the coupling constants and phase shifts out of a digital filter that has been previously designed, which is passed as a parameter to the algorithm. For the sake of brevity, we will omit a full derivation with a detailed explanation of the process, and will limit ourselves here to the most important steps. The interested reader is referred to the excellent book by Madsen and Zhao for a deeper discussion [55].

First of all, we start by recalling that the outputs of our RAMZI filter can be expressed as the complex sums of two all-pass filters (equations 2.8 and 2.9). For simplicity, we might rewrite these expressions as

$$H(z) = \frac{1}{2}\left[A_1(z) - A_2(z)\right] = \frac{P(z)}{D(z)} \tag{2.13}$$

$$G(z) = \frac{-j}{2}\left[A_1(z) + A_2(z)\right] = \frac{Q(z)}{D(z)} \tag{2.14}$$

where $P(z)$ and $D(z)$ are the numerator and denominator of the filter that we wish to implement. These are normally obtained by means of a digital filter synthesis algorithm from a set of target specifications. Note that both $H(z)$ and $G(z)$ share a common denominator ($D(z)$), but the numerator of $G(z)$, termed $Q(z)$, is unknown.

One of the basic properties of RAMZI filters is that the order of the filter being implemented is equal to the total number of rings. Note that, as a consequence of the layout topology, odd order filters (N $= 1, 3, 5\ldots$) will occupy roughly the same chip area as the next even order filter (N $= 2, 4, 6\ldots$), since one ring is missing in one of the arms but not in the other one. This means that even order filters are usually preferred for practical implementations, as we get one more degree of freedom for approximately the same area. From now on, it is assumed that the target filter has even order. We also need to recall that, due to power conservation, the two outputs of our filter are power complementary, as expressed in equation 2.10. In the Z-transform domain, this property can be rewritten as

$$P(z)P_r(z) + Q(z)Q_r(z) = D(z)D_r(z) \tag{2.15}$$

where the r subscript stands for a *reverse* polynomial, which for an N-th order filter ($P(z) = p_0 + p_1z^{-1} + p_2z^{-2} + \ldots + p_Nz^{-N}$) is defined as

$$P_r(z) = z^{-N}P^*(1/z^*) = p_N^* + p_{N-1}^*z^{-1} + \ldots + p_0^*z^{-N} \tag{2.16}$$

The apparently complicated expression of equation 2.16 is in fact a very simple transformation. It is just a filter whose coefficients are the complex conjugates (*) of the original ones, but flipped in order. Now, we further assume that the target input filter has real coefficients and that the numerator ($P(z)$) has even symmetry ($p_n = p_{N-n}$), as it is the case for even-order optimum passband filter designs. We might then summarize the synthesis procedure as follows [55]:

1. Find an auxiliary polynomial, called $R(z)$, out of the numerator and denominator of the target input filter

$$R(z) = z^{-N}D(1/z)D(z) - P^2(z) \tag{2.17}$$

2. Compute recursively the coefficients of $Q(z)$ from $R(z)$ as follows

$$q_n = q_{N-n} = \frac{r_n - \sum_{k=1}^{n-1} q_k q_{n-k}}{2q_0} \quad \text{for } n \geq 2 \tag{2.18}$$

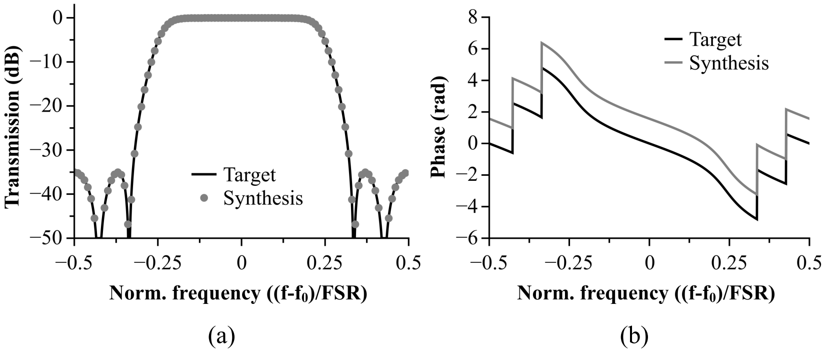

Figure 2.5: (a) Magnitude response (in dB) of a 4-th order Chebyshev type II filter designed using Matlab$^{\text{TM}}$ (black solid line). The response of the synthesized filter is also shown as a dotted grey line. (b) Idem for the phase transfer function (in rad.). The phase of the synthesized filter is shown here as a solid grey line. It differs only by a constant phase, which has no physical meaning.

with $q_0 = \sqrt{r_0}$ and $q_1 = r_1/2q_0$.

3. Find the roots of $P(z) + jQ(z)$ and $P(z) - jQ(z)$, and keep only those that are inside the unit circle (i.e. minimum phase). These roots are the poles of $A_1(z)$ and $A_2(z)$, respectively. The total number of poles is equal to the filter order (N), with $A_1(z)$ and $A_2(z)$ having each half of them. Also note that, since both $P(z)$ and $Q(z)$ have real coefficients, the roots of $P(z) - jQ(z)$ are the complex conjugates of the roots of $P(z) + jQ(z)$.

4. Let the minimum phase roots of $P(z)+jQ(z)$ be denoted as $\{x_1, x_2, \ldots, x_{N/2}\}$. The coupling constants (κ_i) and relative phase shifts (ϕ_i) of the upper/lower rings can now be calculated using the following formulas

$$\kappa_i^{\text{Up}} = \kappa_i^{\text{Down}} = 1 - |x_i|^2 \tag{2.19}$$

$$\phi_i^{\text{Up}} = -\phi_i^{\text{Down}} = \angle x_i \tag{2.20}$$

where $\angle$ stands for the phase of a complex number (in radians), and $i = 1, \ldots, N/2$.

5. Finally, we need to compute the extra phase shifts in both arms of the interferometer (β_u and β_d). These are given by

$$\beta_u = \angle\left\{ (G(1) + jH(1)) \prod_{i=1}^{N/2} \frac{1 - x_i}{1 - x_i^*} \right\} - \sum_{i=1}^{N/2} \phi_i^{\text{Up}} \tag{2.21}$$

$$\beta_d = -\beta_u \tag{2.22}$$

n	p_n	q_n	κ_n	ϕ_n	β_u	β_d
0	0.1391	1.0000	-	-	0.9525	-0.9525
1	0.3922	-0.0245	0.4890	1.5029	-	-
2	0.5345	0.5610	0.9430	-1.7232	-	-
3	0.3922	0.0315	0.4890	-1.5029	-	-
4	0.1391	0.0291	0.9430	1.7232	-	-

Table 2.2: Coefficients of both the numerator (p_n) and denominator (q_n) of the target filter. The synthesized values of the coupling constants (κ_n) and phase shifts (ϕ_n, β_u and β_d, in radians) are also shown.

As an example, Figs. 2.5(a) and 2.5(b) show the magnitude and phase responses of a 4-th order Chebyshev type II filter (solid black lines) together with the synthesized responses using the aforementioned algorithm (dotted and solid grey lines, respectively). The target filter has an attenuation of 35 dB and a normalized passband width (Δf/FSR) of 0.65, and was designed with the filter design and analysis toolbox of Matlab$^{\text{TM}}$. The resulting coupling constants and relative phases are shown in Table 2.2, along with the target filter coefficients.

2.4.3 Practical considerations

Up to know, we have worked in a rather abstract fashion, and have assumed so far that our structure is made of *generic* power couplers, phase shifters and integrated single-mode waveguides. In practice, the different power couplers need to be transformed into specific photonic structures capable of yielding the required coupling constants, and the same goes for the phase shifters. Besides, there exists a plethora of other real-life limitations that are normally not contemplated during the design and synthesis stage, but that the designer needs to bear in mind in order to succeed during a practical filter implementation. The most important of those limitations are briefly discussed below.

1. **The maximum attainable FSR is limited by the minimum possible ring perimeter**. The length of the ring perimeter basically determines the propagation time ($\tau = 1/\text{FSR}$) that it takes for an optical signal to propagate through it. In practice, this time delay can only be calculated once the power couplers have been designed, because the power coupler length also contributes to the propagation delay. This is particularly true for high contrast platforms such as SOI, where the minimum bending radius is very small as compared to the length of the coupler. For medium contrast platforms, such as InP, the bending radius is usually the main limiting factor since it needs to be high to keep bending losses low. The FSR can thus be expressed as

$$\text{FSR} = \frac{c_0}{n_g^s L_s + n_g^c L_c + 2\pi R n_g^b} \tag{2.23}$$

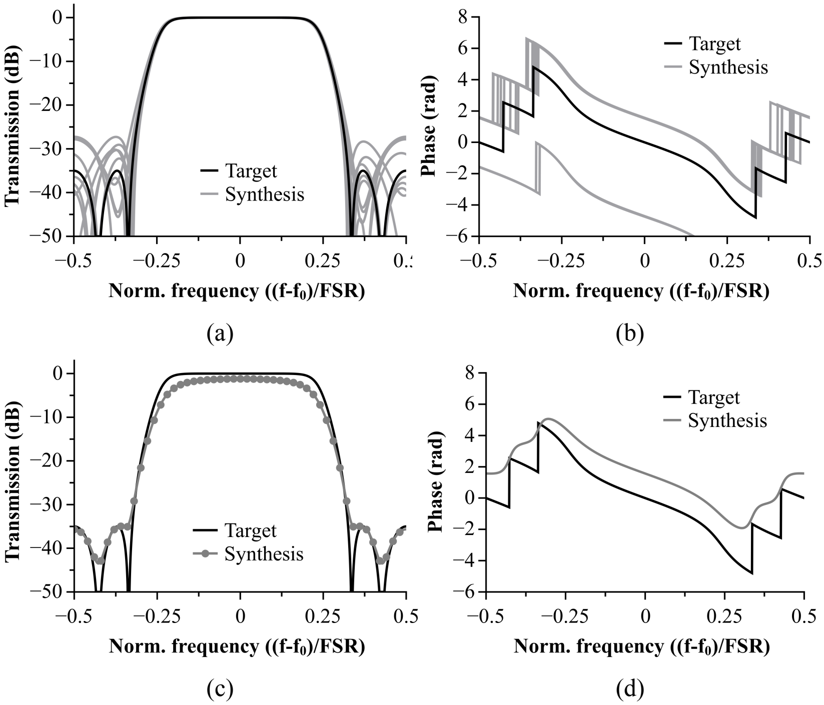

(a) (b)

(c) (d)

Figure 2.6: (a) Magnitude response (in dB) of the ideal Chebyshev type II filter of Table 2.2 (black solid line). Ten simulations considering phase and amplitude errors with independent, uniform random distributions are plotted superimposed as solid grey lines. (b) Idem for the phase response. (c) Magnitude response (in dB) of the same filter when losses are taken into account. (d) Idem for the phase response.

where n_g^s, n_g^c, and n_g^b are the group indices of the straight, coupler and bent sections, respectively. L_s is the total length of the straight waveguides that compose the ring resonator, L_c is the coupler length, and R is the bending radius. Here, we have assumed a racetrack configuration for the ring.

2. **Manufacturing tolerances can severely affect the filter response**. As it has been explained, the transfer function of the filter depends on the relative positions of the poles and zeros of the ring resonators. These poles are determined by the relative positions of their resonant wavelengths, which are of course sensitive to both the exact geometry and composition of the waveguides [68]. Due to inhomogeneities in both the wafer thickness and refractive indices of the epitaxial layers, as well as geometry variations during lithography and etching, significant deviations of the resonances are known to occur, especially in high contrast technologies [69]. These errors also affect power couplers, although usually in a much less severe way if they are

implemented by means of multimode interference couplers (MMIs).

To give an idea of the impact that manufacturing deviations can have on the filter response, Figs. 2.6(a) and 2.6(b) show an overlap of 10 simulations of the same filter shown in Figs. 2.5(a) and 2.5(b). Each simulation is run assuming that the phase and amplitude errors can be modelled as independent, uniform random variables contained in the range of ±1° and ±1%, respectively. As it can be seen, the response of the filter is greatly affected, especially the level of attenuation in the stopband. Thus, meeting the transfer function specifications either requires either a highly reproducible and stable process [70], or to use post-compensation elements, such as thermo-optic heaters or current-injection phase shifters.

3. **High propagation/bending losses can smooth the filter response**. This effect can be easily understood by noting that, as losses increase, the magnitude of the poles and zeros moves away from their original position on the complex plane. Figs. 2.6(c) and 2.6(d) show the overlapped transfer functions of our ideal Chebyshev filter and its response in a more realistic situation, assuming 1 dB of total propagation losses inside each ring. The losses not only reduce the maximum transmission and the width of the passband [50], but they also smooth the depth of the notches and the filter roll-off.

4. **Post-fabrication tuning mechanisms can introduce unwanted side effects**. Since manufacturing tolerances tend to yield filters out of target specifications, tuning mechanisms are normally indispensable [68, 69]. So far, most experimental results have reported the use of either thermo-optic heaters or current-injection phase shifters, which are typically available in most generic and specific photonic integration platforms. The benefit of these mechanisms, however, comes at a certain cost. First, the complexity of the measurement process increases substantially. Typically, one requires to manually probe and control up to tens of individual DC pads while monitoring the filter output so as to adjust is transfer function. On the other hand, unwanted effects related to the physical mechanisms on which these techniques rely start to show up. For example, the high amount of electrical current needed to fully adjust a single filter can cause significant heating of the chip mount, degrading the performance of other on-chip devices, such as lasers or modulators [71]. Besides, the heat generated to control one ring can propagate through the chip substrate and affect neighbour rings, turning the chip tuning into a multidimensional, non-linear optimization problem with tens of coupled independent variables. In that sense, current-injection phase shifters are free of the aforementioned problems. However, they can add significant extra losses at high pump currents, affecting even further the transfer function as discussed in the previous point.

5. **Polarization rotation in sharp bends can affect the filter response in uncontrolled ways**. In mid and low contrast technologies, such as

InP and TriPleX, the modes inside a curved waveguide tend to be slightly shifted outwards, presenting an asymmetry of the field profile. The bend also modifies the intensity of the vertical (E_y) and horizontal (E_x) components of the TE and TM modes, respectively, which are no longer negligible against the dominant horizontal (E_x) and vertical ones (E_y) [72]. As a result of this mode hybridization, both TE and TM polarizations might get excited at the output of a bend even when only one polarization is launched at its input. In fact, this effect has already been explored as a way of implementing polarization rotators in InP technology [73]. The drawback of this effect is that most lattice filters are optimized for one polarization. If rotation occurs, then the power in the unwanted polarization can coherently build up while propagating within the PIC, leading to high conversion efficiencies. Since the orthogonal mode experiences a different set of phase shifts and coupling constants, then the response of the filter can get severely affected depending on the degree of polarization conversion. This effect will nevertheless be explained in more detail in chapter 7.

2.5 Conclusions

In this chapter, a brief introduction to the design and synthesis of optical lattice filters has been given. Contrary to other existing approaches, such as arrayed waveguide and Echelle gratings, optical lattice filters are easily reconfigurable, and can be described using the well-known formalism of digital filters. This is a very interesting feature, as it allow designers to leverage the powerful techniques developed in the DSP world for the realization of integrated optical filters.

After briefly reviewing this beautiful connection using a simple MZI as an example, we have discussed the most common lattice architectures, highlighting their main advantages and disadvantages. These include cascaded MZIs, cascaded ring-loaded MZIs, cascaded ring resonators and ring-assisted MZIs. In particular, we have seen that RAMZI filters are an interesting alternative to the other topologies, as they can implement canonical passband filters but with a reduced complexity. This means a lower number of ring resonators, which implies a smaller footprint and power conssumption.

A summary of the synthesis algorithm for even order RAMZI structures has been given, together with an example of such algorithm in the design of a 4-th order Chebyshev type II filter. Finally, we have also provided a brief list of important practical considerations that need to be considered for a successful design of such devices, and we have illustrated their effect via simulations. They include manufacturing deviations in the coupling constants and phase shifters, optical propagation losses, thermal crosstalk among adjacent rings, as well as polarization rotation in bent waveguides.

Part II

Optical couplers and reflectors based on multimode interference mechanisms

Chapter 3

2x2 Multimode interference couplers with variable power splitting ratios

3.1 Introduction

In the previous chapter, we saw that optical couplers are essential for the implementation of ring-assisted Mach-Zehnder interferometer filters (RAMZI). However, we did not provide details about the specific way in which these devices can be implemented, since these are completely irrelevant at the synthesis stage. It is once the coupling constants have been determined that the designer needs to choose among the available coupler architectures.

Integrated optical couplers are, together with filters, among the most common of the passive components that can be found in any photonic integrated circuit (PIC). It is no wonder then that many alternatives have been developed for their implementation, including: symmetric and asymmetric directional couplers [74,75], symmetric MZIs with tapered waveguides [76], as well as straight [77], cascaded [78], bent [79] or tapered [56] multimode interference couplers (MMIs). Choosing the right option for each application requires an in-depth knowledge of their practical advantages and disadvantages, something that is largely determined by the designer previous experience. In general, both directional couplers and tunable MZIs are easy to design, but are very sensitive to manufacturing errors. On the contrary, MMIs require a bit more of design work but yield much better resilience against fabrication tolerances [80]. Also, they can be designed to operate over a very broad wavelength range.

In this chapter, we will bridge the gap between generic and real couplers. In particular, we will elaborate on the theory, design and experimental characterization of tapered 2x2 MMIs for the implementation of optical couplers with variable power splitting ratios. First, we will start by briefly reviewing the basic operation principle behind canonical (i.e. not tapered) MMIs. Then, we will proceed to explain how 2x2 MMIs might be tapered to achieve variable splitting ratios, as it was first proposed by Besse et al. [56]. Next, a general design procedure for such devices will be described, which provides the designer with a set of well defined steps that need to be followed in order to design a tapered 2x2 MMI with a given power splitting ratio. This is followed by detailed design data of several devices for a generic Silicon-On-Insulator (SOI) foundry. Finally, experimental results of several devices fabricated in a multi-project wafer run (MPW) will be discussed. This will give us an idea of the real performance of such structures after fabrication, both within the same wafer and from wafer to wafer. Numerical simulations about the impact of manufacturing tolerances are described as a separate topic in the last section. We will analyze a practical case study, and see how fabrication errors affect the performance of an InP-based 4x4 MMI acting as a 90° optical hybrid for coherent optical communication receivers.

3.2 Basic MMI theory

Since the initial suggestion by Bryngdahl [81], and the first pioneering experimental demonstration by Ulrich and Ankele in the 1970s [82], multitude of papers have focused on developing and studying the theoretical and practical aspects behind MMIs. Two of the most well-known investigations about their principle of operation are due to both Soldano and Bachmann et al. [80,83], who over the course of the 1990s published two seminal articles where the main ideas behind self-image formation (i.e. spatial Talbot effect) in planar waveguides were explained in detail. These included not only the prediction and calculation of the positions where images are formed, but also their amplitudes and relative phases.

In order to understand how MMIs work, we first need to recall that an MMI is basically made of an integrated planar waveguide that is wide enough to support a high number of propagation modes. Additionally, single-mode waveguides are used to access the multimode region. A schematic diagram of an NxM MMI and a 3D representation of a 2x2 MMI can be seen in Figs. 3.1(a) and 3.1(b), where the main parameters of interest, such as length and width, are also shown. Figure 3.1(c) is an scanning electron microscope (SEM) picture of one of the devices designed and fabricated in this thesis, which is shown for illustration purposes. In general, the multimode waveguide is designed in such a way that only multiple modes exist in the x direction. In that case, well-known simplification approaches such as the Effective Index Method (EIM) can be employed, and the vertical direction (y) can be neglected ([80] and Appendix A). Each mode can thus be described by a one dimensional function of x ($E_n(x)$), and its associated propagation constant (β_n). These can be found for example after solving Maxwell equations with the right boundary conditions using a waveguide mode solver. When light with an arbitrary field profile is launched into an MMI via any of their access waveguides, some of the supported modes will be excited, leading to an interference pattern as the modes beat along their propagation inside the multimode region. The field

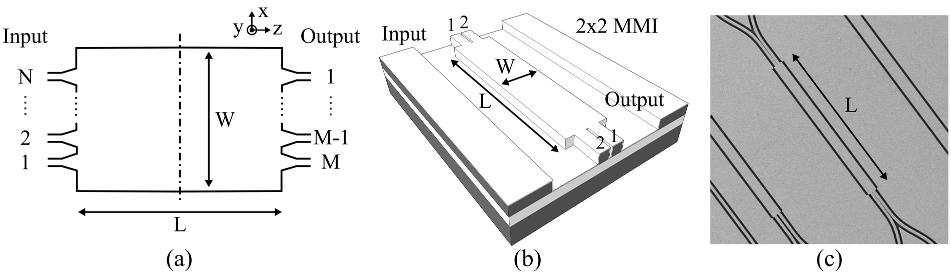

Figure 3.1: (a) General diagram of an NxM MMI. (b) 3D diagram of a 2x2 MMI. (c) SEM picture of a 2x2 MMI fabricated in thick SOI.

profile at any given propagation distance ($f_{out}(x,z)$) can be expressed as

$$f_{out}(x,z) = \sum_{n=0}^{N-1} c_n E_n(x) e^{-j\beta_n z} \tag{3.1}$$

where c_n are complex coefficients computed by performing an overlap integral between the N propagating modes of the MMI and the field profile at the access waveguide ($f_{in}(x)$). These are given by

$$c_n := \frac{\int f_{in}(x) E_n(x) dx}{\int E_n^2(x) dx} \tag{3.2}$$

For the particular case of high index contrast platforms, such as InP and SOI technologies, the modes are highly confined in the lateral dimension. This means that, in virtue of the EIM approach mentioned before, the mode profiles and its associated propagation constants (Figs. 3.2(a) and 3.2(b)) can be approximated by [80, 83]

$$E_n(x) \simeq \sqrt{\frac{2}{W}} \sin\left(\frac{\pi(n+1)x}{W}\right), \qquad x \in [0, W] \tag{3.3}$$

$$\beta_n \simeq n_{eff}^{\mathrm{WG}} k_0 - \frac{(n+1)^2 \pi^2}{2 n_{eff}^{\mathrm{WG}} k_0 W^2}, \quad \forall n = 0, 1, \ldots N-1 \tag{3.4}$$

where W is the MMI's width, n_{eff}^{WG} is the effective index of the waveguide core, as explained in Appendix A, and $k_0 = 2\pi/\lambda_0$ is the free space wavenumber at at a certain nominal vacuum wavelength (λ_0).

Due to the generic form of equation 3.1, one might think at first sight that the interference pattern formed within the MMI will yield arbitrary, although predictable, field profiles at each possible distance, as seen in Fig. 3.3(a). Remarkably, this is not the case. There exist special periodic positions along the MMI length where multiple replicas of the input field pattern appear. These are called *self-images*, and their existence is a natural consequence of the quadratic

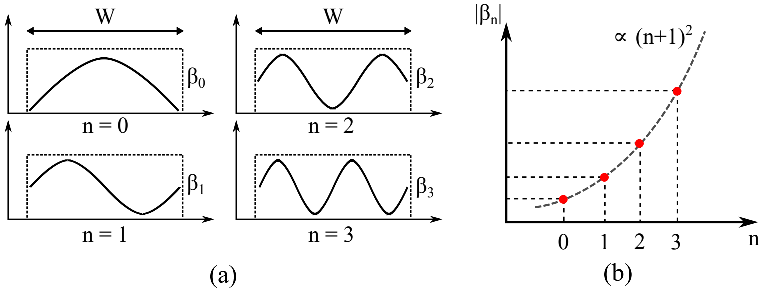

Figure 3.2: (a) Field profiles of the lowest order propagation modes. (b) Quadratic dependence of β_n with mode number n.

dependence with n of the propagation constants. In fact, it can be proved that after substitution of equations 3.3 and 3.4 into equation 3.1, it can be rewritten as

$$f_{out}(x', z') = \sum_{m=\pm 1}^{\pm N} b_m \exp\left(j2\pi\xi m - j\pi\zeta m^2\right) \tag{3.5}$$

where ξ and ζ are just scaled versions of x and z

$$\xi = \frac{x}{2W} \tag{3.6}$$

$$\zeta = -\frac{\pi z}{2k_0 n_{eff}^{\mathrm{WG}} W^2} \tag{3.7}$$

and b_m is given by

$$b_m = \mathrm{sgn}(m)\frac{c_{|m|-1}}{j\sqrt{2W}} \exp\left(-jk_0 n_{eff}^{\mathrm{WG}} z\right) \tag{3.8}$$

Here, sgn() stands for the sign function.

Note that when $N \to \infty$, equation 3.5 becomes a well-known formula, also called the *Jacobi theta function*. For $\zeta = p/q$, with p and q co-prime integers greater than 1, the previous summation can be expanded as [84]

$$f_{out}(\xi', \zeta = \frac{p}{q}) = \frac{1}{\sqrt{q}} \sum_{m=0}^{q-1} g(\xi' - \frac{m}{q}) \exp\left(j\Phi(m, p, q)\right) \tag{3.9}$$

One one hand, ξ' is defined as

$$\xi' = \xi - \frac{1}{2} e_p \tag{3.10}$$

where e_p is 0 (1) if p is even (odd).

On the other hand, $g(s)$ can be expressed as

$$g(s) = \begin{cases} f_{in}(2Ws) & : 0 \leq s < 1/2 \\ -f_{in}(2W(1-s)) & : 1/2 \leq s < 1 \end{cases} \tag{3.11}$$

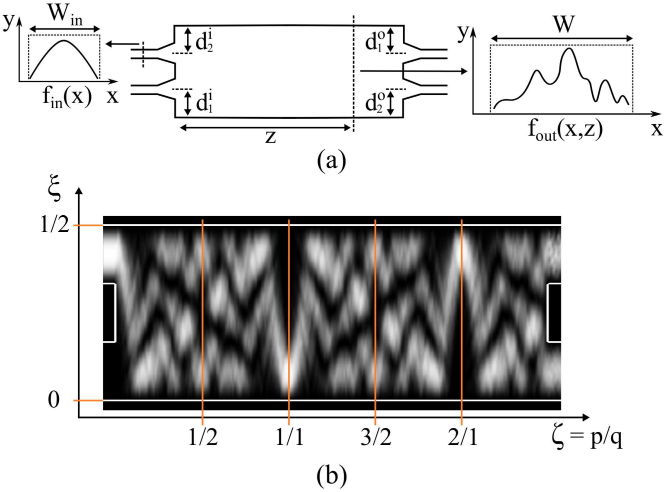

Figure 3.3: (a) Field propagation within an MMI. (b) Simulation of a real device, where the self-imaging effect becomes evident.

where

$$s = (\xi' - \frac{m}{q}) \mod 1 \tag{3.12}$$

The field profile inside the multimode region ($x \in [0, W]$) can be finally obtained, except for a constant phase factor, by evaluating the normalized ξ variable in the interval $[0, 1/2]$. By doing so, it can be seen that at certain periodic distances along the multimode waveguide ($\zeta = p/q$, with $p = 1, 2 \ldots$), q spaced replicas (self-images) of the input field profile ($f_{in}(x)$) are formed at the transverse plane, as in Fig. 3.3(b). Each self-image has an amplitude equal to $1/\sqrt{q}$, and a relative phase shift ($\exp \Phi(m, p, q)$) that depends on the index of the output position m and the values of both p and q [84]

$$\exp(j\Phi(m,p,q)) = \frac{1}{\sqrt{q}} \sum_{k=1}^{q} \exp\left(j\frac{\pi}{q}[2k(m + \frac{1}{2}qe_p) + pk^2]\right) \tag{3.13}$$

The length at which the first single self-image is formed is approximated by $z = 4n_{eff}^{\mathrm{WG}} W^2/\lambda_0$. In practice, this distance is expressed as $3L_\pi$, where L_π is defined as the beating length of the two lowest-order modes

$$L_\pi = \frac{\pi}{\beta_0 - \beta_1} \tag{3.14}$$

The self-imaging effect is the key behind the great practical importance of MMIs. Exploiting the existence of the input field replicas, optical couplers can be implemented by just placing input/output waveguides at the right positions on the access planes. Note that equation 3.9 tells us that the spatial Talbot

Interference	General	Paired	Symmetric
Inputs x Outputs	NxN	2xN	1xN
1^{st} image	$3L_\pi$	L_π	$3L_\pi/4$
1^{st} N-th image	$3L_\pi/N$	L_π/N	$3L_\pi/4N$
Excitation	None	$c_n = 0$	$c_n = 0$
requirements		$\forall n = 2, 5, 8, \ldots$	$\forall n = 1, 3, 5, \ldots$
Input(s) location(s)	Any	$d_1^i, d_2^i =$ W/3	$d_1^i =$ W/2

Table 3.1: Types and properties of MMIs with restricted interference mechanisms [80].

effect only produces output images of equal intensity. In other words: only NxN optical couplers with uniform power splitting can be obtained when using straight multimode waveguides, where N is the number of both input and output ports, respectively. However, there are degenerate situations where two self-images that appear at the same position on the output plane can coherently interfere with each other, leading to another image with a different intensity. This concept of MMIs with *overlapping* self-images was developed in great detail by Bachmann [77], and it helped to generalize in a rigorous manner the restricted interference ideas introduced by Soldano [80]. Soldano realized that, depending on the position and shape of the input field profiles (d_1^i and d_2^i in Fig. 3.3(a)), different sets of propagation modes could be excited. Apart from the most general case discussed above, where all modes propagate, locating a single input waveguide at the center of an MMI ($\mathrm{d}_1^i = \mathrm{d}_2^i = \mathrm{W}/2$) will only excite symmetric modes ($c_n = 0$, $\forall n = 1, 3, 5, \ldots$) if $f_{in}(x)$ has even symmetry, which is the case for single-mode integrated waveguides. This is called *symmetric* interference. Similarly, locating a pair of input waveguides at a distance of W/6 from the center ($\mathrm{d}_1^i = \mathrm{d}_2^i = \mathrm{W}/3$) will only excite a restricted set of modes ($c_n = 0$, $\forall n = 2, 5, 8, \ldots$), which is known as *paired* interference. These MMI configurations are summarized in Table 3.1, after [80].

3.3 Tapered 2x2 MMIs

Bachmann et al. not only generalized the ideas of Soldano, but he further proved that by carefully positioning the input/output waveguides of an MMI, non-uniform power splitting is possible [77]. For the particular case of 2x2 MMIs, it was shown that there exist 4 different configurations (namely, types “A”, “B”, “C” and “D”) that produce 4 different power splitting ratios (50/50, 100/0, 85/15 and 72/28, respectively). Here, the power splitting ratio is defined as the fraction of power in the cross port (κ_{cross}) divided by the fraction of power in the bar port (κ_{bar}), both expressed in %. This ratio is comprised between 0 (0/100) and $+\infty$ (100/0), and gives a measure of how much input power exists through the cross output port as compared with the bar one. Besides, note that this ratio is independent of the excess losses, as far as both ports experience the same level of attenuation, which is usually the case as most MMIs are symmetric.

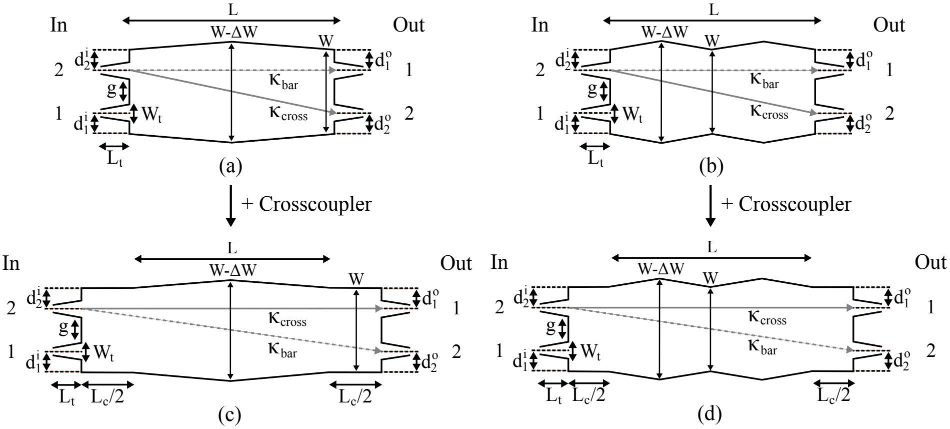

Figure 3.4: (a) Schematic diagram of types “A”, “C” and “D” with no crosscoupler. (b) Idem for type “B”. Note that this is a symmetrized version of the original device proposed in [56]. (c) Schematic diagram of types “A”, “C” and “D” when a crosscoupler is employed. (d) Idem for type “B”.

Later on, Besse and co-workers worked upon this idea [56], and demonstrated that the aforementioned devices could be used as the starting point for the design of 2x2 couplers with variable splitting ratio. This can be achieved by adiabatically tapering the width of the MMI, therefore introducing a mode dependent phase shift that ultimately leads to a change in the intensity of the output self-images with respect to the original distribution. Besse et al. theoretically and experimentally showed that obtaining continuous splitting ratios between 50/50 and 100/0 with just a few % error in both output ports was possible, and provided analytical formulas for the design of such devices. Furthermore, it was shown that to extend the splitting ratio range between 0/100 and 50/50, crosscouplers could be added to exchange the positions of the output ports. A schematic diagram for types “A”, “C” and “D” is shown in Fig. 3.4(a), while type “B” is shown in Fig. 3.4(b). Figures 3.4(c) and 3.4(d) show the same devices with their corresponding crosscouplers. Table 3.2 contains their main geometrical parameters, such as MMI length (L), crosscoupler length (L_c), the positions of the input/output waveguides ($d_1^i, d_2^i/d_2^o, d_1^o$), as well as the minimum MMI width (W_{min}) as a function of the access taper width (W_t) and the minimum gap between waveguides (g).

To sum up: continuous power splitting ratios between 0/100 and 100/0 can be obtained by introducing a width tapering in 2x2 MMIs. These devices are compact, intrinsically tolerant to manufacturing errors, and can operate over a broad bandwidth. Thus, they are ideal candidates for the design and implementation of couplers with variable splitting ratio in RAMZI filters. The formulas and general design procedure for such devices are described in more detail in the next section.

Type	$W_{\min}$	d_1^i, d_2^i	d_2^o, d_1^o	L	L$_c$	$\kappa_{\text{cross}}/\kappa_{\text{bar}}$
A	$3(W_t+g)$	$W/3$,$W/3$	$W/3$,$W/3$	$L_\pi/2$	L_π	50/50
B	$3(W_t+g)$	$W/3$,$W/3$	$W/3$,$W/3$	L_π	L_π	100/0
C	$2(W_t+g)$	$W/4$,$W/4$	$W/4$,$W/4$	$3L_\pi/4$	$3L_\pi$	85/15
D	$(5/2)(W_t+g)$	$W/5$,$2W/5$	$2W/5$,$W/5$	$3L_\pi/5$	$3L_\pi$	72/28

Table 3.2: Geometrical parameters of the MMIs with non-uniform power splitting ratios proposed by Bachmann et al. [77]. The minimum width ($W_{\min}$) is also shown as a function of both the access taper width (W_t) and the minimum waveguide spacing (g).

3.4 Design procedure

The steps required in the design of a tapered 2x2 MMI are summarized as follows:

1. Choose an MMI type ("A", "B", "C" or "D") whose nominal coupling constant for the cross port (κ_{cross}) is as close as possible to the design target κ. That is, $\kappa \simeq \kappa_{\text{cross}}$. If it is the case that κ falls in the range between 0% and 50%, then we must look for an MMI type whose nominal coupling constant for the bar port (κ_{bar}) is as close as possible to the design target. Later, a crosscoupler must be added. For example, if we wish to implement a coupler with $\kappa = 20\%$, we need to design an MMI type whose κ_{bar} is as close as possible to 20%, and then use a cross coupler once the MMI has been designed. In this case, one might use for example a type "C" device (85/15), to get a nominal coupling constant for the bar port of 15%.

2. Once the MMI type has been determined, the relative positions of the input and output waveguides are automatically set in order to ensure that the self-images are coupled to them with minimum losses (d_1^i, d_2^i and d_2^o, d_1^o in Table 3.2). Also, we know that in any fabrication technology a minimum gap (g) between access waveguides must be left so as to ensure proper opening during lithography and etching. All this information is used together with the width of the access taper (W_t) to determine the minimum possible width of the MMI ($W_{\min}$), according to the formulas of Table 3.2.

3. In general, keeping the width of an MMI as low as possible enhances the operation bandwidth. As a consequence, the width of the tapered 2x2 MMI is usually left equal to $W_{\min}$, provided that a sufficient number of propagation modes are supported by the waveguide (typically more than 4 or 5). If the waveguide does not meet this requirement, then the width must be increased. Also note that one must ensure that the gap among access waveguides is wide enough so that no optical coupling occurs.

4. Next, we proceed to compute the beating length (L_π) of the two lowest order modes (β_0 and β_1). For that, we must know both the waveguide cross-section

and the refractive indices of the employed materials for the chosen technology. The modes cam then be found either by numerical approximations, such as the EIM, or by using commercial solvers based in more sophisticated computational techniques.

5. Analytical formulas from [56] are then used to find the incremental width (ΔW) of the MMI taper for the specific coupling target (κ). These are given by

$$\Delta W = 2W\left(\frac{1}{2}-\frac{2}{\pi}\arccos\sqrt{\kappa}\right) \tag{3.15}$$

$$\Delta W = W\left(-\frac{2}{\pi}\arccos\sqrt{\kappa}\right) \tag{3.16}$$

$$\Delta W = 4W\left(\frac{1}{4}-\frac{2}{\pi}\arccos\sqrt{\kappa}\right) \tag{3.17}$$

$$\Delta W = \frac{-2W}{0.71}\left(0.355-\frac{1}{0.563\pi}\arccos\sqrt{\frac{\kappa-0.2}{0.8}}\right) \tag{3.18}$$

   for types “A”, “B”, “C” and “D”, respectively. Please note that in these expressions κ must be converted to linear units in order to be consistent with the definition of the arccos() function. Again, if the coupling constant falls between the range 0% and 50%, then we must modify the previous equations, substituting κ (expressed in linear untis) for $\kappa' = 1 - \kappa$. Also, note that ΔW can yield negative values. These simply mean that the width of the MMI is *increased* with respect to the original width W, while positive values mean that the width of the MMI is *decreased*.

6. Once ΔW has been determined, the formulas provided in [56] are employed again to find an analytical approximation to the length of the MMI coupler. This new length (L') is actually different from the length of the nominal devices due to the tapering of the MMI body, and it is computed as

$$L' = \frac{(W-\Delta W)}{W}L \tag{3.19}$$

   where L is the nominal length of the MMI type shown in Table 3.2.

7. Now that an initial guess has been found for all geometrical parameters, a numerical optimization is performed to obtain the exact splitting ratio and to reduce excess losses. This can be done by using for example fully vectorial 3D propagation methods, such as FDTD, although computation time can be drastically reduced if one combines the beam propagation method (BPM) and an EIM approximation. In this approach, the structure is reduced to an equivalent 2D geometry by means of the EIM (see Appendix A), and then BPM is used to propagate the fields within the device and compute the transmitted power and phase relations at the outputs [85].

MMI	#1	#2	#3	#4
Ratio	50/50	85/15	95/05	85/15
Type	A	C	B	B
L'	122.96	184.95	211.95	184.55
ΔW	0	0	-1.44	-2.53
d_1^i, d_2^i	3.28,3.28	2.51,2.51	3.32,3.32	3.32,3.32
d_2^o, d_1^o	3.28,3.28	2.51,2.51	3.32,3.32	3.32,3.32
W_t	2.75	3.35	2.7	2.7
MMI	#5	#6	#7	#8
Ratio	75/25	65/35	55/45	72/28
Type	C	D	D	D
L'	247.18	170.36	200.04	147.76
ΔW	-3.26	-1.5	-3.34	0
d_1^i, d_2^i	2.53,2.53	2.02,4.02	2.01,4.01	2,4
d_2^o, d_1^o	2.53,2.53	2.02,4.02	2.01,4.01	2,4
W_t	2.83	2.83	2.8	2.5

Table 3.3: MMI design parameters. All dimensions are given in μm. A common width for the access and multimode waveguides of 0.45 μm and 10 μm were employed, respectively. The length of the taper is also equal for all designs ($l_t = 50\ \mu m$).

3.5 Tapered 2x2 MMIs in SOI

3.5.1 Design

The aforementioned procedure was followed for the design of several tapered 2x2 MMIs with different power splitting ratios, which are shown in Table 3.3. The devices were then fabricated in a SOI multi-project wafer run (MPW) offered by OpSIS IME. The cross-section of this technology consists of a 2 μm thick buried oxide layer, over which a 220 nm silicon (Si) layer and a silicon dioxide (SiO_2) over-cladding are deposited. Two rib waveguides were employed with 130 nm and 160 nm etch depth (h) from top of the Si layer, respectively, as seen in Fig. 3.5(a).

The design procedure was as follows. First, the target coupling constants were associated with the best MMI type, although some non-optiumum variations were introduced to analyze their performance. Here, we only considered coupling constants in the range between 50% and 100%, so crosscouplers were not required. Next, a film-mode matching (FMM) mode solver was used for cross-section analysis (PhoeniX Software BV). The wavelength dependence of the refractive indices was included in the software through the use of parametrized Sellmeier equations. For all the MMIs subject to design, the body width was set to 10 μm, which proved enough to satisfy the design rules of the fabrication process in the input/output access planes. Third, the first and second order mode propagation constants (β_0 and β_1) were found at a wavelength of 1.55 μm for TE polarization, and the beat length

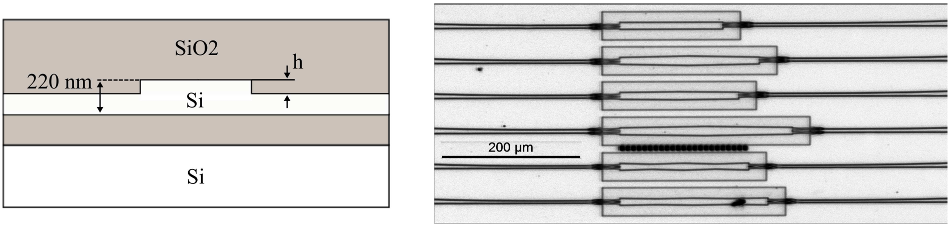

(a) (b)

Figure 3.5: (a) Cross-section of the SOI waveguide. (b) Microscope picture of the fabricated devices.

$L_\pi = \pi/(\beta_0 - \beta_1)$ was computed from these. The effective indices for the first and second mode given by the solver are n_{eff}^0=2.84849 and n_{eff}^1=2.84548. Therefore the beat length results into L_π=257.48 μm. Fourth, equations 3.15 to 3.19 were used to obtain a first guess of the width variation (ΔW) and body length (L'). The positions of the access waveguides ($d_1^i, d_2^i, d_2^o, d_1^o$) were computed from the formulas of Table 3.2.

The final step consisted of using BPM for a numerical optimization of the structure. The cross-section was reduced vertically to a 2D waveguide using an optimized EIM (Appendix A). This was done by first finding the effective index for the core region (n_{eff}^{WG}), and then the effective index of the cladding was calculated by numerically solving with a bisection method for the modes of the reduced structure to match the previously calculated L_π on the original cross-section. Tapers are required to minimize excess losses, imbalance and reflections as described in [86]. As a consequence, multiple BPM simulations were run to find iteratively both the optimum MMI geometry (L', ΔW) and the input/output tapers length and width (l_t and W_t). The optimization was performed for a nominal wavelength of $\lambda_0 = 1.55$ μm. The final body shapes and parameters for the MMIs are given in Table 3.3, as mentioned before.

3.5.2 Experimental results

Fabrication

The designs were fabricated on two different wafers, named A and B from now onwards, using a 248 nm CMOS line. The difference between wafers A and B was the etch depth (h) for the rib waveguides: 130 nm and 160 nm. From the dies delivered by the fab, those exhibiting dimensions closest to target were retained for measurements. These dimensions were provided by the foundry, and included waveguide widths as well as width and spacing of on-chip test gratings. The target grating width and spacing were both 315 nm. Metrology showed grating widths in the [321,333] nm range, and grating spacing in the [296-312] nm range. The target waveguide width was 500 nm, and metrology showed widths between 520 and 541 nm. The number of dies with metrology in these ranges amounted to 3

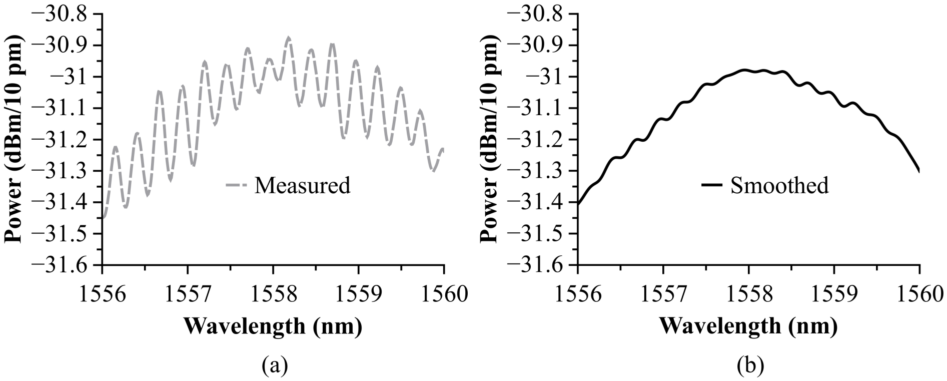

Figure 3.6: (a) Measured transmission spectrum of a test straight waveguide. FP peaks due to spurious reflections are clearly observed. (b) Same spectra, but smoothed with a 0.71 nm window.

dies per wafer, namely A1, A2 and A3 for wafer A, and B1, B2, B3 for wafer B. A picture of the fabricated devices is shown in Fig. 3.5(b). All the layouts included focusing grating couplers (FGC) to couple light vertically into/out of the chips. Both the FGCs and the waveguides connected to the MMIs supported only TE polarization.

Characterization setup

The characterization setup consists of a set of three motorized positioners. Two of them are used for holding the fibers vertically at the right angle to couple light into the FGCs (10° with respec to the normal to the chip surface), whereas the third one holds the sample on top of a thermally controlled ($\simeq$25 °C) vacuum chuck. A CCD camera vision system is also mounted in a motorized stage and a LED lamp is used for illumination. For the measurements, the fibers were aligned manually in two steps. Firstly, the fibers were approximated to the FGC locations by visual inspection. The approximated height location can be obtained when the fiber and its shadow overlap. Secondly, a broadband light source was connected to one of the fibers, whereas a power meter was connected at the the other end. The positions of the input and output fibers were then optimized with the motorized stages to obtain maximum power. After the fibers alignments were optimized, an Optical Spectrum Analyzer (OSA) was used to record the spectra with a resolution of $\simeq$10 pm.

Test structures and stability

Previously to measuring the MMIs, straight waveguides were measured in order to gather information about the different features observed in preliminarily recorded

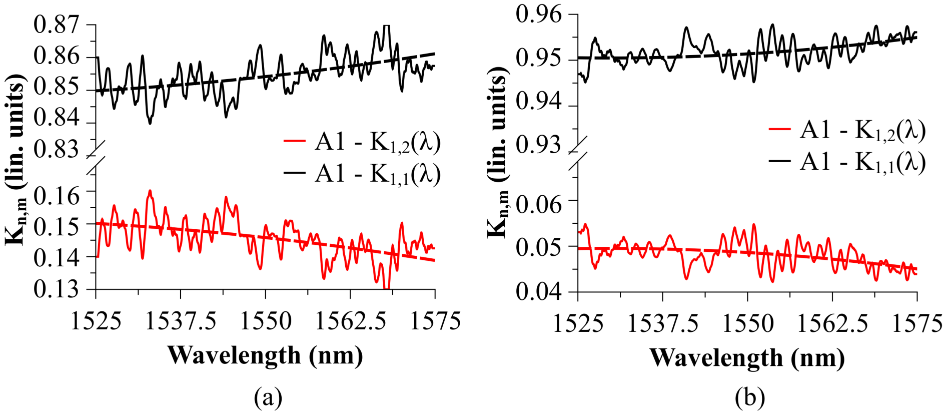

Figure 3.7: (a) and (b) Measured coupling ratios for MMIs#2 and #3 on die A1, respectively. Measured data is shown as solid red and black lines, while second-order polynomial fittings are also shown as dashed lines with the same colours.

traces. A single straight waveguide was measured repeatedly, and a set of 8 consecutive traces was obtained. Their average is shown as as dashed grey line in Fig. 3.6(a). Fabry-Pérot (FP) like ripples were observed with a separation between peaks of about $\Delta\lambda$=0.26 nm. These are attributed to spurious reflections either on the chip or in the measurement setup, since they were not present in the spectrum of the optical source. A moving average of 71 points was applied to the measured traces in order to clean the FP peaks. Note that traces were recorded with a 10 pm spectral spacing, which corresponding to 0.71 nm, approximately three times the $\Delta\lambda$ value. The results are also shown in Fig. 3.6(b) as solid black line. All spectral traces recorded for the MMIs were also smoothed as described, before using them in the calculations of coupling ratios detailed in the next subsection.

Coupling ratios

Coupling ratios for the desgined MMIs were derived from spectral traces measured at outputs m when accessed via an input n, termed $S_{n,m}(\lambda)$. The spectral information was captured in logarithmic units, and was later converted to linear units before computing the coupling ratios using the following expression

$$K_{n,m}(\lambda) = \frac{S_{n,m}(\lambda)}{S_{n,1}(\lambda) + S_{n,2}(\lambda)} \tag{3.20}$$

where $n = 1, 2$ and $m = 1, 2$ label the input and output waveguides numbered as shown in Fig. 3.4, respectively. Note that the coupling ratios defined by equation 3.20 are similar to but not the same as the power splitting ratios defined in

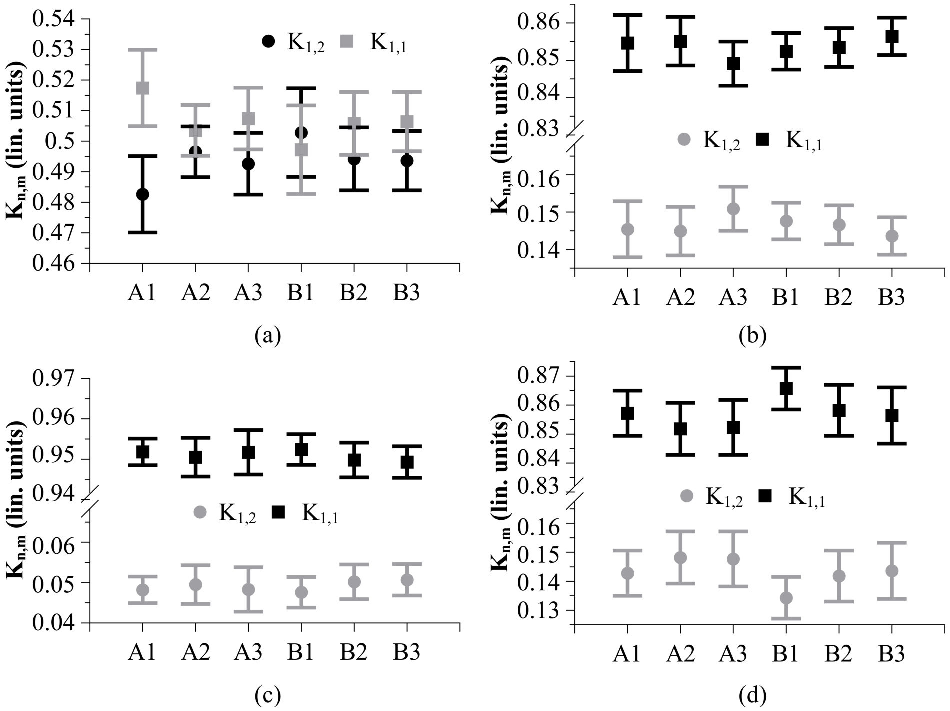

Figure 3.8: (a) to (d) Measured spectral averages and standard deviations of the coupling ratios for MMIs#1 to #4, over the 1525-1575 nm wavelength range, for all dies.

previous sections. Coupling ratios are defined as the ratio of optical power in one output port to the total output power, and they are usually given either in linear units or in %. Just like the splitting ratios, they give an idea of how much power is exiting through one port relative to the other. In fact, the coupling ratios can be thought of as the measured coupling constants that are used to compute the splitting ratio (κ_{cross} and κ_{bar}), but without the associated excess losses.

As an example, $K_{1,1}(\lambda)$ and $K_{1,2}(\lambda)$ are plotted in Figs. 3.7(a) and 3.7(b) for both MMI#2 and MMI#3 in die A1. Second-order polynomial fits are also shown. Results show good agreement with the target coupling constants for each output port, where deviations are approximately in the range of ±0.01 over a 50 nm wavelength span. From these traces, both the spectral average and standard deviation of the all coupling ratios were computed over the measured wavelength range (1525-1575 nm). The results for all dies are compiled in Figs. 3.8 and 3.9. As it can be observed at first sight, very similar performance was obtained for both wafers despite their etch depth difference, which is in good agreement with the sensitivity analysis reported in [87]. MMI#1 samples exhibited coupling ratios around 0.5 with deviations in the whole wavelength range of about ±0.02 for all

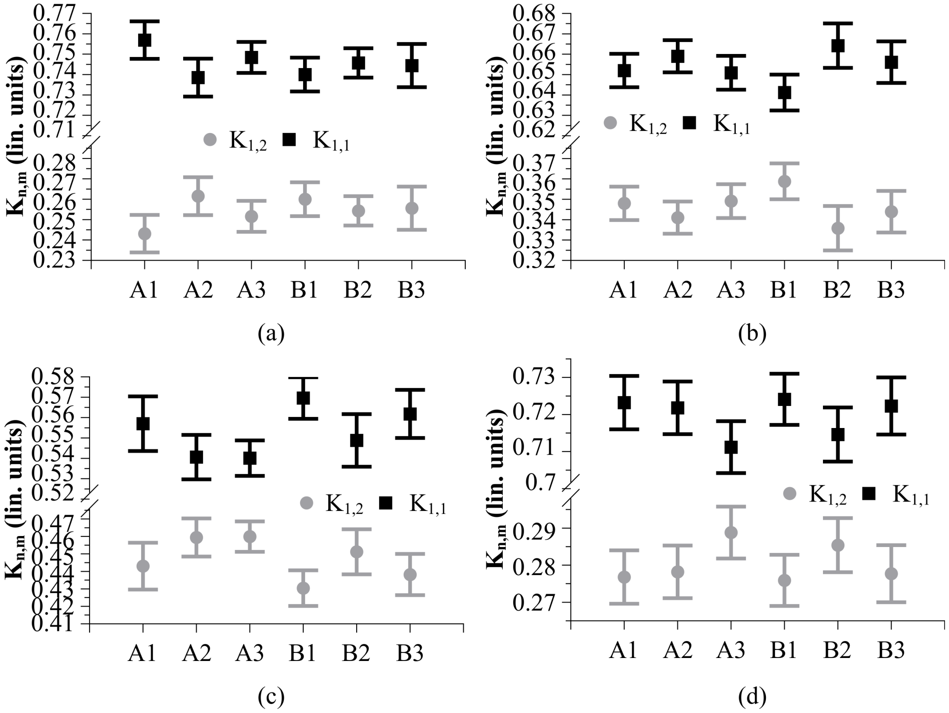

Figure 3.9: (a) to (d) Measured spectral averages and standard deviations of the coupling ratios for MMIs#5 to #8, over the 1525-1575 nm wavelength range, for all dies.

dies, except A1, where some imbalance is appreciated. For MMIs#2 to #4 the graphs are given with broken axes, but with similar intervals around the target coupling ratio. Comparing MMI #2 and #4, which both have 85/15 as a target splitting ratio, the performance of the first proved to be best for all dies. One might be tempted to attribute this to the fact that device #2 is a canonical (straight body) design, whereas #4 has a tapered geometry. However MMI #3 shown in Fig. 3.8(c) is also tapered and exhibits very good performance. In general, it can be observed a general trend where MMIs with a splitting ratio closer to 50/50 exhibit higher fluctuations than those close to 100/0, independently of the their geometry. Insight into this observation can be gained by carefully analysing the way these values are obtained. Note that the spectral traces $S_{n,m}(\lambda)$ are recorded at two different outputs of the MMI, each one connected to a FGC. Ideally both FGCs should have very similar performance (i.e. coupling losses). However, variations of a few tenths of dB are normal during measurement because of both the random nature of the alignment procedure and the intrinsic fabrication tolerances of the technology. In that case, a minor difference in the coupling losses of each FGCs

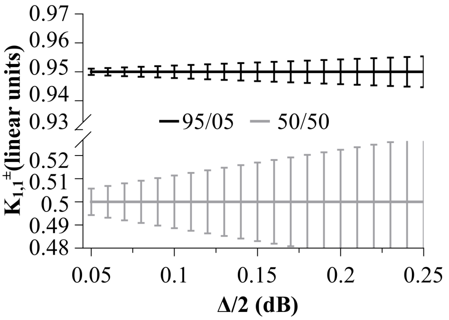

Figure 3.10: Impact of coupling losses variability (Δ/2) on the calculation of measured cross coupling ratios ($K_{1,1}$), as predicted by equation 3.21.

turns equation 3.20 into

$$K^{\pm}_{n,m}(\lambda) = \frac{10^{\frac{\pm(\Delta/2)}{10}} S_{n,m}(\lambda)}{10^{\frac{\mp(-1)^m(\Delta/2)}{10}} S_{n,1}(\lambda) + 10^{\frac{\pm(-1)^m(\Delta/2)}{10}} S_{n,2}(\lambda)} \tag{3.21}$$

where Δ represents the difference between the coupling losses of each FGC (in dB).

Figure 3.10 illustrates the variation in the calculated cross coupling ratio ($K^{\pm}_{1,1}$) of two different ideal couplers with splitting ratios of 95/05 and 50/50, respectively. As it can be seen, for the same level of FGC fluctuations, the calculated coupling ratios are more sensitive when they are closer to 0.5. On the contrary, the sensitivity to this effect is lower for more asymmetric couplers. Therefore, efficiency difference between FGCs, not only between dies but inside the same die too [88], is the most likely cause of the general trends. Still, it can be seen that measured coupling ratios are very close to the target values, with just a few percent differences over a 50 nm wavelength range. These results confirm the ones provided by Besse et al. [56], and prove the suitability of tapered 2x2 MMIs as highly robust couplers for the implementation of integrated optical lattice filters.

3.6 Tolerance analysis case study: A 4x4 MMI-based 90° optical hybrid in InP

3.6.1 Introduction

As it was already discussed in chapter 2, fabrication tolerances need to be considered by designers as an important source of error. Manufacturing uncertainties induce deviations of any device geometry away from its nominal design values, which can affect its overall performance. In the previous section, we measured the impact of such tolerances on the performance of tapered 2x2 MMIs in SOI. Here,

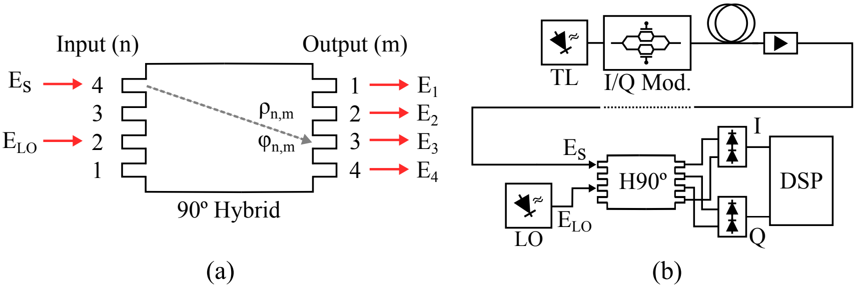

Figure 3.11: (a) Schematic diagram of a 90° hybrid. (b) Location of it within a coherent optical communication system.

we develop in more detail a practical case study. In particular, we proceed to perform a systematic numerical evaluation of the impact that several, simultaneous manufacturing deviations can have in an integrated, 4x4 MMI-based 90° optical hybrid, which was designed using an available generic InP platform. We will focus on understanding their effect on the two most common performance metrics of optical hybrids: amplitude imbalance and phase errors. We have chosen this device for its great practical importance, as it is widely used for the implementation of integrated coherent receivers. Figure 3.11(a) shows a schematic diagram of an ideal 90° hybrid, while Fig. 3.11(b) illustrates its typical location inside a coherent receiver system. Its four outputs provide the necessary amplitude and quadrature phase relations required in heterodyne, balanced coherent detection, which are given as follows

$$\begin{pmatrix} E_1 \\ E_2 \\ E_3 \\ E_4 \end{pmatrix} = \frac{1}{2} \begin{pmatrix} E_s + E_{LO} \\ E_s + jE_{LO} \\ E_s - jE_{LO} \\ E_s - E_{LO} \end{pmatrix} \tag{3.22}$$

where E_m are the complex field coefficients at the mth output port, while E_s and E_{LO} stand for the field coefficients of the signal and local oscillator, respectively.

3.6.2 Simulation procedure

The cross-section of the InP waveguide considered for the simulations can be seen in Fig. 3.12(a), while a 3D representation of the whole device is shown in Fig. 3.12(b). They both summarize material and geometrical parameters, including final design values and manufacturing tolerances. The latter include variations in waveguides' width and length (±0.1 μm), as well as absolute changes in InGaAsP refractive index (±0.004 over the full wavelength range) and core thickness (±0.05 μm). The simulations were performed as follows. Firstly, commercially available software tools (FieldDesigner and OptoDesigner, PhoeniX Software BV) were employed to design the hybrid using a design flow similar to that employed for the 2x2 tapered MMIs. The final device is 20 μm wide and 854.3 μm long,

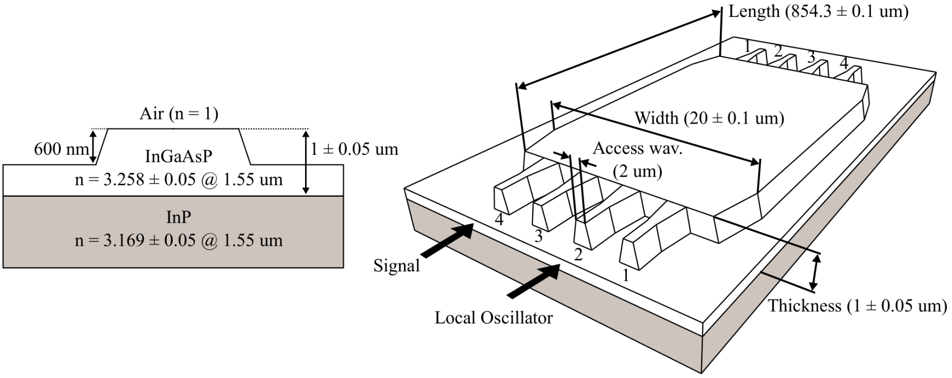

(a) (b)

Figure 3.12: (a) Cross-section of the simulated InP waveguide. (b) 3D diagram of the 4x4 MMI under consideration. Fabrication tolerances are shown along with the nominal design values.

excluding input and output waveguides, and was optimized for 1550 nm. The rib waveguides are comprised of an InGaAsP core (n = 3.258 @ $\lambda = 1.55$ μm) over an InP substrate (n = 3.169 @ $\lambda = 1.55$ μm), with an etch depth measured from the top of the core of 600 nm. No cladding is employed.

Next, an interval around each nominal design value was considered for all parameters under analysis (width, thickness and refractive index). Length deviations were excluded to reduce simulation time, as they have negligible impact on device performance [89]. Each interval was then discretized into 3 data points, which included the nominal as well as the two worst case values. Afterwards, these values were accordingly combined to form all possible ($3^3 = 27$) combinations. Wavelength was varied in steps of 2.5 nm over the C and L bands (1530-1625 nm), where we also accounted for refractive index wavelength dependence of materials (InP and InGaAsP). For every new wavelength point, one simulation cycle was run. Each simulation cycle included 27 Film Mode Matching (FMM) mode-solving calculations of the new MMI cross section; 3D to 2D reduction using an optimized EIM approximation (see Appendix A); and optical field propagation by means of a 2D beam propagation method (2D-BPM). These yielded the hybrid's field transmission coefficients for the two possible input ports (signal and local oscillator), which were automatically computed by the simulation software using mode overlap integrals between the simulated field in the multimode waveguide and the fundamental mode of the output waveguides. Their squared magnitude ($\rho_{n,m}$) gives the transmitted optical power, while their phase ($\phi_{n,m}$) is the relative phase shift between the nth input and mth output ports. All other parameters, such as the width and position of the access waveguides, were kept fixed. Note that the tolerances of the process are very small relative to nominal design values. For example, MMI's width, which is the most critical parameter, has a relative variation of less than 0.5%. Thus, it is expected that any possible process variation con-

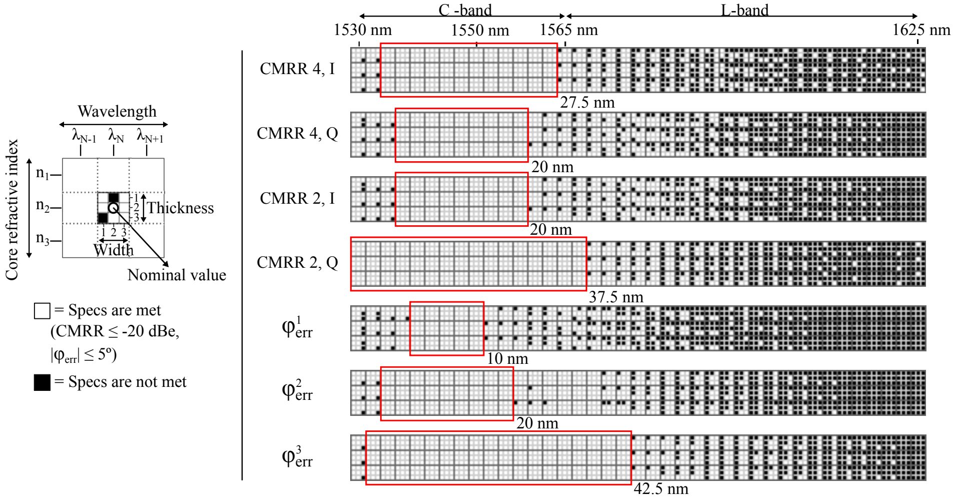

(a) (b)

Figure 3.13: (a) Conceptual representation of the dimensional stacking visualization technique. (b) Representation of the simulated figures of merit as compared against OIF specifications. Bandwidths over which these specifications are met for all possible manufacturing deviations are enclosed by solid red lines.

tained within the aforementioned intervals will lead to smaller changes in MMI's imaging length. The lower the resulting length deviation, the lower power imbalance, excess losses and phase errors. As a consequence, only the upper and lower bounds of these intervals were considered to reduce simulation time, and assumed to represent worst case conditions, which is consistent with previous simulation work on MMI-based 90° optical hybrids [87].

Since our tolerance analysis expands in a 4^{th} dimensional space, a versatile visualization technique called *dimensional stacking* was employed to represent results and gain some preliminary insight into possible relationships among parameters and figures of merit before further post-processing [90]. This concept is illustrated in Fig. 3.13(a). The main idea behind this technique is to recursively represent N-dimensional results by plotting a given pair of dimensions within blocks which correspond to points of other pairs of dimensions. In our case, blocks of 3x3 pixels (black and white coloured) separated by soft grey lines correspond to simultaneous variations of width and thickness where refractive index and wavelength are kept constant. Adjacent 3x3 blocks, separated by dark grey lines, correspond to width and thickness variations for a different refractive index and wavelength (vertical and horizontal direction, respectively). Note that parameter values increase from left to right and from top to bottom. This means that, for example, pixels in the center of each 3x3 block represent nominal design values of width and thickness, while the ones in the upper left corner represent the case in which both width and thickness are reduced with respect the their nominal value (19.9 μm and 0.95 μm, respectively).

3.6.3 Results

Results are shown in Fig. 3.13(b), where hybrid's figures of merit are plotted using the aforementioned visualization technique. On one hand, the common-mode rejection ratios (CMRRs) quantify the power uniformity among those outputs that are routed to the same balanced photodetector, as shown in Fig. 3.11(b). That is, outputs 1 and 4 (I channel); and outputs 2 and 3 (Q channel), respectively. They are mathematically defined as

$$\mathrm{CMRR}_{n,I}\ (\mathrm{dB}_e) = 20\log\left(\frac{|\rho_{n,1}-\rho_{n,4}|}{(\rho_{n,1}+\rho_{n,4})}\right) \tag{3.23}$$

$$\mathrm{CMRR}_{n,Q}\ (\mathrm{dB}_e) = 20\log\left(\frac{|\rho_{n,2}-\rho_{n,3}|}{(\rho_{n,2}+\rho_{n,3})}\right) \tag{3.24}$$

where $\rho_{n,m}$ are the power coupling coefficients at the mth output when the hybrid is accessed via the nth input port. Note that for each I and Q channel there two possible situations, as the hybrid can be accessed by either the signal (4) or local oscillator (2) inputs. The two possible CMRRS for both the signal and local oscillator have been labelled as *CMRR 4, I/Q* and *CMRR 2, I/Q*, respectively.

On the other hand, phase errors measure the deviation of the output signals with respect to the ideal phase response of a perfect 4x4 MMI. They are defined as

$$\phi^1_{\mathrm{err}} = (\phi^1_4-\phi^1_2)-(\phi^4_4-\phi^4_2)+180^\circ \tag{3.25}$$

$$\phi^2_{\mathrm{err}} = (\phi^2_4-\phi^2_2)-(\phi^3_4-\phi^3_2)+180^\circ \tag{3.26}$$

$$\phi^3_{\mathrm{err}} = (\phi^1_4-\phi^1_2)-(\phi^2_4-\phi^2_2)-90^\circ \tag{3.27}$$

where ϕ^m_n stands for the optical phase difference between the nth input and mth output port, respectively, measured in degrees.

In order to reduce the amount of information, pixels are simply coloured white when values go over a certain threshold, and black otherwise. These thresholds were set to match those specified by the Optical Internetworking Forum (OIF) implementation agreement [91], which are normally used as a reference in the literature [92–94]. Even if this threshold operation prevents us from looking at the actual values, a lot of information can be gained at first glance. Firstly, it can be seen that there is a small interval of wavelengths near 1550 nm (target design) where the hybrid meets OIF specifications for all figures of merit, independently of tolerance deviations. Thus, blocks are fully white-coloured, indicating that specifications are satisfied in all cases. As the wavelength is reduced, some black pixels start to show up on the lower right corners. This indicates that reducing wavelength while increasing both waveguide width and guiding layer thickness further confines propagation modes inside the multimode waveguide, which makes

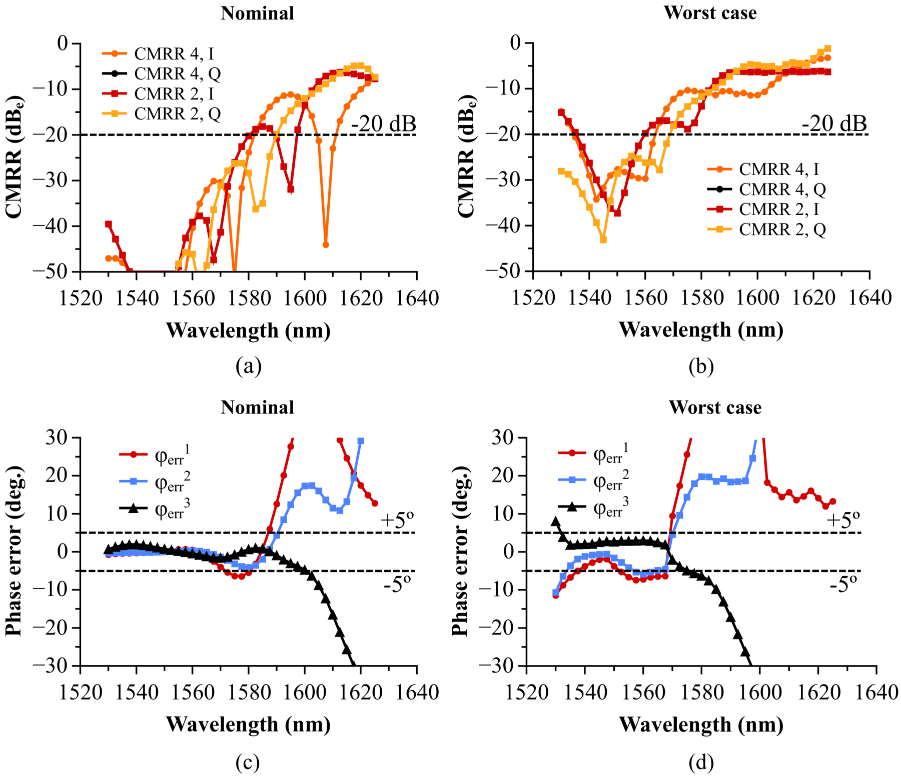

Figure 3.14: (a) Simulated CMRRs for the I and Q channels when the hybrid is accessed through either the local oscillator or signal ports (In-2 and In-4, respectively). Onlly nominal design values are considered. (b) Simulated CMRRs in the worst case tolerance scenario. (c) Simulated phase errors for the nominal design. (d) Simulated phase errors for the worst case tolerance scenario.

optimal length considerably deviate from its nominal design. If the wavelength is increased towards the L band, the opposite effect occurs. This is in agreement with MMI theory, since imaging length gets bigger/lower as the mode confinement increases/decreases [77]. Finally, notice how the black and white patterns in the vertical columns of 3x3 blocks are almost identical when the refractive index is varied. Hence, refractive index variations have negligible impact on device performance, which is mainly determined by width and thickness tolerances.

Simulation results are also shown in Figs. 3.14(a) to 3.14(d), where figures of merit across the C and L bands are plotted both for nominal and worst cases. Maximum values allowed by the Optical Internetworking Forum (OIF) implementation agreement [91] are also shown as dashed black lines. Note that here *worst case* refers to the worst performing device evaluated at each wavelength. This is, at each wavelength every figure of merit is evaluated for all possible combinations of cross-section parameters, and the worst value is chosen each time. Thus, it serves as an upper bound below which all possible hybrids will be located after manufacturing, even though single devices may show significantly better performance. In this way, the nominal design can be compared against an aggregate combination of manufacturing deviations in a real scenario, and it could even be used as a worst case value in the data sheet of the device if it were to undergo mass production.

As it can be seen in Fig. 3.14, taking tolerances into account yields a significant difference in operating bandwidth. If OIF specifications are to be strictly observed (CMRR $\leq$ -20 dBe, $\Delta\phi_{err} \leq \pm 5°$), only 10 nm (1540-1550 nm) are achieved in the worst case. On the contrary, up to 40 nm (1530-1570 nm) are guaranteed for the nominal design, similar to previously reported experimental results using the same technology [95, 96]. Thus, target specifications are only to be met by all manufactured devices over a 10 nm bandwidth in a real mass production environment, where random deviations across the wafer and from wafer to waer are unavoidable. This highlights the importance of taking tolerances into account when determining performance of integrated optical devices via simulation.

3.7 Conclusions

This chapter has been focused on the theory, design and experimental characterization of MMI-based 2x2 optical couplers with variable power splitting ratios. These devices are key for the implementation of optical lattice filters in general, and RAMZI filters in particular, and have been employed for all the optical filters that will be shown in this thesis.

We have first reviewed the basic theory behind the operation of MMIs with uniform power splitting. Next, we have introduced the concept of tapered MMIs, which allows for the implementation of 2x2 couplers with variable power splitting ratios by exploiting the coherent overlapping of degenerate self-images. A general description of the procedure that needs to be followed for the correct design of such devices has been given, followed by a specific example. To be more precise, we have provided design as well as extensive experimental data of multiple tapered 2x2 MMIs fabricated in a generic SOI platform. Our experiments indicate that coupling ratios with a just a few percent of error ($\simeq \pm 2\%$) with respect to the design targets can be obtained over a broad wavelength range ($\simeq$50 nm) using a state-of-the-art SOI fabrication platform, confirming the results provided by previous works in InP [56].

Finally, we have also provided simulation results of manufacturing-induced errors for an InP-based 4x4 MMI working as a 90° optical hybrid. These results confirm the impact that fabrication tolerances can have on device performance. In particular, it was shown that a fourfold reduction in operation bandwidth is obtained (40 nm$\rightarrow$10 nm) when considering real variations in a generic InP foundry. Designers thus need to be aware of them, and account for the existence of these errors in order to better predict the performance of their designs. From a more practical point of view, this work served as a basic starting point for the development of a generic library of simulation routines for the design of tapered 2x2 MMIs, which proved very valuable during the design stages of the different chips presented in this thesis.

Publications

The work done in this chapter lead to the following publications in peer reviewed journals and international conferences:

1. J. D. Doménech, **J. S. Fandiño**, B. Gargallo, and P. Muñoz, "Arbitrary Coupling Ratio Multimode Interference Couplers in Silicon-on-Insulator," *J. Lightw. Technol.*, vol. 32, pp. 2536–2543, July 2014.
2. J. D. Doménech, **J. S. Fandiño**, B. Gargallo, and P. Muñoz, "Arbitrary Coupling Ratio Multimode Interference Couplers in Silicon-on-Insulator," in *17th European Conference on Integrated Optics (ECIO)*, June 2014.
3. **J. S. Fandiño** and P. Muñoz, "Manufacturing Tolerance Analysis of an MMI-Based 90° Optical Hybrid for InP Integrated Coherent Receivers," *IEEE Photon. J.*, vol. 5, pp. 7900512–7900512, Apr. 2013.
4. **J. Fandiño**, P. Muñoz, and J. Capmany, "Manufacturing tolerance analysis of an InP, 4×4 MMI-based 90° optical hybrid for integrated coherent receivers," in *Optical Fiber Communication Conference and Exhibition (OFC)*, pp. 1–3, Mar. 2013.
5. **J. S. Fandiño**, P. Muñoz, and J. Capmany, "Tolerance analysis of a 4×4 MMI-based 90° optical hybrid for 100G coherent receivers," in *16th European Conference on Integrated Optics (ECIO)*, Apr. 2012.

Acknowledgements

J. D. Doménech and I. Artundo from VLC Photonics S.L. are gratefully acknowledged for providing access to the MWP run in the OpSIS IME platform. B. Gargallo is also acknowledged for performing the measurements of the manufactured 2x2 MMIs.

Chapter 4

Multimode interference reflectors based on aluminium mirrors in thick SOI

4.1 Introduction

Optical couplers with variable splitting ratios have already been discussed in detail in the previous two chapters. In the first one, we saw that they are a basic component for the synthesis of optical lattice filters. Afterwards, we reported on the design and experimental characterization of such couplers employing tapered 2x2 MMIs in Silicon-On-Insulator (SOI), and we demonstrated that achieving coupling ratios between 0% and 100% with a just a few % error was possible with state-of-the-art technologies.

In this chapter, we expand this basic idea, and present a new type of integrated device inspired on tapered MMIs: the multimode interference reflector (MIR). Essentially, an MIR is nothing but an MMI that is cut by half and is terminated with a reflective element. However, even this simple concept exhibits some interesting features. Unlike conventional MMIs, which as mentioned above are just power splitters, MIRs behave as integrated broadband mirrors with variable reflection/transmission ratios. Devices with such reflective properties are actually required in many applications, including the design of mirrors for on-chip lasers [97], as well as in the implementation of reflective filters [98].

The MIR concept was first introduced by Xu et al. in 2009 for a 1-port device based on a 1x2 MMI [99], and was later extended by Kleijn et al. for an arbitrary number of input ports [100]. In the seminal paper, a 1x2 MMI was terminated with a reflective structure based on two deep-etched facets at a 45° angle, and was then demonstrated to behave as a broadband mirror with 100% reflectivity. Since the mirror is defined in the same lithography as the waveguides, this approach avoids the use of extra fabrication steps. However, rounding effects during fabrication reduce the reflectivity of the facet-based mirror towards the center, where the tip is located, introducing extra losses and a possible distortion of the reflected interference pattern [99,100]. In order to avoid this undesirable characteristic, the amount of light intensity near this tip should be kept as low as possible, which in turn implies that not every MMI design can be adapted to create its corresponding MIR.

Here, we improve upon the original idea, and report on the design and experimental characterization of 2-port MIRs with arbitrary reflection/transmission ratios that employ aluminium mirrors. The use of the metallic mirror is actually a key differential advantage with respect to the deep-etched facets mentioned before. Although it requires a higher number of fabrication steps (+4), our approach has no limitations on the interference pattern formed at the mirror surface. As a consequence, more MMI types can be accommodated to form their equivalent MIRs, providing the designer with a higher degree of flexibility. Several 2-port MIRs fabricated in this platform with reflectivities in the range between 0 and 0.5 are experimentally demonstrated to proof the feasibility of our idea.

This chapter is organized as follows. First, the general operation principle behind MIRs will be reviewed. Then, and because their greater practical importance, we will focus our attention on 2-port MIRs based on aluminium mirrors. We will give general rules about how arbitrary reflectivities between 0 and 1 might be attained in these devices by exploiting the tapered 2x2 MMIs structures that were already explained in the previous chapter. Next, a simple quasi-analytical model for the aluminium mirror will be presented, which combines the Effective Index Method (EIM) and Fresnel equations in multilayered media. Fourth, the design of such 2-port MIRs in a thick SOI technology will be briefly described. Finally, the experimental characterization of the devices will be presented, along with a summary of the main results and conclusions.

4.2 Operation principle

In order to understand how MIRs work, it is best quickly review some of the basic theoretical principles behind MMIs. As we already saw in chapter 3, MMIs are based on the spatial Talbot effect that arises in planar multimode waveguides. Given a certain field pattern at the input of an MMI ($f_{in}^{+}(x)$), a finite number of modes ($E_n(x)$) will be excited within the multimode section. The output pattern at any given position along the waveguide ($f_{out}^{+}(x,z)$) is given by

$$f_{out}^{+}(x,z) = \sum_{n=0}^{N-1} c_n^{+} E_n(x) e^{-j\beta_n^{+} z} \tag{4.1}$$

where c_n^{+} are the complex overlap coefficients between $f_{in}^{+}(x)$ and $E_n(x)$, as described in chapter 3, and β_n^{+} stands for the propagation constant of the n-th mode. Here, we have added the + superscript on purpose, so as to distinguish between the forward-propagating (+) and the backward-propagating (-) modes.

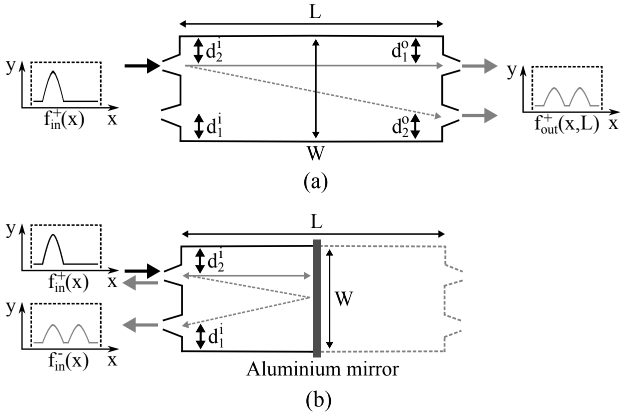

Figure 4.1: (a) 2x2 MMI. (b) Equivalent 2-port MIR with an aluminium mirror.

It can be proved that, if the propagation constants follow a quadratic law, then there exist fixed periodic positions along the multimode section where the output field pattern is made of a finite number of evenly spaced replicas of the input field [80]. Figure 4.1(a) illustrates this concept for a 2x2 MMI. If a set of single-mode waveguides are placed right where these images appear (d_1^o and d_2^o), then all the optical power will be evenly collected, leading to the creation of optical couplers with a fixed number of input/output ports. Also remember that non-even power splitting can be achieved by tapering the MMI width [56].

MIRs are just like MMIs, but working in reflection. They are created by simply taking an already designed MMI of width W and length L, cutting it by half and then terminating one of its ends with a reflective structure. In that case, the reflected field pattern ($f_{in}^-(x)$) at the input of the MIR is given by

$$f_{in}^-(x) = \sum_{n=0}^{N-1} c_n^+ \rho_n E_n(x) e^{-j\beta_n^+ L/2} e^{+j\beta_n^- L/2} \tag{4.2}$$

where ρ_n is the complex reflection coefficient experienced by each mode upon reflection on the mirror, and β_n^- is the propagation constant of the backward n-th mode. Note that the original sum has now been expressed as a contribution from a forward ($+L/2$) as well as a backward ($-L/2$) propagation path.

In our case, the optical mirror is formed by depositing a thin layer of aluminium ($\simeq$ 150 nm) on top of a silica buffer layer ($\simeq$ 250 nm) [101]. If we assume that this metallic mirror is perfect and has no losses, all the forward-propagating modes in the multimode section will be perfectly coupled to their corresponding backward-propagating ones, while keeping the same amplitude and phase relations among them. Mathematically, this can be expressed as

$$\rho_n = 1 \tag{4.3}$$

By further noting that $\beta_n^- = -\beta_n^+$, the reflected field pattern ($f_{in}^-(x)$) at the

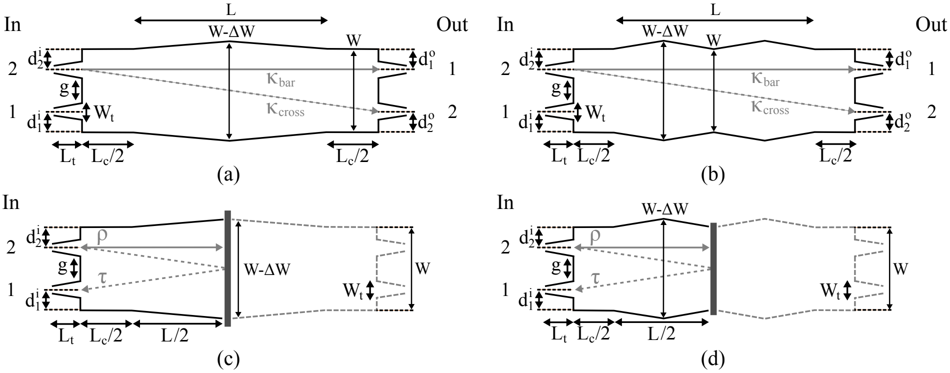

Figure 4.2: (a) Geometry of tapered 2x2 MMIs for types “A”, “C” and “D”. (b) Idem for type “B”. (c) and (d) Equivalent 2-port MIRs.

input of the MIR can be finally expressed as

$$f_{in}^{-}(x) = \sum_{n=0}^{N-1} c_n^{+} E_n(x) e^{-j\beta_n^{+} L} = f_{out}^{+}(x, L) \tag{4.4}$$

In other words: the same interference pattern that otherwise would be formed at the output plane of the original MMI ($f_{out}^{+}(x, L)$) will appear reflected at the access plane of the MIR. If the locations of the input waveguides (d_1^i and d_2^i) match with the positions of these reflected images, then all the reflected power is captured again, creating an MIR.

4.3 2-port MIRs with arbitrary reflectivity

Following the same ideas described above, it can be proved that the four types of tapered 2x2 MMIs described in the previous chapter (see Table 3.2) can be readily adapted to create 2-port MIRs with arbitrary power reflection/transmission ratios (ρ/τ). In this case, ρ/τ is defined as the fraction of reflected optical power in the input port (ρ) divided by the fraction of transmitted optical power in the adjacent port (τ). The word reflectivity will be later employed to denote just ρ, and will be expressed either in linear units or in %. Schematic diagrams of the two possible geometries of tapered 2x2 MMIs and their equivalent 2-port MIRs with aluminium mirrors are shown in Figs. 4.2(a) to 4.2(d). As it can be seen, the design of a 2-port MIR first involves the design of a tapered 2x2 MMI. Afterwards, a mirror is simply added at half of its length. However, one needs to observe some extra considerations in order to make sure that the MIR is correctly designed.

First, a 2x2 MMI with a power splitting ratio given by $\kappa_{cross}/\kappa_{bar}$ will turn into a 2-port MIR with a reflection/transmission ratio of $\rho/\tau = \kappa_{bar}/\kappa_{cross}$. That is, the fraction of optical power given by κ_{bar} will be reflected back at the input

Schematic	Type	d_1^i, d_2^i	L/2	$L_c/2$	ρ/τ
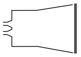	A	$W/3, W/3$	$L_\pi/4$	$0 \mid \mathit{L_\pi/2}$	50/50 | *50/50*
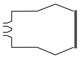	B	$W/3, W/3$	$L_\pi/2$	$0 \mid \mathit{L_\pi/2}$	0/100 | *100/0*
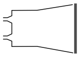	C	$W/4, W/4$	$3L_\pi/8$	$0 \mid \mathit{3L_\pi/2}$	15/85 | *85/15*
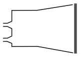	D	$W/5, 2W/5$	$3L_\pi/10$	$0 \mid \mathit{3L_\pi/2}$	NA | *72/28*

Table 4.1: Geometrical parameters of 2-port MIRs. Those in italics are obtained after introduction of a crosscoupler. N/A = Not applicable.

where the power was launched, while the fraction of optical power given by κ_{cross} will appear at the other input. This is illustrated in Figs. 4.2(a) to 4.2(d), where solid and dashed grey arrows have been drawn representing the different optical paths. Since tapered 2x2 MMIs without crosscouplers can only implement splitting ratios between 50/50 and 100/0, this means that reflection/transmission ratios are limited to the range between 50/50 and 0/100.

Second, it must be noted that type D devices (72/28) without a crosscoupler are asymmetric. That is, their input and output waveguides are not located at the same distances from the sides of the MMI ($d_1^i = W/5$ against $d_2^o = 2W/5$, and $d_2^i = 2W/5$ against $d_1^o = W/5$). As a consequence, the reflected images will not match with the position of the input waveguides, so an MIR with a reflection/transmission ratio around 28/72 can not be implemented with this particular MMI type.

Third, note that the previous limitation on the achievable reflection/transmission ratios can be avoided by the introduction of so-called *crosscouplers*, just like it was done for tapered 2x2 MMIs in the previous chapter. If we lengthen the original structure with a non-tapered multimode section, it is possible to extend this range between 50/50 and 100/0. As a consequence, tapered 2x2 MIRs can be designed with arbitrary reflectivies between 0% and 100%. For types "A" to "C", whose inputs are symmetric with respect to the center of the MIR, the presence of a crosscoupler inverts the reflection/transmission ratio. For type "D", the presence of a crosscoupler leads to output images which are now located at the same distances as the input waveguides from the sides of the MMI ($d_1^i = d_2^o$ and $d_2^i = d_1^o$). Contrary to the previous situation, the requirements of the input/output positions are met, and this device can indeed be used as a 2-port MIR with a reflection/transmission ratio of 72/28.

Table 4.1 summarizes the main geometrical parameters of the four types of 2-port MIRs that can be derived from the tapered 2x2 MMIs of Table 3.2. Please note that, as mentioned before, ρ/τ changes for types A to C when a crosscoupler is added. This feature has been included in the table by separating the two possible

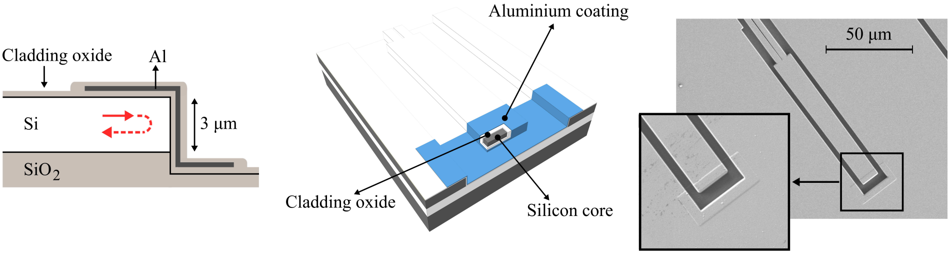

(a) (b) (c)

Figure 4.3: (a) Cross-section of the aluminium mirror layer stack. (b) 3D Model of a 2-port MIR with an aluminium mirror. (c) SEM picture of a fabricated device.

ratios with a vertical bar (|), where those with a crosscoupler have been highlighted in italics. As it can be seen, type "D" only works after the introduction of a crosscoupler, as explained before. L_π is defined in equation 3.14 in chapter 3.

4.4 Aluminium mirror modelling

As a novelty with respect to previous works, the MIRs presented here make use of aluminium (Al) mirrors, which are nothing but a thin film of metal ($\simeq$ 150 nm) deposited on top of an open end silicon (Si) waveguide, with an intermediate buffer layer ($\simeq$ 250 nm) of silicon dioxide (SiO_2) as a cladding. This deposition ensures a uniform reflectivity over the whole mirror facet, and thus avoids the problem of the original structure based on two deep-etched facets proposed by Xu et al. [99]. A cross-section of such mirrors is shown in Fig. 4.3(a). Figure 4.3(b) shows a schematic 3D representation of a 2-port MIR, while Fig. 4.3(c) contains an scanning electron microscope (SEM) picture of a fabricated device, where the deposited metal film can be easily appreciated.

The key idea behind these mirrors lies on the fact that the reflectivity of the aluminium coating is enhanced through the use of an intermediate silica layer ($\simeq$ 250 nm), which is grown before metal deposition. That is, the reflectivity of the structure shown in Fig. 4.3(a) is greater when a thin silica layer is placed between the silicon and the aluminium film, compared to what would be obtained if the aluminium were directly deposited on top of the silicon. This effect only occurs at a certain range of wavelengths, and is due to thin-film interference. The incident light interferes with itself on the silica film, enhancing reflection when the backward-propagating waves combine coherently at the output. More details about this structure and its performance can be found in [101].

In order to correctly design 2-port MIRs based on this approach, it is desirable to have a proper understanding of the possible effects of the mirror on overall device performance. We start here our analysis with a commonly employed technique for the simulation and design of MMIs, where the 3D problem is reduced to a simpler

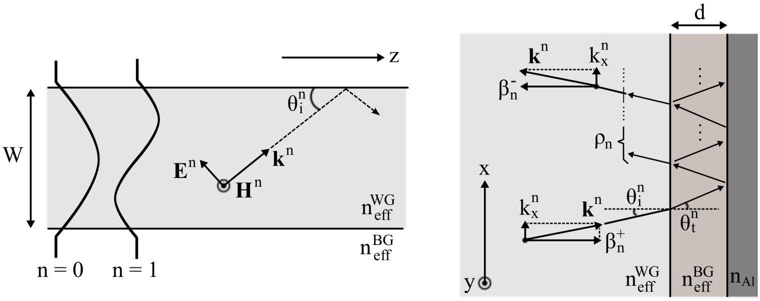

(a) (b)

Figure 4.4: (a) Equivalent slab waveguide after applying the EIM. Each mode (n = 0, 1...) is represented here as a plane wave bouncing back and forth at the waveguide interfaces with a certain angle (θ_i^n). (b) Schematic representation of the resonant reflection of a plane wave (mode) upon incidence on the multilayer structure that forms the aluminium mirror.

2D geometry with use of an optimized EIM [80]. More details on this simulation technique are explained in Appendix A. In brief, the EIM eliminates the vertical dimension by finding two effective refractive indices for both the core (n_{eff}^{WG}) and the cladding (n_{eff}^{BG}) of an infinite slab waveguide. Those indices are optimized in such a way that this waveguide has the same self-imaging length as that of the original 3D MMI. Thus, any mode propagating inside the real (3D) MMI section relates to a mode of the corresponding infinite slab waveguide, whose thickness is equal to the MMI width. According to [102], the modes of a slab waveguide might be understood as plane waves bouncing back and forth on the core/cladding interface (see Fig. 4.4(a)). Each plane wave propagates at a different angle θ_i^n, which is related to effective index of the n-th mode (n_{eff}^n) by

$$\theta_i^n = \arccos\left(\frac{\beta_n^+}{|\mathbf{k}^n|}\right) = \arccos\left(\frac{n_{eff}^n}{n_{eff}^{WG}}\right) \tag{4.5}$$

where $|\mathbf{k}^n| = 2\pi n_{eff}^{WG}/\lambda_0$, being λ_0 the vacuum operation wavelength.

Under the previous assumptions, the aluminium mirror can be then modelled to first order as an infinite planar interface between three different media: The effective core of the waveguide, the effective cladding and the aluminium layer, as depicted in Fig. 4.4(b). The electric field reflection coefficient in both modulus and phase (ρ_n) that each mode experiences upon reaching the reflecting surface is now easily obtained by applying the well-known Fresnel equations for multilayer structures [103]. Considering three layers and only TE propagation, which correspond to p-polarized plane waves, the electric field reflection coefficient for the n-th mode can be expressed as

$$\rho_n = \frac{\rho_{12}^n + \rho_{23}^n \exp\left(-j4\pi(d/\lambda_0)n_{eff}^{BG}\cos\theta_t^n\right)}{1 + \rho_{12}^n\rho_{23}^n \exp\left(-j4\pi(d/\lambda_0)n_{eff}^{BG}\cos\theta_t^n\right)} \tag{4.6}$$

where d is the thickness of the cladding oxide layer, and θ_t^n is the transmitted angle after the first planar interface, which is obtained by applying Snell's law

$$\theta_t^n = \arcsin\left(\frac{n_{eff}^{WG}\sin\theta_i^n}{n_{eff}^{BG}}\right) \tag{4.7}$$

Finally, ρ_{12} and ρ_{23} relate to the electric field reflection coefficients at the two interfaces, and are given by

$$\rho_{12}^n = \frac{(n_{eff}^{BG})^2 n_{eff}^{WG}\cos\theta_i^n - (n_{eff}^{WG})^2 n_{eff}^{BG}\cos\theta_t^n}{(n_{eff}^{BG})^2 n_{eff}^{WG}\cos\theta_i^n + (n_{eff}^{WG})^2 n_{eff}^{BG}\cos\theta_t^n} \tag{4.8}$$

$$\rho_{23}^n = \frac{(n_{Al})^2 n_{eff}^{BG}\cos\theta_t^n - (n_{eff}^{BG})^2[(n_{Al})^2 - (n_{eff}^{BG}\cos\theta_t^n)^2]^{1/2}}{(n_{Al})^2 n_{eff}^{BG}\cos\theta_t^n + (n_{eff}^{BG})^2[(n_{Al})^2 - (n_{eff}^{BG}\cos\theta_t^n)^2]^{1/2}} \tag{4.9}$$

where n_{Al} is the (complex) refractive index of aluminium .

In these formulas, it has been assumed by convention that lossy materials exhibit refractive indices with negative imaginary parts. As a consequence, the square root formula of equation 4.9 yields two different solutions, of which only the one with negative imaginary coefficient must be considered. Once the complex electric field reflection coefficients are found, the reflected interference pattern at the input waveguides ($f_{in}^-(x)$) can be easily found by applying equation 4.2, with $\beta_n^- = -\beta_n^+$. Since the modes propagate at a slightly different angle, it is expected that the mirror will change their relative amplitude and phases, thus affecting the beating pattern at the output.

We performed some numerical simulations to verify our quasi-analytical analysis. The simulation procedure can be described as follows. First, well-known formulas for the refractive indices of Si and SiO$_2$ were employed to compute n_{eff}^{WG} and n_{eff}^{BG} using a mode solver based on the Film Mode Matching (FMM) method, where the cladding index (n_{eff}^{BG}) was optimized using the procedure explained in Appendix A. Then, these indices were fed into an in-house Matlab$^{\mathrm{TM}}$ code that computes both the mode field profiles and propagation constants of an infinite slab with a given width, and then performs the field propagation along the 2-port MIR. This includes mode overlap integrals at both input and outputs, as well as mode-dependent electric field reflection coefficients given by equation 4.6, where d $\simeq$ 250 nm for this particular platform. Two different MIR types were considered: a type "A" device with $\rho/\tau = 50/50$ and a type "B" device with $\rho/\tau = 0/100$, whose geometrical parameters can be found in Table 4.2. Finally, and to check the validity of our model, simulations were compared against high-resolution 2D FDTD calculations performed with Meep in a 7 node computing cluster [104].

Simulation results are shown in Figs. 4.5(a) and 4.5(b) for type "B" and type "A" devices, respectively. As it can be seen, our quasi-analytical approach yields very similar results to the more rigorous FDTD method. For type "B", both calculations predict a residual reflectivity lower than -25 dB over more than

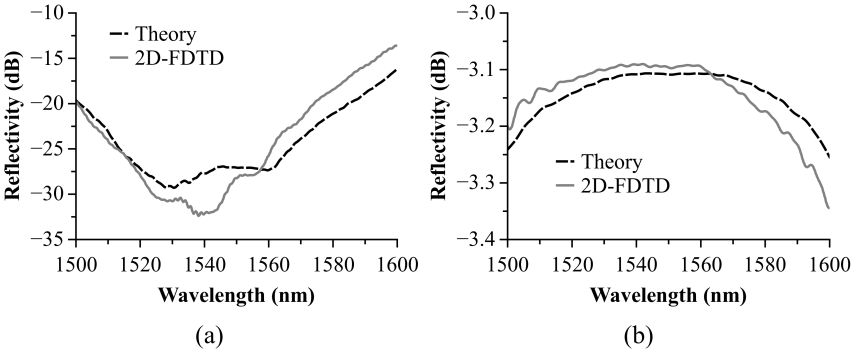

Figure 4.5: (a) Simulated reflectivities for the type "B" device of Table 4.2 (ρ/τ = 0/100), both using FDTD (grey solid line) and the quasi-analytical theory (black dashed line). (b) Idem for the type "A" device of Table 4.2 (ρ/τ = 50/50).

a 40 nm bandwidth (1520-1560 nm), with the quasi-analytical approach yielding slightly more residual reflected power near the design wavelength (1550 nm). For type "A", a reflectivity higher than -3.2 dB over a 60 nm bandwidth (1520-1580 nm) is achieved in both cases, with about 0.1 dB insertion losses at 1550 nm. These correspond to an effective peak reflectivity of 97.7%, in good agreement with previously reported simulation results [101], and points to a negligible performance degradation introduced by the mirror.

In practice, however, fabrication imperfections such as surface roughness and changes in the sidewall angle will affect the reflecting performance of the designed mirror. This will not only introduce extra losses, but also a distortion of the reflected field. The distortion will change the relative amplitudes and phases of the backward-propagating modes, which will cause in turn extra losses and imbalance in the self-images formed at the input of the MIR. Thus, designers might need to consider these effects beforehand, and compensate for a possible reduction of the reflectivity during the design stage.

4.5 Device design

In order to experimentally demonstrate the concept, 5 different 2-port MIRs with reflectivities varying between 0 ($\rho/\tau = 0/100$) and 0.5 ($\rho/\tau = 50/50$) were considered. Given the almost negligible effect introduced by the mirror found in the previous section, and the lack of more realistic experimental data, an ideal metallic mirror was assumed in order to simplify the design process. Under the previous assumption, the effect of the mirror is neglected and the MIRs dimensions can be obtained by simply simulating their equivalent tapered MMIs using the well-known beam propagation method (BPM). The design is thus reduced to that explained

Schematic	Type	d_1^i, d_2^i (μm)	ΔW (μm)	L′/2 (μm)	Target ρ/τ	Sim. ρ/τ
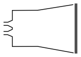	A	3.9,3.9	0	101.92	50/50	49.1/49.6
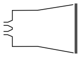	A	3.9,3.9	0.75	88.29	40/60	39.1/59.1
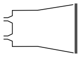	C	2.92,2.92	-2.785	225.77	30/70	30.0/68.1
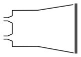	C	2.92,2.92	-1.057	180.39	20/80	19.8/79.0
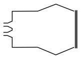	B	3.9,3.9	0	203.84	0/100	0.0/98.9

Table 4.2: Physical dimensions and BPM simulation results of the 5 different fabricated devices. The width is common for all designs (11.7 μm), and no crosscouplers are employed ($L_c/2=0$).

in chapter 3, which can be briely described as follows.

First, 5 different power splitting ratios ($\kappa_{cross}/\kappa_{bar}$) in the range between 50/50 and 100/0 were chosen, namely: 50/50, 60/40, 70/30, 80/20 and 100/0. Tapered 2x2 MMIs with these splitting ratios do not require an extra crosscoupler, which results in shorter devices with an enhanced operation bandwidth [89]. Each of these ratios was then assigned to be implemented by a given MMI type ("A", "B" or "C"), which was done by trying to minimize the difference between the target value and the splitting ratio of the canonical device (50/50, 100/0 and 85/15). Please note that, as explained before, these splitting ratios lead to reflection/transmission ratios between 50/50 and 0/100, this is: 50/50, 40/60, 30/70, 20/80 and 0/100. A common width of 11.7 um for all devices was found to be enough to satisfy the minimum spacing between the 2.8 um wide input waveguides, thus ensuring a proper opening of the access plane during lithography and etching. Next, an optimized EIM and 2D BPM propagations were employed to iteratively find the optimum geometrical parameters of the butterfly MMIs, namely length (L′) and width variation (ΔW).

The equivalent MIR geometries can finally be determined by noting that they are equal to that of the designed butterfly MMIs, except for the length, which is half of it (L′/2). Table 4.2 shows the final parameters of the designed devices, together with their simulated performance. Please note that here negative ΔW correspond with a widening of the MMI body, and viceversa.

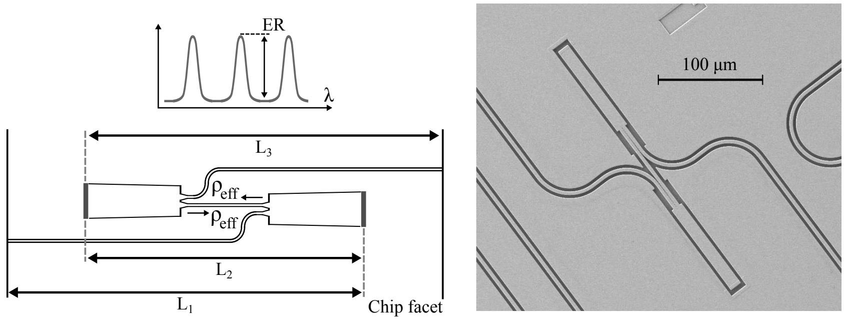

(a) (b)

Figure 4.6: (a) Schematic diagram of the structures employed to measure the effective reflectivities of the devices under test. (b) SEM picture of a test structure.

4.6 Measurement procedure and experimental results

The designed devices were fabricated in a commercially available 3 um thick SOI platform. More details about the fabrication procedure and technology capabilities can be found elsewhere in the literature [101, 105]. Fabry-Pérot (FP) test structures made of a concatenation of two MIRs were employed to extract the wavelength dependent reflectivity, similar to [100]. Figure 4.6(a) shows a schematic diagram of the test structures, while Fig. 4.6(b) is an SEM picture of a fabricated device. The two MIRs form an integrated resonant cavity with a periodic spectrum made of interference fringes. The depth of these fringes, also known as the extinction ratio (ER), depends on the total effective reflectivity of the MIR under test (ρ_{eff}). This includes not only the reflectivity of the MIRs themselves, but also the insertion losses in the access waveguides and the propagation losses within the multimode section. An interesting feature of this indirect approach is that the extinction ratio does not depend on the coupling losses, which can fluctuate from measurement to measurement due to mechanical vibrations and thermal drifts, as well as different roughness levels in the input and output facets. Since the losses in the connecting straight waveguides can be considered negligible ($\leq$0.1 dB), ρ_{eff} is given by [100]

$$\rho_{eff} = \frac{\sqrt{\mathrm{ER}} - 1}{\sqrt{\mathrm{ER}} + 1} \tag{4.10}$$

where ER is the measured extinction ratio, in linear units. Here, we have assumed that the reflectivities of both MIRs that form the FP cavity are identical.

The measurement procedure was as follows. First, red visible light coming from a fiber laser was coupled to a Thorlabs' FiberBench, consisting of a collimator, a free space polarizer and a focusing microscope objective. Visible light was employed in this first step because it allows for a coarse alignment of both input and output stages, which are mounted on top of piezoelectric micropositioners.

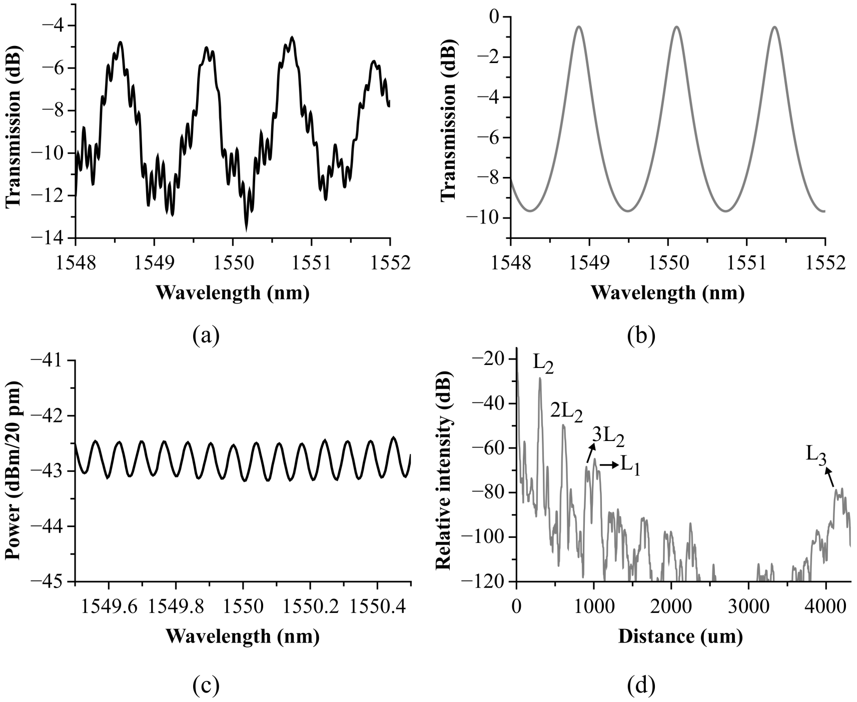

Figure 4.7: (a) Measured spectrum of the type "A" device of Table 2 ($\rho/\tau = 50/50$), after normalization with a test straight waveguide. (b) Simulated spectrum of the same structure using the theoretical model. (c) Measured transmission spectrum of a reference straight waveguide. (d) Relative contributions of the different resonant cavities present in the structure.

Second, a broadband ASE source (ASE-CL-20-S, NP Photonics) was coupled to the FiberBench. The micropositioners were then optimized until maximum power was collected at the output by means of a lensed fiber. The free space polarizer of the input stage was adjusted so that only TE polarization, parallel to the chip surface, was injected into the chip. Finally, captured light was directed into an optical spectrum analyzer (AQ6370C, Yokogawa), where it was recorded and sent to a computer through a GPIB interface. The transmission spectra of test straight waveguides located nearby on the chip were also collected so as to normalize and compensate for the non-flatness of the source. In total, 9 different chips were measured, with 6 test structures each (5 MIRs + 1 straight waveguide). Insertion losses after normalization varied for each structure, but they were about 5 dB on average.

An example of a measured transmission spectrum after normalization is shown in Fig. 4.7(a), corresponding to device 1 in Table 4.2 (type "A", $\rho/\tau = 50/50$). It can be observed how the Fabry-Pérot fringes are affected by spurious ripples.

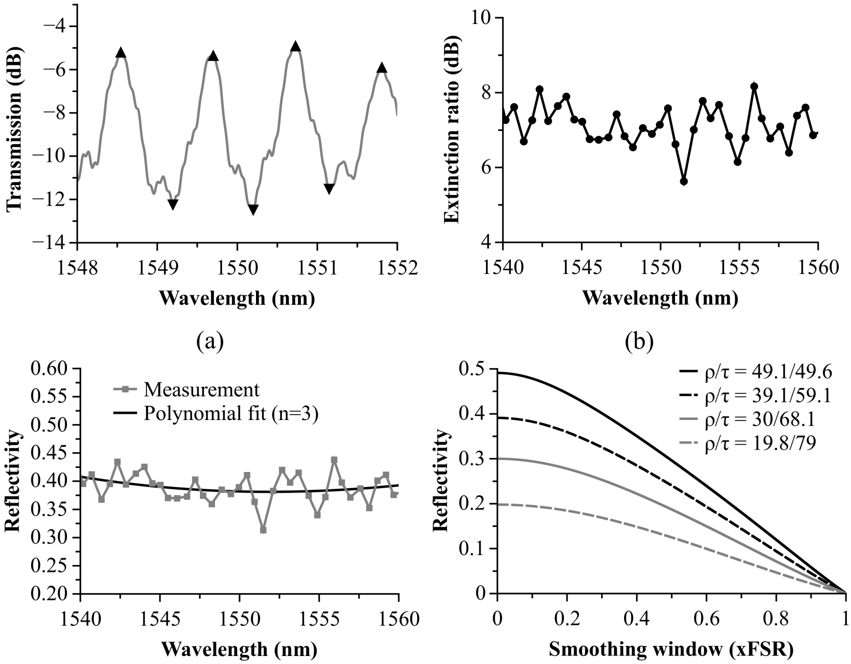

(a) (b)

(c) (d)

Figure 4.8: (a) Measured spectrum of the type “A” device of Table 4.2 ($\rho/\tau = 50/50$), after normalization with a test straight waveguide and smoothed with a 30 point moving average ($\simeq$120 pm). Maxima and minima are also shown as black triangles. (b) Extracted extinction ratios for different wavelengths. (c) Measured reflectivity and third-order polynomial fit (solid black line). (d) Reduction in reflectivity for each device in Table 4.2, as the smoothing window goes from zero to a size equal to the FSR of the FP.

In order to determine whether the metallic mirror is the cause of such ripples, we simulated the response of the test structure of device 1 using our theoretical model. Simulation results are shown in Fig. 4.7(b), where it is shown that the predicted response of the FP is almost ideal. The extra oscillations measured in the real devices can not then be put down to high-order mode excitation, induced phase shifts or other resonant phenomena in the metal mirror. On the contrary, these undesired fringes are explained by the existence of a higher than expected back-reflection from the chip facets, which is in turn attributed to the relatively low performance of the employed antireflection coating.

First, note that high levels of facet reflectivities have already been observed in previous works on the same technology, where ripple values of ±0.5 dB have been reported [101]. In our case, oscillations of up to ±0.25 dB dB have been experimentallly measured in reference straight waveguides (Fig. 4.7(c)). In reality, the

Type	FSR (nm)	Smooth win./FSR	ρ (w/o smooth)	ρ (w/ smooth)
A	1.056	0.113	49.1	47.5
A	1.199	0.1	39.1	38.2
C	0.598	0.2	30	27.76
C	0.714	0.168	19.8	18.8
B	0.66	0.182	0.0	0.0

Table 4.3: Estimated reduction in measured reflectivity due to smoothing.

reference waveguide ripples are probably higher. This is because their Free Spectral Range (FSR=70 pm) is comparable to the resolution of the OSA (20 pm), so they are being directly smoothed during measurement. Second, we have determined the cavity lengths associated with these spurious ripples by performing a Fast Fourier Transform of the autocorrelation of the measured spectrum (Fig. 4.7(d)), similar to what is done in [106]. It can be seen that extra peaks appear aside from the harmonics of the fundamental length (L_2, $2L_2$, $3L_2$), which are associated with the existence of spurious cavities. This plot also allows us to identify where this cavities are created on the chip layout. From the data, we can determine that the main contributions to the ripples arise from spurious cavities formed between the input facet and input MIR (L_1 in Fig. 4.6(a)), as well as between the output facet and the output MIR (L_3). A good match is actually obtained between calculated and real cavity lengths. The fact that the measured ripples in the FPs are higher than in the reference waveguides is simply because the FSRs of these spurious cavities are now comparable or higher than the OSA resolution, and so they are not being smoothed during data acquisition.

Unfortunately, these ripples introduce an indetermination in the measured extinction ratio, which in turn causes noisy fluctuations in the spectral dependence of the reflectivity. In order to reduce this unwanted effect, a moving average of 30 points, equivalent to a 120 pm wide spectral window, was applied to the recorded traces. The result of this smoothing can be seen in Fig. 4.8(a), where maxima and minima are also shown. Every two adjacent minima and maxima points can now be used to compute the extinction ratio at an intermediate wavelength, which is plotted in Fig. 4.8(b). Finally, the extinction ratio in linear units is used to compute the effective reflectivity versus wavelength, as shown in Fig. 4.8(c).

Even though smoothing significantly reduces the wavelength fluctuations of the reflectivity, it is clear that the ripples are still noticeable. In order to have a better estimate, we exploit the fact that the reflectivity varies slowly with wavelength as predicted by both FDTD simulations and the quasi-analytical model, and fit a third-order polynomial to the measured traces over a 20 nm wavelength range (1540-1560 nm). The result is plotted as a solid black line in Fig. 4.8(c). A reflectivity of about 0.4 is obtained over the whole bandwidth, which deviates from the target value of 0.5. This is mainly attributed to the combined effect of

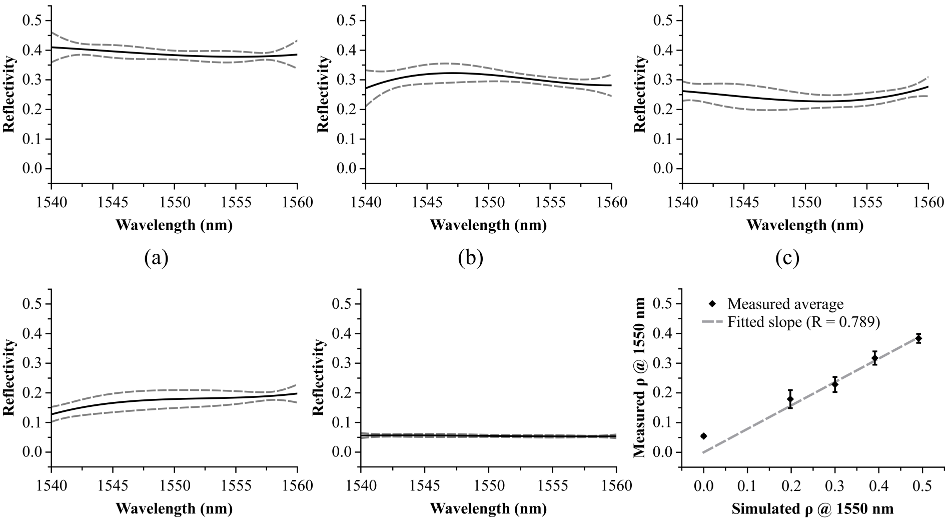

(a) (b) (c)

(d) (e) (f)

Figure 4.9: (a) to (e) Average reflectivities (solid black lines) and standard deviations (grey dashed lines) for the 5 MIRs shown in Table 4.2, computed after measuring 9 different dies. (f) Black diamonds: Measured average and standard deviations of the reflectivities versus the simulated values at 1550 nm. Grey dashed line: Slope fitted to the data that provides an estimate of the average intrinsic losses both in the mirror and in the access waveguides.

both the non-perfect reflectivity of the mirror and the excess losses of the MMI, which are estimated to be around 0.9 dB in total ($0.4/0.491 = 0.81 \simeq 0.9$ dB). Please note that trace smoothing is also responsible for a small reduction of the reflectivity value, as depicted in Fig. 4.8(d). This reduction can be severe if the size of the smoothing window is comparable to the FSR of the FP, and it gets worse for higher reflectivity values. We computed the impact of the smoothing in our simulated structures. Results are shown in Table 4.3. As it can be seen, the worst case corresponds to type "C" ($\rho/\tau = 30/68.1$), where the reflectivity is just reduced by 2.24%. As a consequence, the measured reduction of reflectivity can be mainly attributed to losses in the mirror and the MMI body, and not to the smoothing procedure.

Polynomial fittings were finally performed for all structures in the 9 measured chips, and then these were employed to obtain an statistical estimate of the expected reflectivity fluctuations due to the manufacturing process. Figures 4.9(a) to 4.9(e) show the average (solid black lines) and standard deviations (grey dashed lines) of the wavelength dependent reflectivities for each designed MIR. As it can be seen, all the devices have a maximum standard deviation with respect to the average value of about ±5%. The device with a target $\rho/\tau = 0/100$ (type "B" in Table 4.2) features an average residual reflectivity of about 5%, which we mainly attribute to spurious reflections in the chip facets not eliminated during smoothing. This also explains why this device exhibits a negligible standard deviation in the measured reflectivity, as these reflections are not expected to change significantly during manufacturing. Finally, the average reflectivities and standard deviations for all the devices at the nominal operation wavelength (1550 nm) are plotted in Fig. 4.9(f) against the simulated reflectivities of Table 4.2. By fitting a slope to the data, an estimate of the reflectivity due to the aluminium mirror and the excess losses of the MMI is obtained. As it can be seen in Fig. 4.9(f), the effective reflectivity is around 79%, similar to other previous works [99–101].

4.7 Conclusions

In this chapter, 2-port multimode interference reflectors (MIRs) based on aluminium mirrors have been proposed, designed and experimentally demonstrated in a 3 um thick SOI platform. First, we have given an overall description of how M-port MIRs can be built out of uniform NxM MMIs, provided that some symmetry constraints are ensured. Next, we have focused on 2-port MMIs, and have shown that devices with arbitrary reflection/transmission ratios can be obtained from the tapered 2x2 MMIs described in the previous chapter by introducing aluminium mirrors. Not only that, we have derived analytical expressions for the theoretical modelling of the aluminium mirror, which are in good agreement with more realistic 2D-FDTD simulations.

Several devices with reflectivities varying between 0 and 0.5 were fabricated, and characterization of 9 different dies was done in order to extract statistical data about their performance. The measured wavelength dependent reflectivities showed significant spurious ripples, which have been determined to arise from a higher than expected residual reflection on the chip facets. After appropriate smoothing and polynomial fitting, our results indicate that the average reflectivities of the 2-port MIRs are around 79% lower than the design target values. This has been mainly attributed due to both non-ideal reflection from the mirror and losses in the access waveguides. Besides, maximum standard deviations of the reflectivity of about ±5% are achieved in a 20 nm (1540-1560 nm) wavelength range for all designs.

Contrary to previous approaches, MIRs based on metal mirrors feature a greater degree of flexibility as they do not have restrictions on the shape of the field pattern formed at the reflecting surface. Thus, this type of devices might be interesting for the implementation of future fabrication-tolerant, broadband, on-chip reflectors, finding applications in reflective optical filters and integrated lasers, among others.

Publications

The work done in this chapter lead to the following publications in peer reviewed journals and international conferences:

1. **J. S. Fandiño**, J. D. Doménech, and P. Muñoz, "Two-Port Multimode Interference Reflectors with Aluminium Mirrors in a Micron-Scale SOI Platform," in *European Conference on Optical Communication (ECOC)*, pp. 1–3, Sept. 2015.

2. **J. S. Fandiño**, J. D. Doménech, and P. Muñoz, "Two-port multimode interference reflectors based on aluminium mirrors in a thick SOI platform," *Opt. Express*, vol. 23, pp. 20219–20233, Aug. 2015.

3. P. Muñoz, J. D. Doménech, **J. S. Fandiño**, R. Baños, and B. Gargallo, "Advanced Building Blocks in Thick Silicon on Insulator Technology: Echelle Grating Multiplexers and Reflective Multimode Interference Couplers," in *PIERS Proceedings*, pp. 1864–1869, July 2015.

Acknowledgements

J. D. Doménech and I. Artundo from VLC Photonics S.L. are gratefully acknowledged for providing access to the technology platform, as well as the funding required to manufacture the chips presented in this chapter.

Part III

Microwave photonic applications of integrated optical filters

Chapter 5

Instantaneous frequency measurement

5.1 Introduction

The first two sections of this thesis have been mainly focused on the theoretical and practical aspects behind the implementation of optical lattice filters. We first saw how RAMZI filters with an optimum passband design can be synthesized using well-known algorithms. Afterwards, we continued to show how the required optical couplers can be implemented by means of tapered 2x2 MMIs. Not only that, we demonstrated that 2-port MIRs with tunable reflectivies are also possible based on the same concept.

In this section, we leave behind the implementation details of such structures, and focus on their possible applications. Tunable optical filters are indeed of high interest for microwave photonics (MWP), as they provide a natural mean of linearly processing modulated optical waveforms. During the following chapters, we will elaborate on the demonstration of different MWP systems implemented with InP PICs, all of which employ filters as crucial elements for their correct operation. These PICs have been designed and fabricated within different european research projects, which involved multi-project wafer runs (MPW) offered by two generic InP platforms.

Here, we start with a relatively novel concept in MWP: instantaneous frequency measurement (IFM). Historically, detecting and characterizing electromagnetic activity in nearly real-time has been of critical importance in electronic warfare (EW) systems [107, 108]. For example, radar warning receivers (RWR) installed in military aircrafts intercept and process radar signals. Trains of detected RF pulses are usually classified according to their physical characteristics, and these are then used to identify potential threats, such as hostile surveillance radars and radar guided weapons. Due to the wide range of existent radar equipment, RWR must be able to perform pulse measurements over a broad bandwidth (typically tens of

GHz) while still offering a quasi-instantaneous response. Such stringent requirements are met by means of dedicated IFM subsystems [109, 110]. Thanks to their special architecture, which combines a sophisticated mix of high-speed digital and analog electronics, IFM receivers are used to estimate a variety of RF pulse parameters with sub-microsecond response times, including: center frequency (f_{RF}), pulse width (PW), pulse amplitude (PA) and pulse repetition frequency (PRF). Furthermore, since IFM systems directly measure the instantaneous frequency of the RF signal, on-pulse phase/frequency modulation can also be detected.

While electronic solutions are well established in the EW market, the past few years have seen a remarkable increase in the proposal and development of photonic approaches to IFM [15, 16, 111–124]. The basic operation principle consists in establishing a unique relationship between input RF frequency and the ratio of two measured powers. This mapping between frequency and power (which can be either optical or RF power), is commonly referred to in the literatue as amplitude comparison function (ACF) [122]. Among all the reported approaches, those based on detection and processing of optical powers stand out as the most promising for a near and short term practical implementation [16, 112, 113, 115, 116, 118, 119, 123, 124]. Optical power based techniques avoid the need of extra microwave components and circuits, such as detection logarithmic video amplifiers, and only require the use of high sensitivity photodiodes. In fact, some PICs for IFM have also been recently reported [115, 122], which can be considered as part of the emerging field of integrated microwave photonics [20]. By exploiting the benefits of these technologies, integrated, light-based systems hold the promise for potential low cost, compact footprint and high-bandwidth IFM equipment.

This chapter is divided in two well-defined parts. In the first one, a photonic IFM system capable of measuring the frequency of a CW RF tone is experimentally demonstrated by exploiting the complementary responses of an elliptic RAMZI filter in an InP PIC. The system features a non-ambiguous frequency measurement range of 10 GHz (5-15 GHz), together with a frequency error whose root mean square value (RMS) is lower than 200 MHz. This first part starts with a brief introduction to the operation principle of the technique, and later on discusses the chip fabrication as well as the experimental procedure and the main results. In the second part of this chapter, we set to explore the theoretical limits of an IFM system based on the same technique, but using an MZI instead. This simplifies the theoretical treatment. We start by rising some important questions that are often missed in the literature regarding the impact of realistic impairments, and we then provide an in-depth theoretical analysis of this approach. The derived analytical formulas will help us to ascertain up to which degree such IFM systems achieve their goal, and to determine the most critical parameters on the overall performance, like the bias point of the modulator and the extinction ratio of the filter. The chapter ends with a summary of the main results and conclusions.

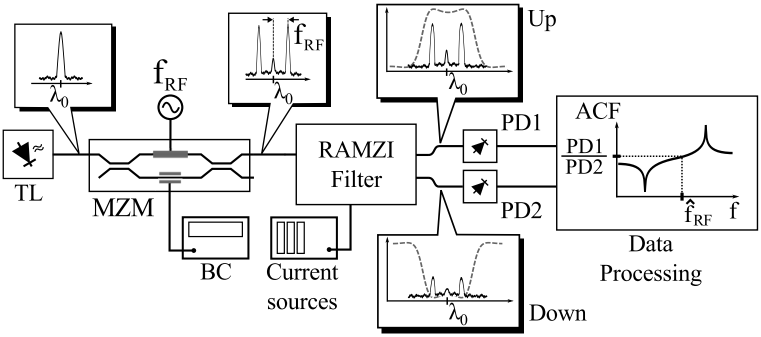

Figure 5.1: Schematic diagram of the photonics-based IFM system. TL: Tunable laser. MZM: Mach-Zehnder Modulator. RAMZI: Ring-assisted Mach-Zehnder Interferometer filter. BC: Bias Controller. PD: Photodetector. ACF: Amplitude Comparison Function.

5.2 A photonic-based IFM receiver integrated in InP

5.2.1 Operation principle

The operation principle behind our IFM system was first proposed and demonstrated by Zou et al. [116]. A system diagram of the technique can be seen in Fig. 5.1, which can be briefly described as follows. First, a CW laser source is injected into a Mach-Zehnder modulator (MZM), whose bias has been previously set at the minimum transmission point. The MZM is being fed by a continuous RF tone of unknown frequency (f_{RF}) and amplitude (A_{RF}). Under ideal circumstances, the modulator bias forces the optical carrier to perfectly interfere destructively with itself at the output of the MZM, self-cancelling out. If the input RF power is low, then mainly the first order modulation sidebands are present in the signal power spectrum, creating what is commonly known as a dual-sideband suppressed-carrier optical modulation (DSB-SC). The signal is afterwards introduced into a complementary optical filter. This is, a filter where the sum of the optical powers exiting through its two outputs is constant (see equation 2.10). We shall call the filter outputs as a function of optical frequency (f) as H(f) (*bar*) and G(f) (*cross*), and the optical power exiting through each of them as P_{bar} and P_{cross}, respectively. Now, because of the complementary nature of the filter, the first-order optical sidebands experience different levels of optical attenuation at each output. These powers are finally measured with two photodiodes (PD1 and PD2 in Fig. 5.1). Their ratio, also known as ACF, is only dependent to first order on the spectral shape of the filter and the RF modulation frequency, which is precisely the parameter of interest. The resulting ACF obtained by using this technique can be expressed in its most general form as

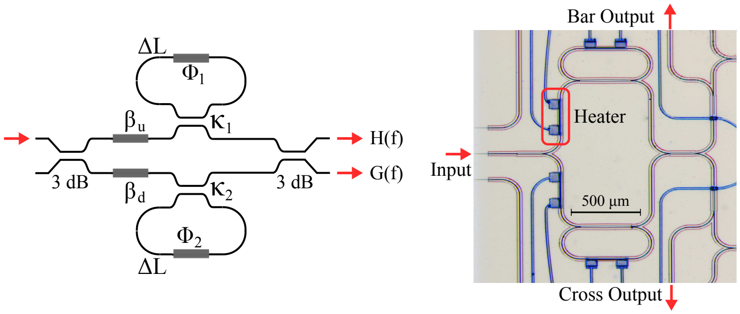

(a) (b)

Figure 5.2: (a) Schematic diagram of a 2nd-order RAMZI filter (b) Picture of the fabricated filter.

$$ACF(f_{\mathrm{RF}}) = \frac{P_{\mathrm{cross}}}{P_{\mathrm{bar}}} = \frac{|G(f_0 + f_{\mathrm{RF}})|^2 + |G(f_0 - f_{\mathrm{RF}})|^2}{|H(f_0 + f_{\mathrm{RF}})|^2 + |H(f_0 - f_{\mathrm{RF}})|^2} \tag{5.1}$$

where f_{RF} is the microwave input frequency to be estimated, f_0 is the frequency of the optical carrier, and $H(f)/G(f)$ represent the complementary transfer functions of the filter, which have already been defined.

As a result, an estimation $(\hat{f}_{RF})$ of the unknown RF frequency can be found by just measuring two DC photocurrents, calculating their ratio and then computing the inverse of the ACF function shown above, provided that $H(f)$ and $G(f)$ are known. While the previously reported approaches based on complementary filters have relied on MZI-like structures [116, 124], our RAMZI filter has a second-order elliptic response. It is composed of a Mach-Zehnder interferometer loaded with one ring on each arm, as depicted in Figs. 5.2(a). It features a passband normalized cut-off frequency of 0.33 at 0.25 dB attenuation, and a stop-band normalized frequency of 0.66 with 18 dB of minimum attenuation. Table 5.1 contains both the coefficients of the original filter and the synthesized coupling constants and phase shifts, while Fig. 5.2(b) shows a picture of the fabricated structure in an InP chip. Because of its higher roll-off (faster transition between the passband and the stopband), the elliptic filter results into a steeper ACF as compared with a single-stage MZI. This can be seen better in Figs. 5.3(a) to 5.3(d), where the

Table 5.1: Coefficients of both the numerator (p_n) and denominator (q_n) of the target filter. The synthesized values of the coupling constants (κ_n) and phase shifts (ϕ_n, β_u and β_d, in radians) are also shown.

n	p_n	q_n	κ_n	ϕ_n	β_u	β_d
0	0.3049	1.0000	-	-	3.7514	-3.7514
1	0.4201	-0.2235	0.7166	-1.3593	-	-
2	0.3049	0.2834	0.7166	1.3593	-	-

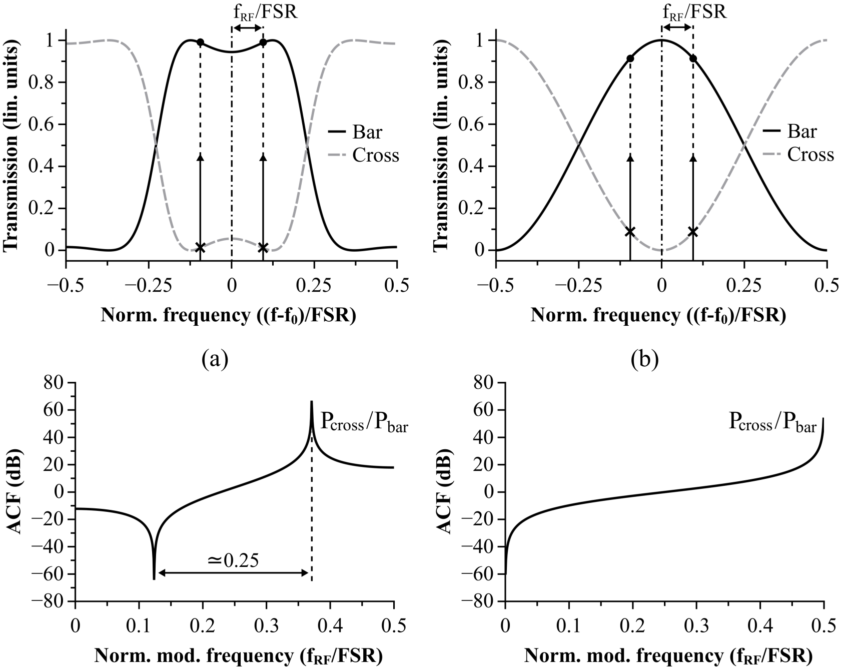

(a) (b)

(c) (d)

Figure 5.3: (a) Complementary transfer functions of the elliptic filter under consideration (see Table 5.1). The optical sidebands of a DSB-SC are shown as they move away in frequency from the carrier, serving to illustrate the operation mechanism. (b) Idem for a single MZI filter, shown for comparison. (c) Simulated ACF of the ideal elliptic filter. (d) Simulated ACF of the MZI.

complementary transfer functions of both types of filters and their corresponding ACFs are shown. As pointed out in [111], this implies that a higher frequency resolution can be achieved for the same free spectral range (FSR), since ACF slope and frequency resolution are directly related. However, this comes at the expense of a reduction in the maximum monotonic bandwidth of the ACF. In this case, it is reduced from 50% of the FSR when using a MZI (Fig. 5.3(d)) to nearly 25%. (Fig. 5.3(c)) It must be noted that monotonicity and power independence of the ACF are fundamental conditions for unambiguously determining the input frequency, since they allow to establish a unique mapping between f_{RF} and a measured power ratio. Besides, note that the transfer function of the filter must be well known in order to avoid frequency errors during the estimation process. Thus, either filter variations caused due to manufacturing tolerances are kept low in order to set an upper limit on the frequency error, or hardware-embedded calibration curves are employed to compensate for systematic errors.

5.2.2 Fabrication

The RAMZI filter shown in Fig. 5.2(b) was designed and fabricated in the InP platform of the Fraunhofer Heinrich Hertz institute (HHI), during one of the MPW runs of the European Commission FP7 EuroPIC project. The cross-section of the employed waveguides is similar to that shown in Fig. 3.12(a). They are made of a bulk quaternary InGaAsP layer without any cladding, grown on top of a Fe-doped InP substrate. HHI offers three types of etch depths, which allow the designer to choose among different levels of field confinement. For our RAMZI filter, the waveguides were 2 μm width and had an etch depth of 1.7 μm, as compared to the 0.6 μm of Fig. 3.11(a). The bends of the ring resonators and the MZI both have a radius of 150 μm, and the couplers were implemented by means of tapered 2x2 MMIs following the same procedure that was described in previous chapters. Their coupling constants have already been shown in Table 5.1. Finally, note the presence of thermo-optic heaters for fine tuning the response of the filter. This RAMZI filter was part of a more complex chip, originally intended to work as a frequency discriminator for microwave photonic links (see chapter 6).

5.2.3 Experimental procedure

The experimental procedure used to measure the filter can be described as follows. First, the filter transfer function was measured and adjusted to match as closely as possible to its ideal simulated response. This was done by coupling an ASE light source into the chip while recording the filter transmission spectrum at the output with a high resolution Optical Spectrum Analyzer (OSA), and then normalizing it with respect to a reference waveguide on the same chip. During this process, the filter response was manually adjusted by means of on-chip thermo-optic heaters, which allow for compensation of the optical phase errors that result from the non-uniformities of the fabrication process. After adjustment, the currents injected into the heaters were recorded and kept fixed, while the chip was maintained at a constant temperature ($\simeq \pm 0.1$°C) with a closed-loop temperature controller (ILX Lightwave, LDT-5412) using a 10 kΩ NTC thermistor and a Peltier cell. The total estimated electrical power employed for chip tuning was about 163.3 mW. Measured spectra after optimization are shown in Fig. 5.4(a), normalized with respect to the filter insertion losses. The simulated spectra of the filter, shown as dashed black and grey lines, are also shown in the background. Please note that these have been shifted in frequency to better overlap with the measured ones, in order to offer a better graphical comparison. The FSR is about 0.375 nm ($\simeq$ 46.7 GHz @ 1550 nm), which according to Fig. 5.3(c) implies a monotonic measurement range ($\simeq$ 25% of the FSR) of around 11.68 GHz.

Once the filter was optimized, the wavelength of a CW tunable laser (Yenista Tunics T100R, 15 mW) was set to match the center wavelength of the filter (1551.684 nm). The optical source was then injected into an external MZM (Sumitomo DEH1.5-40PD-ADC, V_π=5.5 V, 30 GHz bandwidth) driven by a CW microwave signal (+7 dBm, Agilent PNA E8364A) and manually low-biased with a

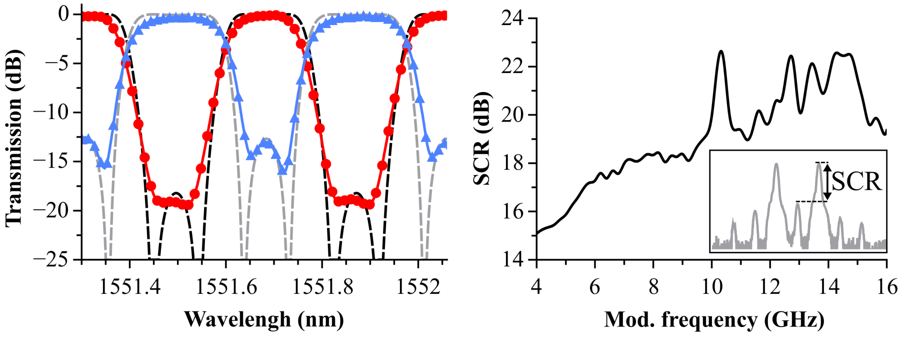

(a) (b)

Figure 5.4: (a) Measured transmission spectra (solid red and blue lines) of the RAMZI filter. Ideal responses are shown as dashed black and grey lines, for comparsion. (b) Measured Sideband-to-Carrier (SCR) ratio versus modulation frequency. The inset shows a measured modulation spectra as a solid grey line, where the SCR is defined.

voltage source. The generated DSB-SC modulation was subsequently polarization filtered (TE mode) by a free space polarizer, and lens-coupled into the chip. After passing through the on-chip filter, the optical power was collected at the output with a lensed fiber (Yenista Optics) and directed into an optical power meter. Finally, the data was stored for further post-processing. Multiple data points were collected by conveniently automating the setup with a GPIB interface, so as to estimate temporal stability and frequency error uncertainty. A total of 20 frequency sweeps (from 0.2 to 20 GHz, in steps of 0.2 GHz) were performed over a 20 min interval for each individual output port (40 min in total).

5.2.4 Results and discussion

The raw data was post-processed and 20 different ACF curves were obtained, one for each frequency sweep. Their sample mean was then calculated in order to get the best possible estimate of the system ACF. The result is plotted in Fig. 5.5(a) (solid black line). As predicted by simulations, a measurement range of about 11 GHz (5-16 GHz) is obtained. Not only that, the peaks and dips of the ideal ACF shown in Fig. 5.3(c) have been considerable reduced. In order to understand why this happens, note that the ACF shown in Fig. 5.3(c) was obtained by simulating the behaviour of the system under ideal circumstances. It was assumed that the optical carrier is completely suppressed and that the filter responses are perfectly implemented and have no losses. However, this is not the case in practice. First of all, the measured transfer functions of the filters do not present the same deep notches in the stopband (see Fig. 5.4(a)). Second, there always remains a certain amount of optical carrier power after the low-biased MZM, which depends on the

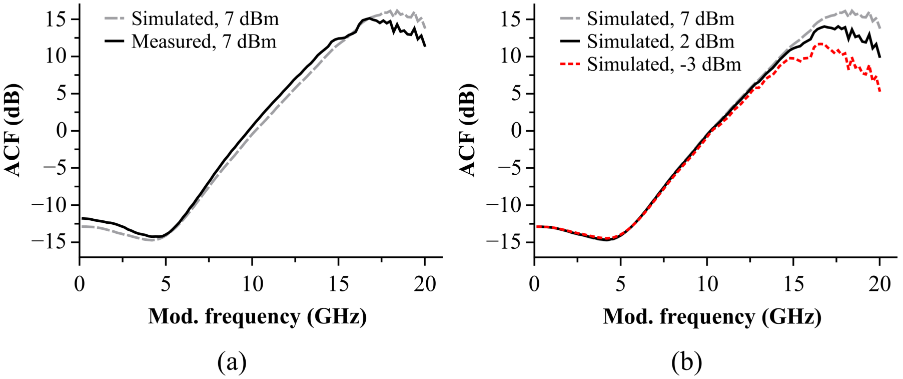

Figure 5.5: a) Measured mean ACF (solid black line) and simulated ACF for the same power (dashed grey line). The simulation includes the data of Figs. 5.4(a) and 5.4(b), as explained in the text. (b) Simulated ACFs for different RF powers, showing how the ACF changes with input power.

extinction ratio of the device. In fact, the presence of this residual power directly affects the shape of the ACF. The higher the optical carrier power relative to the power of the sidebands (measured as the Sideband-to-Carrier ratio, or SCR), the lower the slope of the ACF, since the power ratio tends to be more constant.

In order to account for this non-ideal behaviour, the SCR was measured during the experiments by directly connecting the output of the modulator to the OSA. The results are shown in Fig. 5.4(b), along with an inset showing a measured DSB-SC spectra during the experiment. Now, by combining both the finite SCR and the real responses of the filters, a more realistic simulation can be run. Simulations for different input RF powers, a parameter which was not varied during the experiment, can also be obtained. The results are plotted in Fig. 5.5(a) and 5.5(b), which clearly show a better agreement with the measured data and illustrate how the slope of the ACF gets reduced the RF power is decreased.

Note that, due to the RF power dependence of the ACF, a unique calibration curve from where input frequencies can be inferred given a measured power ratio does not exist. If one of them is chosen as such, microwave signals with equal frequency but RF powers that differ from that used for calibration will result into a biased frequency estimate. This will be explained in more detail in the next section of this chapter, where possible solutions to solve this problem are also discussed. Besides, note that any spurious power fluctuations, such as those caused by mechanical or thermal drifts, will lead to a spread in the measurement, typically characterized by a standard deviation. Both effects thus need to be taken into account when estimating the frequency error of the system. As the RMS value of the frequency error takes into account both effects (bias and standard deviation), it serves as a good figure of merit that gives an idea of the error statistics during the measurement process. The RMS of the frequency error can be computed as

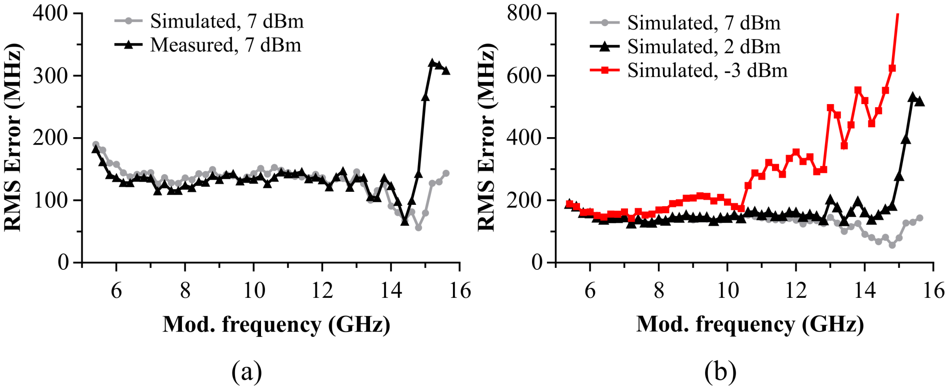

Figure 5.6: (a) Measured RMS value of the frequency error as a function of modulation frequency (solid black line). The simulated value for the same RF power is also shown as a dashed grey line, for comparison. (b) Simulated RMS values of the frequency error for different RF powers.

follows. First, a fitting of the measured mean ACF (+7 dBm, solid black line in Fig. 5.5(a)) is chosen as the calibration curve for frequency estimation. As detailed previously, for every input modulation frequency used to test the system, 20 different power ratios were measured. Thus, 20 different frequencies can be estimated by looking up these ratios in the fitted curve. The difference between the resulting frequency value and the one supplied by the Microwave Network Analyzer gives us the frequency error. Now, the RMS error can be computed and plotted against input frequency (Fig. 5.6(a)).

In order to extend this procedure for different RF powers, where no data is available, we must further assume that the fluctuations in optical power are similar as those measured during the experiment. By combining these with the simulated ACFs of Fig. 5.5(b), an estimation of the RMS value for different input RF powers is obtained. In this case, the calibration curve chosen as a reference is the simulated ACF for an input RF power of +7 dBm. Final results are shown in Figs. 5.6(a) and 5.6(b). The measured RMS error remains lower than 200 MHz for a bandwidth of about 10 GHz (5-15 GHz). This is mainly attributed to the effect of the different noise processes affecting the measured optical power. Also note that the frequency error rises around 5 and 16 GHz due to a reduction in the ACF slope. As regards the simulation data, variations of input RF power lead to a significant increase in error. At lower frequencies the simulated ACFs are similar to the reference curve. Thus, the bias error is low and the RMS error is mainly given by power noise. At higher frequencies, the ACFs tend to diverge so the bias contribution to the RMS error increases. In fact, an estimated RMS error above 600 MHz is obtained over the same bandwidth for a RF power of -3 dBm, which is just 10 dB lower as that used in the experiment.

The measured frequency error in our experiment is similar to previously reported approaches based on integrated optics [115,122], with 93.6 MHz and 200 MHz, respectively. As an advantage, it only requires the use of low-speed photodiodes and simple electronics, as compared with [122] where RF power detection is employed. Moreover, operation is simpler and faster than that presented in [115], since there is no need to sweep the chip temperature. However, improvements in carrier suppression and reduction of random power fluctuations must be achieved in order to ensure a lower frequency error. Thanks to recent advances in photonic integration, these impairments might well be solved in the near future, both by fitting all active and passive components inon a single InP chip (reducing external noise sources) and applying advanced techniques for carrier suppression in integrated MZMs. In fact, suppression ratios as high as 39 dB have been recently reported [125].

5.3 Exploring the practical limits of photonic IFM receivers

5.3.1 Introduction

If one carefully reviews the recent literature about photonics-based IFM receivers, it will quickly become apparent that so far most reported results have focused on proof-of-principle experimental demonstrations. That is, not much effort has been put into understanding the theoretical limits of practical systems, which are usually impaired by a set of unavoidable effects. For example, in the previous section we pointed out to the fact that the presence of a residual optical carrier in the modulator output can induce a significant bias error in the estimated frequency of the received signal, and that this error is in fact dependent on input RF power. Since a residual optical carrier arises from amplitude imbalance and phase errors in the modulator, it is obvious then that their impact on system performance should be carefully considered.

Not only that, most published papers assume a continuous wave (CW) RF input, and then proceed to perform a frequency domain analysis under highly ideal conditions. This is useful in order to illustrate the main working principle behind each technique, while it also provides a theoretical basis for the experimental data. However, this simplified approach has two important shortcomings. First, a frequency domain analysis is only able to compute the response of an IFM system under CW operation, and is not able to capture the temporal behaviour of the system. This is in fact of great importance in practical IFM receivers where very short (and possibly chirped) RF pulses need to be measured. Second, idealistic theoretical analyses often neglect key effects that can impose severe performance constraints. A notable exception is a recent work by Harmon et al. [126], where a model for analog photonic links that can be applied to some IFM approaches is presented. This model accounts for some realistic effects like phase errors in the MZM and an MZI used as a filter, as well as bias amplitude imbalance in the same MZI. However, other important parameters (such as MZM amplitude imbalance and photodiodes dark currents) are not included, and only CW operation is considered.

In this section, we set to explore the theoretical limits of the same IFM technique that has been described in the first part of this chapter. We provide, to the best of our knowledge, the first time-domain-based theoretical analysis of this approach. As a key difference, the second-order elliptic filter has been replaced with a simpler MZI filter. We have focused on this particular filter architecture because an MZI only requires a single bias electrode, which eliminates the need of complex control electronics for the continuous adjustment of the filter transfer function. This makes this architecture particularly suited for a simpler implementation as a PIC with current state-of-the-art technology. Furthermore, the simplicity of this filter naturally lends itself to be described by closed-form formulas, helping to better ascertain its intrinsic limitations, as well as to perform calibration corrections after measurements. Our analysis allows to compute the impact of amplitude imbalance and phase errors in both the MZM and the MZI, as well as the effect of temporal phase/frequency modulation in an incoming RF pulse, among other impairments (such as insertion losses and non-zero dark currents). Thus, it can serve as a powerful analysis and design tool for the development of IFM systems based on this particular technique, as well as for better understanding experimental data. Moreover, the results of our analysis show that great attention must be paid to the dependence of system performance with input RF power. Particularly, frequency error can be significantly degraded when considering realistic parameter values on the photonic system. This is an important consideration that must be addressed with care when comparing photonics-based IFM systems with their electronic counterparts, which typically boast outstanding dynamic range specifications.

This part is organized as follows. First, and starting from a series of reasonable assumptions, a time domain analysis is fully developed. Second, some temporal trade-offs that follow from these equations are discussed. Third, numerical simulations are performed to evaluate the relative impact of each considered parameter on system performance. Fourth, realistic values extracted from state-of-the-art components are employed to illustrate the significant effect of input RF power on the frequency bias error. Finally, possible techniques for mitigating this effect are proposed along with a summary of the main results and conclusions.

5.3.2 IFM Theory

Time domain analysis

The schematic diagram of the IFM technique under analysis is shown in Fig. 5.7. Note that it is very similar to that of Fig. 5.1. However, the RAMZI filter has now been replaced with a simpler MZI, and the MZM is now a push-pull MZM, as we will explain shortly. We now start by assuming that at the input of our system there is an arbitrary, real, passband microwave signal of the form

$$V_{RF}(t) = A_{RF}p(t)\cos\left(2\pi f_{RF}t + \phi_{RF}(t)\right) \tag{5.2}$$

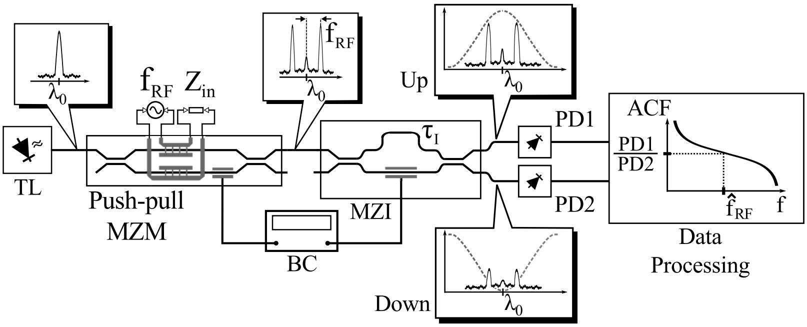

Figure 5.7: Schematic diagram of the photonic IFM system under analysis. TL: Tunable laser. MZM: Mach-Zehnder Modulator. MZI: Mach-Zehnder Interferometer. BC: Bias Controller. PD: Photodetector. ACF: Amplitude Comparison Function.

where A_{RF} is the amplitude, $p(t)$ is a normalized pulse shape (that is, $p(t) \leq 1$), f_{RF} is the central frequency of the RF signal and $\phi_{RF}(t)$ accounts for a possible on-pulse phase/frequency modulation (such as those of chirped radars).

This unknown waveform, of which we wish to estimate its instantaneous frequency (defined as $f(t) = f_{RF} + (1/2\pi)\partial\phi_{RF}(t)/\partial t$), is then employed to modulate a CW laser. From now on, optical signals will be described by low-pass, analytic (i.e. complex-valued) functions of time. These will be written with an upper tilde, in order to distinguish them from the real-valued signals associated with input RF pulses and detected photocurrents. As an example, a CW laser can be simply described as $\tilde{E}_o(t) = \sqrt{P_o}e^{j\phi_o(t)}$, where P_o is the output power and $\phi_o(t)$ models the laser phase noise. For the sake of simplicity, phase noise will not be considered ($\phi_o(t) = 0$).

It has been stated in the previous section that the purpose of the MZM is to encode the microwave signal information into a DSB-SC modulation, from which its instantaneous frequency can be estimated after appropriate optical and electrical processing. As it will be shown later, the ability of the MZM to reduce the power of the optical carrier is crucial for obtaining an RF power independent estimation of the instantaneous frequency. Due to its critical role, appropriate modelling of possible non-ideal effects is mandatory. In fact, not only non-ideal parameters can affect the quality of the DSB-SC modulation, but also the topology of the MZM itself. As shown in the system diagram of Fig. 5.8(a), it is important for the modulation process to take place inside a push-pull MZM. The main reason is that by differentially driving both arms of the push-pull MZM, one can ideally achieve perfect carrier suppression. On the contrary, if only one arm is modulated, then the powers of the optical carriers travelling on each branch are no longer different as, due to energy conservation, a certain fraction of the carrier power in the modulating arm is diverted to create the sidebands. Since they have no equal amplitudes, the two optical carriers can no longer perfectly interfere destructively,

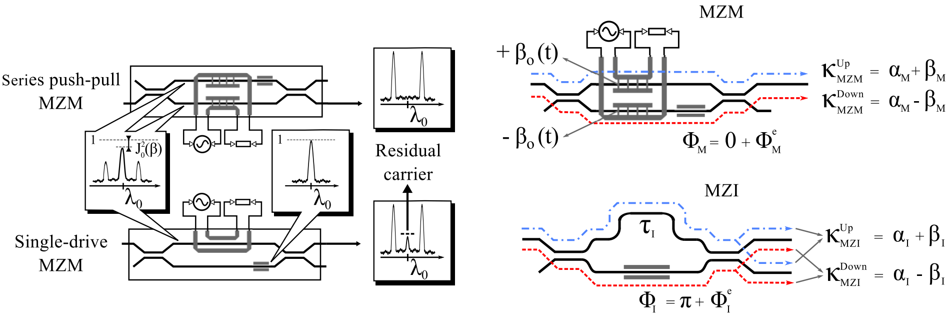

(a) (b)

Figure 5.8: (a) Difference between single-drive and series push-pull operation in a MZM. Note that in the former case the carrier amplitude in each arm is different, while in the latter it remains balanced since the modulation process affects both arms equally. (b) MZI and MZM parameters considered in the theoretical analysis.

even if they are exactly out of phase and no power imbalance exists in the modulator branches. Thus, differentially driving the MZM is of fundamental importance for achieving perfect carrier suppression. For that purpose, either a series push-pull architecture or a dual-drive MZM with an external 180° RF hybrid can be employed. The latter implies that external RF imperfections in the hybrid, such as power imbalance and phase errors, must be additionally accounted for, whereas the former avoids the use of external, expensive RF circuits, reducing costs and simplifying the set-up. This implies that series push-pull MZMs are the optimal choice for this particular application. Fortunately, this is one of the most typical topologies found in both LiNbO3 (x-cut) and InP modulators, so off-the-shelf high-performance components are readily available [127–129].

We will subsequently assume that a series push-pull MZM is being employed, which can be characterized by the following parameters (see Fig. 5.8(b)):

- ϕ_M: Modulator bias phase.

- $\beta_o(t)$: Arbitrary time-varying phase modulation index due to the RF signal. This is, $(1/2)(\pi/V_\pi^{AC})V_{RF}(t)$. Here, V_π^{AC} stands for the dynamic voltage required *in one arm of the MZM* to induce a π phase shift on the travelling optical wave, and the 1/2 factor is due to the push-pull operation. Also notice that V_π^{AC} normally depends on the frequency of the modulating signal. It thus accounts for all those physical processes that can affect modulation efficiency, such as RF losses, as well as impedance and velocity mismatch.

- κ_{MZM}^{Up} and κ_{MZM}^{Down}: Electric field attenuation factors as seen by the laser field when it propagates trough the upper/lower arms of the interferometer, respectively. These only account for losses and imbalance, and thus exclude the phase shifts in the optical couplers.

In practice κ_{MZM}^{Up} and κ_{MZM}^{Down} can not be directly measured. Typically, only the optical transmission curve versus DC voltage is available. This curve is indeed defined by the maximum and minimum optical power transmission points (T_{max} and T_{min}), as well as by the DC bias voltage periodicity. We can however relate the two electric field attenuation factors to the measured MZM transmission curve by noting that $T_{max} = (\kappa_{MZM}^{Up} + \kappa_{MZM}^{Down})^2$ and $T_{min} = (\kappa_{MZM}^{Up} - \kappa_{MZM}^{Down})^2$. In order to simplify the notation, we will rewrite these factors as

$$\kappa_{MZM}^{Up} = \alpha_M + \beta_M \tag{5.3}$$

$$\kappa_{MZM}^{Down} = \alpha_M - \beta_M \tag{5.4}$$

where α_M and β_M are defined as

$$\alpha_M = \frac{\kappa_{MZM}^{Up} + \kappa_{MZM}^{Down}}{2} \tag{5.5}$$

$$\beta_M = \frac{\kappa_{MZM}^{Up} - \kappa_{MZM}^{Down}}{2} \tag{5.6}$$

Now, it is easy to see that

$$T_{max} = 4\alpha_M^2 \qquad T_{min} = 4\beta_M^2 \tag{5.7}$$

which are directly related to the optical extinction ratio (ER) and insertion losses (IL) of the device, in linear units:

$$\mathrm{ER}_M = \tfrac{T_{max}}{T_{min}} = \tfrac{\alpha_M^2}{\beta_M^2} \tag{5.8}$$

$$\mathrm{IL}_M = T_{max} = 4\alpha_M^2 \tag{5.9}$$

Thus, by just measuring both the ER and IL of the MZM, α_M and β_M can be computed through equations 5.8 and 5.9. Ideally, ER $= \infty$ and IL $= 1$, so $\alpha_M = 1/2$ and $\beta_M = 0$. Also note that there are two possible values of β_M, either positive or negative, that result in the same ER. This is due to the fact that it is in general not possible to know which arm is causing more attenuation than the other.

While the electric field attenuation factors are essentially constant with time, the modulator bias phase will slowly drift as a result of changes in the operating conditions of the system, including temperature changes, ageing and static electrical charge accumulation. As a consequence, the bias phase of the modulator needs to be carefully monitored and adjusted. Here, we assume that an automatic bias control circuit is keeping the upper output at the minimum transmission point except for a possible phase error ($\phi_M = 0 + \phi_M^e$), as shown in Fig. 5.8(b). This phase error arises from possible limitations in the technique employed by the bias controller, which typically are in the order of ±1° [130]. In that case, the electric field at the output of the MZM can be finally expressed as

$$\begin{aligned}\tilde{E}_{MZM}(t) \quad = \quad & \tilde{E}_o(t)\Big[(\alpha_M + \beta_M)e^{j\beta_o(t)} \\ & -(\alpha_M - \beta_M)e^{j\phi_M^e}e^{-j\beta_o(t)}\Big]\end{aligned} \tag{5.10}$$

The non-ideal DSB-SC modulation is then introduced into an MZI. Making similar assumptions as in the previous case, we have that the MZI can be described by the following parameters:

- τ_I: Time delay difference between the upper and lower arms of the interferometer, which is related to the FSR of the filter by FSR $= \tau_I^{-1}$. It is assumed that the dispersion of the interferometer delay line is first-order only, since second-order effects (pulse broadening and distortion) are negligible given the low propagation distances of practical integrated devices.

- κ_{MZI}^{Up} and κ_{MZI}^{Down}: Real-valued constants that model the electric field attenuation as seen by the laser when it propagates through the branches of the MZI. As explained before, the related parameters α_I and β_I can be computed by first measuring ER_I and IL_I, and then using equations 5.8 and 5.9. Please note that, if the output coupler is not perfectly balanced, the MZI would need to be modelled using 4 different electric field attenuation constants. These would correspond to the 4 different optical paths that the light follows within the device before it recombines at the output ports. In that case, both outputs of the MZI would need to be individually characterized, yielding different insertion losses and extinction ratios for each port. In most practical devices, however, the imbalance of the MZI is mainly due to the extra loss caused by the longer propagation distance in the upper arm, which can be significant if the FSR is small, and not due to the imbalance of the output coupler. In fact, integrated MZIs typically use MMIs as output couplers, which are well-known for their inherent robustness to manufacturing deviations. If properly designed, these devices show outstanding performance (see for example [89]), and thus their contribution to the overall imbalance can be considered of second order. For simplicity, we will assume that this asymmetry in the output coupler is negligible, so both outputs can be characterized using just two parameters. Nevertheless, these extra variables could be incorporated into the model if they were required.

- ϕ_I: Interferometer bias phase. It is also assumed to be continuously adjusted so that the wavelength of maximum (minimum) transmission when coming out by the upper (lower) output matches the emission wavelength of the laser. That is, $\phi_I = \pi + \phi_I^e$, where ϕ_I^e is a possible phase error due to an imperfect control of the bias point.

As a result, the electric field at the upper/lower output of the MZI can be written down as

$$\begin{aligned}\tilde{E}_{MZI}^{Up}(t) &= \big[(\alpha_I+\beta_I)\tilde{E}_{MZM}(t-\tau_I) \\ &\quad +(\alpha_I-\beta_I)\tilde{E}_{MZM}(t)e^{j\phi_I^e}\big] \qquad (5.11)\\ \tilde{E}_{MZI}^{Down}(t) &= (-j)\big[(\alpha_I+\beta_I)\tilde{E}_{MZM}(t-\tau_I) \\ &\quad -(\alpha_I-\beta_I)\tilde{E}_{MZM}(t)e^{j\phi_I^e}\big] \qquad (5.12)\end{aligned}$$

Finally, both optical signals are detected in a couple of low-speed, high sensitivity photodiodes (PD1 and PD2). The photodetection process will be described as a current source whose output linearly depends with the input, instantaneous, time-averaged optical power ($\overline{P_o}(t) = \frac{1}{T}\int_{t-T/2}^{t+T/2}|\tilde{E}(t)|^2dt$) impinging upon the pin junction. This averaging time is assumed to be much higher than the period of the optical signal, but lower than the temporal variations of the RF pulse amplitude ($p(t)$), so that

$$i(t) \simeq \mathcal{R}\int_{-\infty}^{t}|\tilde{E}(s)|^2h(t-s)ds + I_{\text{Dark}} \tag{5.13}$$

where $\mathcal{R}$ stands for the photodiode's responsivity, I_{Dark} is the photodiode's dark current, and $h(t)$ is the current impulse response of the whole output circuit. Since we are interested in low-speed operation (small bandwidth photodiodes), $h(t)$ can be modelled to first-order as a simple RC circuit: $H(\omega) = (1+j\omega RC)^{-1}$. Its 3 dB RF bandwidth is given by $f_{3dB} = (2\pi RC)^{-1}$, where R is the total output resistance (series + load) and C is mainly dominated by the junction capacitance.

Substituting equation 5.10 into both 5.11 and 5.12 yields the electric fields at the input of the photodiodes. Their time-averaged optical power is easily computed as $\overline{P_o}(t) = |\tilde{E}(t)|^2 = \tilde{E}(t)\tilde{E}^*(t)$, from which output photocurrents can be finally obtained through equation 5.13. Alternatively, this last step can also be done by eliminating those RF beating terms which are not below the cut-off frequency of the photodiode.

Temporal trade-offs

Now, and prior to developing on the exact formulas of the detected photocurrents, it is instructive to have a look at their general form. Due to the multiplication (or beating) among all possible combinations of the delayed and non-delayed modulated electric fields, these electrical signals are made of a linear combination of quasi-DC (low speed) and RF (high-speed) terms. However, it is important to note that, out of all beating terms, only those formed by a multiplication between a delayed and non-delayed signal contain information about the instantaneous frequency that is to be measured. To see this, we can write down the general formula for one of these beating terms as

$$\begin{aligned} i'(t) &\propto \Re\{e^{j\beta_o(t)}e^{-j\beta_o(t-\tau_I)}\} = \\ &= \Re\{e^{jz(t)\cos(\theta(t))}e^{-jz(t-\tau_I)\cos(\theta(t-\tau_I))}\} \end{aligned} \tag{5.14}$$

where by simple identification $z(t) = (1/2)(\pi/V_\pi^{AC})p(t)A_{RF}$, $\theta(t) = 2\pi f_{RF}t + \phi_{RF}(t)$ and $\Re\{\}$ stands for the real part of a complex number.

After employing the well-known Jacobi-Anger expansion

$$e^{jz(t)\cos(\theta(t))} = \sum_{n=-\infty}^{+\infty} j^n J_n\big(z(t)\big)e^{jn\theta(t)} \tag{5.15}$$

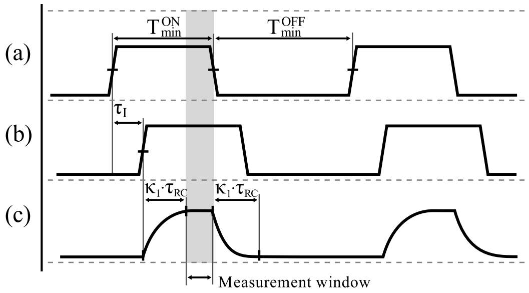
(a)
(b)
(c)
T$_{\text{min}}^{\text{ON}}$
T$_{\text{min}}^{\text{OFF}}$
τ$_\text{I}$
κ$_\text{I}$·τ$_\text{RC}$
κ$_\text{I}$·τ$_\text{RC}$
Measurement window

Figure 5.9: Temporal evolution of signals inside the IFM system. (a) Input RF pulse. (b) Delayed RF pulse after propagation through the long MZI arm. (c) Resulting low-speed photocurrent term containing the information of the instantaneous frequency.

and assuming that the photodiode RC circuit perfectly filters all high-order RF terms, this equation can be reformulated as

$$\begin{aligned} i'(t) &\propto J_o(z(t))J_o(z(t-\tau_I)) + \\ &+ 2\sum_{n=+1}^{+\infty} J_n(z(t))J_n(z(t-\tau_I))\cos\left(n(\theta(t)-\theta(t-\tau_I))\right) \end{aligned} \tag{5.16}$$

Equation 5.16 has some important consequences. First, it tells us that the amplitude of the detected quasi-DC photocurrent is dependent on the first-order difference between time-delayed copies of the RF instantaneous phase ($\theta(t) = 2\pi f_{RF}t+\phi_{RF}(t)$). Given that both τ_I and $z(t)$ are sufficiently small, this difference provides a good estimate ($\hat{f}(t)$) to the instantaneous frequency of the RF signal ($f(t)$) that we want to measure. This is,

$$\begin{aligned} \hat{f}(t) &= \frac{1}{2\pi}\frac{\theta(t)-\theta(t-\tau_I)}{\tau_I} = \\ &= f_{RF} + \frac{1}{2\pi}\frac{\phi_{RF}(t)-\phi_{RF}(t-\tau_I)}{\tau_I} \simeq \\ &\simeq f_{RF} + \frac{1}{2\pi}\frac{\partial\phi_{RF}(t)}{\partial t} = f(t) \end{aligned} \tag{5.17}$$

Thus, the *instantaneous frequency* of the RF signal, and not only central frequency, can indeed be extracted by measuring the amplitude of the quasi-DC photocurrent. Ultimately, this means that chirped RF signals can be measured and characterized, provided that the variation time of the chirped signal is slow enough to be detected by the low-pass response of the photodiodes.

Second, $z(t)$, which is related to the amplitude of the RF waveform, needs to be kept low. Otherwise, contributions due to higher-order terms in the Bessel expansion will start to dominate, inducing an error in the estimated instantaneous frequency. This can be more easily seen by employing the frequency domain formalism mentioned before. When the input RF power is high enough, higher-order harmonics in the signal spectrum dominate over both the carrier and the first-order ones.

Third, the instantaneous frequency can not be obtained unless the temporal duration of the input RF pulse is at least longer than the interferometer time delay ($T_{min} \geq \tau_I$), as shown in Fig. 5.9. Otherwise, the product $J_1(z(t))J_1(z(t-\tau_I))$ will be zero and the instantaneous frequency of the signal will have no impact on the detected photocurrent. Last but not least, the finite response time of the photodiode implies that the steady-state value of the beating term is not reached until a certain time after the RF pulse enters the MZM. Settling times of RC circuits are typically specified as multiples (κ_1) of the RC time constant ($\tau_{RC} = RC$), where the exact value of κ_1 depends on the level of convergence to the final steady-state value specified in %. As a consequence, a reliable estimation of $f(t)$ implies that the minimum duration of an RF pulse must satisfy

$$T_{min}^{ON} \geq \tau_I + \kappa_1 \tau_{RC} \tag{5.18}$$

where κ_1 is an arbitrary real constant. Typically, $\kappa_1 \geq 5$ for a convergence value better than 99%.

Usually, τ_I is much lower than $\kappa_1\tau_{RC}$, so that $T_{min}^{ON} \simeq \kappa_1\tau_{RC}$. Also, since we are only interested in the quasi-DC beating terms, the photodiode 3 dB bandwidth must be much lower than the minimum instantaneous frequency (f_{min}) in order to filter out all unwanted RF contributions. This is, $f_{3dB} = (2\pi\tau_{RC})^{-1} = \kappa_2 f_{min}$, being κ_2 an arbitrary constant much lower than 1. Substituting these relations and defining $\kappa = \kappa_1/(2\pi\kappa_2)$, we finally have that

$$T_{min}^{ON} \geq \frac{\kappa}{f_{min}} \tag{5.19}$$

Thus, it can be seen that there exists an intrinsic trade-off between the minimum temporal width of an input pulse and the minimum measurable instantaneous frequency. As a consequence, quasi-DC instantaneous frequencies ($f_{min} \to 0$) can not be measured except for very long input RF pulses ($T_{min} \to +\infty$).

Using similar arguments, it is also easy to see that $T_{min}^{OFF} \geq \kappa_1\tau_{RC} = T_{min}^{ON}$. As a result, an approximate upper limit on the maximum measurable pulse repetition frequency (PRF) of the input pulses is obtained

$$\mathrm{PRF}_{max} \leq \frac{1}{2T_{min}^{ON}} = \frac{f_{min}}{2\kappa} \tag{5.20}$$

Non-ideal Amplitude Comparison Function

So far, just the general form of the detected low-speed photocurrents has been analyzed in order to get a deeper understanding of its intrinsic temporal trade-offs. Now, we turn to their exact expressions, which will allow us to compute the

$$I_{DC} = 4(1+\frac{1}{\mathrm{ER}_I})(1+\frac{1}{\mathrm{ER}_M}) \tag{5.23}$$

$$i_{\varsigma}(\beta) = 4(1+\frac{1}{\mathrm{ER}_I})(1-\frac{1}{\mathrm{ER}_M})\cos(\phi_M^e)J_o(2\beta) \tag{5.24}$$

$$\sigma = 4(1-\frac{1}{\mathrm{ER}_I})\cos(\phi_I^e) \tag{5.25}$$

$$i_{\Delta}(\beta) = \left[(1-\cos(\phi_M^e))+\frac{1}{\mathrm{ER}_M}(1+\cos(\phi_M^e))\right]J_o^2(\beta) \tag{5.26}$$

$$\begin{aligned} i_{\Sigma}(\beta, f_{RF}, \phi_{RF}(t)) &= 2\sum_{n=+1}^{+\infty}\left[(1-(-1)^n\cos(\phi_M^e))+\frac{1}{\mathrm{ER}_M}(1+(-1)^n\cos(\phi_M^e))\right] \\ &\quad J_n^2(\beta)\cos(n[2\pi f_{RF}\tau_I+\phi_{RF}(t)-\phi_{RF}(t-\tau_I)]) \end{aligned} \tag{5.27}$$

---

effect of each parameter on system performance. To do this, we will assume for simplicity that the amplitude of an input RF pulse has reached a steady state after a certain time (as seen in Fig. 5.9), so that $z(t) = \beta = (1/2)(\pi/V_{\pi}^{AC})A_{RF}$. Appropriate substitutions and a considerable amount of algebra yield the following equations:

$$i^{\mathrm{Up}} = \eta\Big(I_{DC} - i_{\varsigma}(\beta) + \sigma[i_{\Delta}(\beta) + i_{\Sigma}(\beta, f_{RF}, \phi_{RF}(t))]\Big) + I_{\mathrm{Dark}} \tag{5.21}$$

$$i^{\mathrm{Down}} = \eta\Big(I_{DC} - i_{\varsigma}(\beta) - \sigma[i_{\Delta}(\beta) + i_{\Sigma}(\beta, f_{RF}, \phi_{RF}(t))]\Big) + I_{\mathrm{Dark}} \tag{5.22}$$

where i^{Up} and i^{Down} are the detected quasi-DC photocurrents in the upper/lower photodiodes (PD1 and PD2, respectively), $\eta = (\mathrm{IL}_M\mathrm{IL}_I\mathcal{R}P_o/16)$, I_{Dark} is the photodiode's dark current, and the definition of all the other terms can be found in equations 5.23 to 5.27. Note that both extinction ratios (ER_M, ER_I) and insertion losses (IL_M, IL_I) are given in linear units.

The exact form of the ACF when the currents are sampled by a couple of ideal analog-to-digital converters can now be immediately computed as

$$\mathrm{ACF}(\beta, f_{RF}, \phi_{RF}(t)) = \frac{i^{\mathrm{Up}}}{i^{\mathrm{Down}}} \tag{5.28}$$

Although complex at first sight, the final ACF is made of mainly three types of terms. The first one (I_{DC}) does not depend on the characteristics of the RF signal, but only on the parameters of the optical system. The second and third ones ($i_\varsigma(\beta)$ and $i_\Delta(\beta)$) are dependent on RF power through the parameter β (phase modulation index). The last one, $i_\Sigma(\beta, f_{RF}, \phi_{RF}(t))$, depends on RF power, central frequency and RF instantaneous phase, and contains the contributions from first and high-order harmonics in the signal spectrum. Under a first-order approximation most of these residual terms can be usually neglected, leading to an ACF which is essentially independent of RF power. However, as we shall see in the next section, the impact of a combination of realistic parameter values induces significant deviations in its shape. Furthermore, they introduce a non-negligible RF power dependence of the ACF curve that should be carefully taken into account in the design stage of any photonics-assisted IFM system based on this particular technique.

5.3.3 Simulation results and discussion

Thanks to the developed theoretical analysis, it is now easy to quantitatively assess the influence of each parameter on system performance. As it has been stated, the core of this particular IFM technique relies on establishing a direct one-to-one relationship between the ratio of two detected optical powers and the instantaneous frequency of an arbitrary RF signal. In order for the system to yield accurate results, this mapping must be unique and independent of any other characteristic of the RF signal, such as power, which means that the ACF should not vary for RF pulses of different amplitudes. Furthermore, the exact shape of the ACF must be precisely known. Otherwise, systematic bias errors are introduced in the instantaneous frequency recovery process. Under perfect system operation, the measured ACF should fit a curve of the form

$$\mathrm{ACF}(f(t)) = \frac{1+\cos\left(2\pi f(t)/\mathrm{FSR}\right)}{1-\cos\left(2\pi f(t)/\mathrm{FSR}\right)} \tag{5.29}$$

Without loss of generality, the ACF has been defined here as P_{bar} divided by P_{cross}. In practice, realistic parameter values in the optical system, such as finite extinction ratios in both the MZI and MZM, significantly deviate the measured ACF from its ideal response. Thus, insight into the relative impact of each individual parameter can be gained by just looking at how much the non-ideal ACF deviates from its perfect response when these parameters fluctuate around their ideal values. Higher ACF deviations for similar parameter fluctuations will mean higher system sensitivity, helping us to determine the most critical ones. From now on, we will assume for simplicity that the input signal is not chirped, so that $f(t) = f = f_{RF}$.

Impact of individual parameters in system performance

As a first example, consider the effect of a non-zero phase error due to imperfect operation of the bias controllers in both the MZI and the MZM. In the MZI case

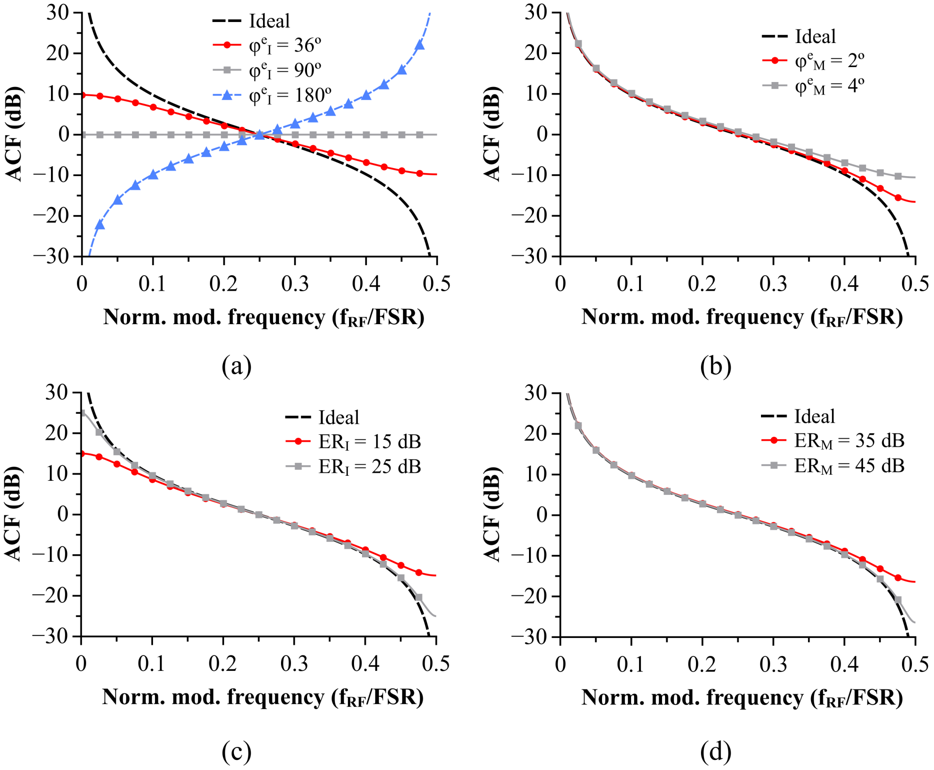

(a) (b)

(c) (d)

Figure 5.10: Simulated ACFs for different system imperfections. (a) Bias phase error in the MZI (ϕ_I^e). (b) Bias phase error in the MZM (ϕ_M^e). (c) Finite extinction ratio in the MZI (ER$_I$). (d) Finite extinction ratio in the MZM (ER$_M$). Simulation values for all four figures are: Z$_{in}$ = 50 Ω, P$_{RF}$ = 0 dBm, V_π^{AC} = 3 V, P$_o$ = 20 mW and $\mathcal{R}$ = 0.9 A/W. All other parameters, except that under analysis, are assumed ideal.

(Fig. 5.10(a)), this phase error induces a wavelength offset between the MZI spectral transfer function and the optical carrier. As a result, the ACF shape changes, since the optical attenuations seen by the first-order sidebands as the RF frequency is being swept are now different. For example, a value of $\phi_I^e = 90°$ would yield a completely flat ACF. This is due to the fact that the optical carrier would be now situated at the quadrature bias point of the MZI, where the attenuation induced by the upper/lower MZI outputs at different RF frequencies is exactly the same, independently of modulation frequency. A value of $\phi_I^e = 180°$ would be equivalent to computing the inverse ratio ($i^{\text{Down}}/i^{\text{Up}}$), which is an horizontally mirrored image of the original ACF. In the MZM case (Fig. 5.10(b)), the existence of a bias phase error leads to a non-infinite suppression of the optical carrier, even if ER$_M$ = $+\infty$. This is due to the fact that the upper/lower branch of the MZM are

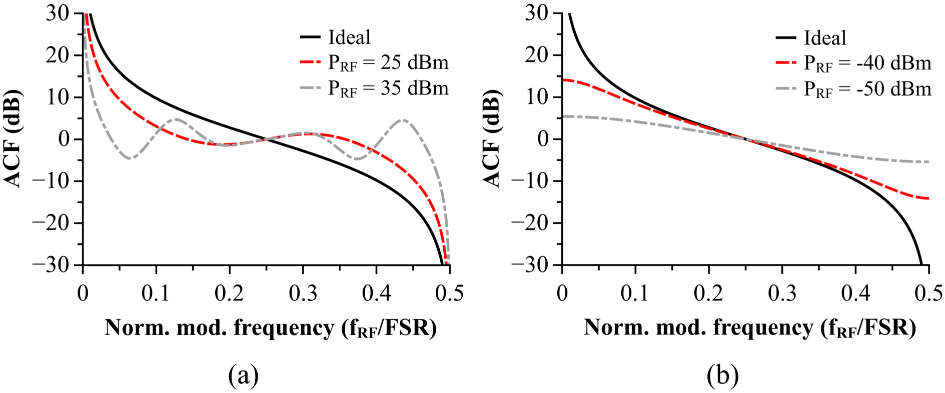

(a) (b)

Figure 5.11: Effect of (a) high powers and (b) low powers in the ACF. Simulation values are: $Z_{in} = 50\ \Omega$, $V_{\pi}^{AC} = 3$ V, $P_o = 20$ mW, $\mathcal{R} = 0.9$ A/W and $I_{\text{Dark}} = 1$ nA. All other parameters are ideal.

no longer perfectly ouf ot phase. Now the ACF is modified asymetrically, which can be easily understood by noting that there exists a contribution to the total photocurrent due to the residual optical carrier. In the lower branch (minimum transmission point of the MZI) this residual carrier is completely suppressed since it is located at the MZI notch, and thus does not affect i^{Down}. However, in the upper branch (maximum transmission point of the MZI) the relative contribution of this term to i^{Up} gets higher as the first-order optical sidebands get more and more attenuated (higher normalized frequencies). Thus, the ACF gets more distorted at higher normalized frequencies, as it is shown in Fig. 5.10(b). Also note that this effect is very sensitive in the MZM case.

Next, the impact of a non-infinite ER in the Mach-Zehnders can be examined. For the MZI case, it is well-known that this implies an upper bound on the ratio between the maximum and minimum transmission points of the transfer function. Thus, a finite ER yields an upper/lower bound on the ACF, which in fact occurs when the first-order sidebands are located at either the notch of the lower branch ($f_{RF} = 0$) or at the notch of the upper branch ($f_{RF} = FSR/2$). As a result, the ACF symmetrically deviates from the ideal one, and its maximum/minimum values match the ER of the MZI (see Fig. 5.10(c)). In the MZM (Fig. 5.10(d)), the effect of a finite ER is essentially equal to that of a bias phase error: Because of the imperfect amplitude imbalance in the MZM arms, the optical carrier is not perfectly suppressed, and this basically leads to an asymmetrical deviation of the ACF due to the same reasons as those mentioned in the previous paragraph. Again, note that the impact of a residual optical carrier is significantly higher than that of a finite ER in the MZI. Similar ACF deviations are obtained in the MZM case for extinction ratios that are 20 dB higher than those in the MZI.

Last, it is also important to analyze how and why the ACF shape changes for different input RF power levels. As an example, two extreme situations are

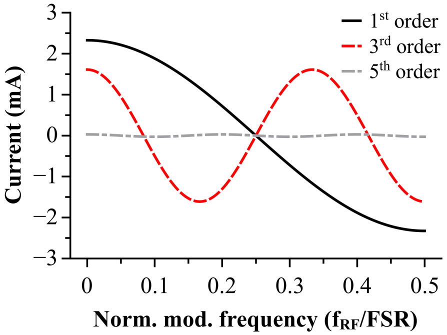

Figure 5.12: Contribution of different order harmonic terms ($n = 1, 3, 5$) to the upper photocurrent (i^{up}). Simulation values are the same of those of Fig. 5.11, with P$_{RF}$ $=$ $+$25 dBm.

plotted in Figs. 5.11(a) and 5.11(b). Figure 5.11(a) illustrates the effects of an extremely high input RF power, while Fig. 5.11(b) shows the effect of very low powers. In the first case, the ACF gets considerably distorted because of the high value of the phase modulation index (β). At this point, the contributions to the total photocurrent due to the high-order harmonics ($J_2^2(\beta)$, $J_3^2(\beta)$ ...) dominate over the first-order ones ($J_1^2(\beta)$), which is a direct consequence of the behaviour of the Bessel functions at high β values. For illustration purposes, the contribution of these terms to the upper photocurrent is shown in Fig. 5.12 for an RF power of +25 dBm. It can be seen that the third-order term is already significant. Only odd orders (n = 1, 3, 5) are shown because, under ideal conditions, all even order terms are zero. In the second case (Fig. 5.11(b)), the amplitude of the first-order sidebands goes to zero as β decreases. Neglecting all other system parameters, this implies that the relative contribution of this term to the total photocurrent decreases as compared to that of the dark current, which is constant and does not depend on RF power. As a result, the ACF gets flatter and flatter as the RF power decreases, and the ratio approaches that of the two residual dark currents, which is 1 (0 dB) assuming that they are equal. These two examples show that, even considering almost perfect operation, there exists an optimum RF power at which the ACF is closest to the ideal response.

Combined impact of parameters in system performance

So far, all simulations have considered only one parameter at time. While this served our purpose of understanding their individual impact, it does not provide a complete vision on the interaction and combined effect of all of them at the same time. Consequently, we now consider a more realistic situation, where reasonable values for all system parameters based on state-of-the-art devices and integration technologies are included. These can be found in Table 5.2

Name	Value	Units	References
Z_{in}	50	Ω	
V_π^{AC}	3	V	[128, 129]
IL_M	5	dB	[129]
ER_M	25	dB	[129]
ϕ_M^e	±1°	degrees	[130]
IL_I	5	dB	
ER_I	25	dB	
ϕ_I^e	±1°	degrees	[130]
P_o	20	mW	
$\mathcal{R}$	0.9	A/W	[131]
I_{Dark}	1	nA	[131]

Table 5.2: Simulation parameters.

along with appropriate references, when needed. Simulation results are plotted in Figs. 5.13(a) and 5.13(b). Figure 5.13(a) shows the evolution of the measured ACF over the whole frequency range ([0-FSR/2]) when the input power varies between +10 dBm and -20 dBm, a typical range for commercial, electronics-based IFM systems, which normally reach down to -50 dBm [132]. It can be seen that the ACF at +10 dBm is near the optimum point mentioned in the previous paragraph, where just a small deviation at both high and low frequencies is observed due to optical system imperfections (phase errors, amplitude imbalance, etc.). When the power is reduced, though, the ACF flattens and asymptotically tends to a constant value of +25 dB. This can be understood by noting that the photocurrents generated by the residual optical carrier now dominate over the dark current contribution, which is fairly small in state-of-the-art, low-speed InGaAs photodiodes. As a consequence, when RF power is very low the ACF approximates the extinction ratio of the MZI (25 dB in this case), which is in fact the optical power ratio between the carrier at the maximum transmission point (MZI upper branch) and the minimum transmission point (MZI lower branch).

It can also be observed that in all cases the maximum deviation from the ideal response takes place at high frequencies. Thus, if no calibration curves are employed and equation 5.29 is directly used to estimate the input instantaneous frequency, the error introduced by this distortion will reach its maximum at FSR/2. In other words: when an RF signal with f = FSR/2 enters the IFM system, the normalized bias error of the measurement process (defined as $f_e = |\hat{f} - f|/FSR$) is maximum. This value provides an upper limit on performance and can be easily computed as follows. First, the non-ideal photocurrent ratio when f = FSR/2 is computed using equation 5.23 ($ACF(\beta, FSR/2, 0)$). Afterwards, this ratio is inserted into equation 5.29, which can be solved to get an estimate of the

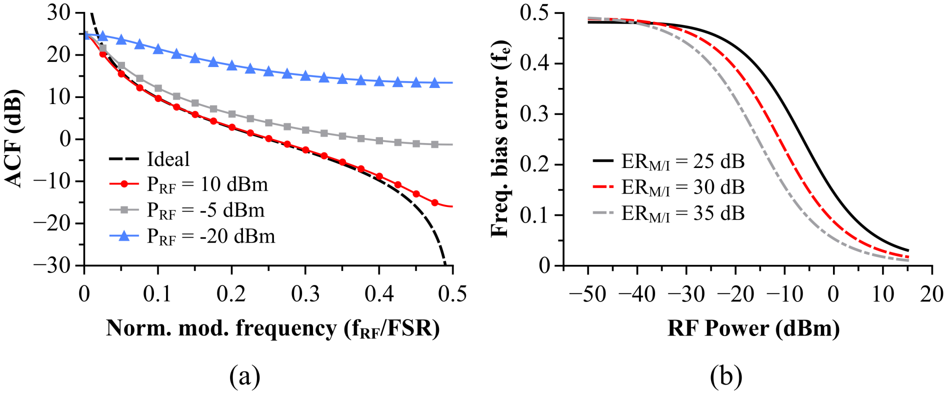

Figure 5.13: (a) Evolution of ACF with different RF powers. (b) Normalized frequency bias error versus input RF power, assuming different values of both ER_M and ER_I. All other simulation parameters are listed in Table 5.2.

instantaneous frequency ($\hat{f}$). Finally, the difference between this estimate and 0.5 (normalized frequency when $f = \mathrm{FSR}/2$) is calculated, which gives the normalized bias error (f_e). The whole process is described by the equation below

$$f_e = |\frac{1}{2\pi} \arccos\left(\frac{(\mathrm{ACF}(\beta, FSR/2, 0) - 1)}{(\mathrm{ACF}(\beta, FSR/2, 0) + 1)}\right) - 0.5| \tag{5.30}$$

The dependence of f_e versus RF power is shown in Fig. 5.13(b) for three different values of both ER_M and ER_I. At high RF powers, the ACF is closest to the optimum point, and a normalized error below 0.05 is obtained for the three cases. As RF power goes below 0 dBm, the bias error rapidly increases until it reaches the maximum possible value (0.5), due to the fast evolution of the ACF as the first-order sidebands approach the residual optical carrier level. The threshold at which this happens is lower for higher extinction ratios, though errors are still significant over the whole power range.

From the previous simulations it can be concluded that, even when using state-of-the-art equipment, stringent limitations exist on the dynamic range of this photonics-assisted IFM technique. As a first approach to solve this issue, a calibration procedure at a fixed RF power can be employed. This basically entails characterizing the ACF after fabrication and then embedding it into the system hardware. Afterwards, the parametrized curve is used during the estimation process instead of equation 5.29, which eliminates the non-zero bias error that exists even near the optimum working point. However, this approach only yields accurate results over a limited RF power range, as the ACF significantly worsens at low RF powers and thus the parametrized curve is no longer valid. In that case, multiple ACF calibration curves measured at different input RF powers would be needed. This approach would in turn require a way to quickly measure the RF power of the input pulse previous to the estimation process, and then choosing the curve that was calibrated at a similar RF power. Another option, that could even be used in combination with the previous ones, would be to add a limiting amplifier at the input RF stage. Limiting amplifiers basically provide a constant RF power signal at their output even if the input power fluctuates over a wide dynamic range. In fact, they are commonly employed in electronic-based IFM receivers [109]. With an auxiliary limiting amplifier, the system could be optimized in such a way that the output RF power of the amplifier would be near the optimum working point of the photonic IFM system, thus minimizing error degradation over a wider dynamic range. In any case, complexity and cost would be added to the final solution.

5.4 Conclusions

In the first part of this chapter, a photonics-based system that is capable of estimating the unknown frequency of a CW microwave signal has been reported. Its operation principle relies on exploiting the different attenuations that a DSB-SC modulation experiences when passing through a RAMZI filter, featuring a second-order elliptic response and fabricated in a generic InP platform. Using this approach, a frequency measurement bandwidth of 10 GHz (5-15 GHz) has been experimentally demonstrated, achieving a root mean square value of the frequency error lower than 200 MHz. Simulations have also been run that demonstrate the negative influence of a reduced optical SCR in system performance, with a RMS error above 600 MHz when the RF power is reduced by 10 dB. Similar to other optical power-based approaches, this system only requires low-speed phsotodetectors and electronics, and it could be fully integrated on a single InP chip.

In the second part, we have developed a time domain model for the analysis of impairments in a photonics-assisted IFM technique based on a DSB-SC optical modulation and an MZI filter. Unlike previous works, our model considers all major optical and electrical effects, such as amplitude imbalance and phase errors in the MZM and the MZI, as well as dark currents in the photodiodes. Furthermore, it includes the effect of phase/frequency modulation in the RF pulse, which is an essential feature for the analysis of modern radar signals. Numerical simulations indicate that a finite carrier suppression arising mainly from imperfections in the MZM leads to significant degradation of the IFM system performance.

In particular, it has been shown that both the extinction ratio and the bias phase error in the MZM are the most critical parameters for achieving a low frequency error. Our simulations also demonstrate that the system ACF strongly depends on input RF power, thus leading to a poor performance in terms of dynamic range even when using parameter values from state-of-the-art devices. Overall, our results suggest that a careful analysis and assessment of the impact of RF power needs to be done when designing and reporting on the performance of photonics-based IFM systems. Some ideas for alleviating this problem have also been discussed, such as the combined use of calibration curves and limiting amplifiers in the input RF stage. With further advances in carrier suppression and calibration techniques, InP technology might represent a promising opportunity for the realization of future high bandwidth, all-optical and reduced footprint IFM systems.

Publications

The work done in this chapter lead to the following publications in peer reviewed journals and international conferences:

1. **J. S. Fandiño** and P. Muñoz, "Analysis of System Imperfections in a Photonics-Assisted Instantaneous Frequency Measurement Receiver Based on a Dual-Sideband Suppressed-Carrier Modulation," *J. Lightwave Technol.*, vol. 33, pp. 293–303, Jan. 2015.

2. **J. S. Fandiño** and P. Muñoz, "Photonics-based microwave frequency measurement using a double-sideband suppressed-carrier modulation and an InP integrated ring-assisted Mach-Zehnder interferometer filter," *Opt. Lett.*, vol. 38, pp. 4316–4319, Nov. 2013.

3. **J. S. Fandiño** and P. Muñoz, "Instantaneous frequency measurement system by means of a complementary optical filter monolithically integrated in InP," in *International Topical Meeting on Microwave Photonics (MWP)*, pp. 290–293, Oct. 2013.

4. **J. S. Fandiño**, M. Rius, J. Mora, P. Muñoz, and J. Capmany, "Optical Single Sideband Transmitter Using Phase Modulation and a Photonic Integrated Filter," in *International Topical Meeting on Microwave Photonics (MWP)*, pp. 154–157, Oct. 2013.

Acknowledgements

J. D. Doménech and I. Artundo from VLC Photonics S.L. are gratefully acknowledged for providing access to the MPW run of the EuroPIC consortium, where the chip discussed in this chapter was fabricated.

Chapter 6

Frequency discrimination for microwave photonic links

6.1 Introduction

The transmission of broadband RF signals over long distances with both very low loss and distortion has been one of the long-standing challenges of the microwave photonics community for years. Silica-based single-mode fibers have been actively explored for that purpose, finding use in a wide range of applications, such as CATV systems, antenna remoting and mobile backhauling [10, 11].

However, in short to medium distances, the total RF gain of an intensity modulated-direct detection (IM-DD) microwave photonic link (MWPL) is not limited by fiber propagation loss, but rather by the low efficiencies of the modulation and detection processes. Besides, the intrinsic non-linear transfer function of the commonly employed Mach-Zehnder modulator (MZM) imposes a fundamental limit on the achievable Spurious-Free Dynamic Range (SFDR) of the MWPL [133]. As a result, considerable effort has been put into developing new system architectures and techniques that could overcome the limitations of the traditional IM-DD approach [134].

In particular, frequency modulation-direct detection (FM-DD) links have emerged as a plausible alternative. In this scheme, an optical source is first frequency modulated, either by directly driving a semiconductor laser or by using an external modulator. At the receiver end, the transmitted signal is sent through an optical filter, also called a *frequency discriminator*, that turns its instantaneous frequency variations into an intensity modulated optical waveform. In that way, the signal can be finally recovered by a simple photodetector instead of employing more complex coherent techniques. Note that external modulators usually exploit the Pockels effect in crystalline materials, such as lithium niobate [135], where the induced phase shift is proportional to the applied voltage. As a consequence, a very high SFDR could in theory be achieved with a suitable design and implementation of the receiver optical filter, given that it performs this frequency to intensity conversion in a linear fashion.

The first experimental demonstrations of this approach were based on discrete components, including Mach-Zehnder interferometers (MZI) [136–139] and fiber Bragg gratings [140]. However, in both cases the solutions are bulky, lack reconfigurability, and thus prevent the possible implementation of a compact discriminator. More recently, photonic integrated circuits (PICs) have also been explored as a mean of achieving compact, high-performance filters for frequency discrimination. Different structures and technologies have been demonstrated so far, including PICs based on cascaded ring resonators in Si_3N_4 TriPleX technology [141], as well as multi-stage MZI lattice filters and ring-assisted MZIs (RAMZI) filters in Silica-on-Silicon [44, 142, 143].

In this chapter, we present the design and experimental demonstration of a fully integrated, InP-based receiver for FM-DD analog optical links. The core of the PIC is a tunable integrated optical filter that works as a frequency discriminator, which is later followed by a high-speed balanced photodetector. The filter employed in the previous chapter for IFM was actually just a small part of this chip. We will first start with a short historical review of the FM-DD concept, commenting on the most recent contributions made by several authors. However, we will employ here a simple time-domain formalism to illustrate the main theoretical idea, which will also help us to shed some light on the ideal transfer function that the discriminator needs to have in order to achieve a linear frequency to intensity conversion. Next, we will proceed to describe the design of the PIC, including the system level specifications of the integrated optical filter as well as the chip layout. Finally, we will discuss the results of the experimental characterization, highlighting the practical problems associated with this architecture of MWPL and potential ways to solve these challenges. The chapter ends with some concluding remarks.

6.2 Theoretical background

The FM-DD concept is in itself an evolution of the so called class-AB microwave photonic link architecture, whose origins can be traced back to a couple of papers by Darcie et al. in the mid 2000 [144, 145]. In these seminal articles, Darcie et al. proposed a new modulation idea for MWPLs that was actually inspired by classic techniques employed for designing electronic amplifiers. In class-AB amplifiers, 2 sets of transistors are operated in a complementary fashion, each one amplifying either the positive (+) or negative (-) part of the incoming signal. In general, a small bias current (also known as *quiescent current* [146]) is fed into both sets in order to minimize the crossover distortion, which is produced when the signal crosses zero. Later on, the two outputs are combined to provide a complete reconstruction of the input waveform. The use of a small quiescent current is key, as it sacrifices efficiency at the expense of achieving a lower distortion. Similarly, the idea behind class-AB MWPLs is to employ two low-biased MZMs working in a complementary fashion, where each one provides either the positive or negative

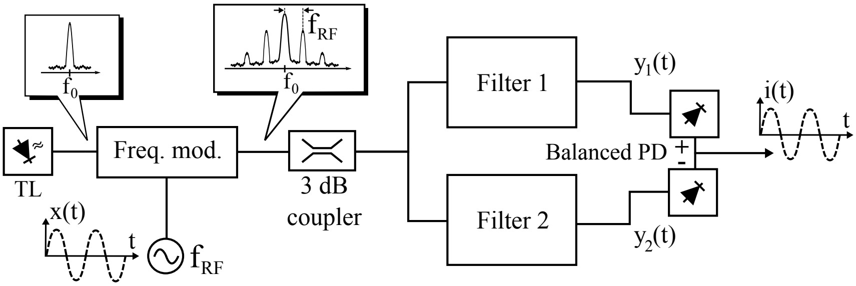

Figure 6.1: Architecture of a FM-DD MWPL link.

part of the RF signal to be transmitted down the link. At the receiver end, the signal is recovered by means of a balanced photodetector. The use of a low-bias reduces the total DC power impinging on the photodetector, thus minimizing both the shot and RIN noises and potentially increasing the SFDR of the MWPL.

Later on, the same authors set to improve upon this concept, and proposed a new MWPL architecture that was termed class-B [140, 147]. Their main idea was to employ a frequency modulated signal in conjunction with two pairs of complementary frequency discriminators, which in this case were implemented with two custom Fiber Bragg gratings. A schematic diagram of the technique can be seen in Fig. 6.1, while the filter responses employed by Darcie are shown in Fig. 6.2(a). Remember that, by definition [148], a frequency modulated signal has an instantaneous frequency that is directly proportional to the input RF signal. Intuitively, one might think that, when that signal were introduced into a complementary pair of frequency discriminators, the instantaneous changes in frequency would translate into instantaneous changes in the output optical power. The positive/negative cycle of this signal will be provided by the upper/lower frequency ramps, so there would be no need for a low bias. As a consequence, the signal at the output of the discriminators would be intensity modulated with virtually no distortion, and could be finally recovered with a balanced photodetector.

It turns out that this idea was subtly flawed, as it was proofed by Wyrwas et al. in a later paper [149]. The main error was confusing the time and frequency domains, and assuming that a signal with an instantaneous frequency that changes sinusoidally with time can be regarded as a tone with a central frequency that is increasing and decreasing, with a period equal to that of the modulating waveform. In reality, the Fourier transform of such a signal is a well-known expansion in terms of the Bessel functions of the first kind, and in the frequency domain is just an infinite set of tones with decreasing amplitudes that are spaced from the carrier by an integer multiple of the modulation frequency. Wyrwas noticed this misunderstanding, and then performed a detailed theoretical analysis of the main figures of merit in this kind of link, including the intermodulation distortion terms. He found that the transfer function proposed by Darcie was not correct because of two reasons. First, it had a V-like shape (as in Fig. 6.2(a)), with a null exactly

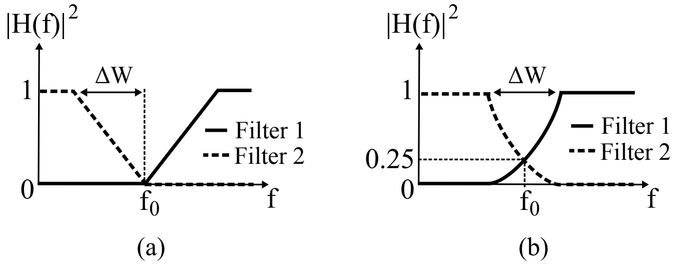

Figure 6.2: (a) V-shaped filter with linear ramps in *optical intensity*. (b) X-shaped filters with linear ramps in *electric field* (quadratic in intensity).

at the optical frequency of the carrier. This meant that the optical carrier would be completely suppressed, and thus the link would have almost zero gain, as the fundamental component is mainly the result of the beating between the first-order sidebands and the optical carrier. Second, a transfer function with a linear ramp in *optical intensity* would not result in a distortion free modulation. Instead, a linear ramp in *electric field* must be employed (quadratic behaviour in *optical intensity*, as in Fig. 6.2(b)), followed by a balanced photodetector with a very high common mode rejection ratio (CMRR). This is just the same as the PROUD concept proposed by Azaña et al. [150].

The model developed by Wyrwas is useful when it comes to compute the figures of merit of the MWPL under very general conditions. However, the basic concept can be illustrated in a simpler way by following a time-domain formalism. Lets consider the complex low-pass equivalent of a frequency-modulated signal

$$x(t) = \sqrt{P_0} e^{j\phi_i(t)} \tag{6.1}$$

where P_0 is the average optical power, and $\phi(t)$ accounts for an instantaneous phase modulation that is being produced by an external RF waveform. The instantaneous frequency $f(t)$ of such a signal is just given by [148]

$$f(t) = \frac{1}{2\pi} \frac{\partial \phi(t)}{\partial t} \tag{6.2}$$

so that, by virtue of the Second Fundamental Theorem of Calculus [151], we have that

$$\phi(t) = 2\pi \int_{-\infty}^{t} f(s) ds \tag{6.3}$$

Assume that we now split this signal in two with a 50% coupler, and that we send the split signals through a pair of frequency discriminator filters ($H_1(\omega)$ and $H_2(\omega)$) with a couple of transfer functions that are given by

$$H_1(\omega) = \frac{j}{2} + ja\omega \tag{6.4}$$

$$H_2(\omega) = \frac{j}{2} - ja\omega \tag{6.5}$$

where a is a constant that accounts for the slope of the discriminators, in units of $[s/rad]$. If we further assume passive filters with no losses, then the maximum value of $|H(\omega)|$ is 1, so a can be simply expressed as

$$a = \frac{1}{\Delta W} \tag{6.6}$$

where ΔW is the bandwidth over which the response of the frequency discriminator (in modulus) goes from 0 to 1. The modulus squared of these transfer functions has a quadratic behaviour, like those plotted in Fig. 6.2(b).

Finally, the two signals are detected in a balanced photodetector, as shown in the schematic diagram of Fig. 6.1. In order to obtain the final expression for the photocurrent in the time domain, $i(t)$, we must recall two important properties of the Fourier transform. First, the optical signals after filtering are given in the frequency domain by the product of the Fourier transforms of the filters' impulse responses ($H_1(\omega)$ and $H_2(\omega)$) and the input signal ($X_1(\omega)$ and $X_2(\omega)$)

$$Y_1(\omega) = H_1(\omega)X_1(\omega) \tag{6.7}$$

$$Y_2(\omega) = H_2(\omega)X_2(\omega) \tag{6.8}$$

Second, the time derivative of a differentiable function ($f(t)$) is expressed in the frequency domain as the Fourier transform of the original signal ($F(\omega)$) times $j\omega$. That is

$$\mathcal{F}\{\frac{\partial f(t)}{\partial t}\} = j\omega F(\omega) \tag{6.9}$$

As a consequence, and assuming that the bandwidths of the signal are small enough so as to fall within the slope region of the discriminators, we have that

$$y_1(t) = j\frac{x(t)}{\sqrt{2}}\left(\frac{1}{2} + \frac{2\pi f(t)}{\Delta W}\right) \tag{6.10}$$

$$y_2(t) = j\frac{x(t)}{\sqrt{2}}\left(\frac{1}{2} - \frac{2\pi f(t)}{\Delta W}\right) \tag{6.11}$$

and their modulus squared are given by

$$|y_1(t)|^2 = \frac{P_0}{2}\left(\frac{1}{2} + \frac{2\pi f(t)}{\Delta W}\right)^2 \tag{6.12}$$

$$|y_2(t)|^2 = \frac{P_0}{2}\left(\frac{1}{2} - \frac{2\pi f(t)}{\Delta W}\right)^2 \tag{6.13}$$

$$\tag{6.14}$$

We can now compute an expression for the detected photocurrent, as it must be proportional to the difference between these two quantities. After some straightforward algebra, we finally obtain that

$$i(t) \propto |y_1(t)|^2 - |y_2(t)|^2 = \frac{4\pi}{\Delta W}P_0 f(t) \tag{6.15}$$

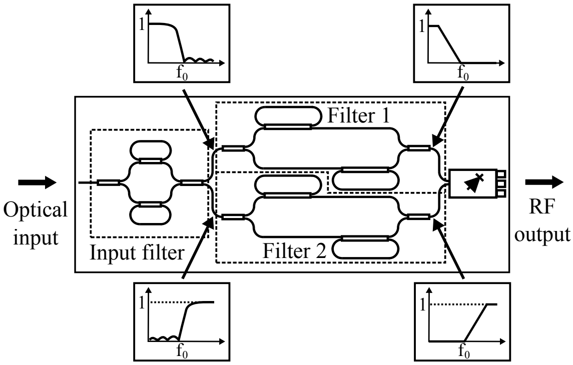

Figure 6.3: Diagram of the designed FM-DD PIC. Transfer functions are schematically shown at the different output ports of each filter for illustration purposes.

A few conclusions can be readily drawn by direct inspection of equation 6.15. First, the recovered signal is indeed proportional to the instantaneous frequency of the signal. Thus, at least in theory, a perfect link with an infinite SFDR could be implemented as far as the filter has the right transfer function (X-shaped, linear slope in *electric field* or quadratic in *optical intensity*) and the balanced photodetector has an infinite CMRR. In practice, any slight deviation from the ideal filter shape will yield even and odd order intermodulation (IMD) and harmonic distortion (HMD) products, while a non perfectly balanced photodetector will yield mainly even products of the same kind.

Second, there exists a trade-off between the link gain (G_{RF}) and the maximum transmission bandwidth. A linear detection is only guaranteed when the power of the RF signal is low enough so that the high-order terms of the Bessel expansion fall within the passband of the discriminators. Thus, if we want to increase the bandwidth, then ΔW must be increased in order to comply with this constraint. However, this will in turn reduce the amplitude of the detected photocurrent, as it is inversely proportional to ΔW, reducing the link gain.

Finally, it is important to realize that the cancellation of the IMD and HMD terms depends on the exact amplitude and phase relationships between the harmonics of the frequency-modulated signal [149,152]. If such a signal is sent through a fiber, then the dispersion introduced by it will change the relative phase shifts between the different components, introducing a residual intensity modulation that can indeed become very strong at long distances. Thus, dispersion compensation fibers should be deployed before the receiver, as it was also noticed by Wyrwas [149].

Name	κ_1	ϕ_1	κ_2	ϕ_2	β_u	β_d
Input filter	0.7176	-1.3735	0.7176	1.3735	5.3301	-2.1885
Filter 1	0.9144	3.6530	0.3814	3.6343	0.7948	-0.7948
Filter 2	0.9144	2.4477	0.3814	2.4290	0.7948	-0.7948

Table 6.1: Coupling constants (in lin. units) and optical phase shifts (in *rad*) for the three filters.

6.3 Design and layout

In order to integrate the aforementioned frequency discriminator architecture into a single monolithic chip, an integrated optical filter with a custom spectral response was designed. At that time, we were not yet aware of the research made by Wyrwas regarding the optimum transfer function for the frequency discriminator, so we based our approach on the architecture proposed by Darcie et al. [140] (Fig. 6.2(a)), which was also employed in a later experimental demonstration by Marpaung et al. [141, 153]. While Marpaung approach was based on an concatenation of ring resonators, here we chose to use a combination of three different RAMZI filters (Fig. 6.3), in order to have a better control over the filter response. First of all, an *Input filter* is used to split the spectrum of the incoming optical signal in two distinct frequency bands, one above and one below the optical carrier. It was designed as a second order Elliptic filter to ensure maximum roll-off, featuring a passband normalized cut-off frequency of 0.33 at 0.25 dB attenuation, and a stopband normalized frequency of 0.66 with 18 dB of minimum attenuation. Afterwards, the two outputs of this filter are fed into the inputs of two complementary frequency discriminators with negative and positive slopes, respectively, which we should call from now on as *Filter 1* and *Filter 2*. These were designed to have a linear ramp in *optical intensity*, and their coefficients were extracted from a previous design by Madsen [55].

Once the filters were designed, the synthesis algorithm described in chapter 2 was employed to obtain the values for all coupling constants and optical phase shifts. They are summarized in Table 6.1, following the notation of Fig. 2.4(a) in chapter 2. Note that, although the linear frequency discriminators have a complementary response (and thus the same coupling coefficients), their optical phases must be different in order to ensure that they are properly aligned in frequency with the right passband of the *Input filter*. Their Free Spectral Range (FSR) must also be approximately half of it, so the linear ramp is only applied to either the upper or lower band of the transmitted spectrum. As a result, the perimeter of the ring resonators in *Filter 1* and *Filter 2* is around twice that of the rings in the *Input filter*, except for the small deviations in length used to introduce the appropriate phase offsets. Figures 6.4(a)-(d) show the ideal simulated responses of the optical filters.

The chip was manufactured as part of the EuroPIC EU FP7 project, using a state-of-the-art InP generic integration platform offered by the Heinrich Hertz

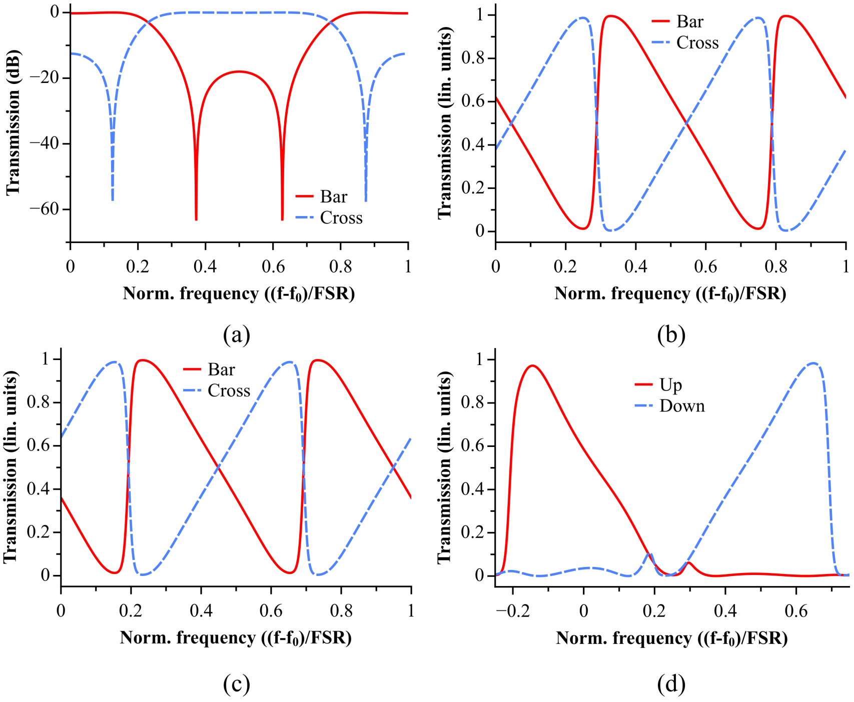

(a)

(b)

(c)

(d)

Figure 6.4: (a) Simulated transfer functions of the two complementary outputs (*Bar* and *Cross*) of the *Input filter*. (b)-(c) Simulated transfer functions of *Filter 1* and *Filter 2*, respectively, designed to provide a linear ramp in optical intensity. (d) Total response at the input of each branch of the photodetector.

Institute (HHI) in Berlin [34]. In order to minimize the bending radius (150 μm) and maximize the FSR, deeply etched rib waveguides were employed. These are made of an InGaAsP core over an InP substrate, with no cladding on top, and they are etched about 1.7μm from the top of the quaternary layer. A 2 μm width was chosen for the optical routing waveguides to ensure single-mode behaviour for both polarizations. Regarding the optical couplers, they were implemented with 12 μm-wide tapered MMIs using the same design routine as described in chapter 3. Table 6.2 contains the final design values of these devices, including the target and simulated coupling constants.

A picture of one of the manufactured dies is shown in Fig. 6.5. It has an area of only 6x6 mm^2. Due to the high sensitivity of the filter to the relative optical phases of the ring resonators and the MZI arms, multiple thermo-optic heaters were placed in every possible optical path associated with the design variables, in order to allow both for post-fabrication fine tuning. Besides, two horizontal rows of metal pads with a pitch of 250 μm were allocated on either sides of the chip for

Type	d_1^i, d_2^i (μm)	ΔW (μm)	L' (μm)	Target $\kappa_{cross}/\kappa_{bar}$	Sim. $\kappa_{cross}/\kappa_{bar}$
A	4.0,4.0	0	201.28	50/50	49.2/49.3
C	3.0,3.0	-2.320	416.75	72/28	71.7/26.3
B	4.0,4.0	-1.064	475.62	91/9	89.0/7.7
A	4.0,4.0	-0.926	231.837	38/62	37.3/61.2

Table 6.2: Physical dimensions and BPM simulation results of the 4 MMI couplers. A common width of 12 μm was used for all designs.

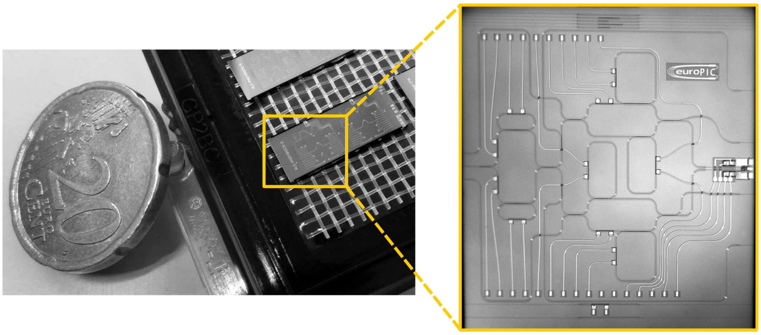

Figure 6.5: Pictures of the manufactured chips.

easier access with multi-contact DC probes. Finally, a balanced photodetector with integrated bias tee, offered as a building block in the platform, was placed at the discriminator outputs. It featured a bandwidth higher than 35 GHz, a responsivity of about 0.54 A/W, and large signal saturation current of 10 mA. The balanced configuration has a common mode rejection ratio specification greater than 25 dB. Besides, auxiliary waveguides were routed to the inputs and outputs of the three filters, providing an easy access to independently probe the response of each one.

6.4 Experimental characterization and discussion

6.4.1 Optical filters

An experimental setup as shown in Fig. 6.6 was arranged to characterize and adjust the optical lattice filters. First, the light coming from a high-power ASE source is coupled into the chip after passing through a collimator, a free-space linear polarizer and a long working distance microscope objective. By ensuring that the incoming light beam is horizontally polarized (parallel to the chip surface) only TE modes are excited. This control is essential since differences in effective indices between TE (horizontal) and TM modes (vertical) propagating within the waveguides of the structure lead to different optical phases in both MZI arms and ring resonators, affecting the measured response. After polarization filtering and coupling, the light is captured by a lensed fiber at the different chip outputs and

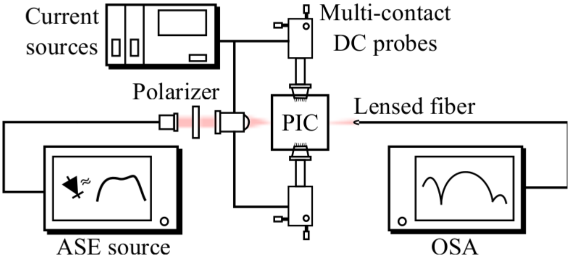

Figure 6.6: Experimental setup employed for the characterization and adjustment of the RAMZI filters.

the corresponding transfer functions are recorded by measuring the transmission spectrum with a high-resolution Optical Spectrum Analyzer (OSA). Afterwards, the spectra is normalized with a straight waveguide located on the same chip. Two multi-contact DC probes were connected to an array of current source modules to drive the different thermo-optic heaters.

During characterization, it was observed a significant thermal crosstalk because of the high number of heaters and the tightly packaged layout. This implied that, once the response of each filter had been adjusted individually, it would change when another filter was tuned. After a significant number of manual trial-and-error iterations, a set of transfer functions resembling the original target responses over a limited wavelength interval were obtained. These are shown in Fig. 6.7(a)-(d), normalized with a straight waveguide located on the same chip. The *Input filter* features a highly periodic response, with its *Bar* and *Cross* transfer functions being very similar to the design targets. This means that the tapered MMIs were correctly designed, and that the dispersion of the two ring resonators that compose the structure was almost identical. Note that the measured insertion losses for this filter, which are around 6.5-7.5 dB for both the *Bar* and *Cross* outputs, are actually about 3 dB lower. This is due to the fact that a pair of 3 dB couplers were located right after these two outputs (see Fig. 6.5), in order to route auxiliary waveguides with which to measure its transfer function. Its FSR is about 49 GHz.

On the contrary, it can be seen that both *Filter 1* and *Filter 2* show a transfer function that slowly changes with wavelength. This is attributed to the fact that the tapered MMIs in the upper and lower ring resonators have different lengths. Since the group index of the MMI is slightly different from that of the single-mode waveguides, the dispersion of the two ring resonators is different, which implies a small modulation of the relative phase shift as a function of frequency. The filters are no longer periodic, but nevertheless is possible to obtain a frequency response similar to the target ones over a small wavelength interval. *Filter 1* and *Filter 2* have approximate insertion losses of 6.2 and 6.8 dB, respectively, which are about twice the insertion loss for the *Input filter* if the auxiliary coupler is not taken into account. This is consistent since they are about twice as long. In fact, their measured FSRs are around 28 GHz, compared to the 49 GHz of the *Input*

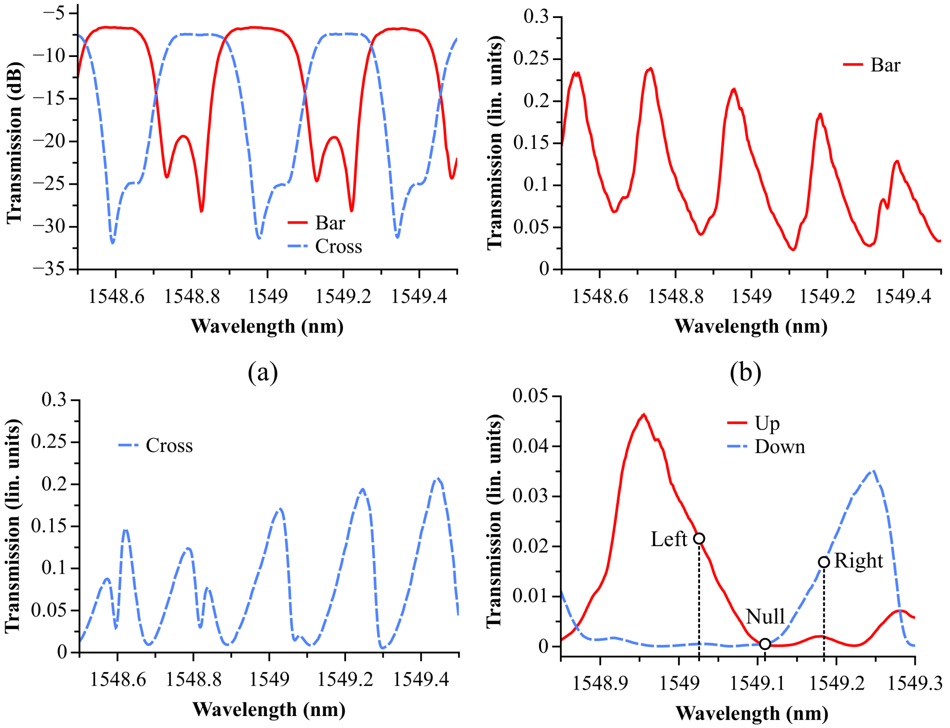

(a) (b)

(c) (d)

Figure 6.7: (a) Measured transfer functions of the two complementary outputs (*Bar* and *Cross*) of the *Input filter*. (b) Measured transfer function for the *Bar* output of *Filter 1*. (c) Idem for the *Cross* output of *Filter 2*. (d) Cascaded responses at both inputs of the photodetector. Three wavelength points were the system linearity was measured are marked for clarity: Left = 1549.022 nm, Null = 1549.109 nm and Right = 1549.184 nm.

filter. The total response for the upper and lower branches of the discriminator can be seen in Fig. 6.7-(d). Their insertion losses are around 13.4 dB and 14.5 dB, respectively. Again, note that these values include the 3 dB loss of to the auxiliary couplers.

6.4.2 Linearity and dynamic range

The experimental setup used for characterizing the RF performance of the FM-DD chip is shown in Fig. 6.8(a). First, a tunable laser (Ando AQ6317C, 0.7 dBm output power, RIN = -145 dB/Hz) is modulated by an electro-optic phase modulator (JDS Uniphase, V_π = 9.1 V, 10 GHz modulation bandwidth, 3.5 dB insertion losses), which is fed by two RF signals at f_1 and $f_2 = f_1 + \Delta f$ generated by an

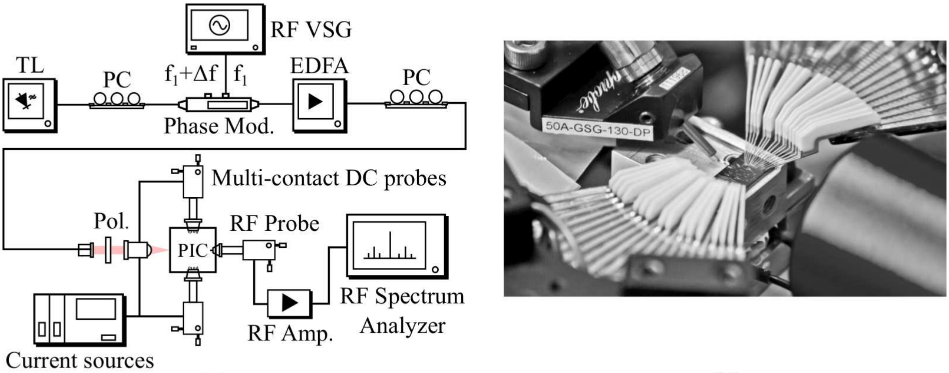

(a) (b)

Figure 6.8: (a) Experimental setup employed for the two-tones test. (b) Close up picture of the chip mount during measurement.

RF Vector Signal Generator (Agilent E8267C). Here, Δf was arbitrarily chosen to be 1 MHz. The polarization at the input of the modulator is adjusted with a manual polarization controller. The modulated signal is subsequently amplified by an EDFA (optical gain = 18.3 dB) prior to free-space polarization filtering and coupling into the chip. A high-bandwidth RF probe (PicoProbe 50A, up to 50 GHz) with a Ground-Signal-Ground configuration is used to extract the RF signal from the balanced photodiode, which is polarized with the same multi-contact DC probes as the ones used for filter tuning. Finally, a high-bandwidth (40 GHz), high-gain (30 dB) RF amplifier (SHF-8010) is placed before a RF spectrum analyzer (Agilent N9020A-526 MXA), which measures the output RF powers at both the fundamental and intermodulation distortion frequencies. The chip is kept at room temperature by means of a closed-loop temperature controller with a Peltier cell located just below the metal mount, thus minimizing possible wavelength drifts of the filters. A close up picture taken during measurements is shown in Fig. 6.8(b), where the chip, the probes and the objective are clearly visible.

We performed a standard two-tones test, which consists in sweeping the input RF power while measuring the output RF powers of both the fundamental components (f_1 and f_2) and the third-order intermodulation products ($2f_1 - f_2$ and $2f_2 - f_1$). These terms arise from the beating of the second-order harmonics ($2f_1$ and $2f_2$) with the fundamental components, so they normally fall within the signal bandwidth causing most of the non-linear distortion. Figure 6.9(a) shows the usual distribution of the most important tones. As suggested by previous works [44,142], the linearity of the FM-DD system in terms of third-order intermodulation distortion products (IMD3) should be maximized when the optical carrier is placed in the middle of the discriminator slope (50% power transmission), and not in the transmission null as it was proposed by Darcie et al [140]. For the sake of comparison, we chose three different wavelength points in the discriminator transfer function. They are shown in Fig. 6.7(d) (*Left* = 1549.022 nm, *Null* = 1549.109 nm

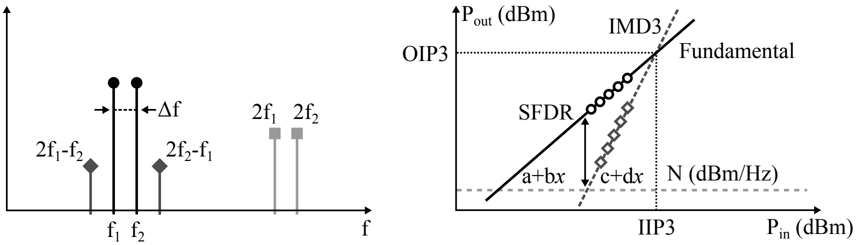

(a) (b)

Figure 6.9: (a) Schematic diagram of the most important frequency components that appear in a two-tones test. (b) Typical SFDR measurement.

and *Right* = 1549.184 nm). At each of these three wavelengths, the RF power of the two tones exiting the signal generator was varied (7, 9, 11 and 13 dBm, respectively), and the output RF powers of the fundamentals and IMD3 products were manually recorded. This was done for 5 different test frequencies (f_1 = 1, 3, 5, 7 and 9 GHz). Additionally, the RF power going into the modulator was calibrated to take into account frequency dependent losses of coaxial cables and transitions. Note that, as predicted by theory, the IMD3 product should exhibit a cubic dependence with input RF power [142], while the fundamental should be proportional to it. The data obtained during the power sweep can then be used to fit a pair of straight lines to the fundamental ($y = a + bx$) and IMD3 powers ($y = c + dx$) in logarithmic units, as it is illustrated in Fig. 6.9(b). From the fitted curves, the SFDR can be computed, which is given by the following equation

$$\text{SFDR (dB.Hz}^{2/3}) = \frac{2}{3}\,[\text{OIP3 (dBm)} + \text{N (dBm/Hz)}] \qquad (6.16)$$

where N is the measured noise floor, normalized in units of dBm/Hz, and OIP3 stands for the third-order output intercept point, which is the theoretical point where the output RF powers of both the fundamental and the IMD3 terms are equal. The OIP3 is related to the third-order input intercept point (IIP3) and the link gain (G), as follows

$$\text{OIP3 (dBm)} = \text{IIP3 (dBm)} + \text{G (dB)} \qquad (6.17)$$

The fitted slopes of the fundamental and IMD3 products (b and d, respectively) are shown in Figs. 6.10(a) and 6.10(b). It can be seen that, while the slopes of the fundamental terms all have values close to 1, as predicted by theory, a significant variation is observed in the slopes of the IMD3 products. This is attributed to both the high V_π of the employed modulator and the high optical losses of the system. The latter arise from the free-space polarizer plus fibers and connectors (4.4 dB), the fiber-to-chip coupling (7 dB/facet) and the own filters (around 13 dB). All in all, they resulted in a very low total RF gain (<40 dB in the best case), even with the RF amplifier (+30 dB) and the EDFA. As a consequence, the measured

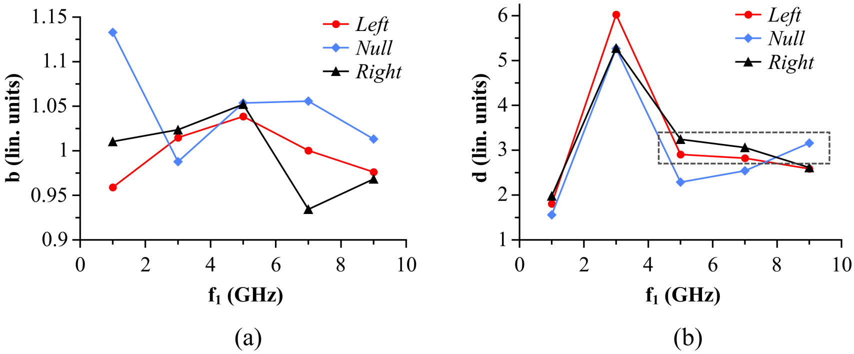

(a) (b)

Figure 6.10: (a) Fitted slopes for the fundamental component. (b) Fitted slopes for the IMD3 products. Those points close to the ideal value (3) are enclosed with a dashed grey line.

Wav.	f_1(GHz)	b	d	IIP3(dBm)	OIP3(dBm)	G(dB)	SFDR(dB.Hz$^{2/3}$)
Left	5	1.04	2.91	34.13	-11.17	-45.30	79.22
Left	7	1.00	2.82	33.38	-13.02	-46.41	77.99
Null	9	1.01	3.16	28.37	-28.88	-57.25	67.41
Right	5	1.05	3.24	26.23	-25.98	-52.21	69.35
Right	7	0.93	3.06	29.14	-26.15	-55.29	69.23

Table 6.3: Measured slopes of the fundamental (b) and IMD3 products (d), IIP3s, OIP3s, Gains and SFDRs for the selected points of Fig. 6.10(b).

power values of the IMD3 terms were close to the sensitivity limit of the RF spectrum analyzer, which introduced significant fluctuations that translated into a poor slope fitting. A few data points were nevertheless valid, namely 5 GHz at *Left* and *Right*, 7 GHz at *Left* and *Right*, and 9 GHz at *Null*. They have been enclosed with a grey dashed line in Fig. 6.10(b).

These slopes, as well as the measured IIP3s, OIP3s, Gains and SFDRs for the selected points are summarized in Table 6.3. Besides, the RF power sweeps of the best and worst case situations are plotted in Figs. 6.11(a) and 6.11(b). SFDR values between 79.22 and 67.41 dB.Hz$^{2/3}$ were obtained. These are 10.78-22.6 dB.Hz$^{2/3}$ below those obtained for the Si_3N_4 discriminator (90 dB.Hz$^{2/3}$) [141], while no SFDR has been reported yet for the Silica-on-Silicon planar lightwave circuit discriminators [44, 143]. From the aforementioned values, it can be seen that the FM-DD chip is highly non-linear, and that there is considerable room for improvement.

For example, the SFDR could be directly increased by reducing additional sources of noise not related to the optical carrier. Removing the EDFA preamplifier and increasing the laser output power from +0.7 dBm to +19 dBm would result

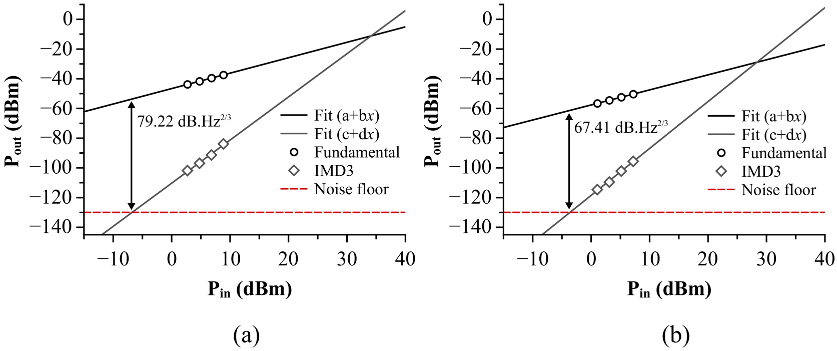

Figure 6.11: (a) and (b) SFDR measurements for the best and worst cases, respectively.

in the same received photocurrent. This would make the EDFA unnecessary, eliminating its contribution to the noise floor. An RF amplifier with lower noise figure will also contribute to reduce the detected noise power spectral density. Additionally, optical losses could be reduced. By eliminating the free-space setup and connector losses using a spot-size converter [154], a net increase around 10 dB in optical power could be achieved. The RF gain would in turn be increased by 20 dB, which would translate into an SFDR increase of 13.33 dB.Hz$^{2/3}$.

Another significant yet more challenging way of improvement would require achieving a more ideal discriminator transfer function. As it has been theoretically shown, a frequency discriminator with a linear ramp in *optical intensity* inevitable produces a certain amount of third-order distortion during the FM-IM conversion process, as compared to a discriminator with a linear ramp in *electric field* [149]. By a proper redesign of our frequency discriminators, this extra distortion could in principle be eliminated. This would result in a MWPL with a very high SFDR, which would be limited only by the non-linearities of modulators and photodetectors when working under high RF and optical power conditions.

6.5 Conclusions

In this chapter, the design and experimental characterization of an InP PIC working as a receiver for FM-DD MWPLs have been presented. First, we have illustrated the key idea and potential benefits behind the FM-DD approach, while discussing the most recent contributions by several authors. As we have seen, the right choice of the frequency discriminator transfer function is crucial for obtaining maximum performance. In particular, it has been demonstrated using a simple time-domain model that an X-shaped response with two linear raps in *electric field* provides a theoretically distortion-free response, as it was first demonstrated by Wyrwas using a frequency-domain model.

Second, we have provided a description of the PIC design process, which involved the synthesis and layout of three second-order RAMZI filters. They were designed to provide two V-shaped linear ramps in *optical intensity*, following the original approach by Darcie et al. [140]. The filters' couplers were implemented by means of tapered 2x2 MMIs. Couplers' dimensions, the results of the synthesis algorithm and simulations of the synthesized transfer functions have been provided and discussed. The chips, which occupy an area of only 6x6 mm^2, were fabricated in a generic InP platform with 1.7 μm-etched waveguides and a small bending radius of 150 μm. They included multiple thermo-optic heaters for fine tuning, auxiliary inputs and outputs for measuring the individual responses of each filter, as well as a high-speed balanced photodetector (up to 35 GHz) with an integrated bias tee.

In the second part of the chapter, we have focused on discussing the experimental setups used for characterizing the chips, as well as the main results and conclusions. First, the optical filters were tuned and characterized individually. Due to the strong thermal crosstalk that arises from the tightly packaged layout and high number of heaters, a manual iterative process of trial-and-error was followed in order to adjust the transfer functions to the original design targets. Measured FSRs are 49 GHz for the *Input filter*, and 28 GHz for both *Filter 1* and *Filter 2*. Insertion losses for the upper and lower discriminator branches are around 13.4 and 14.5 dB, which include 3 extra dBs due to a pair of auxiliary couplers located after the *Input filter*.

Finally, a standard two-tones test was performed in order to characterize the non-linear behaviour of the FM-DD PIC. This was done at 5 different modulation frequencies (f_1 = 1, 3, 5, 7 and 9 GHz) and 3 distinct wavelengths, which corresponded with the three main points of interest of the discriminator transfer function. Due to the high RF losses (>40 dB), the powers of the measured IMD3 products were closer to the sensitivity of the RF spectrum analyzer, even when using both optical and electrical amplification. As a consequence, only a few points were found to follow the theoretical cubic dependence with input RF power. Measured SFDRs for these selected points are in the range between 67.41 and 79.22 dB.Hz$^{2/3}$, which are lower than other similar PICs published in the literature. Potential ways for improvement, such as reducing optical losses by means of spot-size converters and using a laser with higher power, have been discussed. In fact, redesigning the filters to match the ideal transfer function proposed by Wyrwas could ultimately led to high performance links with very large SFDRs, a promising alternative that would overcome the traditional limitations of current IM-DD approaches.

Publications

The work done in this chapter lead to the following patents, as well as publications in peer reviewed journals and international conferences:

1. **J. S. Fandiño**, J. D. Doménech, P. Muñoz, and J. Capmany, "Integrated InP frequency discriminator for Phase-modulated microwave photonic links,"

Opt. Express, vol. 21, pp. 3726–3736, Feb. 2013.

2. **J. S. Fandiño**, J. D. Doménech, P. Muñoz, and J. Capmany, "Design and Experimental Characterization of an InP Photonic Integrated Circuit Working as a Receiver for Frequency-Modulated Direct-Detection Microwave Photonic Links," in *Proc. of SPIE OPTO*, vol. 8627, pp. 862708–862708–8, Feb. 2013.

3. **J. S. Fandiño**, P. Muñoz, and J. Capmany, "Design of a Frequency Modulation-Direct Detection Microwave Photonic Link receiver monolithically integrated in InP generic technology," in *16th European Conference on Integrated Optics (ECIO)*, Apr. 2012.

4. **J. Sánchez Fandiño**, J. Capmany Francoy, and P. Muñoz Muñoz, "Receptor integrado de clase B para enlaces fotónicos de microondas modulados en fase," Patente T201200004, Universidad Politécnica de Valencia (Spain), 2012.

Chapter 7

Coherent microwave photonic filters

7.1 Introduction

Current forecasts for fixed and mobile network connections predict a dramatic increase in both global data traffic and number of users in the short to mid term [155]. For example, the amount of IP data served by wireless networks will increase in just a decade by a factor of more than 100, from 3 exabytes in 2010 to 500 exabytes in 2020 [156]. The actual trend towards higher data rates means that an optimum usage of the available radioelectric spectrum will become mandatory in the near future to maximize transmission capacity. Operators will be able to allocate and take advantage of all existing RF resources in real time, dynamically adjusting their networks to the users' requirements. To fulfil this vision, carrier aggregation technologies will become fundamental. These will allow several, not necessarily contiguous, frequency channels to be joined together on-demand to increase modulation bandwidth.

As a consequence, manufacturers have been faced with the increasingly difficult problem of designing tunable multi-band RF front ends, while still providing acceptable performance, compact footprint and a reduced power consumption [157]. Until now, the capability of RF front ends to switch among different bands has relied on the tunability of their integrated duplexer, which is located just before the antenna to filter and isolate both the transmitter and receiver channels. Current commercial products can accommodate several operation bands, where tunability is achieved by means of internally switched RF paths that drive different fixed frequency duplexers [158]. These are based on piezoelectric technologies, namely surface and bulk acoustic waves (SAW and BAW, respectively) RF filters [159]. However, this parallel approach will be put under significant strain as the increasing number of bands leads to higher design complexities and chip sizes.

Microwave photonics (MWP), on the other hand, has long promised with the development of fully reconfigurable, broadband RF filters. Most of the MWP filter architectures that have been experimentally demonstrated so far have made use of optical fibers and discrete component [160]. This has two important drawbacks. First, because of instability issues associated with manipulating optical fibers, slow polarization rotations and optical phase drifts due to temperature and mechanical vibrations are unavoidable. As a consequence, most research works up to now have focused on demonstrating filters operating in the incoherent regime. That is, those where the coherence time of the source is much shorter than the minimum delay time. However, more elaborate experimental setups are needed in order to implement filters with complex-valued coefficients [13], which are required for a full tunability of its transfer function. Second, and probably more important, MWP filters based on fibers and discrete optical components are both bulky and expensive.

As a result, there has been a growing interest in developing integrated MWP filters to solve the aforementioned issues. Different approaches have included exploiting stimulated Brillouin scattering in both chalcogenide (As_2S_3) [161–163] and Silicon-on-Insulator (SOI) waveguides [164]; four-wave mixing in silicon nanowires [165]; slow light concepts in photonic crystal waveguides [42]; as well as implementing coherent MWP filters by means of tunable, integrated optical filters in silicon nitride (Si_3N_4) [54, 166], indium phosphide (InP) [40, 49] and SOI [41, 167–169]. Despite the impressive results in terms of tunability and rejection levels, none of these works has yet reported on a truly integrated RF photonic filter. That is, in all cases only the filter was integrated, with all the extra required elements such as lasers, modulators and photodetectors placed off chip.

In this chapter, we continue the path towards complete miniaturization, and report on the design and experimental characterization of a fully integrated coherent MWP filter in InP. Fully integrated means that the photonic integrated circuit (PIC) contains not only the tunable filter, but it also includes sources, modulators and detectors in the same monolithic substrate. In our case, coherent MWP filtering is achieved by exploiting the well-known mapping between the optical and electrical domains that happens when a laser source is modulated with a single-sideband (SSB) scheme and sent through an optical filter [170]. To first order, the transfer function of the optical system after the SSB modulator is transferred to the end-to-end RF response of the MWP link, except for a constant amplitude and phase factor. Note that integrated optical filters work in the coherent regime, where a complete interference between delayed copies of electromagnetic fields is obtained. A a result, a complete reconfigurability of its transfer function is usually possible, thus avoiding the inconveniences of incoherent approaches. Moreover, we have already seen in the previous chapters that these tunable filters can be easily implemented using optical lattice filters, which are then manufacturable using PICs. Similar to what happened with Moore's law in the electronics industry, integrated optics could significantly reduce the footprint and cost of these systems, paving the way for their final commercialization and opening new market opportunities.

This chapter is organized as follows. First, we will succinctly describe the basic

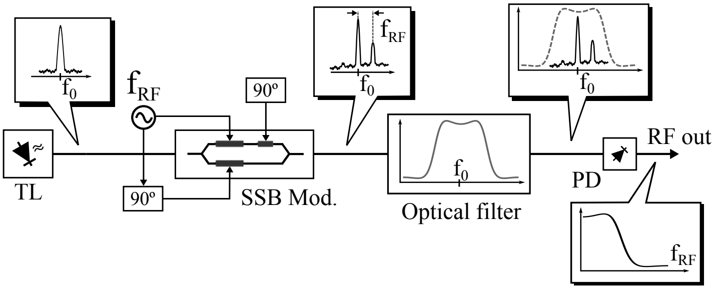

Figure 7.1: Schematic diagram of a coherent MWP filtering system. TL: Tunable laser. SSB Mod.: Single-sideband modulator. PD: Photodetector.

theoretical principles behind the concept of SSB-based coherent MWP filtering. Afterwards, we will continue to report on the design and experimental characterization of the chip. The design and layout section will explain the steps followed in the design of the most important building blocks (BB), including simulations of their expected performance. Next, details about PIC fabrication and packaging will be provided. Finally, a detailed characterization of the performance of its different components is reported, along with system level experiments. The chapter ends with some conclusions and futures lines of work.

7.2 Theoretical background

A schematic diagrams of a coherent MWP filter system is shown in Fig. 7.1. To understand how it works, lets start by assuming that a laser with an average power P_0 and center frequency f_0 is injected into a single-sideband optical modulator (SSB), which is in turn being driven by an RF tone. The tone has the following form

$$V_{\mathrm{RF}}(t) = A\cos\left(2\pi f_{\mathrm{RF}} t\right) \tag{7.1}$$

where A is the RF amplitude (in volts) and f_{RF} is the modulation frequency (in Hz).

The complex low-pass equivalent of the optical signal at the output of the modulator can be expressed, neglecting optical losses, as follows

$$\tilde{E}_{\mathrm{SSB}}(t) = \frac{\sqrt{P_0}}{2}\left[e^{j\pi A\cos\left(2\pi f_{\mathrm{RF}}t\right)/V_\pi} + je^{j\pi A\sin\left(2\pi f_{\mathrm{RF}}t\right)/V_\pi}\right] \tag{7.2}$$

Here, V_π stands for the π voltage of each phase shifter (also in volts), and P_0 represents the optical power of the input laser signal, as mentioned before.

Usually, the amplitude of the RF tone is much lower than the π voltage of the modulator, so the small-angle approximation holds. That is, $e^{jx} = (1-x^2/2)+jx$ for $x \ll 1$. For the sake of simplicity, we will further neglect the second-order powers of the input signal. After a bit of straightforward algebra, equation 7.2 can be finally expressed as

$$\tilde{E}_{\mathrm{SSB}}(t)=\frac{\sqrt{P_0}}{2}\left[(1+j)+j\frac{\pi}{V_\pi}Ae^{j2\pi f_{\mathrm{RF}}t}\right] \tag{7.3}$$

The Fourier transform of this waveform leads to

$$\tilde{E}_{\mathrm{SSB}}(f)=\frac{\sqrt{P_0}}{2}\left[(1+j)\delta(f)+j\frac{\pi}{V_\pi}A\delta(f-f_{\mathrm{RF}})\right] \tag{7.4}$$

which precisely corresponds with a single-sideband modulation. If we introduce this signal into an optical filter, then at the output we get

$$\tilde{E}_{\mathrm{out}}(f)=\frac{\sqrt{P_0}}{2}\left[(1+j)H(0)\delta(f)+j\frac{\pi}{V_\pi}AH(f_{\mathrm{RF}})\delta(f-f_{\mathrm{RF}})\right] \tag{7.5}$$

where $H(f)$ stands for the complex low-pass equivalent frequency response of the optical filter. That is, $H(0)$ means that the filter is evaluated at the operating wavelength of the laser (f_0, or λ_0 in the wavelength domain). The previous equation can be converted back to the time domain as

$$\tilde{E}_{\mathrm{out}}(t)=\frac{\sqrt{P_0}}{2}\left[(1+j)H(0)+j\frac{\pi}{V_\pi}AH(f_{\mathrm{RF}})e^{j2\pi f_{\mathrm{RF}}t}\right] \tag{7.6}$$

Finally, after detection, we get a time-varying photocurrent that is proportional to the modulus squared of $\tilde{E}_{\mathrm{out}}(t)$. Neglecting the DC terms, the RF component is given by [170]

$$i(t)\propto|H(0)||H(f_{\mathrm{RF}})|\cos\left(2\pi f_{\mathrm{RF}}t+\angle H(f_{\mathrm{RF}})-\angle H(0)\right) \tag{7.7}$$

Equation 7.7 means that, when an optical single-sideband modulation enters an optical filter and is later photodetected, the RF response of the whole system is nothing but a copy of the filter transfer function, except for a complex constant. As a consequence, a direct mapping between the optical and RF domains is obtained, excluding of course the existence of extra spurious intermodulation and harmonic distortion products, which are inherent to all MWP links. Equation 7.7 is also useful to understand other basic properties of this technique.

First, note that the optical carrier should always fall within the passband of the optical filter. Otherwise, the losses of the MWP filter would increase rapidly, as they are proportional to $|H(0)|^2$. Thus, only low-pass filters, or at least filters with a small frequency content near DC, can be implemented. This problem can nevertheless be avoided with the use of a carrier injection scheme, where two optical couplers are placed right after the tunable laser and before the photodetector. In this scheme, the optical carrier is actually eliminated on purpose by the optical filter. However, it is coupled again with the SSB signal right before photodetection, so the optical beating between the optical sideband and the carrier can still take place.

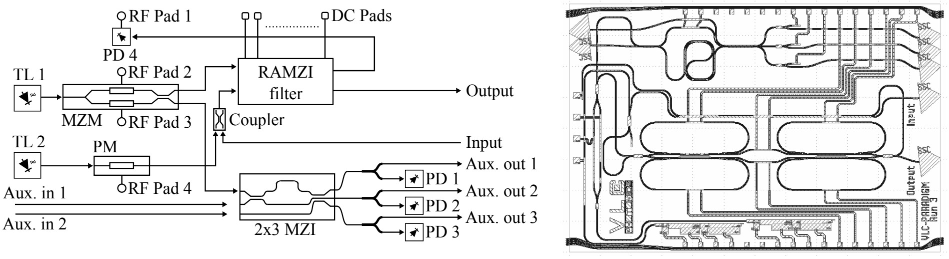

(a) (b)

Figure 7.2: (a) Block diagram of the designed InP PIC. (b) Mask layout.

Second, note that the transfer function of the RF filter can be shifted in a straightforward way. One just needs to tune either the center frequency of the laser (f_0) or the center frequency of the optical filter, and the whole frequency response of the RF filter will change accordingly. This is especially useful for example in carrier aggregation technologies, where filters need to be tuned over a wide range of frequency bands.

7.3 Design and layout

A diagram of the designed InP PIC and its different building blocks (BBs) is shown in Fig. 7.2(a). The final chip layout can be seen in Fig. 7.2(b). Note that this diagram is somewhat more complex than the basic coherent filtering scheme of Fig. 7.1. This is because the PIC was actually designed to implement not one, but up to three different MWP functionalities, depending on the configuration of its BBs: coherent MWP filtering without carrier injection, instantaneous frequency measurement (see chapter 5) and all optical single-sideband generation. As mentioned in the introduction chapter, this idea is very similar to that of a reconfigurable microwave photonics processor. However, we will limit ourselves here to the first of these applications.

For the case of coherent filtering, the diagram can be briefly explained as follows. First, light coming out of a tunable laser (TL 1) based on distributed Bragg reflectors (DBR) is injected into a dual-drive modulator (MZM), which is made up of a symmetric Mach-Zehnder interferometer with a couple of electro-optic phase shifters, one on each arm. By introducing two RF signals with a 90° phase shift between them, and later tuning the optical bias point by applying a reverse voltage in one of the phase shifters, an SSB modulation can be generated. This signal is then sent through a reconfigurable optical filter. As in previous chapters, the filter is based on a RAMZI architecture tunable via thermo-optic heaters, where the optical couplers are implemented with tapered 2x2 MMIs. Finally, the signal at one of the two outputs of the filter is routed to an on-chip photodetector (PD 4), where the optical to electrical conversion takes place. The other output is routed as an auxiliary waveguide to a spot-size converter located on one of the chip facets

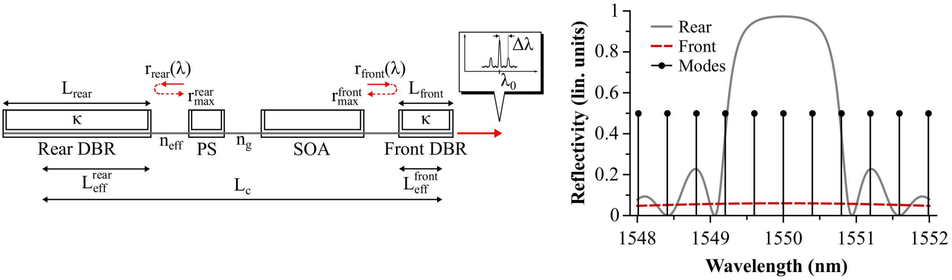

(a) (b)

Figure 7.3: (a) Block diagram of the designed DBR laser. (b) Simulated reflection spectra for both the rear and front DBR sections. Cavity modes are also shown.

(*Output*). There also exists an extra auxiliary waveguide (*Input*) that is routed to the other free input of the RAMZI filter. Together, these auxiliary waveguides provide a mean of characterizing the filter response with external equipment. The design of the most important BBs (i.e. DBR lasers, filter and modulator) are briefly described below.

7.3.1 Tunable lasers

The InP platform where the chip was manufactured, which is described in more detail in one of the next subsections, did not provide at the time of design a fully operational laser as an independent BB. However, it offered all the BBs required to build a DBR laser. That is: tunable DBR mirrors, semiconductor optical amplifiers (SOA) and current-injection phase shifters (PS). The DBR mirrors provide feedback for the laser cavity, which is formed by a gain section (SOA) and a phase-shifting element to provide fine wavelength control. A diagram of such a device is shown in Fig. 7.3(a), where all the parameters of interest have been highlighted for clarity.

The length (L) of each DBR mirror that creates the laser cavity is an important design parameter. Together with the grating coupling strength (κ, in cm^{-1}), it determines the maximum reflectivity (r_{max}, in linear units), power reflection spectra ($r(\lambda)$, in linear units) and effective length (L_{eff}) of the DBR, which are given by [171]

$$r_{\text{max}} = \tanh^2(\kappa L) \tag{7.8}$$

$$r(\lambda) = \left|\frac{\kappa \sinh(\epsilon L)}{\xi \sinh(\epsilon L) + j\epsilon \cosh(\epsilon L)}\right|^2 \tag{7.9}$$

$$L_{\text{eff}} = \frac{L\sqrt{r_{\text{max}}}}{2\,\text{arctanh}\left(\sqrt{r_{\text{max}}}\right)} \tag{7.10}$$

$\mathrm{L}_{\mathrm{front}}$	50 μm	$\mathrm{L}_{\mathrm{eff}}^{\mathrm{front}}$	24.49 μm	$r_{\mathrm{max}}^{\mathrm{front}}$	6 %	$\mathrm{n}_{\mathrm{eff}}$	3.265	L_{c}	808.15 μm
$\mathrm{L}_{\mathrm{rear}}$	500 μm	$\mathrm{L}_{\mathrm{eff}}^{\mathrm{rear}}$	98.66 μm	$r_{\mathrm{max}}^{\mathrm{rear}}$	97.34 %	n_{g}	3.739	$\Delta\lambda$	0.398 nm

Table 7.1: DBR design parameters.

In equation 7.9, ϵ and ξ are defined as

$$\epsilon = \sqrt{\kappa^2 - \xi^2} \tag{7.11}$$

$$\xi = 2\pi n_{\mathrm{eff}} \left(\frac{1}{\lambda} - \frac{1}{\lambda_0} \right) \tag{7.12}$$

where n_{eff} is the effective index of the optical waveguides, and λ_0 is the Bragg wavelength. That is, the wavelength at which $r(\lambda)$ is maximum.

The final values for the designed DBR lasers and some important technological parameters are given in Table 7.1. These include the length of the front and rear DBR sections (L_{front} and L_{rear}); their effective length ($L_{\mathrm{eff}}^{\mathrm{front}}$ and $L_{\mathrm{eff}}^{\mathrm{rear}}$) and maximum reflectivities ($r_{\mathrm{max}}^{\mathrm{front}}$ and $r_{\mathrm{max}}^{\mathrm{rear}}$); the total cavity length including the gain and phase shifting sections (L_{c}); the effective and group indices of the waveguides (n_{eff} and n_{g}); as well as the estimated wavelength spacing between modes ($\Delta\lambda$). Using the values from Table 7.1 and equations 7.8 to 7.12, the reflection spectra of the two gratings can also be plotted. They are shown in Fig. 7.3(b) together with a symbolic representation of the cavity modes, where it can be seen that up to three of them fit within the passband of the narrowest grating (rear DBR).

7.3.2 RAMZI filter

This component is crucial for the correct operation of the whole chip, as the ability to reconfigure its transfer function is key for implementing a tunable coherent MWP filter. It was designed as a fourth order Chebyshev type II filter, thus ensuring a flat passband and a sharper roll-off at the expense of ripples in the stopband. It features a stopband normalized cut-off frequency of 0.65 at 35 dB of attenuation, and the length of its rings was designed to target a Free Spectral Range (FSR) of 20 GHz. This filter is exactly the same one that was analysed in section 4 of chapter 2, so both the filter coefficients and the synthesized coupling constants and optical phase shifts are those of Table 2.2. Its ideal magnitude and phase responses, as well as the simulated ones considering average propagation losses of 5.5 dB/cm, are shown in Figs.7.4 (a) and 7.4(b). This time, however, the frequency axis has been normalized against the target FSR of 20 GHz. Since it is a 4th order filter, 4 ring resonators are coupled to the arms of the interferometer through tapered 2x2 MMIs. Couplers' dimensions together with target and simulated coupling constants are summarized in Table 7.2 Thermo-optic heaters with a 200 μm length were also added to ensure that the filter could work after introduction of phase errors during fabrication.

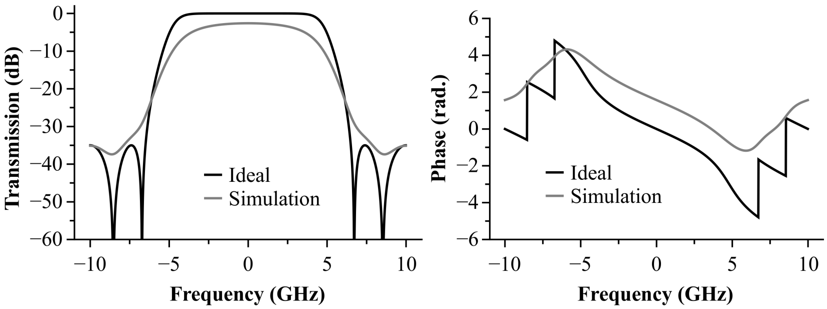

(a)

(b)

Figure 7.4: (a) Magnitude response (in dB) of the ideal (solid black line) and lossy (solid grey line) RAMZI filter. (b) Idem for the phase response.

Width	d_1^i, d_2^i	ΔW	L’	Target $\kappa_{cross}/\kappa_{bar}$	Sim. $\kappa_{cross}/\kappa_{bar}$
10.5	2.63,2.63	0	461.9	50/50	47.9/48
12.0	4.0,4.0	-0.921	462.8	94/06	92.2/5.6

Table 7.2: Dimensions (in μm) and BPM simulation results of the RAMZI filter couplers.

7.3.3 Dual-drive MZM

A balanced, dual-drive Mach-Zehnder modulator was placed right after the optical source (TL 1). It consists of a symmetric interferometric structure, where two optical paths are split with a 1x2 MMI and later recombined at the output with a 2x2 MMI coupler. A pair of electro-optic phase modulators (680 μm long) are located on both arms, which were provided as BBs by the foundry. According to the design manual, their π voltage should be in the order of 3 V.

Note that the MZM was placed as close as possible to chip facet where the RF pads are located (see Fig. 7.5). This minimizes extra stray capacitance added by the metal routing, thus maximizing modulation speed. Also, special care was put into ensuring minimum optical imbalance in the MZM, by introducing for example a dummy crossing between RF tracks and optical waveguides.

7.4 Experimental results

7.4.1 Fabrication and packaging

The designed PIC was manufactured within the PARADIGM EU FP7 project (FP7-ICT-2009-5/257210). The PARADIGM initiative aimed at facilitating access to state-of-the-art InP foundries following a generic approach. That is, by providing external users with a set of predefined BBs that are not trivial to de-

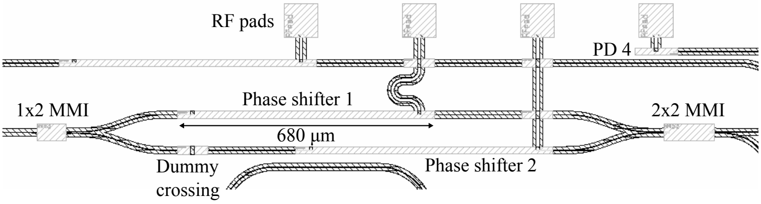

Figure 7.5: Mask layout of the designed dual-drive MZM modulator.

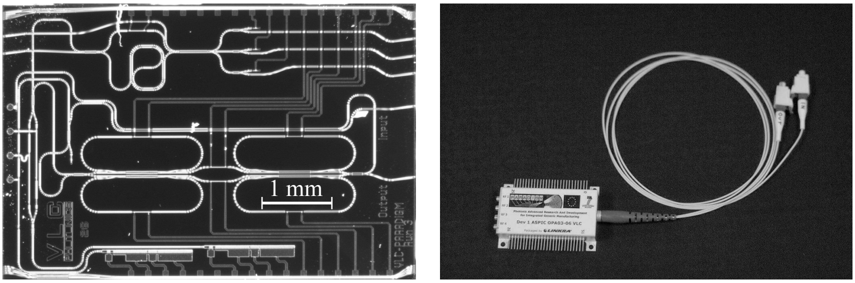

(a) (b)

Figure 7.6: (a) Picture of a fabricated die. (b) Packaged chip.

sign, and then sharing the cost of PIC fabrication via multi-project wafer runs (MPW). In this case, the chip was manufactured in a non-insulating InP platform offered by the private company Oclaro (United Kingdom). Deeply etched waveguides are made of an n-doped InP substrate over which an InGaAsP multi-quantum well structure is grown, forming the waveguide core. Afterwards, the core region is covered with a layer of p-doped crystalline InP. Finally, the whole structure is etched by about 3.6 μm from the top of the p-doped region. The deep etch results in a high mode confinement, which allows for a tight bending radius of 150 μm. In this case, a waveguide width of 1.5 μm was chosen. According to the design manual, it should experience propagation losses of about 5.5 dB/cm. Angled spot-size converters with both vertical and lateral tapers were also provided, featuring estimated coupling losses below 1 dB.

PICs with many DC and RF pads are very complex to measure. They require the use of multi-contact DC and RF probes, which are bulky and do not always fit easily together in the same setup. Furthermore, a wrong movement or external vibration can cause severe damage. It is for those reasons that the chip was sent to be packaged right after fabrication, so its characterization would become easier. This service was actually offered by some members of the PARADIGM consortium, among which the italian company Linkra was chosen. In fact, the whole layout was designed in such way that it would adhere to a standard template provided by this company. In the template, the location and number of optical inputs/outputs, as well as DC and RF pads, are predefined (see Fig. 7.6(a)). A maximum of 48 DC

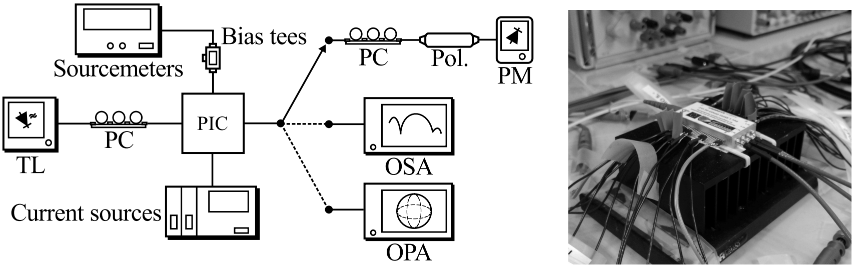

(a) (b)

Figure 7.7: (a) Diagram of the experimental setup employed for BB characterization. TL: Tunable laser. PC: Polarization controller. OPA: Optical polarization analyzer. Pol: In-line fiber polarizer. PM: Power meter. OC: Optical coupler. OSA: Optical spectrum analyzer. (b) Picture of the package during characterization.

pads can be employed, which are all located on the upper/lower facets of the die. Additionally, up to 4 RF pads are available to the designer, all placed close to the left chip facet. As for the optical part, up to two standard single-mode fibers can be accommodated by the metallic mount, and coupled to a pair of spot-size converters on the right chip facet. Figures 7.6(a) and 7.6(b) show a picture of a fabricated die (6x4 mm^2) and a packaged PIC, respectively. Inside the metallic enclosure, the RF pads of both the MZM and the photodetectors (PDs) are wire-bonded to a ceramic substrate that routes the RF signals to external GPPO connectors (DC to 65 GHz). The DC pads are also wire-bonded to metal tracks on a different substrate, which are then connected to a set of equally spaced pins in the external mount. A thermistor and a Peltier cell are located right below the chip to provide accurate temperature control.

7.4.2 Experimental setup

The experimental setup that was arranged for characterization of the chip BBs is shown in Fig. 7.7(a). The chip package was first covered with a thin layer of thermally conductive paste, and mechanically attached to a heat sink with a couple of soft rubber bands. Since the pitch between DC pins was not standard (1.5 mm), and thus not compatible with most of the laser diode mounts available in the market (2.54 mm), a custom electronics interface had to be built. This included multiple 3-pin and 2-pin connectors with the right spacing soldered to banana cables. Heat shrinking foams were also added between neighbouring connectors to prevent electrical short circuits. A close-up picture of the package once it was wired and placed on top of the heat sink can be seen in Fig. 7.7(b). All the cables corresponding to the thermo-optic heaters of the RAMZI filter were connected to a set of laser diode controllers (Thorlabs LDC-8010) operating as constant current sources. The same was done for the four sections of the TL 1 and TL 2 lasers.

The GPPO connectors corresponding to the RF pads of both branches of the MZM (RF pad 2 and 3) and the RF photodetector (RF pad 4) were interfaced with coaxial cables of the same type, and then connected to three bias tees (SHF Communications, SHF-BT-45-D, 20 kHz-45 GHz). These allowed the electro-optic modulators and depletion regions to be reversed bias with a constant voltage, which was provided by a set of voltage sources (Promax FAC-662B) and sourcemeters (Keithley 2401). Finally, the internal thermistor and Peltier cell were driven by an external temperature control module (Thorlabs TED 8020) to ensure constant room temperature operation (25°).

As for the optical part, recall that only two external fibers were available (*Input* and *Output* in Fig. 7.2(a)). The *Input* fiber was connected to a tunable laser followed by a manual polarization controller. The *Output* fiber was connected to up to three different sets of equipment, depending on the experiment: a manual polarization controller followed by an in-line fiber polarizer and a handheld power meter, for both polarization alignment and measuring the output power of the lasers; a polarization analyzer (Agilent 8509C), for observing polarization rotation inside the chip waveguides; and an optical spectrum analyzer (OSA, Advantest Q8384). The OSA worked in combination with the laser to measure the response of the RAMZI filter, as well as independently to capture laser and modulation spectra. The experiments carried out so far have included a characterization of the different BBs, as well as a system level evaluation of the coherent MWP filtering functionality. They are described in more detail in the following subsections.

7.4.3 Tunable lasers

As a first step, the SOA sections of the two TLs were pumped with two external current sources and their corresponding emission spectra at the *Output* fiber were collected with an OSA. Figures 7.8(a) and 7.8(b) show the results when pumping both lasers with a current of 60 mA, well above the measured threshold ($\simeq$15 mA). TL 1 features a clean spectrum, with one main mode plus a few side modes. The measured side mode suppression ratio (SMSR) is more than 40 dB, and the mode spacing is 0.399 nm, which agrees very well with the calculated value of Table 7.1. The measured power at the output is higher than -8 dBm. This power, however, is measured after propagation through the MZM and the RAMZI filter. Thus, the real output power is probably a few dBs higher, although giving an exact number is not possible since the on-chip insertion losses of the filer and the MZM are unknown.

The spectrum of the second laser (TL 2) points to the existence of spurious reflections in the signal path, which cause the onset of extra side modes and a significant overall degradation (Fig.7.8(b)). From the measured mode spacing (0.0378 nm), the cavity must be about 8.58 mm long. This value matches with the presence of a terminating photodiode after a 3 dB coupler that is located in the path of the laser signal (see Fig. 7.8(c)). The termination photodiode is thus not sufficiently attenuating the signal, which is being reflected back and affecting the laser resonance at high output powers.

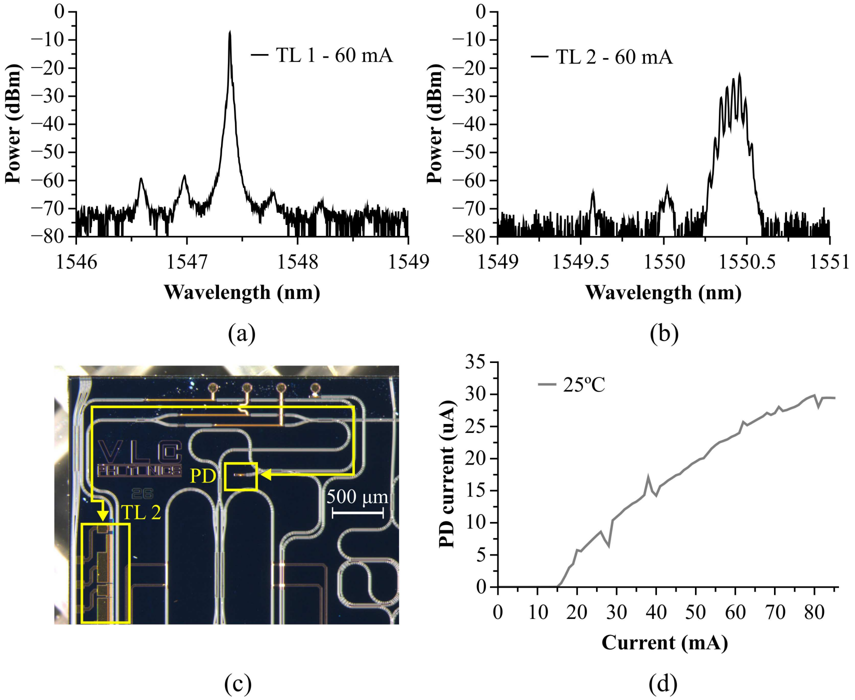

Figure 7.8: (a) and (b) CW spectra of both TL 1 and TL 2. (c) Cavity formed by the output of TL 2 and a termination photodiode, which creates spurious side modes. (d) PI curve of TL 1.

To measure the PI curve of TL 1, we exploited the fact that the power emitted by the laser is captured by the tree DC photodetectors placed after the 2x3 MZI (PD 1, PD 2 and PD 3 in Fig. 7.2(a)). Thus, summing the three DC photocurrents should give a signal which is proportional to the total emitted power. Even though this current can not be related to the real output power, it is useful in order to characterize the laser threshold and saturation currents. Figure 7.8(d) shows this curve for a temperature of 25°, when TL 1 is biased from 0 to 85 mA. The threshold current at this temperature is approximately 15 mA, and the saturation current is around 80 mA. The discontinuities in the PI curve are attributed to mode hopping during the bias sweep, as the wavelength of the laser changes for different currents injected in the SOA section.

In order to evaluate wavelength tunability, we recorded multiple spectra at the *Output* fiber for different currents injected both in the PS and rear DBR sections of the lasers, respectively. This experiment was done only with TL 1, since the presence of extra side modes in TL 2 due to spurious reflections in the terminating PD prevented its correct operation . Figures 7.9(a) and 7.9(b) show the results. As it can be seen, the center wavelength can be tuned (blue shifted) by more than

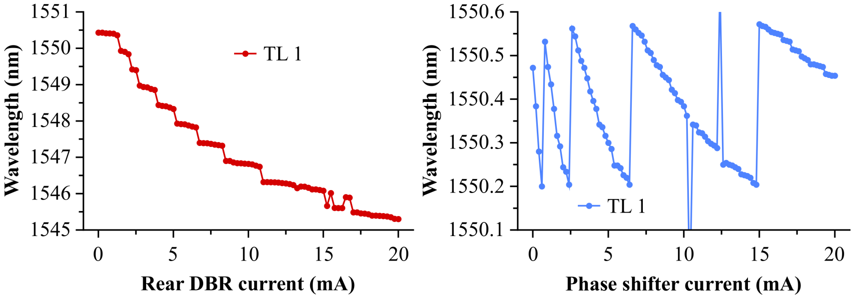

(a) (b)

Figure 7.9: (a) Wavelength shift versus current when pumping the rear DBR section of TL 1. (b) Idem when pumping the intra-cavity phase shifter (PS).

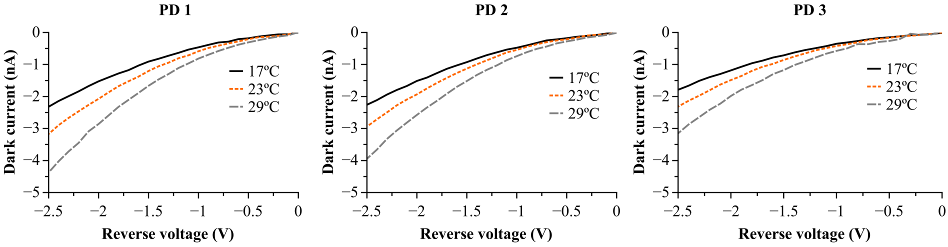

(a) (b) (c)

Figure 7.10: (a) to (c) Dark currents of PD 1 to PD 3, respectively, for different reverse voltages and operation temperatures.

5 nm using the rear DBR section, while the PS section allows for a full fine control of the mode within a mode spacing span ($\simeq$0.4 nm). These values were more than enough for achieving a continuous tunability of the MWP filter over its full FSR (20 GHz $\simeq$ 0.16 nm), so a continuous wavelength tuning mechanism to prevent mode hopping was not implemented.

7.4.4 Photodiodes

The dark currents of the photodiodes were characterized with a sourcemeter (Keithley 2401), which can measure the current flowing through the p-n junction while applying a fixed reverse voltage. Figures 7.10(a) to 7.10(c) shows measured dark currents for the three on-chip DC photodetectors (PD1, PD2 and PD3), as a function of reverse voltage and for different operation temperatures. Typical values are between 1 and 3 nA for a reverse voltage of -2 V at 25°C.

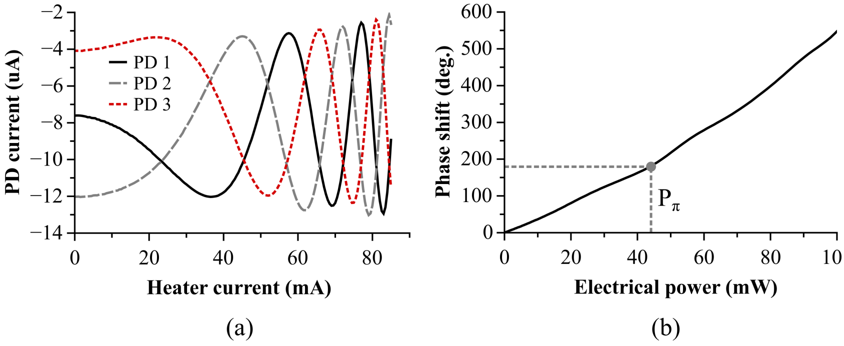

(a) (b)

Figure 7.11: (a) Measured currents at the output of the three DC PDs when the current injected into the heater of the 2x3 MZI was varied between 0 and 85 mA. (b) Calculated phase shift versus electrical power. P_π is also shown.

Id. number	1	2	3	4	5	6	7
Resistance (Ω)	25.5	28.5	28.4	18.4	23.0	26.1	25.9

Table 7.3: Measured resistance of all the on-chip thermo-optic heaters.

7.4.5 Thermo-optic heaters

Multiple thermo-optic heaters were placed all over the chip to compensate for phase errors in the RAMZI filter response after fabrication, as it has already been explained in previous chapters. All of them have a length of 200 μm, which according to the design manual corresponds with a resistance of about 38 Ω (±10%). Their actual resistances were measured with a manual multimeter, and the results are shown in Table 7.3.

As it can be seen in Fig. 7.2(a), the chip includes a 2x3 MZI. The purpose of this interferometer is to work as a tunable filter with complementary outputs, so as to implement an instantaneous frequency measurement system similar to that of chapter 5. However, one can also think of a 2x3 MZI as a phase diversity receiver for differential phase-modulated digital signals [172]. As a consequence, it is possible to extract the phase change versus electrical power introduced by a thermo-optic heater located in one of it arms by just measuring the variations in output power at its three outputs. The process is identical to that described in [172].

In this case, it was done by first pumping TL 1 with 60 mA, and then measuring the photocurrents in the three DC PDs located at the output of the 2x3 MZI (PD 1, PD 2 and PD 3) for different currents injected through the heater (Fig. 7.11(a)). After some post-processing, and knowing that the measured resistance of the employed heater is 18.4 Ω, the optical phase change was versus electrical power can be computed. It is shown in Fig. 7.11(b). The measured P_π, which is the electrical power required to introduce a 180° optical phase shift, is around 43.8 mW.

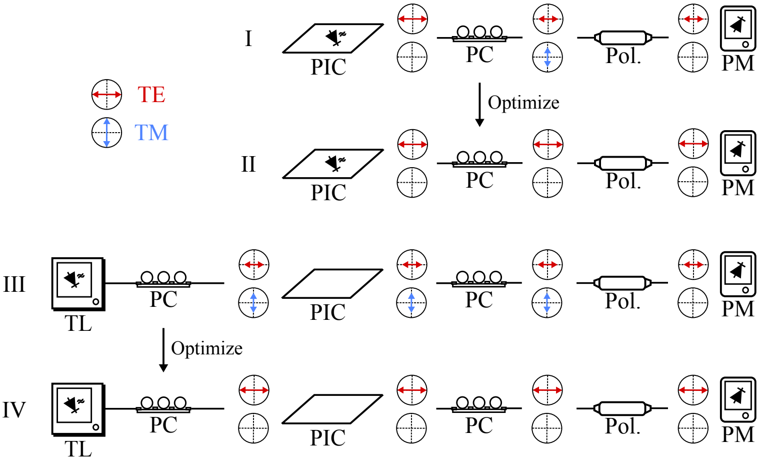

Figure 7.12: Polarization alignment procedure employed to characterize the RAMZI filter.

7.4.6 RAMZI filter and polarization rotation issues

In order to characterize the RAMZI filter of the packaged chip, the auxiliary *Input* and *Output* fibers were employed. The problem here is that the fibers of the package provided by Linkra are not polarization maintaining. Thus, when light from an external source is injected into the chip, it is not generally possible to prevent the excitation of both TE and TM modes in the deeply etched waveguides to which those fibers are coupled. This is of high concern, as the whole chip was designed for TE polarization, and care must be taken so that a random mix of polarizations is not propagating within the PIC.

To solve the aforementioned problem, a polarization alignment procedure was devised. It requires a manual polarization controller, an in-fiber polarizer and a power meter to be connected at the PIC *Output* fiber; and a tunable laser and another manual polarization controller to be connected at the *Input* one, as shown in Fig. 7.12. This procedure, which will be described shortly, ensures that only TE is excited at the auxiliary *Input* waveguide. It is based on two key assumptions. First, on-chip lasers only emit TE polarized light. Second, integrated waveguides preserve the state of polarization as the light propagates within the PIC. If that is the case, then we might proceed as follows. In step I, an on-chip laser (TL 1 in this case) is switched on. If the two previous assumptions are true, then we know that the polarization coming out of the PIC is horizontally polarized (TE). However, the optical fiber connected to the auxiliary *Output* waveguide will randomly rotate this state of polarization, so that an unknown mixture of both TE and TM will be finally injected into the in-fiber polarizer. In step II, we proceed to adjust the manual polarization controller at the output, until a maximum power level is measured in the power meter. At this point, it is ensured that the TE component of the light coming out of the chip is aligned with the transmission axis of the in-

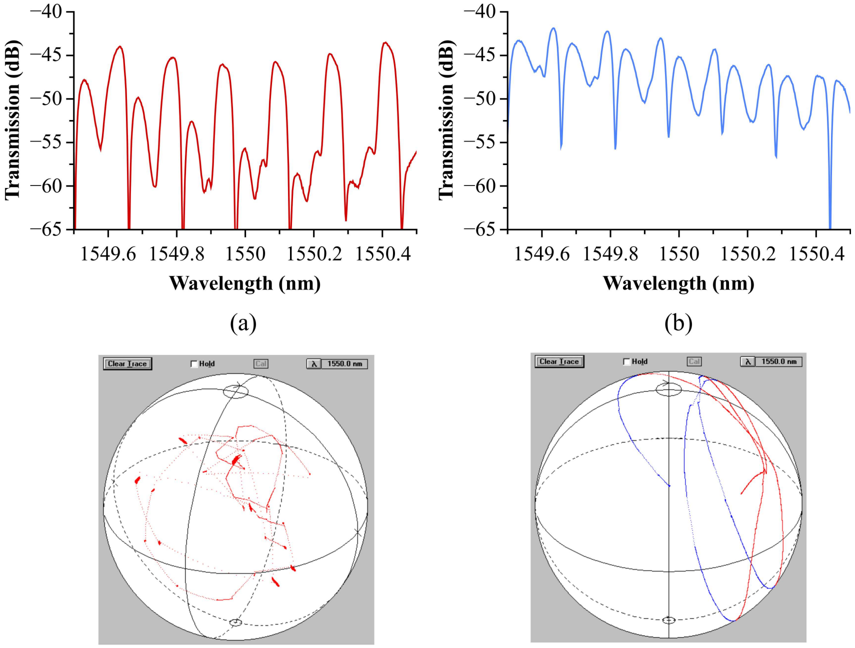

(a)

(b)

(c)

(d)

Figure 7.13: (a) and (b) Filter transmission spectra for two random input polarizations. (c) Measured state of polarization at the *Output* fiber for different currents pumped into the rear DBR section of TL 1. (d) Idem for one of the thermo-optic heaters of the RAMZI filter, with TL 1 kept at a fixed wavelength.

fiber polarizer. If there were any TM power it would be immediately eliminated. This process is equivalent to having a free-space polarizer coupled to the output facet and aligned with the horizontal axis (TE) of the chip, as in Fig. 7.14(a).

In step III, we switch off the on-chip laser and switch on instead an external tunable laser source. Again, as the single-mode fibers that connect the external laser with the PIC scramble the polarization, we do not know how much power is being coupled to the TE and TM modes of the integrated *Input* waveguide. However, we know that the PIC preserves polarization. As a consequence, any power coupled to the TE (TM) mode at the *Input* waveguide will also appear as TE (TM) at the chip *Output* waveguide. Besides, we already adjusted the output polarization controller in steps I and II. This means that any TM component at the chip output will be blocked by the in-fiber polarizer, and only the TE component, for which the chip was designed, will be measured. We only need now to maximize power by using the input polarization controller, which is finally done in step IV. Once the power is maximized, we know that only TE is being excited.

Note that, once the above procedure is completed, changing the input polarization should only change the amplitude of the measured transfer function (the amount of power coupled to the TE mode), but not its shape. However, this did not happen during the measurements. Figures 7.13(a) and 7.13(b) show a couple of measured transmission spectra when changing the input polarization after the alignment procedure. They are completely different, which pointed out to the fact that polarization was actually rotating inside the chip. In order to check this hypothesis, we switched on the TL 1 laser and measured the polarization state of light at the *Output* fiber using an optical polarization analyzer (Agilent 8509C). If there were no polarization rotation, changing the wavelength of the laser using either the PS or the rear DBR section should induce a change of output power, as each wavelength is affected differently by the transfer function of the RAMZI filter. However, the output polarization should remain constant. Figure 7.13(c) shows that the polarization is changing when a current between 0 and 5 mA is pumped into the rear DBR section, which confirms the earlier observations. A similar reasoning goes for the thermo-optic heaters of the RAMZI filter. If there were no polarization rotation, changing the relative optical phase shifts would change the transfer function of the filter. If the laser is now being kept at a fixed wavelength, we should only observe a change in output power, but polarization should remain constant. Figure 7.13(d) shows the measured polarization change when one of the filter thermo-optic heaters was pumped with a current between 0 and 80 mA, with TL 1 now being kept at a constant wavelength. It confirms that both polarizations are actually propagating inside the filter, as the polarization completely rotates over the Poincaré sphere.

We further experimentally verified this hypothesis using one of the non-packaged dies delivered by the foundry. A bare chip was placed in a free-space characterization setup, where free space polarizers can be employed to selectively filter the input and output polarizations, as shown schematically in Fig. 7.14(a). In this case, we used a broadband ASE source that was first polarization filtered and then coupled into the auxiliary input 1, which is routed to the input of the 2x3 MZI as shown in Fig. 7.2(a). The light at the auxiliary output 3 was collected and free-space polarization filtered, and then fed into an OSA. A picture of this setup can be seen in Fig. 7.14(b), while results are shown in Figs. 7.14(c) and 7.14(d). The former shows the transfer function of the 2x3 MZI when TE is excited at the input, but only TE (or TM) is measured at the output. The latter is the same, but when TM is excited. As it can be seen, there exists a significant polarization crosstalk (from -10 to -15 dB), which concludes that polarization rotation is happening inside the chip, presumably at the bends.

Polarization rotation is a well-known effect in integrated optical waveguides [72, 73], which can be described as follows. In straight sections, single-mode waveguides normally support both quasi-TE and quasi-TM modes, whose horizontal/vertical electric field components are much greater than their vertical/horizontal ones, respectively. That is, $\mathrm{E}_x^{\mathrm{TE}}/\mathrm{E}_y^{\mathrm{TE}} \gg 1$ and $\mathrm{E}_y^{\mathrm{TM}}/\mathrm{E}_x^{\mathrm{TM}} \gg 1$. However, if one solves for the modes of the same cross-section inside a tight bend, it will observe that the aforementioned condition does not longer hold as the bending radius gets smaller. The modes start to get hybridized, and the negligible field components ($\mathrm{E}_y^{\mathrm{TE}}$, $\mathrm{E}_x^{\mathrm{TM}}$) become stronger relative to the dominating ones ($\mathrm{E}_x^{\mathrm{TE}}$, $\mathrm{E}_y^{\mathrm{TM}}$).

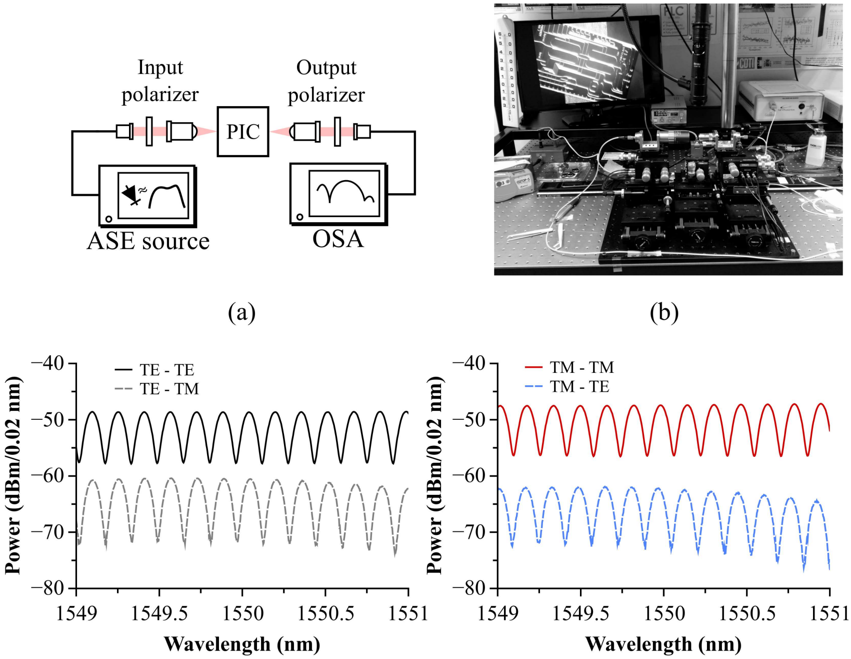

(a) (b)

(c) (d)

Figure 7.14: (a) and (b) Schematic diagram and picture, respectively, of the free-space setup used to measure polarization rotation inside the 2x3 MZI. (c) Transmission spectra for both output polarizations (TE and TM) when only TE is excited at the input. (d) Idem for TM excitation.

Unfortunately, mode hybridization can get significantly enhanced in waveguide cross-sections that are not symmetrical in the vertical direction [72]. Even though this asymmetry might be already present due to the way waveguides are defined in a specific photonic platform, it will be nevertheless produced naturally during lithography and etching, as real manufactured waveguides always feature slanted sidewalls with a small angle (θ). As an example, the cross-section of the waveguides in the Oclaro platform is schematically shown in Fig. 7.15(a), which was described in an earlier paragraph. In this case, note that the waveguide is intrinsically asymmetric even without considering slanted walls, since the refractive indices of both the n-doped and p-doped InP regions are slightly different.

Polarization rotation is known to occur mainly at straight/bend interfaces, as shown in Fig. 7.15(b). Here, we have assumed a simple case for illustration purposes, where a couple of perpendicular straight waveguides are connected with a 90° bend. If a pure TE mode is launched at the input straight section, mode hybridization will excite both TE and TM modes in the bent waveguide. Neglecting radiation losses and higher-order modes, we can understand this situation as if there were an optical coupler between orthogonal polarizations, where the

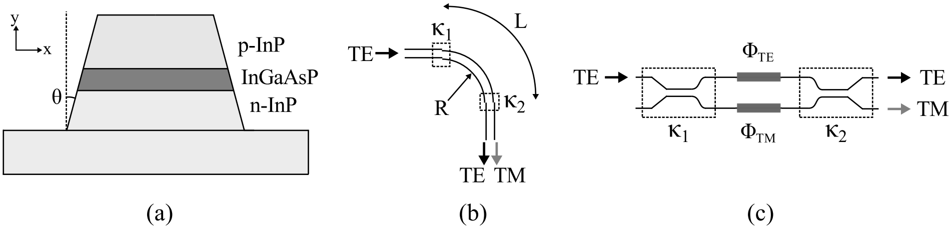

Figure 7.15: (a) Cross-section of the deeply etched waveguides in the Oclaro platform. (b) and (c) Polarization rotation in a 90° bend, which can be modelled as a symmetric MZI.

coupling constant (κ_1) specifies how much of the input power of the straight TE mode is coupled to the TM mode of the bent section, while $1 - \kappa_1$ is the amount of power coupled to its corresponding TE mode. Afterwards, each polarization will travel inside the bend with different effective indices, which will yield different relative phase shifts (ϕ_{TE} and ϕ_{TM}) before the output interface. Here, the TE and TM modes of the straight and bent sections will exchange power again (κ_2). As illustrated in Fig. 7.15(c), the whole process can be viewed as an MZI, whose two input/output ports represent the orthogonal modes before and after the bend, respectively. The input/output couplers, parametrized by κ_1 and κ_2, model the inter-modal coupling at the straight/bent interfaces, while ϕ_{TE} and ϕ_{TM} represent the different optical phase shifts seen by each orthogonal polarization due to their different effective indices. Depending on the radius (R) and arc length (L) of the bend, a different amount of polarization crosstalk will be observed at the output waveguide, which will also change with operation wavelength.

Numerical simulations performed for the Oclaro cross-section of Fig. 7.15(a) are shown in Fig. 7.16. Figures 7.16(a) to 7.16(c) show the expected TE and TM powers at the output of a bend with a radius (R) of 150 μm as a function of its arc length (L), for three different values of θ (0°, 5° and 10°). Note the periodic behaviour of the response, just like what would be expected for an MZI. Besides, the critical dependence of polarization crosstalk (TE/TM, in dB) with the sidewall angle is clearly observed, as it increases from a maximum of -60 dB to around -20 dB when the angle is only increased by just 5°. Figure 7.16(d) summarizes this critical dependence. It plots the expected polarization crosstalk as a function of θ, for a 90° bend with the same 150 μm radius.

Finally, it must be noted that polarization rotation is a coherent process. Thus, even if low values of crosstalk are observed at a single bend, rotation might build up as the light propagates within a large structure, causing significant crosstalk at the output. Optical cavities, such as ring resonators, are also known to enhance this effect, as the light effectively sees a longer optical path near the resonance [72]. To sum up, we believe that the significant polarization rotation observed in the PIC is due to a combination of two effects. First, a higher than expected value of the sidewall angle in the fabricated waveguides. Second, a coherent enhancement

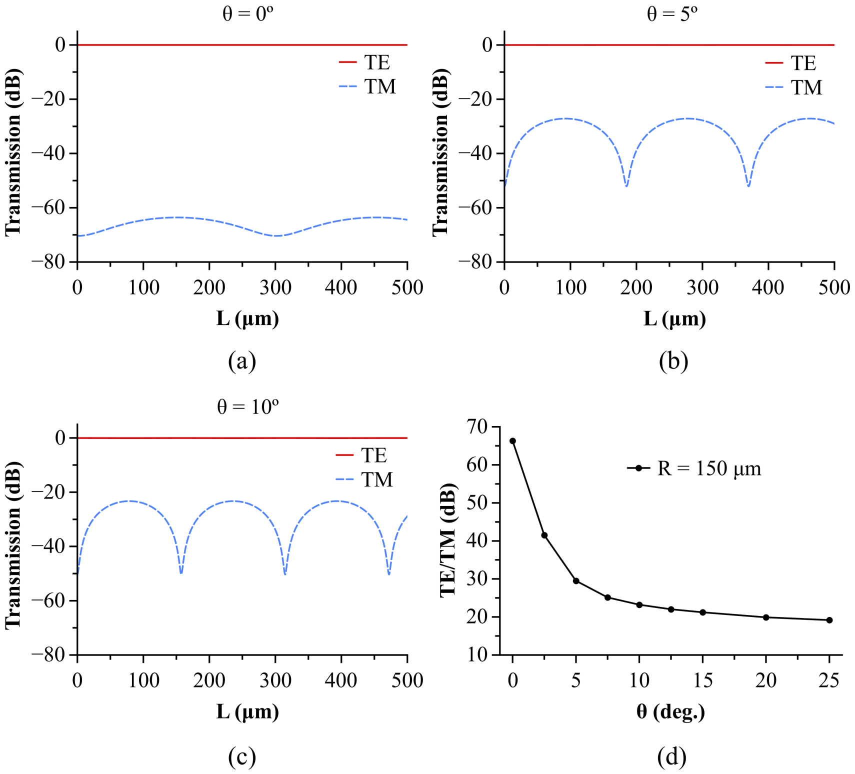

(a) (b)

(c) (d)

Figure 7.16: (a) to (c) Evolution of the TE and TM powers at the output of a bend with R =150 μm, as a function of the arc length (L), for different values of θ. (d) Polarization crosstalk (TE/TM, in dB) for a 90° bend with R =150 μm.

of the polarization rotation effect due to the resonant nature of the rings within the RAMZI filter. Future designers for this technology should be aware of such issue, and should draw waveguides with a bigger bending radius so as to minimize this effect as much as possible.

7.4.7 Dual-drive MZM

The main purpose of the dual-drive MZM is to generate an SSB modulation. This requires the RF signals driving both arms to be 90° out of phase, while the modulator should be biased at the quadrature point. Unfortunately, the bias voltage that needs to be applied to the modulator for it to be at quadrature is generally unknown. The usual procedure is to connect the two RF inputs to a broadband 90° RF hybrid, and then to slowly tune the bias point while observing the output spectrum in an OSA for a fixed modulation frequency. A bias voltage is finally chosen for which the ratio between the powers of the lower and upper

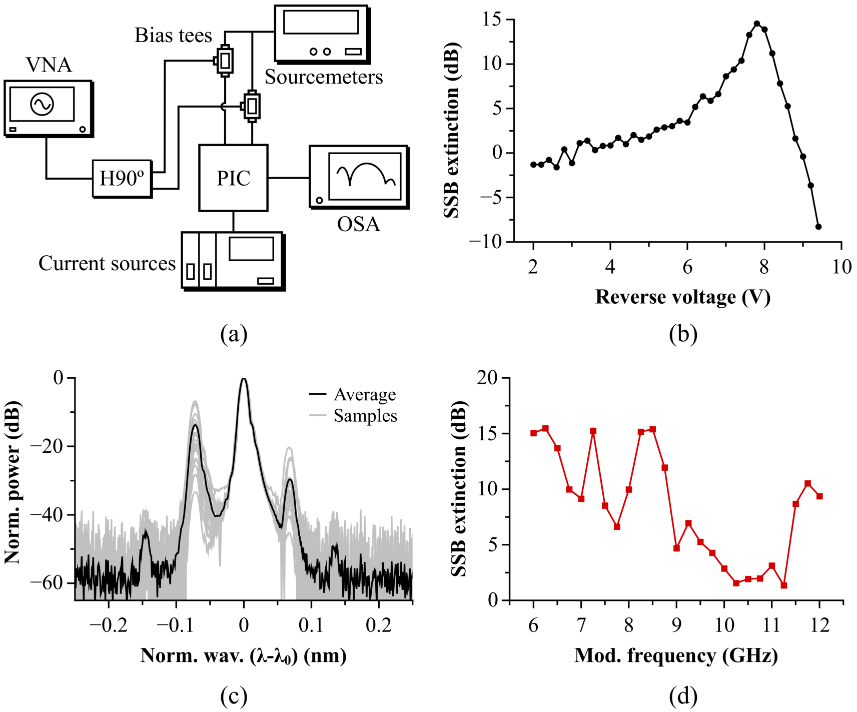

(a) (b)

(c) (d)

Figure 7.17: (a) Experimental setup employed for characterizing the dual-drive MZM. VNA: Vector network analyzer. H90°: 90° RF hybrid. OSA: Optical spectrum analyzer. (b) Median SSB extinction as a function of the bias voltage. (c) Overlapped spectra for a bias voltage of -8 V (optimum). (d) Dependence of the SSB extinction with modulation frequency for the same bias point.

sidebands is maximum (SSB extinction, in dB).

In our case, there exists an extra difficulty: the optical spectrum measured at the output of the chip is not that of the modulator itself, but that of the modulated signal after passing through the RAMZI filter. As a consequence, the measured ratio does not match with the real ratio at the output of the modulator. One possible solution would be to first measure the response of the RAMZI filter, and then compensate for it. However, due to polarization rotation in the waveguide bends, the transmission response of the filter when measured externally does not match the internal response as seen by the laser signal. Thus, this approach is not possible.

A feasible approach is that shown in Fig. 7.17(a). It can be described as follows. A microwave vector network analyzer (VNA, Agilent PNA-X, N5245A, 10 MHz-50 GHz) first generates an RF tone with constant amplitude and frequency. This tone is injected into a 90° RF hybrid (Marki microwave, QH0R714, 0.7-14.5 GHz), whose two outputs are then connected to a couple of broadband bias tees (SHF Communications, SHF-BT-45-D, 20 kHz-45 GHz). In turn, they are used to drive the two ports of the dual-drive MZM (RF pads 2 and 3, in Fig. 7.2(a)). Now, for each reverse bias, we apply a different set of independent, uniformly distributed random currents in the thermo-optic heaters of the RAMZI filter, and finally capture the modulation spectrum exiting through the *Output* fiber. The power ratio between the lower and upper sidebands is measured and stored for each current set. Obviously, it is expected that the measured ratio will fluctuate up and down due to the influence of the RAMZI filter, which is changing for each set of random currents. However, if one stores a sufficiently high number of modulation spectra, then the median ratio extracted from these measurements will converge to the real value. That is, the real SSB extinction as it would be measured at the output of the modulator. In our experiment, a tone of +5 dBm and a frequency of 8.5 GHz was used to modulate the MZM. Besides, a constant reverse voltage of -2V was applied in one of the MZM arms, while the bias in the other arm was swept between 2 and 9.4 V in steps of 0.2 V. For each value, we applied a set of 25 different, independent, uniformly distributed random currents in the 6 thermo-optic heaters of the RAMZI filter, and the output spectrum was captured in an OSA (Advantest Q8384). After adequate post-processing, the final results are shown in Figs. 7.17(b) to 7.17(d).

Figure 7.17(b) shows the dependence of the median SSB extinction (ratio between lower and upper sidebands, in dB) with bias voltage. As it can be seen, it reaches a maximum of around 14 dB at -8 V, which is the optimum bias point. This is better illustrated in Figure 7.17(c), where an overlap of all the measured spectra (solid grey lines) is shown for this optimum bias voltage. They have been conveniently renormalized and shifted in wavelength, so that the fluctuations of the SSB extinction around the median value could be better appreciated. A black solid line represents the average of all these responses. Finally, Fig. 7.17(d) shows what happens when we do the same procedure, but this time keeping the optimum voltage (-8 V) and instead sweeping the RF frequency with the same power. As it can be seen, the achieved extinction is not constant with modulation frequency. For example, it goes below 5 dB for frequencies between 9 and 11 GHz, while it also shows a couple of dips around 7 and 8 GHz. We attribute this behaviour to poor RF performance of the modulator electrodes, which were in fact not adequately terminated with 50 Ω loads. At high frequencies a great part of the RF power is probably bouncing back through the transmission lines, creating standing wave patterns that are significantly affecting its broadband modulation behaviour, and introducing unwanted power and phase imbalances.

7.4.8 Coherent MWP filtering

Both polarization rotation and the poor performance of the MZM make a fully controlled coherent MWP filtering scheme difficult. This is because we can not longer relate the measured RF response of the system to the optical transfer function of the RAMZI filter. First, because the response of the filter itself is unknown,

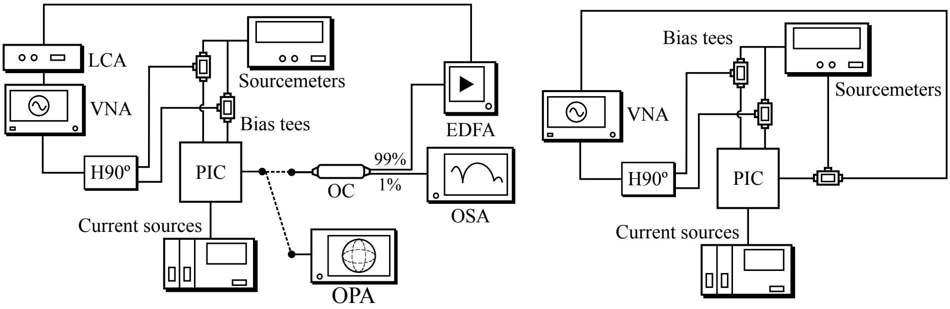

(a) (b)

Figure 7.18: (a) Experimental setup of the electrical to optical (E/O) measurement. VNA: Vector network analyzer. LCA: Lightwave component analyzer. H90°: 90° RF hybrid. EDFA: Erbium-doped fiber amplifier. OC: Optical coupler. OSA: Optical spectrum analyzer. OPA: Optical polarization analyzer. (b) Idem for the electrical to electrical (E/E) measurement.

and we can not change it at will. And second, because the SSB extinction is very poor and changes with frequency.

Nevertheless, we carried out some RF experiments to see if at least the basic functionality could be demonstrated, even if the response is far from the design target. The first one involved measuring the electro/optical (E/O) response of the system. That is, modulating the dual-drive MZM and afterwards detecting the signal at the output of the RAMZI filter with an external photodetector. In the second one, we did an electrical to electrical (E/E) evaluation. That is, exciting the chip with an electrical signal and measuring the output RF signal in the internal RF photodetector (PD 4), just as the chip was originally intended to operate. The two experiments are briefly discussed in the following subsections.

Electrical to optical (E/O)

An schematic diagram of the E/O experiment is shown in Fig. 7.18(a). First, TL 1 is switched on, and a VNA and a 90° RF hybrid are employed to modulate the dual-drive MZM. This is polarized at the optimum bias point (-8 V). After the SSB modulation goes through the RAMZI filter, it is collected at the *Output* fiber. Next, the signal is split in two distinct paths by a 99%/01% optical coupler (OC). One one hand (1%), it is directed into an OSA. On the other hand (99%), it is amplified by an erbium-doped fiber amplifier (EDFA) and sent into a lightwave component analyzer (LCA, Agilent N4373C). The LCA is an external module plugged into the VNA that measures the response of certain types of electro-optical systems, such as modulators. Besides, and optical polarization analyzer can be connected to measure the polarization rotation of the laser.

Once everything was ready, we first verified that pumping different currents in the thermo-optic heaters modified the RF response of the whole system, as it

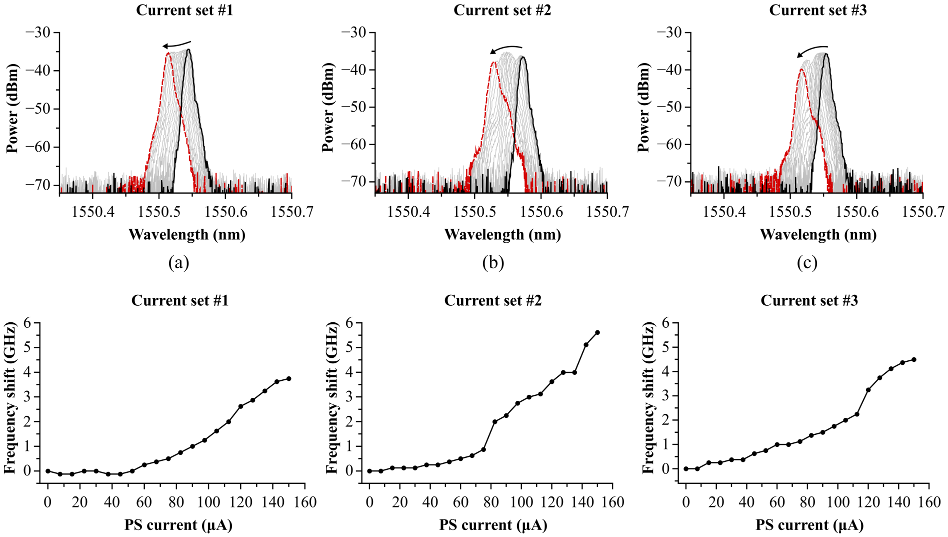

(a) (b) (c)

(d) (e) (f)

Figure 7.19: (a) to (c) Measured emission spectra of TL 1 vs current injected into the PS section, for three different sets of currents in the thermo-optic phase shifters of the RAMZI filter (#1, #2 and #3). (d) to (f) Shift in the central frequency of TL 1 for the same conditions.

was expected. Then, we randomly changed these values until a response similar to the target filter shape was obtained. We found three distinct sets of currents (termed #1, #2 and #3) that yielded three different, although similar, responses. Finally, we stored the E/O responses of the filter for these three cases when different currents were applied to the PS shifting section of TL 1, which changed the center wavelength of the laser. The changes in laser wavelength were recorded by capturing the output emission spectra in the OSA. Results are shown in both Figs. 7.19(a) and 7.19(f) and Figs. 7.20(a) to 7.20(i).

First, an overlapped representation of all the measured optical emission spectra of TL 1 can be seen in Figs. 7.19(a) to 7.19(c) for the three different current sets. From them, we computed the curves of Figs. 7.19(d) to 7.19(f). They represent the shift in the laser central frequency caused by current injection in the PS. The laser central frequency is shifted between 4 and 6 GHz for this current range (0 to 155 μA).

The different E/O responses obtained during the wavelength sweep are next shown in Figs. 7.20(a) to 7.20(c). The solid black line represents the initial response, when no current was injected into the PS, while the red dashed line is the response that corresponds with the maximum injected current. All the responses exhibit a tunable low-pass behaviour, where the width of the band is reduced by decreasing (increasing) the laser wavelength (frequency). The measured -3 dB bandwidths as a function of the pumping current are plotted in Figs. 7.20(d) to 7.20(f).

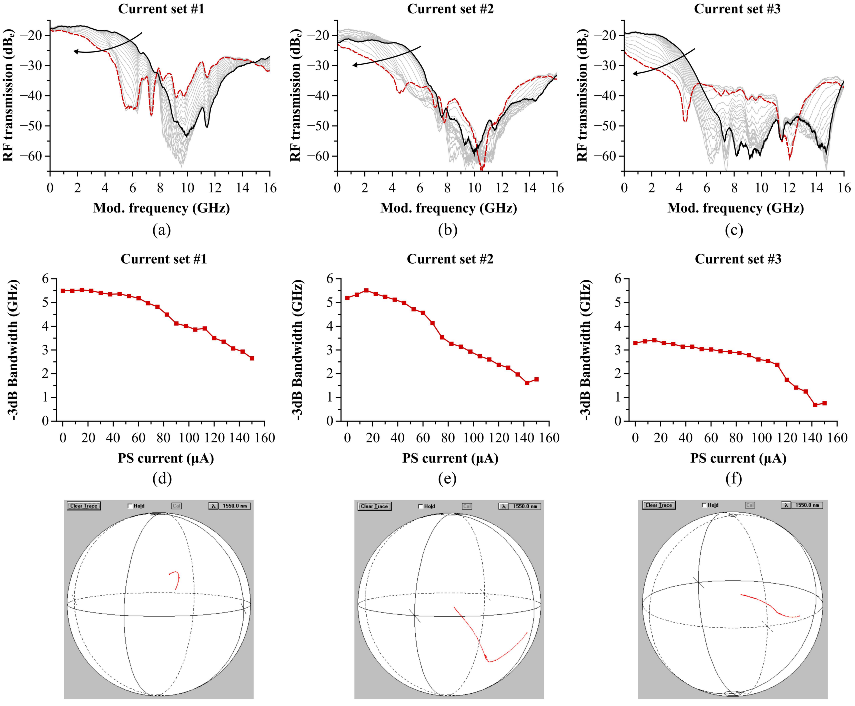

(a) (b) (c)

(d) (e) (f)

(g) (h) (i)

Figure 7.20: (a) to (c) Measured RF responses (E/O) of the coherent MWP filter as the central wavelength of TL 1 is shifted (see Fig. 7.19), for three different sets of currents in the thermo-optic heaters of the RAMZI filter (#1, #2 and #3). The solid black line corresponds to the initial response, while the dashed red line is the measured response for the maximum pumping current. All the measurements in between are shown as light grey lines. (d) to (f) Evolution of the -3 dB bandwidth as a function of the PS current. (g) to (i) Polarization rotation observed at the output.

For the first current set (#1), the -3 dB bandwidth decreases from a maximum of 5.5 GHz to a minimum of 2.5 GHz (3 GHz range), which is similar to the increase in the frequency of the laser (4 GHz) of Fig. 7.19(d). For the second current set (#2), the -3 dB bandwidth goes from a maximum of 5 GHz down to 1.5 GHz (3.5 GHz range), in contrast to the increase of almost 6 GHz of the laser frequency shown in Fig. 7.19(e). Finally, the third current set (#3) shows a -3 dB bandwidth that decreases from 3.5 to 0.5 GHz (3 GHz range), also different from the 4.5 GHz increase in laser central frequency of Fig. 7.19(f).

The difference in these values, as well as the observed evolution of the RF filter response for different PS currents, might be explained by both polarization rotation in the bends and the frequency-dependent SSB extinction of the dual-drive MZM. This is shown in Figs. 7.20(g) to 7.20(i). As the laser wavelength

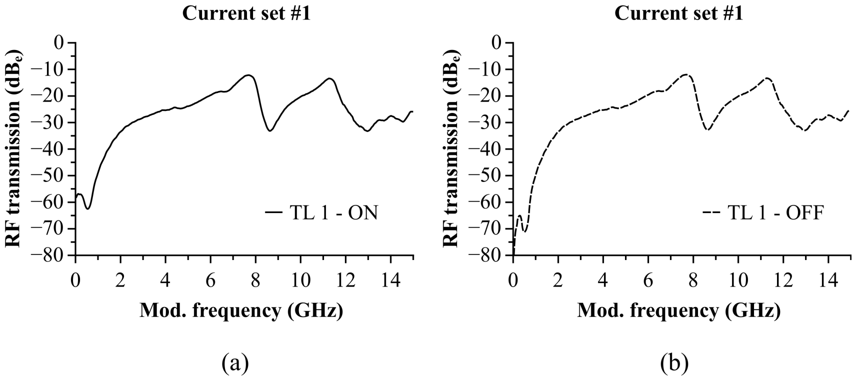

Figure 7.21: (a) Measured E/E response when TL 1 is switched on. (b) Idem when TL 1 is switched off.

decreases, the polarization state of the signal inside the PIC changes, and so the transfer function of the RAMZI filter.

Electrical to electrical (E/E)

The second experiment was similar to that described in the previous section. However, this time the signal going out of the RAMZI filter was not collected at the *Output* fiber, but was detected internally using an RF photodetector (PD 4), as shown in Fig. 7.18(b). For that purpose, PD 4 was connected to another bias tee and reverse biased at -2 V, while its RF output was directly connected to the VNA.

We then measured the E/E response of the system, but in this case the laser wavelength was kept constant. Figure 7.21(a) shows the measured RF response (E/E) when the current set #1 was applied in the thermo-optic heaters. As it can be seen, the response is quite different from those of Fig. 7.20(a). In fact, the measured response does not change much even when TL 1 is switched off, as only a small drop for those frequencies lower than 1 GHz is appreciated (Fig. 7.21(b)).

The explanation for this unexpected behaviour lies in the existence of a significant RF crosstalk. Note that, as shown in Fig. 7.5, PD 4 was placed very close to the MZM electrodes inside the chip, with no further electrical isolation measures. As a consequence, the input RF signals in both MZM arms are contaminating the measured photocurrent, which is orders of magnitude smaller due to the inherent losses of the MWP link. Only for very low frequency values the RF crosstalk becomes negligible, and a small difference can be appreciated. This is because the relative size of the MZM electrodes is now much smaller than the RF wavelength, and so they do not behave as integrated antennas. Unfortunately, this unwanted effect ultimately prevents the E/E operation of this PIC, for which it was originally designed.

7.5 Conclusions and future work

In this chapter, we have reported on the design and experimental characterization of an InP PIC designed to operate as a fully integrated, coherent MWP filter. We have first started by reviewing the basic operation principles behind a coherent approach, which is based on the one-to-one mapping between the optical and electrical domains that occurs when a SSB modulation is employed. Afterwards, we have provided a general description of the basic BBs that make up the chip, and how they are interconnected to implement the required functionality. An explanation of the design steps followed to design such BBs has been provided, followed by their experimental characterization. This included the tunable lasers, as well as the on-chip photodetectors, modulators, RAMZI filter and thermo-optic heaters. Finally, a system level evaluation of the photonic filtering scheme was performed.

During the course of the measurements, some detrimental effects were identified and studied in more detail. In particular, a significant polarization rotation was observed in the deeply etched waveguides, which was later confirmed by means of simulations. This prevented the external measurement of the RAMZI filter, which could not be then controlled and tuned to match the original design target. Besides, severe RF crosstalk was observed when performing full electrical to electrical (E/E) measurements of the coherent MWP filter. Nevertheless, the basic tuning functionality was demonstrated using an electrical to optical (E/O) approach, were an auxiliary waveguide was employed to inject the output of the RAMZI filter into an external photodetector. Three reconfigurable low-pass filters were obtained, whose -3 dB bandwidth could be tuned by about 3-4 GHz by changing the wavelength of one internal tunable laser (TL 1).

Future designs should be aware of all the data collected over the course of these measurements, and minimize risks associated with polarization rotation, as well as RF crosstalk. In particular, optical waveguide bends should use a much higher bending radius. Besides, the RF pads should be isolated and spaced as much as possible. Finally, a proper termination of the MZM arms with a right broadband load would be beneficial to increase the performance of the SSB modulation.

Publications

The work done in this chapter lead to the following contributions in international conferences:

1. P. Muñoz, J. Capmany, **J. S. Fandiño**, J. D. Doménech, R. Baños, J. D. Martínez, S. Sirci, and V. Boria, "Microwave photonics beat filter monolithically integrated on an indium phosphide chip (invited paper)," in *17th International Conference on Transparent Optical Networks (ICTON)*, pp. 1–4, July 2015.

2. P. Muñoz, J. Capmany, D. Pérez, J. H. den Besten, **J. S. Fandiño**, and J. D.

Doménech, “Integrated microwave photonics: State of the art and future trends,” in *16th International Conference on Transparent Optical Networks (ICTON)*, pp. 1–4, July 2014.

Chapter 8

Conclusions and future work

Microwave photonics (MWP) has been an intense research topic for many years. From ultra-wideband signal generation to highly tunable RF filters, MWP has long promised with the advent of a new class of photonics-based RF systems, which would feature better performances and new functionalities as compared to their electronic counterparts. However, for it to become a technological reality, significant improvements must bet yet done, particularly regarding size, power consumption and cost. Those limitations have ultimately given birth to a relatively new research field known as integrated microwave photonics (IMWP), which aims to harness the potential of photonic integration to solve the aforementioned problems.

The basic motivation behind this thesis has been to advance the state-of-the-art in IMWP. To be more precise, we have first focused on both the design and experimental aspects behind the implementation of tunable, integrated optical filters based on a ring-assisted Mach-Zehnder interferometer architecture (RAMZI). Second, we have explored the use of such devices in different IMWP applications, where tunable optical filters can be very useful. The main contributions made during the realization of this thesis can be summarized as follows:

- In chapter 3, tapered 2x2 MMIs featuring arbitrary power splitting ratios have been experimentally demonstrated in a generic Silicon-on-Insulator (SOI) platform. Our results confirm that this kind of coupler is an excellent choice for the implementation of RAMZI filters. It is compact, easy to design and robust against manufacturing deviations, with just a few % error in the coupling ratios over a broad wavelength range. Besides, we have run exhaustive simulations of a 4x4 MMI working as a 90° optical hybrid for coherent optical communication systems. These have shown that, for this specific application, fabrication errors might not be neglected, even when using MMI-based devices.

- Multimode interference reflectors (MIRs) based on aluminium mirrors have been experimentally demonstrated for the first time in chapter 4. Several devices fabricated in a thick SOI platform were designed and measured. Experiments confirmed the high bandwidth and excellent reflective properties of this kind of mirror, which could be of great interest for implementing on-chip lasers and reflective filters.

- In the first part of chapter 5, we have experimentally demonstrated a photonic system capable of measuring the frequency of an RF tone over a 10 GHz bandwidth, with a root mean square error of less than 200 MHz. The key idea was to exploit a double-sideband suppressed-carrier optical modulation (DSB-SC) together with the complementary responses of a second-order RAMZI filter, which was designed and fabricated in a generic InP plaftorm. In the second part of the same chapter, we have developed an in-depth theoretical analysis of this photonic approach to instantaneous frequency measurement (IFM). The results of this analysis have confirmed earlier experimental observations, and point to the critical impact that a residual optical carrier due to imperfections in the dual-drive Mach-Zehnder modulator can have on system performance. Besides, it has been shown that this IFM technique has a relatively poor dynamic range performance, even under ideal conditions.

- In chapter 6, a fully integrated receiver for frequency-modulated microwave photonic links has been designed and experimentally demonstrated. The photonic integrated circuit (PIC), fabricated in a generic InP platform, features three independent RAMZI filters that work together to implement a frequency discriminator. It also includes an on-chip, broadband balanced photodetector. The reasons behind the use of a frequency discriminator to detect frequency modulated signals are twofold. First, it is simpler than a coherent scheme. Second, it could theoretically yield a distortion-free link if the right filter shape were employed. Experimental results for the PIC have included a characterization of the optical filters, as well as a standard two-tones test to quantify its linearity. Due to both high overall losses and a non-ideal filter shape, a poor spurious-free dynamic range (SFDR) was obtained, which could nevertheless be theoretically improved by a redesign of the frequency discriminator and the introduction of spot-size converters.

- Finally, chapter 7 has explored the possibility of implementing coherent MWP filters by combining tunable RAMZIs with single-sideband modulation (SSB). A fully integrated system, including optical sources, modulators, optical filters and detectors, has been designed, fabricated in an InP platform and finally packaged for an easier characterization. Detailed experimental data has been given on the performance of its basic building blocks (BBs), as well as about the system level experiments. Due to the existence of both polarization rotation and RF crosstalk, which severely affected the performance of the whole system, the complete functionality of the PIC could not be demonstrated. However, a set of three tunable low-pass filters were achieved using external detection.

8.1 Future work

Open questions and future lines of work might include:

- The development of new tunable optical filter architectures with a higher immunity against fabrication errors.
- The demonstration of integrated lasers and reflective filters, such as reflective arrayed waveguide gratings, using MIRs.
- The experimental demonstration of a fully integrated and packaged IFM system in a generic photonic platform.
- The study and development of adiabatic bends and other techniques to mitigate or prevent polarization rotation in waveguide bends.
- The investigation on the origins and causes of RF crosstalk in integrated photonic circuits, as well as on possible solutions to prevent the problem.
- The design and experimental demonstration of a completely integrated microwave photonics processor, capable of performing multiple IMWP tasks in a single monolithic substrate.
- To explore the use of hybrid photonic technologies for the implementation of IMWP systems, which could take advantage of both the low losses of purely passive platforms (such as Si_3N_4) and the active capabilities of InGaAsP/InP.

Appendix A

2D simulation of 3D devices: the effective index method

Designing complex photonic integrated circuits (PIC) is a simulation intensive task. PIC designers normally follow a bottom-up approach, where the cross-sections of the chip waveguides are first simulated with mode solvers. Aftewards, either the calculated mode profiles are used for computing overlap integrals, for example, or the effective and group indices of the propagating modes are employed in tools with a higher degree of abstraction, such as photonic circuit-level simulators. These simulators employ low-level technology values to predict the behaviour of the PIC at a large scale, including the transmission response of optical filters.

A common problem faced by all PIC designers is that most photonic devices, such as multimode interference couplers (MMIs) and arrayed waveguide gratings (AWGs), are electromagnetically large. That is, their physical size is hundreds to thousands times the operation wavelength, which is typically in the order of 1 μm for technologies working in the near-infrared. As a consequence, full 3D simulations with rigorous methods like the finite-difference time-domain (FDTD) approach are totally prohibitive from a computational point of view, as they would take days or even weeks to simulate in a normal personal computer. And that without considering simulation sweeps for performance optimization, where dozens of simulations can be run for a single device.

It is for all those reasons that alternative approaches have been developed over the years, that allow PIC designers to simulate electromagnetically big structures within reasonable times. Arguably, the most popular approach is to use an optimized version of the so-called effective index method (EIM), which was originally developed as a quasi-analytical approximation for solving the modes of a rectangular dielectric waveguide, such as that shown in Fig. A.1(a).

The EIM is based on a divide and conquer strategy. The problem of finding the modes of a rectangular cross-section is divided in two simpler problems whose solutions are known. In particular, it is assumed that the original waveguide can

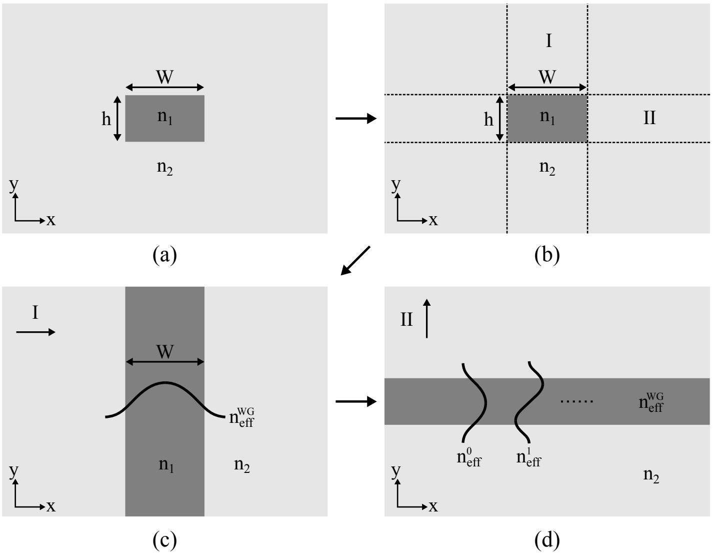

(a) (b)

(c) (d)

Figure A.1: (a) Waveguide cross-section. (b) Sectioning of the original problem with the EIM. (c) Step I. (d) Step II.

be viewed as the combination of two infinite slab waveguides, which are the only type of purely dielectric rectangular waveguides with analytical solution [102]. This strategy is schematically illustrated in Fig. A.1(b). In step I (Fig. A.1(c)), an infinite slab of the same width (W), core (n_1) and cladding (n_2) refractive indices as the original waveguide is solved . We shall call the effective index of the fundamental mode of such structure as n_{eff}^{WG}. In step II (Fig. A.1(d)), an infinite slab of the same height (h) and cladding (n_2) refractive index as the original waveguide is considered. However, the refractive index of the core is now assumed to be equal to n_{eff}^{WG}. Once this waveguide is solved, the effective indices of the different modes (n_{eff}^{0}, $n_{eff}^{1} \ldots$) should approximate those of the initial structure when found with a 2D mode solver. If one is interested in finding the TE modes of the original waveguide, then step I should first find the fundamental TE mode, and step II should look for the TM modes. On the contrary, if one is interested in finding the TM modes of the original waveguide, then step I should first find the fundamental TM mode, and step II should look for the TE modes.

In general, the EIM is not a very good approximation as it depends a lot on the specific waveguide cross-section and index contrast. However, some optimization tricks for particular structures have been developed that yield more accurate results. Here, we will focus on MMIs, which have been subjected to intensive study throughout this thesis. The general problem is stated in Fig. A.2. Lets assume that we want to design a 1x2 MMI, and that we want to optimize its dimensions to achieve minimum imbalance and insertion losses. As multiple simulation sweeps will be required, we are interested in speeding up the process as much as possi-

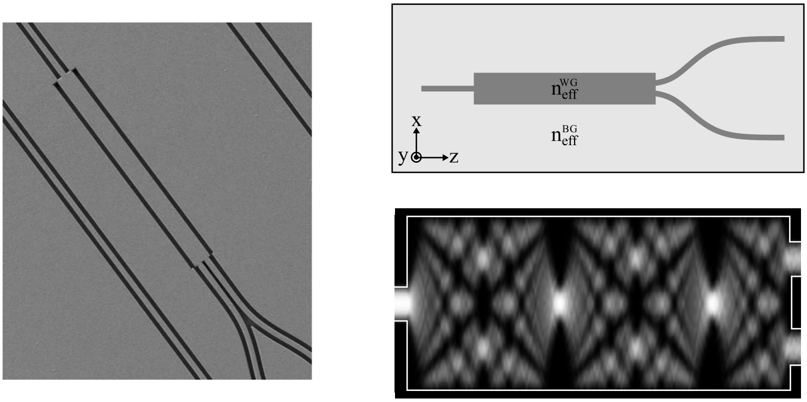

(a) (b)

Figure A.2: (a) 3D 1x2 MMI under analysis. (b) Equivalent 2D structure after the reduction procedure.

ble, so a faster but equally accurate alternative to full 3D simulations needs to be found. In particular, we are interested in finding an equivalent 2D structure, as shown in the upper figure of Fig. A.2(b), where the vertical dimension has been eliminated, yet its performance for the same physical dimensions is very similar to that of the original 3D device (Fig. A.2(a)). The only two parameters that we can play with are the refractive index of the core (n_{eff}^{WG}) and the effective index of the cladding, or background (n_{eff}^{BG}). For the particular case of MMIs, we need to optimize both n_{eff}^{WG} and n_{eff}^{BG} so that the beating length (L_{π}^{Slab}) of the planar device is equal to that of the original 3D structure (L_{π}). That is, $\mathrm{L}_{\pi}^{Slab} = \mathrm{L}_{\pi}$. As a consequence, the values obtained during the 2D simulations should approximate with a relatively high degree of accuracy those that would be otherwise obtained with a full 3D approach (Fig. A.2(b), bottom).

The optimization method considering TE polarization, which is by far the most common, can be described as follows. First, a commercial mode solver is employed to find both the fundamental and first-order TE modes of the MMI cross-section. We shall call their corresponding effective indices as n_{eff}^{0} and n_{eff}^{1}, as shown in Fig. A.3(a) and A.3(b). According to equation 3.14 from chapter 3, the beating length is given by

$$L_{\pi} = \frac{\pi}{\beta_0 - \beta_1} = \frac{\lambda_0}{2(n_{eff}^{0} - n_{eff}^{1})} \tag{A.1}$$

where λ_0 is the vacuum wavelength.

Next, we proceed with step I and consider an infinite slab waveguide of the same width as the MMI, and whose refractive indices are given by those of the core (n_1) and the cladding (n_2). After solving this waveguide analytically, we find the fundamental TE mode, whose refractive index is precisely n_{eff}^{WG}. Afterwards, we have to find n_{eff}^{BG}, which is done in an iterative way. We proceed with step II,

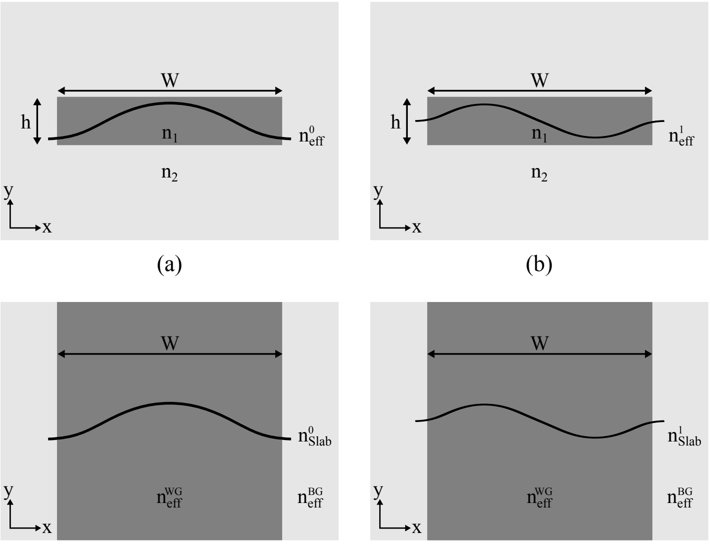

(a) (b)

(c) (d)

Figure A.3: (a) and (b) Fundamental and first order modes (n_{eff}^0 and n_{eff}^1, respectively) of the 1x2 MMI. (c) and (d) Fundamental and first order modes (n_{Slab}^0 and n_{Slab}^1, respectively) of the equivalent slab waveguide.

and consider another infinite slabe waveguide of the same height (h) as the original MMI waveguide, but with a core refractive index given by n_{eff}^{WG}. The two fundamental TM modes of such slab (n_{Slab}^0, n_{Slab}^1) will give us the beating length of the planar structure (L_π^{Slab})

$$L_\pi^{Slab} = \frac{\lambda_0}{2(n_{Slab}^0 - n_{Slab}^1)} \tag{A.2}$$

All is left to do is to optimize the value of n_{eff}^{BG} until both L_π^{Slab} and L_π are equal. Once an optimum value for n_{eff}^{BG} is found, a 2D simulation can be peformed, and the device can be simulated using simpler approaches such as the beam propagation method (BPM) [85].

Appendix B

List of publications

B.1 Journal papers

1. **J. S. Fandiño**, J. D. Doménech, and P. Muñoz, “Two-port multimode interference reflectors based on aluminium mirrors in a thick SOI platform,” *Opt. Express*, vol. 23, pp. 20219–20233, Aug. 2015.

2. **J. S. Fandiño** and P. Muñoz, “Analysis of System Imperfections in a Photonics-Assisted Instantaneous Frequency Measurement Receiver Based on a Dual-Sideband Suppressed-Carrier Modulation,” *J. Lightwave Technol.*, vol. 33, pp. 293–303, Jan. 2015.

3. J. D. Doménech, **J. S. Fandiño**, B. Gargallo, and P. Muñoz, “Arbitrary Coupling Ratio Multimode Interference Couplers in Silicon-on-Insulator,” *J. Lightw. Technol.*, vol. 32, pp. 2536–2543, July 2014.

4. **J. S. Fandiño** and P. Muñoz, “Photonics-based microwave frequency measurement using a double-sideband suppressed-carrier modulation and an InP integrated ring-assisted Mach-Zehnder interferometer filter,” *Opt. Lett.*, vol. 38, pp. 4316–4319, Nov. 2013.

5. **J. S. Fandiño** and P. Muñoz, “Manufacturing Tolerance Analysis of an MMI-Based 90° Optical Hybrid for InP Integrated Coherent Receivers,” *IEEE Photon. J.*, vol. 5, pp. 7900512–7900512, Apr. 2013.

6. **J. S. Fandiño**, J. D. Doménech, P. Muñoz, and J. Capmany, “Integrated InP frequency discriminator for Phase-modulated microwave photonic links,” *Opt. Express*, vol. 21, pp. 3726–3736, Feb. 2013.

B.2 Conference papers

1. **J. S. Fandiño**, J. D. Doménech, and P. Muñoz, “Two-Port Multimode Interference Reflectors with Aluminium Mirrors in a Micron-Scale SOI Platform,” in *European Conference on Optical Communication (ECOC)*, pp. 1–3, Sept. 2015.

2. P. Muñoz, J. D. Doménech, **J. S. Fandiño**, R. Baños, and B. Gargallo, “Advanced Building Blocks in Thick Silicon on Insulator Technology: Echelle Grating Multiplexers and Reflective Multimode Interference Couplers,” in *PIERS Proceedings*, pp. 1864–1869, July 2015.

3. P. Muñoz, J. Capmany, **J. S. Fandiño**, J. D. Doménech, R. Baños, J. D. Martínez, S. Sirci, and V. Boria, “Microwave photonics beat filter monolithically integrated on an indium phosphide chip (invited paper),” in *17th International Conference on Transparent Optical Networks (ICTON)*, pp. 1–4, July 2015.

4. P. Muñoz, J. Capmany, D. Pérez, J. H. den Besten, **J. S. Fandiño**, and J. D. Doménech, “Integrated microwave photonics: State of the art and future trends,” in *16th International Conference on Transparent Optical Networks (ICTON)*, pp. 1–4, July 2014.

5. J. D. Doménech, **J. S. Fandiño**, R. Baños, and P. Muñoz, “Opto-electronic wavelength tracker in Silicon-on-Insulator,” in *17th European Conference on Integrated Optics (ECIO)*, June 2014.

6. J. D. Doménech, **J. S. Fandiño**, B. Gargallo, and P. Muñoz, “Arbitrary Coupling Ratio Multimode Interference Couplers in Silicon-on-Insulator,” in *17th European Conference on Integrated Optics (ECIO)*, June 2014.

7. **J. S. Fandiño** and P. Muñoz, “Instantaneous frequency measurement system by means of a complementary optical filter monolithically integrated in InP,” in *International Topical Meeting on Microwave Photonics (MWP)*, pp. 290–293, Oct. 2013.

8. **J. S. Fandiño**, M. Rius, J. Mora, P. Muñoz, and J. Capmany, “Optical Single Sideband Transmitter Using Phase Modulation and a Photonic Integrated Filter,” in *International Topical Meeting on Microwave Photonics (MWP)*, pp. 154–157, Oct. 2013.

9. **J. Fandiño**, P. Muñoz, and J. Capmany, “Manufacturing tolerance analysis of an InP, 4×4 MMI-based 90° optical hybrid for integrated coherent receivers,” in *Optical Fiber Communication Conference and Exhibition (OFC)*, pp. 1–3, Mar. 2013.

10. **J. S. Fandiño**, J. D. Doménech, P. Muñoz, and J. Capmany, “Design and Experimental Characterization of an InP Photonic Integrated Circuit Working as a Receiver for Frequency-Modulated Direct-Detection Microwave Photonic Links,” in *Proc. of SPIE OPTO*, vol. 8627, pp. 862708–862708–8, Feb. 2013.
11. **J. S. Fandiño**, P. Muñoz, and J. Capmany, “Design of a Frequency Modulation-Direct Detection Microwave Photonic Link receiver monolithically integrated in InP generic technology,” in *16th European Conference on Integrated Optics (ECIO)*, Apr. 2012.
12. **J. S. Fandiño**, P. Muñoz, and J. Capmany, “Tolerance analysis of a 4×4 MMI-based 90° optical hybrid for 100G coherent receivers,” in *16th European Conference on Integrated Optics (ECIO)*, Apr. 2012.

B.3 Others

1. J. D. Doménech, **J. S. Fandiño**, B. Gargallo, R. Baños, and P. Muñoz, “Silicon opto-electronic wavelength tracker based on an asymmetric 2x3 Mach-Zehnder Interferometer,” *Waves*, vol. 6, no. 1, pp. 29–34, 2014.
2. **J. Sánchez Fandiño**, J. Capmany Francoy, and P. Muñoz Muñoz, “Receptor integrado de clase B para enlaces fotónicos de microondas modulados en fase,” Patente T201200004, Universidad Politécnica de Valencia (Spain), 2012.

Bibliography

[1] T. H. Maiman, “Stimulated optical radiation in ruby masers,” *Nature*, vol. 187, pp. 493–494, 1960.

[2] A. Javan, W. R. Bennett, and D. R. Herriott, “Population Inversion and Continuous Optical Maser Oscillation in a Gas Discharge Containing a He-Ne Mixture,” *Phys. Rev. Lett.*, vol. 6, pp. 106–110, 1961.

[3] K. C. Kao and G. A. Hockham, “Dielectric-fibre surface waveguides for optical frequencies,” *Proc. IEE*, vol. 113, no. 7, pp. 1151–1158, 1966.

[4] G. P. Agrawal, *Fiber-Optic Communication Systems, 4th Edition.* Wiley, 2010.

[5] “The Nobel Prize in Physics 2009.” Nobel Media AB 2014. http://www.nobelprize.org/nobel_prizes/physics/laureates/2009/.

[6] A. J. Seeds, “Microwave photonics,” *IEEE Trans. Microw. Theory Techn.*, vol. 50, no. 3, pp. 877–887, 2002.

[7] A. J. Seeds and K. J. Williams, “Microwave Photonics,” *J. Lightw. Technol.*, vol. 24, no. 12, pp. 4628–4641, 2006.

[8] R. J. Mears, L. Reekie, I. M. Jauncey, and D. N. Payne, “Low-noise erbium-doped fibre amplifier operating at 1.54 μm,” *Electron. Lett.*, vol. 23, no. 19, pp. 1026–1028, 1987.

[9] J. Capmany and D. Novak, “Microwave photonics combines two worlds,” *Nature Photon.*, vol. 1, no. 6, pp. 319–330, 2007.

[10] D. Novak, “Enabling microwave photonic technologies for antenna remoting,” *IEEE LEOS Newsletter*, vol. 23, no. 2, pp. 21–24, 2009.

[11] J. A. Chiddix, H. Laor, D. M. Pangrac, L. D. Williamson, and R. W. Wolfe, “AM video on fiber in CATV systems: need and implementation,” *IEEE J. Sel. Areas Commun.*, vol. 8, no. 7, pp. 1229–1239, 1990.

[12] W. Ng, A. A. Walston, G. L. Tangonan, J. J. Lee, I. L. Newberg, and N. Bernstein, "The First Demonstration of an Optically Steered Microwave Phased Array Antenna Using True-Time-Delay," *J. Lightw. Technol.*, vol. 9, no. 9, pp. 1124–1131, 1991.

[13] J. Capmany, J. Mora, I. Gasulla, J. Sancho, J. Lloret, and S. Sales, "Microwave Photonic Signal Processing," *J. Lightw. Technol.*, vol. 31, no. 4, pp. 571–586, 2013.

[14] J. Yao, F. Zeng, and Q. Wang, "Photonic Generation of Ultrawideband Signals," *J. Lightw. Technol.*, vol. 25, no. 11, pp. 3219–3235, 2007.

[15] L. V. T. Nguyen and D. B. Hunter, "A photonic technique for microwave frequency measurement," *IEEE Photon. Technol. Lett.*, vol. 18, no. 10, pp. 1188–1190, 2006.

[16] H. Chi, X. Zou, and J. Yao, "An Approach to the Measurement of Microwave Frequency Based on Optical Power Monitoring," *IEEE Photon. Technol. Lett.*, vol. 20, no. 14, pp. 1249–1251, 2008.

[17] G. C. Valley, "Photonic analog-to-digital converters," *Opt. Express*, vol. 15, no. 5, pp. 1955–1982, 2007.

[18] Y. Han and B. Jalali, "Photonic Time-Stretched Analog-to-Digital Converter: Fundamental Concepts and Practical Considerations," *J. Lightw. Technol.*, vol. 21, no. 12, pp. 3085–3103, 2003.

[19] A. L. Ricchiuti, D. Barrera, S. Sales, L. Thevenaz, and J. Capmany, "Long fiber Bragg grating sensor interrogation using discrete-time microwave photonic filtering techniques," *Opt. Express*, vol. 21, pp. 28175–28181, Nov 2013.

[20] D. Marpaung, C. Roeloffzen, R. Heideman, A. Leinse, S. Sales, and J. Capmany, "Integrated microwave photonics," *Laser & Photonics Reviews*, vol. 7, no. 4, pp. 506–538, 2013.

[21] J. Capmany, I. Gasulla, and D. Pérez, "Microwave photonics: The programmable processor," *Nature Photon.*, vol. 10, pp. 6–8, 2015.

[22] E. I. Ackerman and C. H. Cox, "RF fiber-optic link performance," *IEEE Microwave Magazine*, vol. 2, no. 4, pp. 50–58, 2001.

[23] L. N. Langley, M. D. Elkin, C. Edge, M. J. Wale, U. Gliese, X. Huang, and A. J. Seeds, "Packaged semiconductor laser optical phase-locked loop (OPLL) for photonic generation, processing and transmission of microwave signals," *IEEE Trans. Microw. Theory Techn.*, vol. 47, no. 7, pp. 1257–1264, 1999.

[24] S. A. Pappert, C. K. Sun, R. J. Orazi, and T. E. Weiner, "Microwave fiber optic links for shipboard antenna applications," in *IEEE International Conference on Phased Array Systems and Technology*, pp. 345–348, May 2000.

[25] D. B. Hunter, L. G. Edvell, and M. A. Englund, “Wideband Microwave Photonic Channelised Receiver,” in *IEEE International Topical Meeting on Microwave Photonics (MWP)*, pp. 249–252, Oct. 2005.

[26] J. M. Payne and W. P. Shillue, “Photonic techniques for local oscillator generation and distribution in millimeter-wave radio astronomy,” in *IEEE International Topical Meeting on Microwave Photonics (MWP)*, pp. 9–12, Nov. 2002.

[27] A. Yariv, “The Beginnings of Optoelectronic Integrated Circuits - A Personal Perspective,” *J. Lightw. Technol.*, vol. 26, no. 9, pp. 1172–1175, 2008.

[28] R. Shubert and J. H. Harris, “Optical Surface Waves on Thin Films and Their Application to Integrated Data Processors,” *IEEE Trans. Microw. Theory Techn.*, vol. 16, no. 12, pp. 1048–1054, 1968.

[29] S. E. Miller, “Integrated Optics: An Introduction,” *Bell System Technical Journal*, vol. 48, no. 7, pp. 2059–2069, 1969.

[30] F. Kish *et al.*, “500 gb/s and beyond photonic integrated circuit module transmitters and receivers,” in *Optical Fiber Communications Conference and Exhibition (OFC)*, pp. 1–3, Mar. 2014.

[31] R. Nagarajan *et al.*, “10 channel, 100gbit/s per channel, dual polarization, coherent QPSK, monolithic InP receiver photonic integrated circuit,” in *Optical Fiber Communications Conference and Exhibition (OFC)*, pp. 1–3, Mar. 2011.

[32] M. Hochberg and T. Baehr-Jones, “Towards fabless silicon photonics,” *Nature Photon.*, vol. 4, pp. 492–494, 2010.

[33] “Towards a foundry model in micro- and nanophotonics: A vision for Europe,” tech. rep., EC FP6 NoE ePIXnet Steering Committee, March 2007.

[34] M. K. Smit *et al.*, “An introduction to InP-based generic integration technology,” *Semiconductor Science and Technology*, vol. 29, no. 8, p. 083001, 2014.

[35] K. A. Williams, E. A. J. M. Bente, D. Heiss, Y. Jiao, K. Ławniczuk, X. J. . M. Leijtens, J. J. G. M. van der Tol, and M. K. Smit, “InP photonic circuits using generic integration,” *Photon. Res.*, vol. 3, no. 5, pp. B60–B68, 2015.

[36] R. Soref, “The Past, Present, and Future of Silicon Photonics,” *IEEE J. Sel. Topics Quantum Electron.*, vol. 12, no. 6, pp. 1678–1687, 2006.

[37] H. Rong, R. Jones, A. Liu, C. Oded, D. Hak, A. Fang, and M. Paniccia, “A continuous-wave raman silicon laser,” *Nature*, vol. 433, pp. 725–728, 2005.

[38] K. Wörhoff, R. Heideman, A. Leinse, and M. Hoekman, “TriPleX: a versatile dielectric photonic platform,” *Advanced Optical Technologies*, vol. 4, no. 2, pp. 189–207, 2016.

[39] W. Ng, D. Yap, A. Narayanan, and A. Walston, “High-precision detector-switched monolithic GaAs time-delay network for the optical control of phased arrays,” *IEEE Photon. Technol. Lett.*, vol. 6, no. 2, pp. 231–234, 1994.

[40] E. J. Norberg, R. S. Guzzon, J. S. Parker, L. A. Johansson, and L. A. Coldren, “Programmable Photonic Microwave Filters Monolithically Integrated in InP-InGaAsP,” *J. Lightw. Technol.*, vol. 29, no. 11, pp. 1611–1619, 2011.

[41] M. S. Rasras, K.-Y. Tu, D. M. Gill, Y.-K. Chen, A. White, S. S. Patel, A. Pomerene, D. Carothers, J. Beattie, M. Beals, J. Michel, and L. C. Kimerling, “Demonstration of a Tunable Microwave-Photonic Notch Filter Using Low-Loss Silicon Ring Resonators,” *J. Lightw. Technol.*, vol. 27, no. 12, pp. 2105–2110, 2009.

[42] J. Sancho, J. Bourderionnet, J. Lloret, S. Combrié, I. Gasulla, X. Stephane, P. Sales, S. ad Colman, D. Lehoucq, G. ad Dolfi, J. Capmany, and A. R. De Rossi, “Integrable microwave filter based on a photonic crystal delay line,” *Nat. Commun.*, vol. 3, p. 1075, 2012.

[43] A. Ramaswamy, L. A. Johansson, J. Klamkin, H.-F. Chou, C. Sheldon, M. J. Rodwell, L. A. Coldren, and J. E. Bowers, “Integrated Coherent Receivers for High-Linearity Microwave Photonic Links,” *J. Lightw. Technol.*, vol. 26, no. 1, pp. 209–216, 2008.

[44] J. M. Wyrwas *et al.*, “Linear phase-and-frequency-modulated photonic links using optical discriminators,” *Opt. Express*, vol. 20, no. 24, pp. 26292–26298, 2012.

[45] D. Pérez, I. Gasulla, and J. Capmany, “Software-defined reconfigurable microwave photonics processor,” *Opt. Express*, vol. 23, no. 11, pp. 14640–14654, 2015.

[46] L. Zhuang, C. G. H. Roeloffzen, M. Hoekman, K.-J. Boller, and A. J. Lowery, “Programmable photonic signal processor chip for radiofrequency applications,” *Optica*, vol. 2, no. 10, pp. 854–859, 2015.

[47] C. K. Madsen and G. Lenz, “Optical All-Pass Filters for Phase Response Design with Applications for Dispersion Compensation,” *IEEE Photon. Technol. Lett.*, vol. 10, no. 7, pp. 994–996, 1998.

[48] C. K. Madsen, “General IIR Optical Filter Design for WDM Applications Using All-Pass Filters,” *J. Lightw. Technol.*, vol. 18, no. 6, pp. 860–868, 2000.

[49] R. S. Guzzon, E. J. Norberg, J. S. Parker, L. A. Johansson, and L. A. Coldren, "Integrated InP-InGaAsP tunable coupled ring optical bandpass filters with zero insertion loss," *Opt. Express*, vol. 19, no. 8, pp. 7816–7826, 2011.

[50] M. S. Rasras, D. M. Gill, S. S. Patel, K.-Y. Tu, Y.-K. Chen, A. E. White, A. T. S. Pomerene, D. N. Carothers, M. J. Grove, D. K. Sparacin, J. Michel, M. A. Beals, and L. C. Kimerling, "Demonstration of a Fourth-Order Pole-Zero Optical Filter Integrated Using CMOS Processes," *J. Lightw. Technol.*, vol. 25, no. 1, pp. 87–92, 2007.

[51] P. Dong, N.-N. Feng, D. Feng, W. Qian, H. Liang, B. J. Lee, D. C. andn Luff, T. Banwell, A. Agarwal, P. Toliver, R. Menendez, T. K. Woodward, and M. Asghari, "GHz-bandwidth optical filters based on high-order silicon ring resonators," *Opt. Express*, vol. 18, no. 23, pp. 23784–23789, 2010.

[52] S. Ibrahim, N. K. Fontaine, S. S. Djordjevic, B. Guan, T. Su, S. Cheung, R. P. Scott, A. T. Pomerene, L. L. Seaford, C. M. Hill, S. Danziger, Z. Ding, K. Okamoto, and S. J. B. Yoo, "Demonstration of a fast-reconfigurable silicon CMOS optical lattice filter," *Opt. Express*, vol. 19, no. 14, pp. 13245–13256, 2011.

[53] M. Cherchi, S. Ylinen, M. Harjanne, M. Kapulainen, T. Vehmas, T. Aalto, G. T. Kanellos, D. Fitsios, and N. Pleros, "Fabrication-tolerant optical filters for dense integration on a micron-scale SOI platform," in *Proc. of SPIE*, vol. 8990, pp. 89900F–89900F–7, 2014.

[54] H. Yu, M. Chen, Q. Guo, M. Hoekman, H. Chen, A. Leinse, R. G. Heideman, R. Mateman, S. Yang, and S. Xie, "Si3N4-Based Integrated Optical Analog Signal Processor and Its Application in RF Photonic Frontend," *IEEE Photon. J.*, vol. 7, no. 5, pp. 1–9, 2015.

[55] C. K. Madsen and J. H. Zhao, *Optical Filter Design and Analysis: A Signal Processing Approach.* Wiley, 1999.

[56] P. A. Besse, E. Gini, M. Bachmann, and H. Melchior, "New 2×2 and 1×3 Multimode Interference Couplers with Free Selection of Power Splitting Ratios," *J. Lightw. Technol.*, vol. 14, no. 10, pp. 2286–2293, 1996.

[57] Y. Sano and T. Yoshino, "Fast Optical Wavelength Interrogator Employing Arrayed Waveguide Grating for Distributed Fiber Bragg Grating Sensors," *J. Lightw. Technol.*, vol. 21, no. 1, pp. 132–139, 2003.

[58] J. S. Parker, A. Bhardwaj, P. R. A. Binetti, H. Yung-Jr, and L. Coldren, "Monolithically Integrated Gain-Flattened Ring Mode-Locked Laser for Comb-Line Generation," *IEEE Photon. Technol. Lett.*, vol. 24, no. 2, pp. 131–133, 2012.

[59] A. Rahim, S. Schwarz, J. Bruns, K. Voigt, G. Winzer, L. Zimmermann, C. G. Schaffer, and K. Petermann, "Silicon Photonic Implementation of a Scalable O-OFDM Demultiplexer," *IEEE Photon. Technol. Lett.*, vol. 25, no. 20, pp. 1977–1980, 2013.

[60] D. Marpaung, L. Chevalier, M. Burla, and C. Roeloffzen, "Impulse radio ultrawideband pulse shaper based on a programmable photonic chip frequency discriminator," *Opt. Express*, vol. 19, no. 25, pp. 24838–24848, 2011.

[61] W. Bogaerts, P. Dumon, D. Van Thourhout, D. Taillaert, P. Jaenen, J. Wouters, S. Beckx, V. Wiaux, and R. G. Baets, "Compact Wavelength-Selective Functions in Silicon-on-Insulator Photonic Wires," *IEEE J. Sel. Topics Quantum Electron.*, vol. 12, no. 6, pp. 1394–1401, 2006.

[62] M. K. Smit and C. Van Dam, "PHASAR-Based WDM-Devices: Principles, Design and Applications," *IEEE J. Sel. Topics Quantum Electron.*, vol. 2, no. 2, pp. 236–250, 1996.

[63] C. Cremer, N. Emeis, M. Schier, G. Heise, G. Ebbinghaus, and L. Stoll, "Grating Spectrograph Integrated with Photodiode Array in InGaAsP/InGaAs/InP," *IEEE Photon. Technol. Lett.*, vol. 4, no. 1, pp. 108–110, 1992.

[64] D. K. Armani, T. J. Kippenberg, S. M. Spillane, and K. J. Vahala, "Ultra-high-Q toroid microcavity on a chip," *Nature*, vol. 421, no. 6926, pp. 925–928, 2003.

[65] Y. Hu, R. M. Jenkins, F. Y. Gardes, E. D. Finlayson, G. Z. Mashanovich, and G. T. Reed, "Wavelength division (de)multiplexing based on dispersive self-imaging," *Opt. Lett.*, vol. 36, no. 23, pp. 4488–4490, 2011.

[66] K. Jinguji and M. Oguma, "Optical Half-Band Filters," *J. Lightw. Technol.*, vol. 18, no. 2, pp. 252–259, 2000.

[67] B. E. Little, S. T. Chu, H. A. Haus, J. Foresi, and J.-P. Laine, "Microring Resonator Channel Dropping Filters," *J. Lightw. Technol.*, vol. 15, no. 6, pp. 998–1005, 1997.

[68] W. A. Zortman, D. C. Trotter, and M. R. Watts, "Silicon photonics manufacturing," *Opt. Express*, vol. 18, no. 23, pp. 23598–23607, 2010.

[69] W. Bogaerts, P. De Heyn, T. Van Vaerenbergh, K. De Vos, S. Kumar Selvaraja, T. Claes, P. Dumon, P. Bienstman, D. Van Thourhout, and R. Baets, "Silicon microring resonators," *Laser & Photonics Reviews*, vol. 6, no. 1, pp. 47–73, 2012.

[70] F. Horst, W. Green, S. Assefa, S. M. M. Shank, Y. A. Vlasov, and B. J. Offrein, "Cascaded Mach-Zehnder wavelength filters in silicon photonics for low loss and flat pass-band WDM (de-)multiplexing," *Opt. Express*, vol. 21, no. 10, pp. 11652–11658, 2013.

[71] G. Gilardi, Y. Weiming, H. R. Haghighi, X. J. M. Leijtens, M. K. Smit, and M. J. Wale, “Deep Trenches for Thermal Crosstalk Reduction in InP-Based Photonic Integrated Circuits,” *J. Lightw. Technol.*, vol. 32, no. 24, pp. 4864–4870, 2014.

[72] F. Morichetti, A. Melloni, and M. Martinelli, “Effects of Polarization Rotation in Optical Ring-Resonator-Based Devices,” *J. Lightw. Technol.*, vol. 24, no. 1, pp. 573–585, 2006.

[73] C. van Dam, L. H. Spiekman, F. P. G. M. van Ham, F. H. Groen, J. J. G. M. van der Tol, I. Moerman, W. W. Pascher, M. Hamacher, H. Heidrich, C. M. Weinert, and M. K. Smit, “Novel Compact Polarization Converters Based on Ultra Short Bends,” *IEEE Photon. Technol. Lett.*, vol. 8, no. 10, pp. 1346–1348, 1996.

[74] S. Somekh, E. Garmire, A. Yariv, H. L. Garvin, and R. G. Hunsperger, “Channel optical waveguide directional couplers,” *Appl. Phys. Lett.*, vol. 22, no. 1, pp. 46–47, 1973.

[75] Y. Shani, C. H. Henry, R. C. Kistler, R. F. Kazarinov, and K. J. Orlowsky, “Integrated optic adiabatic devices on silicon,” *IEEE J. Quantum Electron.*, vol. 27, no. 3, pp. 556–566, 1991.

[76] M. Cherchi, S. Ylinen, M. Harjanne, M. Kapulainen, T. Vehmas, and T. Aalto, “Unconstrained splitting ratios in compact double-MMI couplers,” *Opt. Express*, vol. 22, no. 8, pp. 9245–9253, 2014.

[77] M. Bachmann, P. A. Besse, and H. Melchior, “Overlapping-image multimode interference couplers with a reduced number of self-images for uniform and nonuniform power splitting,” *Appl. Opt.*, vol. 34, no. 30, pp. 6898–6910, 1995.

[78] D. J. Y. Feng, T. S. Lay, and T. Y. Chang, “Waveguide couplers with new power splitting ratios made possible by cascading of short multimode interference sections,” *Opt. Express*, vol. 15, no. 4, pp. 1588–1593, 2007.

[79] D. S. Levy, Y. M. Li, R. Scarmozzino, and R. M. Osgood, “A multimode interference-based variable power splitter in GaAs-AlGaAs,” *IEEE Photon. Technol. Lett.*, vol. 9, no. 10, pp. 1373–1375, 1997.

[80] L. B. Soldano and E. C. M. Pennings, “Optical Multi-Mode Interference Devices Based on Self-Imaging: Principles and Applications,” *J. Lightw. Technol.*, vol. 13, no. 4, pp. 615–627, 1995.

[81] O. Bryngdahl, “Image formation using self-imaging techniques,” *J. Opt. Soc. Am.*, vol. 63, no. 4, pp. 416–419, 1973.

[82] R. Ulrich and G. Ankele, “Self-imaging in homogeneous planar optical waveguides,” *Appl. Phys. Lett.*, vol. 27, no. 6, pp. 337–339, 1975.

[83] M. Bachmann, P. A. Besse, and H. Melchior, “General self-imaging properties in N×N multimode interference couplers including phase relations,” *Appl. Opt.*, vol. 33, no. 18, pp. 3905–3911, 1994.

[84] M. V. Berry and S. Klein, “Integer, fractional and fractal Talbot effects,” *J. Mod. Opt.*, vol. 43, no. 10, pp. 2139–2164, 1996.

[85] W.-P. Huang and C. L. Xu, “Simulation of three-dimensional optical waveguides by a full-vector beam propagation method,” *IEEE J. Quantum Electron.*, vol. 29, no. 10, pp. 2639–2649, 1993.

[86] M. T. Hill, X. J. M. Leijtens, G. D. Khoe, and M. K. Smit, “Optimizing Imbalance and Loss in 2×2 3-dB Multimode Interference Couplers Via Access Waveguide Width,” *J. Lightw. Technol.*, vol. 21, no. 10, pp. 2305–2313, 2003.

[87] R. Halir, I. Molina-Fernandez, A. Ortega-Monux, J. G. Wanguemert-Perez, D.-X. Xu, P. Cheben, and S. Janz, “A Design Procedure for High-Performance, Rib-Waveguide-Based Multimode Interference Couplers in Silicon-on-Insulator,” *J. Lightw. Technol.*, vol. 26, no. 16, pp. 2928–2936, 2008.

[88] H. Li, Y. Liu, C. Galland, A. E.-J. Lim, G.-Q. Lo, T. Baehr-Jones, and M. Hochberg, “A High-Efficiency Nonuniform Grating Coupler Realized With 248-nm Optical Lithography,” *IEEE Photon. Technol. Lett.*, vol. 25, no. 14, pp. 1358–1361, 2013.

[89] P. A. Besse, M. Bachmann, H. Melchior, L. B. Soldano, and M. K. Smit, “Optical Bandwidth and Fabrication Tolerances of Multimode Interference Couplers,” *J. Lightw. Technol.*, vol. 12, no. 6, pp. 1004–1009, 1994.

[90] J. LeBlanc, M. O. Ward, and N. Wittels, “Exploring N-dimensional databases,” in *Proceedings of the First IEEE Conference on Visualization*, pp. 230–237, Oct. 1990.

[91] “OIF-DPC-RX-01.1 - Implementation Agreement for Integrated Dual Polarization Intradyne Coherent Receivers,” Sept. 2011.

[92] R. Halir, G. Roelkens, A. Ortega-Monũx, and J. G. Wangüemert-Peréz, “High-performance 90° hybrid based on a Silicon-on-insulator multimode interference coupler,” *Opt. Lett.*, vol. 36, pp. 178–180, Jan. 2011.

[93] S.-H. Jeong and K. Morito, “Compact optical 90° hybrid employing a tapered 2x4 MMI coupler serially connected by a 2x2 MMI coupler,” *Opt. Express*, vol. 18, no. 5, pp. 4275–4288, 2010.

[94] M. Boudreau, M. Poirier, G. Yoffe, and B. Pezeshki, “An integrated InP-based coherent receiver for 40 and 100 Gb/sec telecommunications systems,” in *Optical Fiber Communications Conference and Exhibition (OFC)*, pp. 1–3, Mar. 2009.

[95] R.-Y. Zhang, K. Janiak, H.-G. Bach, R. Kunkel, A. Seeger, S. Schubert, M. Schell, A. Matiss, and A. Umbach, “Performance of InP-based 90°-hybrids QPSK receivers within C-Band,” in *23rd International Conference on Indium Phosphide and Related Materials*, pp. 1–3, May 2011.

[96] H.-G. Bach, A. Matiss, C. C. Leonhardt, R. Kunkel, D. Schmidt, M. Schell, and A. Umbach, “Monolithic 90° hybrid with balanced PIN photodiodes for 100 Gbit/s PM-QPSK receiver applications,” in *Optical Fiber Communications Conference and Exhibition (OFC)*, pp. 1 –3, Mar. 2009.

[97] C. Gordón, R. Guzmán, V. Corral, X. Leijtens, and G. Carpintero, “On-Chip Colliding Pulse Mode-locked laser diode (OCCP-MLLD) using multimode interference reflectors,” *Opt. Express*, vol. 23, no. 11, pp. 14666–14676, 2015.

[98] B. Gargallo, P. Muñoz, R. Baños, A. L. Giesecke, J. Bolten, T. Wahlbrink, and H. Kleinjans, “Reflective arrayed waveguide gratings based on Sagnac loop reflectors with custom spectral response,” *Opt. Express*, vol. 22, no. 12, pp. 14348–14362, 2014.

[99] L. Xu, X. J. M. Leijtens, B. Docter, T. de Vries, E. Smalbrugge, F. Karouta, and M. K. Smit, “MMI-reflector: A novel on-chip reflector for photonic integrated circuits,” in *European Conference on Optical Communication (ECOC)*, pp. 1–2, Sept. 2009.

[100] E. Kleijn, M. K. Smit, and X. J. M. Leijtens, “Multimode Interference Reflectors: A New Class of Components for Photonic Integrated Circuits,” *J. Lightw. Technol.*, vol. 31, no. 18, pp. 3055–3063, 2013.

[101] M. Cherchi, S. Ylinen, M. Harjanne, M. Kapulainen, and T. Aalto, “MMI resonators based on metal mirrors and MMI mirrors: an experimental comparison,” *Opt. Express*, vol. 23, no. 5, pp. 5982–5993, 2015.

[102] B. E. A. Saleh and M. C. Teich, *Fundamentals of Photonics, 2nd Edition*, ch. 8, pp. 299–308. Wiley, 2007.

[103] S. J. Orfanidis, *Electromagnetic Waves and Antennas*, ch. 8, pp. 305–307. Rutgers University, 2008.

[104] A. F. Oskooi, D. Roundy, M. Ibanescu, P. Bermel, J. D. Joannopoulos, and S. G. Johnson, “MEEP: A flexible free-software package for electromagnetic simulations by the FDTD method,” *Computer Physics Communications*, vol. 181, pp. 687–702, Jan. 2010.

[105] K. Solehmainen, T. Aalto, J. Dekker, M. Kapulainen, M. Harjanne, and P. Heimala, “Development of multi-step processing in Silicon-on-Insulator for optical waveguide applications,” *J. Opt. Pure Appl. Opt.*, vol. 8, no. 7, pp. S455–S460, 2006.

[106] E. Kleijn, D. Melati, A. Melloni, T. de Vries, M. K. Smit, and X. J. M. Leijtens, “Multimode Interference Couplers With Reduced Parasitic Reflections,” *IEEE Photon. Technol. Lett.*, vol. 26, no. 4, pp. 408–410, 2014.

[107] P. W. East, “Design techniques and performance of digital IFM,” *IEE Proceedings F (Commun., Radar and Signal Process.)*, vol. 129, no. 3, pp. 154–163, 1982.

[108] H. Gruchala and M. Czyzewski, “The instantaneous frequency measurement receiver in the complex electromagnetic environment,” in *Int. Conf. on Microw., Radar and Wireless Commun (MIKON)*, vol. 1, pp. 155–158, May 2004.

[109] G.-C. Liang, C.-F. Shih, R. S. Withers, B. F. Cole, and J. M. E., “Space-qualified superconductive digital instantaneous frequency-measurement subsystem,” *IEEE Trans. Microw. Theory Techn.*, vol. 44, no. 7, pp. 1289–1299, 1996.

[110] M. de Souza, F. Silva, M. De Melo, and L. R. G. S. L. Novo, “Discriminators for Instantaneous Frequency Measurement Subsystem Based on Open-Loop Resonators,” *IEEE Trans. Microw. Theory Techn.*, vol. 57, no. 9, pp. 2224–2231, 2009.

[111] X. Zou and J. Yao, “An Optical Approach to Microwave Frequency Measurement With Adjustable Measurement Range and Resolution,” *IEEE Photon. Technol. Lett.*, vol. 20, no. 23, pp. 1989–1991, 2008.

[112] H. Emami, N. Sarkhosh, L. A. Bui, and A. Mitchell, “Amplitude independent RFinstantaneous frequency measurementsystem using photonic Hilbert transform,” *Opt. Express*, vol. 16, no. 18, pp. 13707–13712, 2008.

[113] M. V. Drummond, P. Monteiro, and R. N. Nogueira, “Photonic rf instantaneous frequency measurement system by means of a polarization-domain interferometer,” *Opt. Express*, vol. 17, no. 7, pp. 5433–5438, 2009.

[114] J. Zhou, S. Fu, S. Aditya, P. P. Shum, and C. Lin, “Instantaneous Microwave Frequency Measurement Using Photonic Technique,” *IEEE Photon. Technol. Lett.*, vol. 21, no. 15, pp. 1069–1071, 2009.

[115] H. Guo, G. Xiao, N. Mrad, and J. Yao, “Measurement of Microwave Frequency Using a Monolithically Integrated Scannable Echelle Diffractive Grating,” *IEEE Photon. Technol. Lett.*, vol. 21, pp. 45–47, Jan 2009.

[116] X. Zou, H. Chi, and J. Yao, “Microwave Frequency Measurement Based on Optical Power Monitoring Using a Complementary Optical Filter Pair,” *IEEE Trans. Microw. Theory Techn.*, vol. 57, no. 2, pp. 505–511, 2009.

[117] S. Pan and J. Yao, “Instantaneous Microwave Frequency Measurement Using a Photonic Microwave Filter Pair,” *IEEE Photon. Technol. Lett.*, vol. 22, no. 19, pp. 1437–1439, 2010.

[118] X. Zou, W. Pan, B. Luo, and L. Yan, "Photonic Instantaneous Frequency Measurement Using a Single Laser Source and Two Quadrature Optical Filters," *IEEE Photon. Technol. Lett.*, vol. 23, no. 1, pp. 39–41, 2011.

[119] S. Pan, J. Fu, and J. Yao, "Photonic approach to the simultaneous measurement of the frequency, amplitude, pulse width, and time of arrival of a microwave signal," *Opt. Lett.*, vol. 37, no. 1, pp. 7–9, 2012.

[120] W. Li, N. H. Zhu, and L. X. Wang, "Brillouin-assisted microwave frequency measurement with adjustable measurement range and resolution," *Opt. Lett.*, vol. 37, no. 2, pp. 166–168, 2012.

[121] S. Zheng, S. Ge, X. Zhang, H. Chi, and X. Jin, "High-Resolution Multiple Microwave Frequency Measurement Based on Stimulated Brillouin Scattering," *IEEE Photon. Technol. Lett.*, vol. 24, no. 13, pp. 1115–1117, 2012.

[122] D. Marpaung, "On-Chip Photonic-Assisted Instantaneous Microwave Frequency Measurement System," *IEEE Photon. Technol. Lett.*, vol. 25, no. 9, pp. 837–840, 2013.

[123] L. A. Bui and A. Mitchell, "Remoted all optical instantaneous frequency measurement system using nonlinear mixing in highly nonlinear optical fiber," *Opt. Express*, vol. 21, no. 7, pp. 8550–8557, 2013.

[124] B. Lu, W. Pan, X. Zou, B. Luo, L. Yan, X. Liu, and S. Xiang, "Photonic Frequency Measurement and Signal Separation for Pulsed/CW Microwave Signals," *IEEE Photon. Technol. Lett.*, vol. 25, pp. 500–503, March 2013.

[125] Y. Ogiso, Y. Tsuchiya, S. Shinada, S. Nakajima, T. Kawanishi, and H. Nakajima, "High Extinction-Ratio Integrated Mach-Zehnder Modulator With Active Y-Branch for Optical SSB Signal Generation," *IEEE Photon. Technol. Lett.*, vol. 22, no. 12, pp. 941–943, 2010.

[126] S. R. Harmon, V. J. Urick, J. F. Diehl, and K. J. Williams, "Tandem Electrooptic Modulation and Interferometric Detection: Theory and Application," *IEEE Photon. J.*, vol. 5, no. 4, pp. 5501211–5501211, 2013.

[127] E. L. Wooten, K. M. Kissa, A. Yi-Yan, E. J. Murphy, D. A. Lafaw, P. F. Hallemeier, D. Maack, D. V. Attanasio, D. J. Fritz, G. J. McBrien, and D. E. Bossi, "A review of lithium niobate modulators for fiber-optic communications systems," *IEEE J. Sel. Topics Quantum Electron.*, vol. 6, no. 1, pp. 69–82, 2000.

[128] R. A. Griffin, S. K. Jones, N. Whitbread, S. C. Heck, and L. N. Langley, "InP Mach-Zehnder Modulator Platform for 10/40/100/200-Gb/s Operation," *IEEE J. Sel. Topics Quantum Electron.*, vol. 19, no. 6, pp. 158–166, 2013.

[129] K. Prosyk, A. Ait-Ouali, C. Bornholdt, T. Brast, M. Gruner, M. Hamacher, D. Hoffmann, R. Kaiser, R. Millett, K. Velthaus, and I. Woods, “High performance 40GHz InP Mach-Zehnder modulator,” in *Optical Fiber Communication Conference and Exhibition (OFC)*, pp. 1–3, March 2012.

[130] “`http://www.photonicsinc.com/modulator_bias_controller.html`.”

[131] “`http://www.hamamatsu.com/eu/en/index.html`.”

[132] “`http://www.widebandsystems.com/ifm.html`.”

[133] F. Bucholtz, V. J. Urick, M. Godinez, and K. J. Williams, “Graphical Approach for Evaluating Performance Limitations in Externally Modulated Analog Photonic Links,” *IEEE Trans. Microw. Theory Techn.*, vol. 56, no. 1, pp. 242–247, 2008.

[134] T. E. Darcie and J. Zhang, “High-performance microwave-photonic links,” in *IEEE Radio and Wireless Symposium*, pp. 125 –128, Jan. 2008.

[135] R. S. Weis and T. K. Gaylord, “Lithium niobate: Summary of physical properties and crystal structure,” *Applied Physics A*, vol. 37, no. 4, pp. 191–203, 1985.

[136] M. J. LaGasse and S. Thaniyavaru, “Bias-free high-dynamic-range phase-modulated fiber-optic link,” *IEEE Photon. Technol. Lett.*, vol. 9, no. 5, pp. 681–683, 1997.

[137] V. J. Urick, F. Bucholtz, P. S. Devgan, J. D. McKinney, and K. J. Williams, “Phase Modulation With Interferometric Detection as an Alternative to Intensity Modulation with Direct Detection for Analog-Photonic Links,” *IEEE Trans. Microw. Theory Techn.*, vol. 55, no. 9, pp. 1978 –1985, 2007.

[138] J. D. McKinney, K. Colladay, and K. J. Williams, “Linearization of Phase-Modulated Analog Optical Links Employing Interferometric Demodulation,” *J. Lightw. Technol.*, vol. 27, no. 9, pp. 1212 –1220, 2009.

[139] B. M. Haas, V. J. Urick, J. D. McKinney, and T. E. Murphy, “Dual-Wavelength Linearization of Optically Phase-Modulated Analog Microwave Signals,” *J. Lightw. Technol.*, vol. 26, no. 15, pp. 2748 –2753, 2008.

[140] T. E. Darcie, J. Zhang, P. F. Driessen, and J.-J. Eun, “Class-B Microwave-Photonic Link Using Optical Frequency Modulation and Linear Frequency Discriminators,” *J. Lightw. Technol.*, vol. 25, no. 1, pp. 157 –164, 2007.

[141] D. Marpaung, C. Roeloffzen, A. Leinse, and M. Hoekman, “A photonic chip based frequency discriminator for a high performance microwave photonic link,” *Opt. Express*, vol. 18, no. 26, pp. 27359–27370, 2010.

[142] J. M. Wyrwas, M. S. Rasras, Y. K. Chen, M. A. Cappuzzo, E. Y. Chen, L. T. Gomez, F. Klemens, R. Keller, M. P. Earnshaw, F. Padro, C. Bolle, R. Peach, C. Middleton, R. DeSalvo, and M. C. Wu, "Dynamic linearity improvement of phase and frequency modulated microwave photonic links using optical lattice filter discriminators," in *IEEE International Topical Meeting on Microwave Photonics (MWP)*, pp. 41 –44, Oct. 2011.

[143] M. S. Rasras, Y. Chen, K.-Y. Tu, M. P. Earnshaw, F. Pardo, M. A. Cappuzzo, E. Y. Chen, L. T. Gomez, F. Klemens, B. Keller, C. Bolle, L. Buhl, J. M. Wyrwas, M. C. Wu, R. Peach, S. Meredith, C. Middleton, and R. DeSalvo, "Reconfigurable Linear Optical FM Discriminator," *IEEE Photon. Technol. Lett.*, vol. 24, no. 20, pp. 1856 –1859, 2012.

[144] T. E. Darcie, A. Moye, P. F. Driessen, J. D. Bull, H. Kato, and N. A. F. Jaeger, "Noise Reduction in Class-AB Microwave-Photonic Links," in *IEEE International Topical Meeting on Microwave Photonics (MWP)*, pp. 329–332, Oct 2005.

[145] T. E. Darcie and P. F. Driessen, "Class-AB techniques for high-dynamic-range microwave-photonic links," *IEEE Photon. Technol. Lett.*, vol. 18, no. 8, pp. 929–931, 2006.

[146] F. You, S. H. K. Embabi, and E. Sanchez-Sinencio, "Low-voltage class AB buffers with quiescent current control," *IEEE J. Solid-State Circuits*, vol. 33, no. 6, pp. 915–920, 1998.

[147] P. F. Driessen, T. E. Darcie, and J. Zhang, "Analysis of a Class-B Microwave-Photonic Link Using Optical Frequency Modulation," *J. Lightw. Technol.*, vol. 26, no. 15, pp. 2740–2747, 2008.

[148] B. Boashash, "Estimating and interpreting the instantaneous frequency of a signal. I. Fundamentals," *Proceedings of the IEEE*, vol. 80, no. 4, pp. 520–538, 1992.

[149] J. M. Wyrwas and M. C. Wu, "Dynamic Range of Frequency Modulated Direct-Detection Analog Fiber Optic Links," *J. Lightw. Technol.*, vol. 27, no. 24, pp. 5552 –5562, 2009.

[150] F. Li, Y. Park, and J. Azaña, "Complete temporal pulse characterization based on phase reconstruction using optical ultrafast differentiation (PROUD)," *Opt. Lett.*, vol. 32, no. 22, pp. 3364–3366, 2007.

[151] E. W. Weisstein, "Second Fundamental Theorem of Calculus," *From MathWorld – A Wolfram Web Resource.* `http://mathworld.wolfram.com/`.

[152] J. Kim and C. K. Madsen, "Double-Ring Resonance-Enhanced Linear Photonic Frequency Discriminator for Microwave-Photonic Links," *J. Lightw. Technol.*, vol. 32, no. 1, pp. 35–39, 2014.

[153] D. A. I. Marpaung, C. G. H. Roeloffzen, R. B. Timens, A. Leinse, and M. Hoekman, "Design and realization of an integrated optical frequency modulation discriminator for a high performance microwave photonic link," in *IEEE International Topical Meeting on Microwave Photonics (MWP)*, pp. 131–134, Oct. 2010.

[154] M. Hamacher, R. Kaiser, H. Heidrich, P. Albrecht, B. Borchert, K. Janiak, R. Loffler, S. Malchow, W. Rehbein, and H. Schroeter-Janssen, "Monolithic integration of lasers, photodiodes, waveguides and spot size converters on GaInAsP/InP for photonic IC applications," in *International Conference on Indium Phosphide and Related Materials*, pp. 21 –24, 2000.

[155] "VNI Global Mobile Data Traffic Forecast, 2015 - 2020," tech. rep., Cisco Systems, 2016.

[156] J. G. Andrews, S. Buzzi, C. Wan, S. V. Hanly, A. Lozano, A. C. K. Soong, and J. C. Zhang, "What Will 5G Be?," *IEEE J. Sel. Areas Commun.*, vol. 32, no. 6, pp. 1065–1082, 2014.

[157] T. Bauer, C. Eggs, K. Wagner, and P. Hagn, "A Bright Outlook for Acoustic Filtering: A New Generation of Very Low-Profile SAW, TC SAW, and BAW Devices for Module Integration," *IEEE Microwave Magazine*, vol. 16, pp. 73–81, Aug 2015.

[158] R. Aigner, "Filter technologies for converged RF-frontend architectures: SAW, BAW and beyond," in *Topical Meeting on Silicon Monolithic Integrated Circuits in RF Systems (SiRF)*, pp. 136–139, Jan 2010.

[159] R. Aigner, "SAW and BAW Technologies for RF Filter Applications: A Review of the Relative Strengths and Weaknesses," in *IEEE Ultrasonics Symposium (IUS)*, pp. 582–589, Nov 2008.

[160] J. Capmany, B. Ortega, and D. Pastor, "A Tutorial on Microwave Photonic Filters," *J. Lightw. Technol.*, vol. 24, no. 1, pp. 201–229, 2006.

[161] A. Byrnes, R. Pant, E. Li, D.-Y. Choi, C. G. Poulton, S. Fan, S. Madden, B. Luther-Davies, and B. J. Eggleton, "Photonic chip based tunable and reconfigurable narrowband microwave photonic filter using stimulated Brillouin scattering," *Opt. Express*, vol. 20, no. 17, pp. 18836–18845, 2012.

[162] D. Marpaung, B. Morrison, M. Pagani, R. Pant, D.-Y. Choi, B. Luther-Davies, S. J. Madden, and B. J. Eggleton, "Low-power, chip-based stimulated Brillouin scattering microwave photonic filter with ultrahigh selectivity," *Optica*, vol. 2, no. 2, pp. 76–83, 2015.

[163] A. Choudhary, I. Aryanfar, S. Shahnia, B. Morrison, K. Vu, S. Madden, B. Luther-Davies, D. Marpaung, and B. J. Eggleton, "Tailoring of the Brillouin gain for on-chip widely tunable and reconfigurable broadband microwave photonic filters," *Opt. Lett.*, vol. 41, no. 3, pp. 436–439, 2016.

[164] A. Casas-Bedoya, B. Morrison, M. Pagani, D. Marpaung, and B. J. Eggleton, "Tunable narrowband microwave photonic filter created by stimulated Brillouin scattering from a silicon nanowire," *Opt. Lett.*, vol. 40, no. 17, pp. 4154–4157, 2015.

[165] L. R. Chen, J. Li, M. Spasojevic, and R. Adams, "Nanowires and sidewall Bragg gratings in silicon as enabling technologies for microwave photonic filters," *Opt. Express*, vol. 21, no. 17, pp. 19624–19633, 2013.

[166] D. Marpaung, B. Morrison, R. Pant, C. Roeloffzen, A. Leinse, M. Hoekman, R. Heideman, and B. J. Eggleton, "Si3N4 ring resonator-based microwave photonic notch filter with an ultrahigh peak rejection," *Opt. Express*, vol. 21, no. 20, pp. 23286–23294, 2013.

[167] P. Alipour, A. A. Eftekhar, A. H. Atabaki, Q. Li, S. Yegnanarayanan, C. K. Madsen, and A. Adibi, "Fully reconfigurable compact RF photonic filters using high-Q silicon microdisk resonators," *Opt. Express*, vol. 19, no. 17, pp. 15899–15907, 2011.

[168] K.-Y. Tu, M. S. Rasras, D. M. Gill, S. S. Patel, Y.-K. Chen, A. E. White, A. Pomerene, D. Carothers, J. Beattie, M. Beals, J. Michel, and L. C. Kimerling, "Silicon RF-Photonic Filter and Down-Converter," *J. Lightw. Technol.*, vol. 28, no. 20, pp. 3019–3028, 2010.

[169] N.-N. Feng, P. Dong, D. Feng, W. Qian, H. Liang, D. C. Lee, J. B. Luff, A. Agarwal, T. Banwell, R. Menendez, P. Toliver, T. K. Woodward, and M. Asghari, "Thermally-efficient reconfigurable narrowband RF-photonic filter," *Opt. Express*, vol. 18, no. 24, pp. 24648–24653, 2010.

[170] R. Hernández, A. Loayssa, and D. Benito, "Optical vector network analysis based on single-sideband modulation," *Optical Engineering*, vol. 43, no. 10, pp. 2418–2421, 2004.

[171] Y. O. Barmenkov, D. Zalvidea, S. Torres-Peiró, J. L. Cruz, and M. V. Andrés, "Effective length of short Fabry-Perot cavity formed by uniform fiber Bragg gratings," *Opt. Express*, vol. 14, no. 14, pp. 6394–6399, 2006.

[172] R. Halir, L. Vivien, X. Le Roux, D.-X. Xu, and P. Cheben, "Direct and Sensitive Phase Readout for Integrated Waveguide Sensors," *IEEE Photon. J.*, vol. 5, no. 4, pp. 6800906–6800906, 2013.